J/psi-hadron correlations in proton-proton collisions at 13 TeV with ALICE

Lucas Altenkämper

Thesis for the degree of Philosophiae Doctor (PhD)
University of Bergen, Norway
2020

UNIVERSITY OF BERGEN

J/psi-hadron correlations in proton-proton collisions at 13 TeV with ALICE

Lucas Altenkämper

Thesis for the degree of Philosophiae Doctor (PhD)
at the University of Bergen

Date of defense: 17.12.2020

Year: 2020

Title: J/psi-hadron correlations in proton-proton collisions at 13 TeV with ALICE

Name: Lucas Altenkämper

Print: Skipnes Kommunikasjon / University of Bergen

Abstract

The production mechanism of the J/ψ provides a testing ground for the understanding of the strong interaction due to the interplay between perturbative and non-perturbative regimes. It is not yet perfectly understood and some theoretical challenges remain in the description of the underlying processes. New experimental observables like the correlation of J/ψ and associated multiplicity might provide new insights and help to constrain the models. In addition, the J/ψ is an important observable for deconfinement in heavy ion collisions and measurements in proton-proton collisions yield relevant baselines for such studies.

In the analysis presented in this thesis, the angular correlations between unidentified, charged hadrons and inclusive, non-prompt and prompt J/ψ are measured in proton-proton collisions at center-of-mass energies of 13 TeV. The data has been recorded by the ALICE experiment at the CERN LHC in the period from 2016 to 2018 and different triggers are exploited to maximize the available statistics and phase space coverage. The J/ψ mesons are reconstructed in the electron-positron decay channel at mid-rapidity and measured down to vanishing transverse momentum. The correlation functions are determined in different kinematical regimes and the correlated yields are evaluated in addition.

The results shown in this thesis represent the first measurement of the non-prompt and prompt J/ψ correlation functions at mid-rapidity by ALICE. While statistically limited, the results provide a good starting point for the comparison to model calculations and hint at the importance of hard interactions in the J/ψ production mechanism. Indications of differences between minimum bias and high multiplicity events are observed which should motivate future analyses based on higher statistics data samples. The results are compared to PYTHIA simulations which qualitatively agree with the data and seem to reproduce most of the features observed.

Acknowledgement

I would like to express my gratitude towards my supervisors Dieter Röhrich, Ionut Arsene and Fiorella Fionda for the opportunity to explore this fascinating topic. The great working environment, the guidance as well as all the insightful discussions are greatly appreciated. This, of course, also extends to the entire Jpsi2ee and DQ working groups and everybody that showed interest in the analysis. I would furthermore like to thank all my friends and colleagues at the institutes here in Bergen, in Heidelberg and at CERN for the wonderful collaboration. All the discussions, the support and even the distractions meant a great deal to me. My parents Martina and Hildo, my sister Laura, my family and friends were always supportive and incredible patient with me. I did not take this for granted, even if I might not have shown it, and I am truly grateful for that. Last but not least I want to thank my girlfriend Sarah. You had to endure me being occupied near constantly and often irritated but you were always accepting of it. This would not have been possible without your endless support and I will be forever thankful for that.

Contents

1. Introduction

> All you really need to know for the moment is that the universe is a lot more complicated than you might think, even if you start from a position of thinking it's pretty damn complicated in the first place.
>
> Douglas Adams, *Mostly Harmless*

In *The Hitchhiker's Guide to the Galaxy*, Douglas Adams wrote: 'Isn't it enough to see that a garden is beautiful without having to believe that there are fairies at the bottom of it too?' And even though one can appreciate the beauty of nature without deeper questioning, human curiosity still leads us wondering if those 'fairies' exist and what they might be. Or to put it into more scientific terms: What are the makings of the universe? Are there fundamental building blocks that make up everything? And if so, what is their nature?

This line of questioning has motivated scientists for a long time in the search for fundamental building blocks of matter and the quest to understand the nature of interactions amongst them. The first ideas of fundamental units can be traced back to the ancient greek philosopher Democritus, who theorized that matter is composed of indivisible units called atomos[1]. These atoms were thought to exist in different kinds and the qualities of any object are a result of its composition in terms of atoms. About two millennia later in the early 19th century, Dalton used atomic theory to explain the observation he made in chemical experiments that different elements always react in ratios of whole numbers. Further steps towards the identification of fundamental building blocks were the discovery of charged ions in so-called anode rays[2] by Goldstein in 1886 [1] and the subsequent identification of cathode rays with the electron, a subatomic particle of negative charge, by Thomson in 1897 [2]. Thomson was able to show that the electron

[1] The word 'atom' originates in the greek word 'atomos' which translates to 'undivided' or 'uncuttable'.

[2] Anode rays were historically called 'Kanalstrahlen' by the German physicist Goldstein, which translates to 'canal ray' or 'channel ray' in English.

was much lighter than the lightest atom and atoms could thus be ruled out as the most fundamental particles. In 1904, he proposed the plum pudding model [3] to describe the atom, which assumes that the electrons are evenly distributed throughout a volume of positive charge. The contemporary model of matter was further expanded by the Geiger-Marsden experiment, also known as the Rutherford gold foil experiment, in 1911 [4]. The experiment showed that atoms are composed of a concentrated positive charge, the atomic nucleus, surrounded by a cloud of electrons. This model superseded the previous understanding and became known as the Rutherford model of atoms. It was later improved further to the Bohr model of the atom in 1913 [5], which places the electrons surrounding the atomic nucleus in dedicated shells corresponding to the energy states of the atom. Shortly after the formulation of the Bohr model of the atom, the proton was identified as a separate particle by Rutherford [6]. Before this discovery in 1919, the existence of the proton was only indirectly observed through the positive charge of the atomic nucleus. The atom was now understood to be composed of more basic quantities but following observations were going to change the idea of fundamental units again.

In more recent experiments during the 1950s and 60s, a wealth of new particles was discovered. The large number of these newly observed particles, so-called hadrons, was difficult to understand within the contemporary framework of physics. However, it could be explained in fundamental terms by assuming microscopic constituents that form these hadrons similar in spirit but quite unlike the way the atom is composed of smaller units of matter. The first version of such an explanation was introduced in the early 1960s independently by Murray Gell-Mann [7] and George Zweig [8]. Both approaches required the existence of fundamental particles, called quarks by Gell-Mann and aces by Zweig. The wealth of newly discovered particles could then be organized according to the properties of these fundamental particles. Gell-Mann received the Nobel prize in physics in 1969 for his model, which he called the 'Eightfold Way', after the discovery of a particle, the Ω^-, that was predicted by his model. The fundamental units proposed by Gell-Mann and Zweig were initially thought of as a mathematical curiosity rather than actual physical entities due to their fractional charge required by the models. Further discoveries, however, changed this interpretation. In between 1967 and 1973, experiments performed at the Stanford Linear Accel-

erator Center (SLAC) showed that the proton is not a fundamental particle as originally thought, but composed of smaller constituents [9]. These constituents were described by Richard Feynman in his parton model in 1969 [10] in terms of fractional momentum carriers of the proton. The partons observed at SLAC were later identified with the quarks or aces proposed by Gell-Mann and Zweig. Quarks[3] are to this day still considered the fundamental building blocks of matter.

A later discovery showed that the quark model as proposed by Gell-Mann and Zweig was not yet sufficient to describe the nature of fundamental constituents of matter entirely. This discovery was the observation of the J/ψ by two separate groups headed by Burton Richter [11] and Samuel Ting [12] at SLAC and Brookhaven National Laboratory (BNL), respectively, that proved the existence of a fourth quark not included in the original models. Both Richter and Ting were awarded the Nobel prize in physics in 1976 for the discovery of the J/ψ in two independent experiments. The existence of a fourth quark was already theorized as early as 1964-1970 by Sheldon Glashow, James Bjorken, John Iliopoulos, and Luciano Maiani [13, 14] and validated by the observation of the J/ψ, superseding the previous model of quarks. The remaining two of the six quarks of the current standard model of particle physics were discovered at Fermilab in 1977 (bottom quark) [15] and in 1995 (top quark) [16, 17]. These discoveries completed the picture of elementary particles of matter according to our current knowledge.

The picture of what is considered fundamental has changed significantly over the decades, starting from the philosophical idea of the atom to the smallest building blocks observed to date. It is thus impossible to say if the quarks that have been discovered and described theoretically thus far are truly the 'fairies' at the bottom of all. However, quarks and the interactions amongst them are still very much subject of current research and there is much left to uncover.

A Large Ion Collider Experiment (ALICE) is an experiment dedicated to the study of the strong interaction, the force between quarks, at the Conseil Européen pour la Recherche Nucléaire (CERN) in Switzerland. It is one of the four big experiments at the Large Hadron Collider (LHC), with the remaining three being: A Toroidal LHC Apparatus (ATLAS), Compact Muon Solenoid (CMS) and LHC-beauty (LHCb). The goal of the ALICE experiment is the detailed study and

[3]While quarks and aces were originally interchangeable terms describing the same thing, the term quark has established itself over time and ace is not used anymore.

characterization of the Quark-Gluon Plasma (QGP), a deconfined system of quasi-free quarks and gluons which will be described in further detail in section 2.4. Such studies will lead to an improved understanding of the strong interaction and allow to peak deeper into the most microscopic scales accessible to date. The QGP can be produced in the laboratory by utilizing heavy-ion collisions that provide very high energy densities in the interaction region. The LHC has a dedicated heavy-ion program providing lead-lead[4] collisions with center-of-mass energies up to 5 TeV per nucleon pair. In addition, ALICE also studies proton-proton and proton-ion collisions to disentangle different effects that can be observed in either collision type.

The analysis presented in this thesis is based on data collected by ALICE in proton-proton collisions and aims at furthering the understanding of the J/ψ production mechanism. As is discussed in chapter 2, the J/ψ is a very interesting probe for improving the understanding of the strong interaction and the mechanisms involved in its formation are not truly understood yet. Typical measurements of J/ψ mesons are presented by transverse momentum and rapidity differential production cross sections as well as polarization measurements. Some tensions between model predictions and the data are observed as is discussed on exemplary results in section 2.3. The measurement and quantification of correlations between J/ψ mesons and associated hadrons can help to shed light on the production mechanisms by providing additional, independent constraints on models.

This thesis is organized as follows: An overview over the relevant theoretical background is presented in the next chapter, while the experimental apparatus used in the analysis is introduced in chapter 3. Chapter 4 details the data sample and Monte Carlo (MC) simulations the analysis is based on. The analysis method and procedure is described in chapter 5. Systematic uncertainties associated with the measurement are summarized in chapter 6 and finally the results are presented and discussed in chapter 7. The thesis closes with a conclusion and a brief outlook on future prospects in chapter 8.

[4]While lead ions are typically used in the heavy-ion program of the LHC, a short run using xenon ions was also performed in 2017.

2. Theoretical background

There are four fundamental forces in nature: gravity, the electromagnetic force, the weak force and the strong force. While gravity is responsible for effects seen at large scales, like the orbital dynamics in our solar system, it is by far the weakest of the four fundamental forces and thus negligible in the interaction of particles.

At microscopic scales, only the three remaining forces are relevant. All of these three forces govern the interactions between fundamental particles of matter, which are called fermions. The forces are conveyed through so-called exchange bosons that couple to the matter particles and in some cases even other bosons. The bosons are integer spin particles while the fermions have half-integer spin.

The electromagnetic force is conveyed by the massless photon and is, amongst other things, responsible for virtually all interactions between atoms. The effects of the electromagnetic force can thus be observed even at macroscopic scales. It ensures, for example, that the atoms of the paper this thesis is printed on do not pass through the vast empty spaces in between the atoms of the desk it is resting on. All particles that carry electric charge, for example charged leptons like the electron, quarks or even the charged exchange bosons of the weak force, are subject to the electromagnetic force.

The weak force, on the other hand, does not require any specific charge to interact with. It couples to any type of fermion, either electrically charged or neutral. Certain types of interactions even allow for the carriers of the weak force to interact with themselves, which is not possible for the electromagnetic force. The force carriers of the weak force are the charged $W^{\pm}$ and the neutral Z^0 bosons, which were discovered in 1983 at CERN [18, 19, 20, 21] and for which the Nobel prize in physics was awarded to Carlo Rubbia and Simon van der Meer in 1984. In contrast to the massless photon, the weak bosons are quite heavy. Due to the high mass of the $W^{\pm}$ and Z^0 bosons, the weak force is perceived as weaker than electromagnetism although they are similar in coupling strength. The weak force is responsible, amongst other things, for radioactive decays.

While the electromagnetic interaction can generally be described by a dedicated Quantum Field Theory (QFT) called Quantum Electrodynamics (QED), experimental observations are not fully explained by it at all energy scales. This is due to the convergence of the electromagnetic and weak forces at a certain energy scale that roughly corresponds to the mass of the Z^0 boson. Like the photon, the Z^0 is electrically neutral and can take the place of the photon in any type of interaction, replacing the electromagnetic by the weak force. This, however, is penalized by the introduction of the mass of the boson in the propagator term of the interaction. At low energy scales, the contribution of Z^0 compared to photon exchange is thus negligible. This interplay between the two forces is accounted for by introducing a theory that models both interactions simultaneously. The electromagnetic and the weak forces are hereby described within the same theoretical framework called Electro-Weak Theory (EWT).

The strong force is responsible for the existence of hadronic matter like the protons and neutrons within the atomic nucleus. It governs the interactions between quarks, the fundamental particles of matter that make up all hadrons, and the corresponding force carriers: the gluons. Like the photon, the gluons are massless but much unlike the photon, they carry a charge under the strong interaction, which is called color charge. In addition to the interactions between quarks and gluons, the residual of the strong force reaching beyond the confines of hadrons is responsible for binding neutrons and protons inside the atomic nucleus. This is typically referred to as the nuclear force and it can be modeled using effective theories, the description of which exceeds the scope of this thesis. The strong force and its corresponding theoretical description, Quantum Chromodynamics (QCD), will be described in greater detail in section 2.1.

All of the particles are summarized and organized in the so-called standard model of particle physics, where interactions are described by dedicated QFTs. The matter particles are separated into two groups, quarks and leptons, and organized in three families each. The leptons, i.e. electrons, muons and taus, carry an electric charge of -1 e while the quarks carry fractional electric charge of $+\frac{2}{3}$ e and $-\frac{1}{3}$ e for up- and down-type quarks, respectively. In addition to the electric charge, quarks also carry charge under the strong interaction which enables the coupling to gluons. Neutrinos are electrically neutral leptons that, according to the standard model, are grouped together with the charged leptons in the

respective families. Every particle in the standard model also has a corresponding anti-particle with opposite charge, except for the neutral exchange bosons.

The last missing piece to the standard model of particle physics, the Higgs boson, was discovered by ATLAS [22] and CMS [23] at CERN in 2012. The Higgs mechanism and the corresponding boson are responsible for the generation of mass via coupling to the boson in the case of fundamental matter particles and through spontaneous symmetry breaking for the $W^{\pm}$ and Z^0. In 2013, shortly after the independent discovery of the boson by the two experiments, the Nobel prize in physics was awarded to Peter Higgs and Francois Englert for the theoretical description of the mechanism and the prediction of the boson.

In the following chapters, the strong force as well as the corresponding QFT will be described in greater detail. While all of the standard model is worth studying, the focus of this thesis lies on QCD and the formation of bound states of heavy quarks.

2.1. Quantum Chromodynamics

The strong force is described by a non-abelian QFT based on the SU(3) symmetry group, called Quantum Chromodynamics (QCD). Hereby, SU(3) is the minimal symmetry group required to describe the observed behavior of the strong interaction. This can best be exemplified on the Δ^{++} baryon, a hadron that is constituted of three up quarks. Baryons are, due to their half integer spin, fermions and must thus follow Fermi-Dirac statistics. The Pauli exclusion principle, which follows from Fermi-Dirac statistics, states that two fermions of identical wave function can not share the same energy state within a quantum system. A consequence of this is that the total wave function of the baryon must be completely anti-symmetric. The total wave function has several contributing parts: quark flavor, spin, space and charge. Out of those, only the charge can be made anti-symmetric by allowing for (at least) three different charges in QCD. The SU(3) symmetry group gives rise to a quantum number equivalent to the electric charge in QED but which can have three different values according to the order of the symmetry group. Higher order symmetry groups could also provide the features of QCD but SU(3) is the minimal one required to build a theory for the strong interaction.

The charge quantum number in QCD is called color charge and the three

different values are referred to as red, green and blue. Anti-quarks carry anti-color charge and combinations of color and anti-color (mesons) or all three colors (baryons) are color neutral or colorless. Color neutral states do not partake in the strong interaction as the gluons only couple to colored objects. However, constituent quarks inside hadronic bound states can still interact via the strong interaction. Leptons, like the electron, on the other hand are not charged under QCD and are thus not subject to strong interaction. The different combinations of color charges in the SU(3) symmetry group of QCD form a singlet and octet of states, where the color-singlet state is colorless.

In addition to the color charges, the SU(3) symmetry also gives rise to the eight massless gluons, the exchange bosons of the strong interaction, corresponding to the eight color combinations in the octet. As was mentioned before, and is apparent due to the generation corresponding to the color-octet state, the gluons carry color charge. This leads to a very distinct difference between QED and QCD: gluons can couple to each other, a feature that has not been observed for photons. Consequently, the range of QED is infinite while QCD has only a very limited reach of about 1 fm $= 1 \times 10^{-15}$ m, which approximately corresponds to the size of an atomic nucleus.

The QCD Lagrangian, also called the Yang-Mills Lagrangian, encodes all possible elementary interactions via the strong force:

$$\mathcal{L} = \bar{\psi} \left[i \left(\gamma^{\mu} D_{\mu} \right) - m \right] \psi - \frac{1}{4} G_{\mu\nu} G^{\mu\nu}, \tag{2.1}$$

where ψ is the quark spinor, m is the corresponding mass and γ^{μ} are the Dirac-matrices that contain the specific (anti)commutation relations of the theory. D_{μ} and $G^{a}_{\mu\nu}$ are the covariant derivative and the gluon field strength tensor, respectively, and can be written as:

$$D_{\mu} = \partial_{\mu} - \frac{i}{2} g_s A^{a}_{\mu} \lambda_a, \tag{2.2}$$

$$G^{a}_{\mu\nu} = \partial_{\mu} A^{a}_{\mu} - \partial_{\nu} A^{a}_{\mu} + g_s f^{abc} A^{b}_{\mu} A^{c}_{\nu}. \tag{2.3}$$

Hereby, g_s is the coupling strength of the strong interaction and the A^{a}_{μ} are the gluon fields where $a = 1, ..., 8$ is the gluon index. The λ_a are the eight Gell-Mann matrices which are representations of the color symmetry and f^{abc} are the structure constants of SU(3). The Gell-Mann matrices and the structure constants define the algebra of the symmetry group that encodes the color exchange between

the different participating partons. All possible interactions between quarks and gluons can then easily be read of the Lagrangian in equation 2.1 and expressions 2.2 and 2.3 therein. Interactions between two quarks (either qq, $q\bar{q}$ or $\bar{q}\bar{q}$) enter the Lagrangian in the spinor enclosed term via the covariant derivative and the contained gluon field while the mass term is non-interactive. In QCD, such vertices always involve coupling to a gluon, similar to the photon vertices in QED. Pure gluon couplings are represented by the $G_{\mu\nu}G^{\mu\nu}$ term that allows for vertices involving either three or four gluons.

The specific energy scale dependence of the coupling strength is a unique feature of the strong interaction and must thus also be represented in QCD. It has been observed that, contrary to the behavior in QED, the coupling strength of the strong interaction reduces with increasing momentum transfer. The coupling constant $\alpha_s = g_s/4\pi$ takes very large values of $\alpha_s \sim \mathcal{O}(1)$ at low energy scales but decreases at higher scales. The absolute value of the coupling constant can not be predicted from theory but its behavior can be modeled using a renormalization procedure. Hereby, the gluon propagator is regularized in order to terminate diverging integrals which results in the scale dependence of α_s. A comprehensive summary of the corresponding regularization procedure is presented in the review in reference [24]. The resulting scale dependence can be written as:

$$\alpha_s\left(Q^2\right) = \frac{\alpha_s\left(\mu^2\right)}{1 + B\alpha_s\left(\mu^2\right)\ln\left(\frac{Q^2}{\mu^2}\right)}, \tag{2.4}$$

where Q^2 is the energy scale of the interaction and μ^2 is a reference scale at which $\alpha_s(\mu^2)$ must have been measured. Additionally, $B = (11N_c - 2N_f)/12\pi$ where N_c and N_f are the numbers of colors and quark flavors of the theory. Equation 2.4 thus predicts a decrease of α_s with increasing Q^2 for QCD where $N_c = 3$ and $N_f = 6$. The value of α_s is typically measured at a reference scale that is of the order of the Z boson mass, i.e. $\mu^2 \sim m_{\mathrm{Z}}^2$, but other measurements also exist as can be seen in figure 2.1. The figure shows the scale dependence of the strong coupling constant from various measurements. The measured values are also compared to a prediction from renormalization where the mass of the Z boson was used as the reference scale. It can be seen that the behavior of α_s, modeled by renormalization, agrees very well with the data.

The scale dependence of α_s effectively splits QCD in two different regimes:

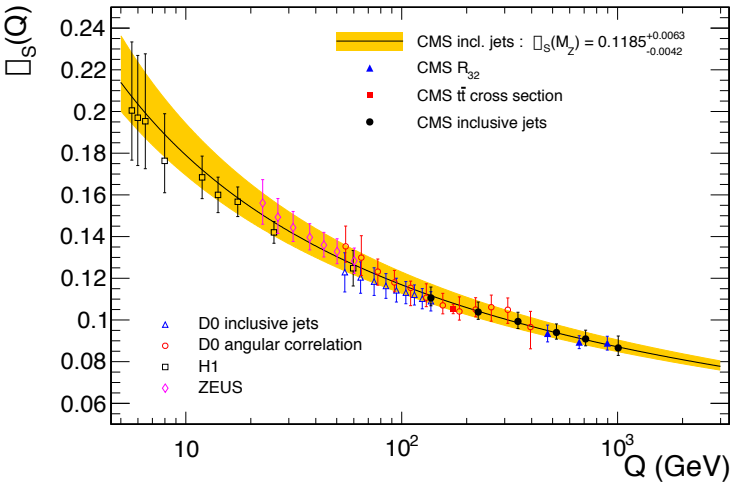

Figure 2.1.: Energy scale dependence of the strong coupling constant α_s from various measurements compared to a prediction of the scale dependence from renormalization. [25]

the coupling constant is very large at low energy scales and the theory behaves non-perturbatively while smaller values at higher scales allow for perturbative calculations. The idea behind perturbation theory is that higher order interactions contributing to a certain process become decreasingly relevant with increasing order of the coupling constant, such that the series converges quickly. This, however, is obviously only true for small coupling constants $\alpha_s \ll \mathcal{O}(1)$. In contrast to QCD, this is always the case for QED due to the small coupling constant $\alpha \sim 1/137$. The so-called running coupling in QCD allows for a perturbative description at high energy scales only, an approach that is often referred to as perturbative QCD (pQCD). At lower energy scales, different approaches have to be used in order to compute interaction rates. One popular approach is lattice QCD, where space-time is discretized on a lattice of fixed resolution and size. Interactions can then be calculated on such discretized space-time points without approximating QCD, but the approach is computationally very intensive. Lattice QCD is furthermore limited to equilibrium quantities and dynamics of the system are not modeled. Effective theories that approximate QCD in one way or another can also be used to calculate interaction rates at non-perturbative energy scales. Important examples for such models are introduced in section 2.3.

One other, very peculiar, feature of the strong interaction is that no free color charges have ever been observed except for in very extreme conditions. Quarks and gluons appear to be always bound into colorless hadrons. This feature is called confinement and it prohibits the free propagation of states of non-vanishing color charges. It has not yet been proven analytically but lattice QCD allows to build a mechanism that binds quarks into colorless states [26], known as a Wilson loops or Wilson lines. The confinement of quarks into colorless objects results in potentially large contributions to the hadron mass from the binding energy. For example the proton, which consists of two up quarks and one down quark, only receives about 1% of its total rest mass from the quark masses. The remainder of the proton mass must thus arise from the binding energy.

Qualitatively, confinement can be understood via the self interaction of gluons. The potential between a quark and an antiquark is compressed into a so-called color flux tube of fixed energy density rather than a dispersed field as is the case in QED. The fixed energy density leads to an ever increasing potential between the two quarks that is proportional to the separation distance. It would thus require an infinite amount of energy to separate two quarks, which provides a naive explanation for the confinement. Furthermore, if two quarks are being separated, the energy stored in the potential will at some point be sufficient to produce additional quark-antiquark pairs that couple to the initial pair. This process is called hadronization in reference to the production of new colorless objects, i.e. hadrons, from the vacuum and the initial partons.

There is also another contribution to the hadronization process besides the breaking of the color flux tube. This process is the radiation of gluons, similar to photon bremsstrahlung in QED, from a quark or gluon. Radiated gluons will further split into quarks or gluons until, eventually, the initial color charge is neutralized and the final state objects are bound within colorless hadrons. As can be seen for example in reference [27], the gluon emission amplitude exhibits the following proportionality:

$$N_g \propto \int_0 \frac{\mathrm{d}k}{k} \int_0 \frac{\mathrm{d}\theta}{\theta}, \tag{2.5}$$

where k is the gluon energy and θ is the angle between the radiated gluon and the initial parton. This proportionality contains two poles or divergencies: $k \to 0$ and $\theta \to 0$, which are called soft or infrared and collinear divergence, respectively.

Due to these divergencies, many gluons will be radiated either at narrow angles or low energies. The processes of gluon radiation, further splitting and subsequent hadronization create a spray of particles predominantly produced within a narrow cone that is usually referred to as a jet. Since hadronization processes are of statistical nature involving many different elementary processes, the breaking of the color flux tube as introduced in the previous paragraph ultimately also results in jet signatures.

Besides the color confinement, another relevant feature of the strong interaction is the so-called asymptotic freedom. The decrease of the coupling constant with increasing energy scale not only allows for a a perturbative description of the interaction but also leads to quarks being less strongly bound. The same effect can be observed when quarks are very densely packed since small length scales correspond to large momentum scales through the uncertainty principle. In the limit of $Q^2 \to \infty$, the coupling constant approaches zero and the quarks are quasi-free within the tightly packed system. This phenomenon is an experimentally well established fact [28] and it will be re-captured again in section 2.4. The discovery of asymptotic freedom in the theory of the strong interaction by David Gross, Frank Wilczek [29, 30] and David Politzer [31] was awarded with the Nobel Prize in Physics in 2004.

2.2. Quarkonia and the J/ψ

So-called quarkonia are bound states of heavy quark-antiquark pairs where the quark mass is higher than the QCD scale $\Lambda_{\mathrm{QCD}} \sim 255$ MeV [32], which is the renormalization scale of QCD. Thus, charm and bottom quarks with masses $m_{\mathrm{c}} = 1.27\ \mathrm{GeV}/c^2$ and $m_{\mathrm{b}} = 4.18\ \mathrm{GeV}/c^2$ [33], respectively, can form bound quarkonium states. However, no bound states of top quarks have yet been observed. This is due to the high mass $m_{\mathrm{t}} = 172.9\ \mathrm{GeV}/c^2$ [33] which leads to large decay rates that prevent the formation of bound states. Prominent examples of quarkonium states are the J/ψ and it's higher mass siblings, bound systems of $\mathrm{c\bar{c}}$, as well as the family of Υ states, bound systems of $\mathrm{b\bar{b}}$. The $\mathrm{c\bar{c}}$ states are typically referred to as charmonium, while $\mathrm{b\bar{b}}$ states are usually called bottomonium. In contrast to light-flavor hadrons like the proton, a large fraction of the quarkonium mass originates in the quark masses rather than the binding energy.

In positronium fashion, bound states of a heavy quark-antiquark pairs can be modeled phenomenologically by a simple, static potential called the Cornell potential:

$$V(r) \propto -\frac{\alpha_s}{r} + \kappa r, \tag{2.6}$$

where κ is a proportionality factor associated with color confinement at large distances. At small distances, the potential exhibits a coulomb-like $1/r$ dependence that allows for the formation of bound states. The masses of the different quarkonium states and the corresponding quantum numbers are shown in the spectra for $c\bar{c}$ and $b\bar{b}$ bound states in figure 2.2.

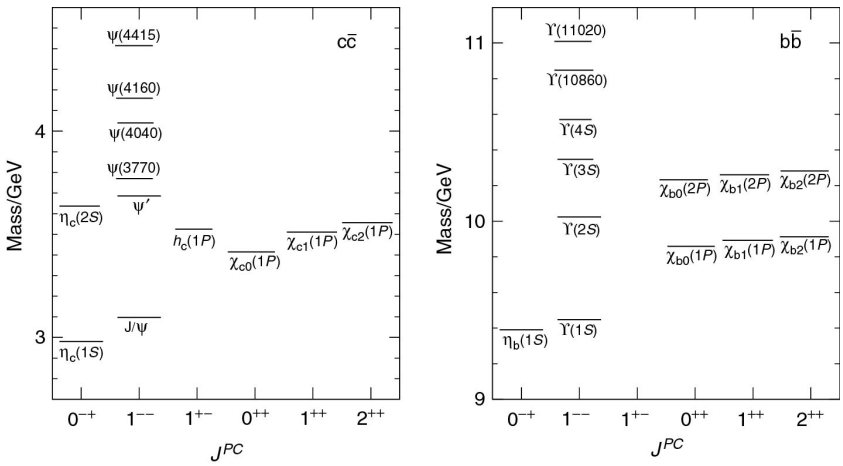

Figure 2.2.: Spectra of $c\bar{c}$ (*left*) and $b\bar{b}$ (*right*) bound states indicating the quantum numbers and masses. [34]

Quarkonia provide a test laboratory for QCD because of the different momentum scales involved in these particular systems. While the initial heavy quarks are typically produced at a perturbative momentum scale p, there are also at least three intrinsic scales where perturbative expansion is not possible. These non-perturbative scales play an especially important role during the formation of the bound state and the interplay between the regimes provides a challenge for precise modelling.

The perturbative scale p of the heavy quark production is defined by the large momentum transfer of the initial scattering process. At LHC energies, the typical

$c\bar{c}$ production process is gluon fusion, i.e. $gg \rightarrow c\bar{c}$, because of the dominance of the gluon parton distribution function (PDF) in the Bjorken-x range that is probed in the TeV-scale collisions at the LHC. In such collisions, the perturbative scale p is typically of the order of the transverse momentum p_T of the produced quarkonium state [35].

The three intrinsic scales for heavy quarkonium states that are usually considered are the heavy-quark mass m_q, the heavy quark momentum in the quarkonium rest frame $m_q v$ and the binding energy of the quark pair $m_q v^2$, where v is the velocity of the heavy quark in the rest frame of the bound state. These non-relativistic scales display the following hierarchy:

$$m_q \gg m_q v/c \gg m_q v^2/c^2. \tag{2.7}$$

Typical quark velocities in the quarkonium rest frame are of the order $v^2 \sim 0.3c^2$ and $v^2 \sim 0.1c^2$ [36] for charmonium and bottomonium states, respectively. Due to the large mass of the quarks bound in these kinds of states, their velocities are relatively low and can even be treated non-relativistically, which is not possible for mesons made of lighter quarks.

The J/ψ is a bound state of the family of charmonium states with a mass and lifetime of $m = 3.0969$ GeV/c^2 and $\tau = 7.2 \times 10^{-21}$ s [33], respectively. It is furthermore a vector meson with quantum numbers $J^{PC} = 1^{--}$, i.e. odd parity and charge parity, which allows leptonic decays that make it experimentally favorable. The surprisingly narrow decay width of $\Gamma = 92.9 \pm 2.8$ keV [33], which corresponds to the relatively long lifetime of the bound state, is due to a combination of reasons. Firstly, the mass of the J/ψ is not high enough to allow for a decay into the two lightest charmed mesons, D^0 and $D^{\pm}$. A possible direct decay through the strong interaction is thus already prohibited. In addition, the decay via annihilation through the strong interaction requires three gluons in order to conserve parity and is suppressed via the OZI-rule [8, 37, 38]. The decay therefore proceeds predominantly via the electromagnetic interaction which, due to the significantly reduced interaction strength in comparison to the strong interaction, leads to a surprisingly long lifetime of the heavy bound state.

In high-energy physics (HEP) experiments, J/ψ are typically grouped according to their production channel. So-called prompt J/ψ are either produced directly in the initial scattering, often referred to as direct production, or from the de-

cay of heavier charmonium states like the $\eta_c(2S)$ or ψ'. The term non-prompt J/ψ refers to those produced from the weak decay of hadrons containing bottom quarks which are often called b-hadrons. The corresponding production vertex is therefore detached from the primary vertex of the event due to the long lifetime of weak decays. If no distinction of the origin is considered, the J/ψ mesons are typically referred to as inclusive. The distinction is important when comparing measurements to theoretical predictions since effective theories are usually concerned with the production of prompt J/ψ. Non-prompt J/ψ production can, on the other hand, be described by modeling the decay of b-hadrons.

2.3. Quarkonium production models

The main difficulty in the theoretical description of J/ψ production are the non-perturbative momentum scales involved in the formation of the bound state. These soft scales, i.e. $m_{\mathrm{q}}v$ or $m_{\mathrm{q}}v^2$ as introduced in the previous section, are often referred to as long distance due to the inverse relation between momentum and distance scales. Short distance, on the other hand, refers to the perturbative momentum scale p involved in the initial production of the heavy quarks. In the context of some theories, the term short distance is also used to refer to the heavy quark mass scale m_{q} to distinguish to the soft scales within the bound state. A crucial first step towards an effective theory to describe the production of (prompt) J/ψ is to prove that short and long distances can be described separately. If such a factorization is indeed possible, the production of the heavy quarks can be calculated directly from QCD using perturbative expansion in the strong coupling. The subsequent non-perturbative evolution into a bound state can then be described separately using effective theories. In all effective model calculations for J/ψ production, factorization is assumed to hold true and it remains to be seen if nature ultimately agrees.

Additionally, the models hold predictive power if the long distance matrix elements, which describe the non-perturbative evolution into bound states, are universal. This means, if they can be fixed by data at one energy, it should be possible to predict the production at different energies. Effective theories usually need some anchor to data and the assumption of universal matrix elements is exploited to various degrees by different models.

Lattice QCD, while being limited to a discretized space-time lattice, can provide first principle predictions for the long distance matrix elements without requiring any approximation of QCD. It is, however, computationally challenging to apply lattice QCD in this regime due to the existence of several scales which pose requirements on the lattice size and spacing that are difficult to meet. However, there might be progress in the future that allows for lattice QCD predictions of quarkonium production. Such predictions of the long distance processes could be used together with perturbatively calculated quark production rates to describe the quarkonium production mechanism fully without resorting to true effective theories.

Effective calculations might involve different phenomenological models that make explicit use of the soft scales, e.g. by expansion in the quark velocity. There are several effective models available amongst which the most popular are: the Color Evaporation Model (CEM), the Color Singlet Model (CSM) and the non-relativistic QCD (NRQCD) approach. The models use different strategies which lead to different strengths or shortcomings and will be introduced in more detail in the following sections. An overview over these state-of-the-art models can be found in reference [35]. The production models and theoretical approaches described in this chapter apply in the same way to all quarkonium states, but the description focuses on the J/ψ. However, it should be noted that due to the higher mass of the quarks in bottomonium states, challenges for the models are typically more expressed when comparing to charmonium production. The expansions and truncations that are used, especially concerning low relative velocities of the quarks within the bound states, are more accurate for bottomonium than charmonium states.

Typical experimental observables that are used in the comparison to theory predictions include total or differential cross sections as well as the polarization of the J/ψ. The cross sections are usually measured as functions of rapidity or transverse momentum and often available for inclusive, prompt and non-prompt J/ψ, while the polarization measurements have, so far, been limited to inclusive J/ψ [39]. The theoretical predictions of the NRQCD and CSM models are usually able to describe the cross section with reasonable precision but have difficulties to match the data on polarization [39]. This is often referred to as the J/ψ production puzzle, but the comparison suffers from the fact that the predictions are

produced for prompt J/ψ while the polarization data are thus far only available for inclusive production. In order to solve the puzzle, theorists and experimentalists have recently turned to a wider range of possible measurements, for example the associated production of J/ψ, in the hope of restricting the models even further. Such measurements include, among other things, the production of J/ψ in jets or the angular correlation of J/ψ and hadrons, the latter of which is the focus of the analysis presented in this thesis.

2.3.1. Color Evaporation Model

The CEM [40, 41, 42] was first proposed in 1977. The model considers the quarkonium production cross section to be proportional to the cross section of the constituent quark-antiquark pair. It is assumed, that every heavy quark pair will evolve into a quarkonium bound state if the invariant mass of the pair is below the threshold for production of two so-called open-flavor mesons, e.g. a pair of D mesons in the case of an initial c$\bar{\text{c}}$ pair. The production cross section is then integrated between the mass of the charmonium state and twice the mass of the lightest D meson. Furthermore, the model is based on a constant probability for the evolution from the heavy quark pair into a bound state which is process as well as energy and momentum independent. This means, that said probability is universal and depends only on the quarkonium type. It can be fixed by comparison to data and the model thus holds predictive power without additional free parameters, but often does not describe the data satisfactorily [43]. More recent implementations of the CEM like the Improved Color Evaporation Model (ICEM) [44], however, show a much better agreement with the data.

Figure 2.3 shows the energy dependence of the p_{T} and rapidity integrated cross section of inclusive J/ψ measured by ALICE at forward rapidity [45]. The data is compared to a prediction from the CEM for direct J/ψ production. While the data includes both prompt and non-prompt contributions, the comparison is largely valid due to the small fraction of non-prompt J/ψ at low p_{T} where most of the yield is located. Nevertheless, this caveat must be considered in the comparison of the model prediction to the data. It can be seen that the data, while sitting at the upper edge of the theoretical uncertainties, are largely compatible to the model predictions. At large collision energies, however, the differences between the data and model increases.

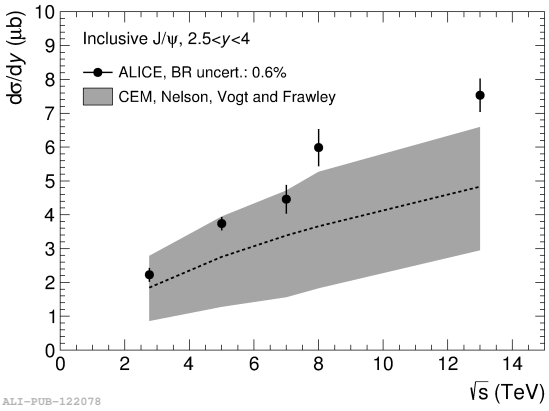

Figure 2.3.: Energy dependence of the integrated production cross section for inclusive J/ψ measured by ALICE at forward rapidity. The data are compared to CEM predictions for direct J/ψ production. [45]

2.3.2. Color Singlet Model

The CSM [46, 47, 48] was first proposed shortly after the discovery of the J/ψ in 1975. As the name suggests, it is based on the idea that the initial charm pair that evolves into the J/ψ bound state is already in a color-singlet state. This means, that the quark-antiquark pair is produced in a combination of color and anti-color that results in a color neutral state. Additionally, it is required that the pair already has the same quantum numbers in terms of spin and angular momentum as the emerging J/ψ.

In typical quantum mechanical fashion, the production rate of the J/ψ (or any other quarkonium state for that matter) in the CSM depends on the absolute value of the quark-antiquark pair wave function as well as its derivates. These are hereby evaluated assuming vanishing separation between the pair. The quantities can only be extracted from a comparison to measurements which leaves no free parameters in the model. After evaluation at a certain energy, the model holds predictive power for measurements at different energies.

Figure 2.4 shows a comparison between CSM predictions for the J/ψ and Υ(1S) production cross section to ALICE data [49]. It can be seen, that higher order expansions in α_s introduce large corrections over the leading order (LO) predictions with next-to-leading order (NLO) and especially next-to-next-to leading order (NNLO) predictions being in much better agreement with the data. This

points to the possibility that the CSM contains important production mechanisms at higher orders in α_s which are not included in the LO expansion. However, it remains to be seen if the expansion in α_s in the CSM is convergent due to the size of the corrections that appear at higher orders. The CSM predictions shown in the figure seem to be in better agreement with the Υ(1S) data, which could be due to the higher mass of the quarks and correspondingly lower relative velocity in the quarkonium rest frame. It should be noted, that the comparisons shown in figure 2.4 contain a caveat that is, that the models show directly produced J/ψ and Υ(1S) which are scaled to the data for inclusive production channels.

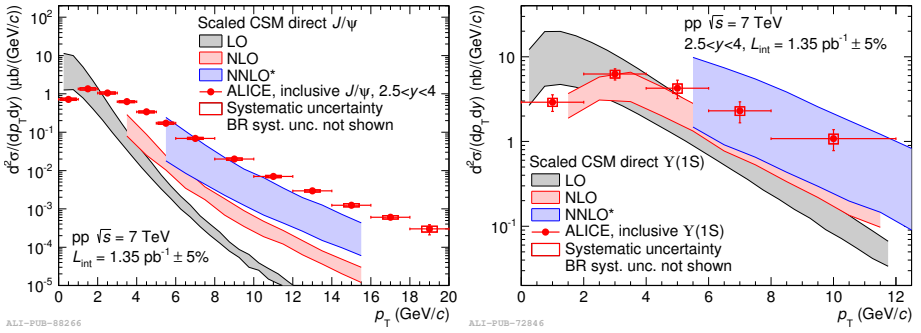

Figure 2.4.: Inclusive J/ψ (*left*) and Υ(1S) (*right*) production cross sections measured at forward rapidity by ALICE in proton-proton collisions at $\sqrt{s} = 7$ TeV. The data are compared to CSM predictions for direct production which have been scaled to inclusive quarkonium production using constant factors. [49]

2.3.3. Non-relativistic QCD approach

The NRQCD approach [50] was first conceived in 1995 and it is the most theoretically sound and successful effective model to describe quarkonium production to date. In addition to the contribution from the color-singlet state, that is also considered in the CSM, it allows the initial quark-antiquark pair to be in a color-octet state. This has certain implications on the predictions from the model in comparison to CSM as more initial states are considered. Particularly initial quark-antiquark pairs in a color-octet state must neutralize their color charge by radiation of gluons in order to form a bound state. Such radiation of color charges could be visible in the angular correlation of J/ψ mesons and hadrons from the

subsequent hadronization of the these gluons. The model makes explicit use of the hierarchy of scales by expanding in the relative heavy quark velocity v for the calculation of the long distance matrix elements. Thus, the model contains a double expansion in powers of v and α_s.

The production cross section of a quarkonium state H can be expressed as a sum of the matrix elements:

$$\sigma(H) = \sum_n \sigma_n(\Lambda)\langle\mathcal{O}_n^H(\Lambda)\rangle, \tag{2.8}$$

where Λ is the ultraviolet cutoff of the theory and σ_n is the production cross section of the heavy quark-antiquark pair. The summation is performed over the color, spin and orbital-angular momentum states n of the initial pair. It should be noted, that the σ_n are only partly short distance quantities as they are convolutions of the parton-level cross sections with the parton distribution functions, where the latter depend on the non-perturbative dynamics of the hadrons in the collision. Especially if the quarkonium is produced at low p_{T}, the perturbative description does not truly hold. The $\langle\mathcal{O}_n^H(\Lambda)\rangle$ are the NRQCD long distance matrix elements that govern the evolution of the initial quark pair into the final quarkonium bound state. Equation 2.8 explicitly contains color-singlet and color-octet contributions due to the sum over the different states n. In contrast to the CSM and CEM models, the production cross section $\sigma(H)$ depends on an infinite number of matrix elements. The sum, however, can be organized as an expansion in orders of v. The main idea behind the NRQCD approach is that such a sum can be truncated at fixed orders in v due to the small relative velocity of the heavy quarks in the rest frame of the bound state. If only color-singlet states are considered for the initial quark-antiquark pair and the expansion in v is truncated at LO, the NRQCD approach simplifies to the CSM.

The long distance matrix elements $\langle\mathcal{O}_n^H(\Lambda)\rangle$ in equation 2.8 are assumed to be universal and can be fixed from fits to data. The model thus holds predictive power which is, however, limited by the validity of the truncation at fixed order in v. Additionally, since the σ_n are only partly short distance quantities, the perturbative calculability of the heavy quark production cross section can reduce the predictive power and introduce limitations in phase space.

The left panel of figure 2.5 shows the p_{T} differential cross section for inclusive J/ψ measure by ALICE at mid rapidity in proton-proton collisions at $\sqrt{s} = 5$ TeV

[51], compared to different predictions from NRQCD models. The model describes the direct production of J/ψ and in order to compare to the measured inclusive J/ψ cross section, the non-prompt contribution is determined from the Fixed-Order-Next-to-Leading Logarithm (FONLL) [52, 53] approach and added on top. The model predictions are in good agreement with the data over the full p_{T} range. One of the models employs a a Color Glass Condensate (CGC) approach in the calculation of the heavy quark pair production cross section which allows to extend the predictions down to low p_{T}. Without the CGC framework, this would not be possible since heavy quark pair production cross sections can not be calculated perturbatively for the full phase space as was mentioned earlier. An introduction to the CGC framework can be found in reference [54].

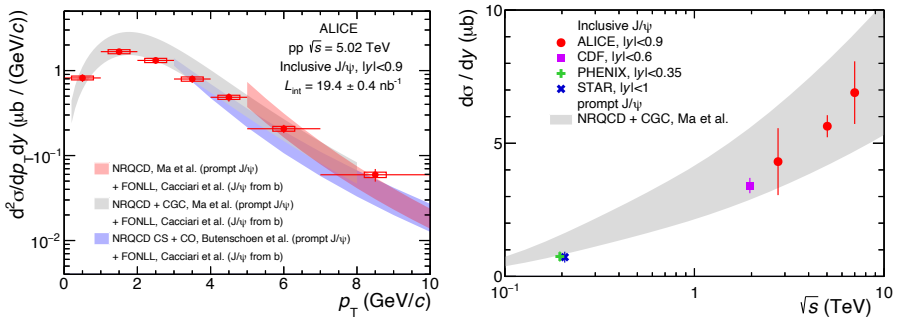

Figure 2.5.: *Left:* p_{T} differential production cross section for inclusive J/ψ measured at mid rapidity in proton-proton collisions at $\sqrt{s} = 5$ TeV by ALICE, compared to different NRQCD model predictions of direct J/ψ production with the non-prompt contribution taken from FONLL. *Right:* Energy dependence of the integrated production cross section for inclusive J/ψ measured at mid rapidity by different experiments, compared to a NRQCD model prediction for direct J/ψ production. [51]

Additionally, the energy dependence of the integrated production cross section for inclusive J/ψ at mid rapidity from different experiments [51] is shown in the right panel of the figure. The data are compared to a NRQCD model prediction for direct J/ψ production which is also utilizing the CGC approach in order to determine the full p_{T} integrated cross section. While the data represents the production cross section for inclusive J/ψ, a comparison to the model prediction for direct production is still reasonable due to the small contribution from non-

prompt production at low p_{T} where the differential cross section is largest. The NRQCD model is in good agreement with the data over a large range of collision energies.

Figure 2.6 shows the inclusive J/ψ polarization in proton-proton collisions at $\sqrt{s} = 8$ TeV measured at forward rapidity by ALICE [39]. The polarization is determined in two different reference frames and compared to model predictions from NRQCD as well as CSM. The data is compatible with vanishing polarization but the models predict a sizable polarization that is in contradiction with the measurement. This indicates that the J/ψ production mechanism is not fully understood, which was previously referred to as the J/ψ production puzzle. One of the NRQCD models shows a vanishing polarization but the prediction is only available for one of the polarization axis and reference frames [45]. It should be noted, though, that the model predictions shown in figure 2.6 are provided for directly produced J/ψ while the measurement corresponds to inclusive production.

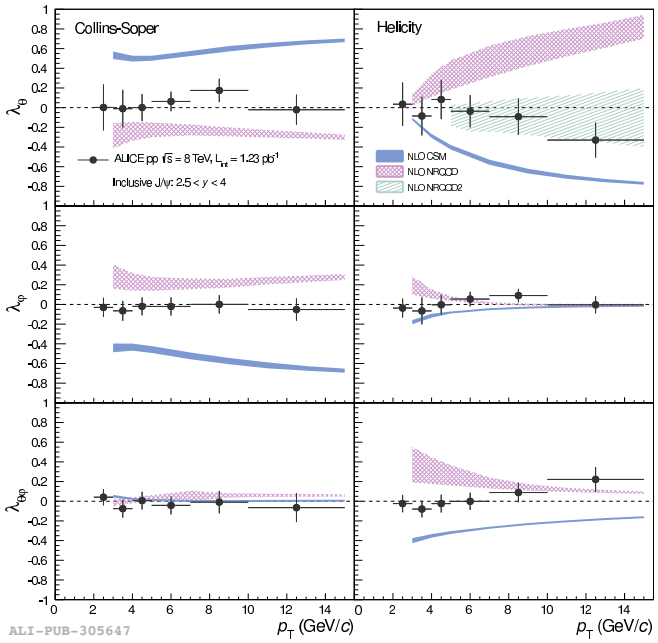

Figure 2.6.: Inclusive J/ψ polarization measured in two reference frames at forward rapidity by ALICE for proton-proton collisions at $\sqrt{s} = 8$ TeV. The data is compared to NRQCD and CSM model predictions. [39]

2.4. Quark-Gluon Plasma and the J/ψ

As a small departure from the main topic of this thesis, it is worthwhile looking at the more extreme states of QCD matter and the significance of the J/ψ as an experimental probe of those. At high energy scales the coupling strength of QCD, as depicted in figure 2.1, decreases rapidly. Eventually, as was described in section 2.1, the partons will be only weakly coupled, which is typically referred to as asymptotic freedom. This provides the basis for the concept of a deconfined state of QCD matter, where quarks and gluons are not bound inside hadrons but can move quasi-freely in a collective system. Such a state of matter is called the QGP and it can be reached at very high temperatures and/or pressures. The sketch of the QCD phase diagram shown in figure 2.7, where the baryon-chemical potential μ_B takes place for the pressure, indicates such regimes. The baryon-chemical potential[1] is, strictly speaking, not equivalent to the pressure of the system but rather a quantity that indicates the imbalance between matter and antimatter. However, it relates to pressure through the inherent matter-antimatter asymmetry in the observable universe and the QCD phase diagram is correspondingly often displayed in terms of the net baryon number. Regular hadronic matter, like the atomic nucleus, exist at relatively low temperatures and pressures with $\mu_B \sim 1$. Different states are separated by either crossover regions, as depicted by the dashed line in figure 2.7, or first order phase transitions which are indicated by solid lines. There might also exist a critical point [55, 56], depicted by the black dot at the intersection of the crossover and first order phase transition regions, analogous to the triple point of the phase diagram for water. Shortly after the Big Bang, the early universe is believed to have existed in a state of QGP before the formation of hadrons. This is marked by an arrow at very high temperatures and vanishing μ_B in the phase diagram as the matter-antimatter asymmetry has not yet developed at that point.

Heavy ion collisions at sufficiently high energies are able to create the deconfined state by reaching very high energy densities. The collisions are followed by a rapid thermalization, allowing the partons to become deconfined in a high temperature environment. Such experiments have been performed at the Alternating Gradient

[1] The baryon-chemical potential is defined as the change in the energy of a system when the total baryonic number, that is the number of baryons minus the number of anti-baryons, changes by one unit.

Synchrotron (AGS) and Super Proton Synchrotron (SPS) at CERN and they are currently undertaken at the Relativistic Heavy Ion Collider (RHIC) at BNL and the LHC at CERN (all marked in figure 2.7). The QGP was most likely first produced in a laboratory at the SPS collider at CERN [57]. The energy densities achieved at AGS, however, were not sufficient to produce a deconfined state of matter.

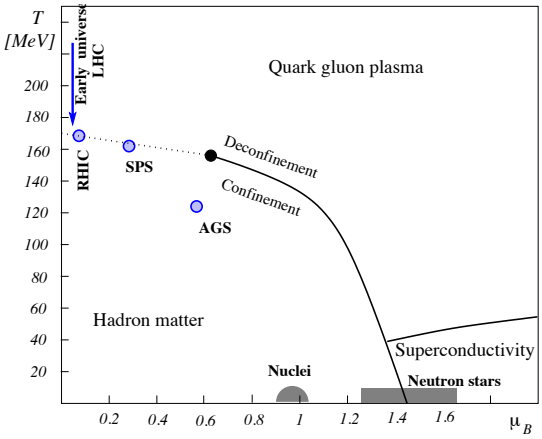

Figure 2.7.: Sketch of the QCD phase diagram in terms of temperature T and baryon-chemical potential μ_B indicating different states of matter as well as regions probed by different collider experiments. [58]

At very high pressures and comparatively low temperatures, it is believed that QCD matter can reach a state of color superconductivity, where quarks form Cooper-Pairs, analogous to superconductivity in electromagnetism [59]. This state, which is situated at high μ_B and low temperatures, as shown in figure 2.7, might exist in neutron stars where hadronic matter is packed so densely due to gravitational pressure that color charges can become deconfined [60]. While color superconductivity is a very interesting concept, it is beyond the scope of this work and will not be discussed in further detail.

The J/ψ and especially its production mechanism is of particular interest as a testbed for QCD, but it also serves as an important probe for the QGP. Heavy quarks are expected to be produced predominantly in the hard partonic scattering processes during the initial stages of the collision since a large momentum

transfer is required to produce such massive quarks. Thus, quarkonium states will experience the full evolution of the system and, since they are susceptible to the strong force, interact with it. In 1986, Matsui and Satz [61] predicted that the deconfined medium of the QGP will suppress charmonia due to a color screening effect, similar to Debye screening. This effect arises from the high density of free color charges and can provide information on the properties of the medium. More specifically, relative suppression of different quarkonium states should point towards the temperature of the medium due to the different sizes of the bound states [62, 63]. The sequential suppression of quarkonia, where less tightly bound states are prone to disappear already at lower temperatures, is commonly know as melting. Due to the sensitivity to the temperature of the system, this melting process can serve as a thermometer.

Amongst quarkonia, the J/ψ is a very prominent probe of suppression in QGP studies due to its relative abundance and rather tightly bound state. However, experimental data has shown, that not only suppression is observed but J/ψ also seem to be regenerated when going from lower energy collisions, for example at RHIC where gold ions are collided at center-of-mass energies per nucleon pair of up to 200 GeV, to higher energies at the LHC. This is illustrated in a comparison of data from the Pioneering High Energy Nuclear Interaction eXperiment (PHENIX) [64] at RHIC and ALICE [65] at the LHC. The left panel of figure 2.8 shows the so-called nuclear modification factor[2] of inclusive J/ψ as a function of the number of participants[3], which relates to the event multiplicity. It can be seen that in both cases, at RHIC and LHC, J/ψ are suppressed in central heavy ion collisions due to color screening. However, a smaller suppression is observed at the LHC when comparing the data directly. This is attributed to the higher energy density and thus larger number of produced charm and anti-charm quarks, which in turn leads to a higher probability of recombination. Thus, offsetting the suppression effect from the medium to some degree. Furthermore, the J/ψ suppression is getting stronger with increasing event multiplicity at RHIC whereas the suppression seems to level off at the LHC.

[2]The nuclear modification factor R_{AA} is defined as the ratio of the production yields in heavy ion collisions to the corresponding production in proton-proton collisions, scaled by the number of binary collisions.

[3]The average number of participants $\langle N_{\mathrm{part}} \rangle$ denotes the number nucleons involved in the collision. Large numbers of participants correspond, loosely speaking, to central head-on collision where the incident ions overlap to a large degree and produce high event multiplicities.

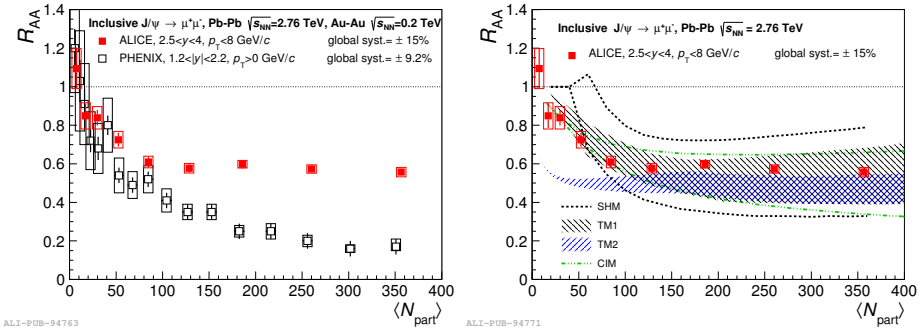

Figure 2.8.: Relative production of J/ψ in heavy ion versus proton-proton collisions (R_{AA}) as a function of the event multiplicity measured by PHENIX and ALICE at forward rapidity (*left*). Additionally, the ALICE data is compared to different model predictions (*right*). [65]

Additionally, the J/ψ suppression measured by ALICE is compared to theoretical models in the right panel of figure 2.8. The theoretical models that are compared to the data are the statistical hadronization model [66], two different transport models [67, 68] and the comover interaction model [69], labelled SHM, TM1, TM2 and CIM, respectively. All models shown in the comparison include recombination to some degree and are in fair agreement with the data, even though they differ quite significantly in their approach. The hadronization model assumes deconfinement and thermal equilibrium of the system as well as eventual hadronization on a statistical basis at the phase boundary of the QGP. The transport models are both based on a transport of the initially produced quarkonia through a deconfined system but differ in the rate equation that controls the dissociation and recombination of J/ψ. The comover model is based on, as the name suggests, quarks moving in coherence with the partonic medium. Further details of the models can be found in the corresponding references and a more in-depth discussion of the comparison to data is given in reference [65]. But even without diving deeper into the details of the different models, the J/ψ can be appreciated as a smoking gun signature of the deconfined state. All models include a description of the dissociation of J/ψ due to the interaction with the quasi-free color charges of the medium, which clearly reflects what is observed in the data.

3. Experimental setup

In this chapter, the experimental setup consisting of the CERN accelerator complex, the ALICE detector and the data reconstruction and analysis software framework are introduced. The description of the accelerator complex includes the full accelerator chain but the focus lies on the main collider: the CERN LHC and the specifics of the proton-proton collision program during the data taking period. Only the sub-detectors of ALICE relevant for the analysis discussed in this thesis are presented in detail. A full description of the experimental design and its performance can be found in references [70, 71]. A brief description of the track reconstruction algorithm is given, and finally the software framework is presented.

3.1. Accelerator complex

The LHC, hosted by CERN and situated in the Geneva area under Swiss and French territory, is the world's largest and most powerful particle collider to date. It is located in a roughly circular underground tunnel of about 27 km circumference that previously housed the Large Electron Positron Collider (LEP). The LHC is designed to accelerate and collide protons with collision energies up to 14 TeV but in Run-2, during which the data presented in this thesis was recorded, it operated at energies not higher than 13 TeV. In addition to the proton program, the LHC also provides a dedicated heavy ion program that mainly utilizes lead ions but in 2017 also performed a brief period of collisions using xenon. Peak luminosities of up to $\mathcal{L} = 10^{34}$ cm^{-2}s^{-1} and $\mathcal{L} = 10^{27}$ cm^{-2}s^{-1} for proton-proton and lead-lead collisions, respectively, can be achieved with the current design of the collider [72]. Luminosity is a quantity that is proportional to the number of collision events per second and thus a measure of the statistics that can be accumulated. It is furthermore defined per surface unit and therefore depends on the cross section of the process that is used to measure the luminosity. Peak luminosity is hereby

a measure of the collider while integrated luminosity corresponds to the amount of data actually recorded by an experiment over a specific period of time.

The LHC is not perfectly circular as the sketch in figure 3.1 suggests, but segmented into eight arcs containing the dipole bending magnets which keep the circulating beams in orbit. In between the arcs, there are eight straight sections whose design depends on the specific purpose of the section. There are four sections covering accelerator needs, like injection and acceleration, and another four sections that house the collisions points for the experiments. The four main experiments, each positioned at one of the dedicated interaction points, are: ALICE, ATLAS, CMS and LHCb, which are all marked in the sketch of the accelerator complex in figure 3.1. In addition to these experiments, there are also three smaller experiments up- or downstream of the interaction points: LHCf, MoEDAL and TOTEM.

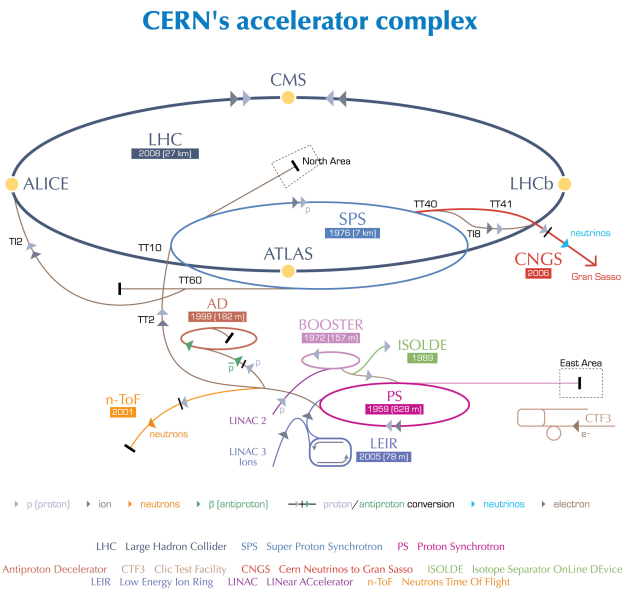

Figure 3.1.: Sketch of the CERN accelerator complex and the LHC, including the pre-accelerator stages LINAC2, PS and SPS involved in the proton acceleration chain. [73]

The full accelerator complex at CERN, which is comprised of pre-accelerates and culminates in the LHC, is sketched in figure 3.1. The proton acceleration chain begins with a hydrogen bottle that provides the protons which are injected into the chain after the electrons are stripped from the hydrogen atoms by an electric field. The first pre-accelerator the protons encounter is the linear accelerator LINAC2 which accelerates the protons to an energy of 50 MeV. Following LINAC2, the protons are further accelerated in the Proton Synchrotron (PS) booster to an energy of 1.4 GeV before entering the PS ring which increases their energy to 25 GeV. The last stage of the acceleration before entering the LHC, as is depicted in figure 3.1, is the SPS that raises the beam energy to the LHC injection energy of 450 GeV [74]. Inside the LHC, the protons are accelerated further to energies of up to 6.5 TeV for a collision energy of 13 TeV. The maximum possible beam energy by design is 7 TeV, which would allow to reach a collision energy of 14 TeV. In addition to providing protons with the required injection energy for the LHC, most accelerators in the chain also have dedicated experimental halls housing detectors designed for lower beam energies.

Even though heavy ion data will not be be discussed in the scope of this work, it should be noted for completeness that the accelerator chain for heavy ion collisions differs slightly from that of protons. This is due to the more complex procedure required to obtain the desired ions. However, as is sketched out in figure 3.1, the chain for protons and ions coincides after injection into the PS.

The beams circulating inside the LHC do not consist of single hadrons or ions, but are segmented into 'pulses' of many particles, so-called bunches. In the case of protons, these bunches consist of about 1.5×10^{11} protons and bunches are spaced by 25 ns with a total maximum number of 2808 bunches circulating in the LHC at any time [75]. These numbers, of course, depend on the specific injection scheme that is used during operation and can vary in between injections. The data taking is supposed to be based on collisions of single protons from opposing beams. However, this is difficult to accomplish due to the bunch structure of the beams crossing in the interaction point. It is thus possible, that several collision events happen at the same time during a single bunch crossing. These events, so-called in-bunch pile-up events, will overlap in the detector and are difficult to disentangle in the data even though they are slightly displaced along the beam axis. The implications of such pile-up events and the corresponding actions that

must be taken to ensure good data quality during the analysis are discussed in more detail in section 5.1.

3.2. ALICE detector

ALICE is the dedicated heavy ion experiment at the LHC, designed to study the deconfined medium produced in such collisions. The high multiplicity environment of heavy ion collisions produces track densities much larger than in proton-proton collisions. Many interesting signatures require the reconstruction and identification of particles in a wide momentum range, which extends from several tens of GeV/c down to a few hundred MeV/c. These conditions place certain requirements on the experimental setup. Excellent particle identification (PID) capabilities are provided down to very low transverse momenta by combining different techniques, depending on the particle specie and momentum range. A very high tracking resolution is reached down to low p_{T}, with typical values of the order of $< 1\%$ around 1 GeV/c [71]. This is achieved thanks to the combination of a fairly low magnetic field and a reduced material budget to minimize multiple scattering effects.

The coordinate system assigns the beam direction as z while x defines the horizontal plane and points towards the center of the LHC. The vertical dimension is given by the y axis and the so-called transverse plane is spanned by x and y. Since the magnetic field is directed along the beam pipe, the momentum is measured in terms of the transverse momentum p_{T} in the x-y plane. The azimuthal angle φ circles around the beam pipe while the polar angle θ spans between z and the transverse plane. However, the rapidity $y = \frac{1}{2} \ln \left(\frac{E+p_z c}{E-p_z c} \right)$ and pseudorapidity $\eta = -\ln \left[\tan \left(\frac{\theta}{2} \right) \right]$ are more commonly used instead of the polar angle. The rapidity is additive under Lorentz transformations and thus convenient in HEP, while η is equal to y for massless particles. Pseudorapidity is often used in place of the polar angle when studying, for example, detector acceptances or unidentified particles while rapidity is preferred for identified particles. Accordingly, the transverse plane at $\theta = \pi/2$ corresponds to $\eta = y = 0$. In order to simplify the identification of different sub-detectors, the two possible directions of η in ALICE are referred to as A- and C-side for $\eta > 0$ and < 0, respectively. The letters are abbreviations for ATLAS and CMS, denoting the orientation along the LHC ring.

The ALICE detector, pictured in the configuration as used for this analysis in figure 3.2, consists of a central barrel inside the L3 solenoid magnet and the muon arm at forward direction. The analysis presented in this thesis is limited to mid-rapidity and does not utilize the muon arm, which will therefore not be presented. The solenoid magnet was originally built for the L3 experiment at LEP that was home in the experimental cavern which now houses ALICE. It can provide a magnetic field of up to 0.5 T in the direction of the beam axis, with two possible polarities. This allows for the measurement of momentum in the transverse plane, i.e. the transverse momentum p_{T}, from the curvature of the tracks inside the magnetic field as well as the determination of the sign of the electric charge from the bending direction. At mid rapidity, particle tracking and identification is provided by the central barrel detectors.

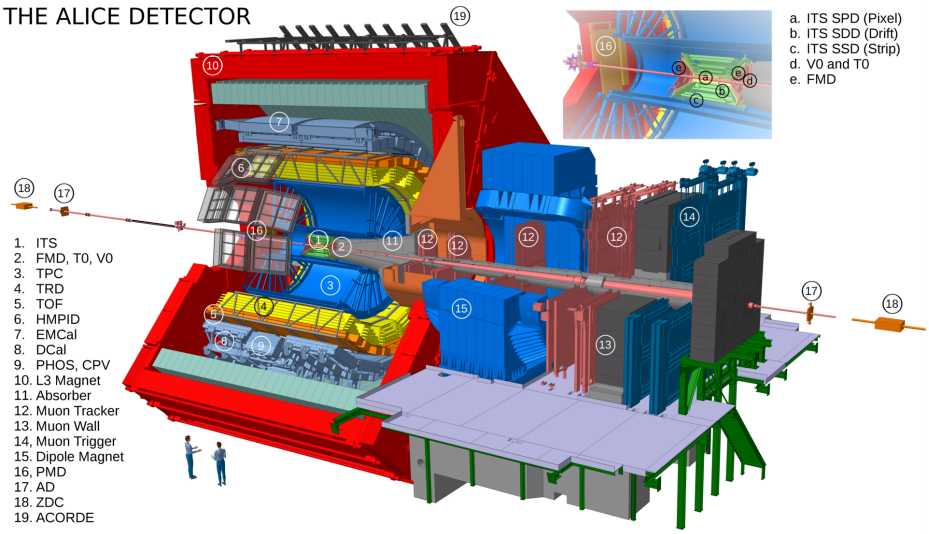

Figure 3.2.: Overview of the ALICE detector and its subsystems in the configuration during data taking in LHC Run 2. The inlay shows a magnified view of the interaction point and the ITS. All sub-detectors are marked by numbers listed in the legend and the central barrel detectors correspond to numbers 1 to 9. [76]

The Inner Tracking System (ITS), surrounding the beam pipe at small radii, is the first central barrel detector that is encountered by particles created in the

interaction point. Following the ITS, particles enter the Time Projection Chamber (TPC), which is a large ionization chamber and the main tracking and PID device of the central barrel. At even larger radii, particles traverse the Transition Radiation Detector (TRD) and the Time-Of-Flight (TOF) system, which can provide additional tracking and particle type information. Then, depending on the azimuthal and polar angle of the track, particles can encounter one of the three electromagnetic calorimeters: the Electromagnetic Calorimeter (EMCal), the Di-Jet Calorimeter (DCal) and the Photon Spectrometer (PHOS); which all cover different regions of the solid angle as is depicted in the schematic in figure 3.2. In this analysis, only EMCal and DCal are used as triggering devices and to improve particle identification at high transverse momenta. PHOS is not used as it has a very limited acceptance which would not be beneficial for the correlation measurement presented in this thesis and it is thus not described in further detail.

More detailed information on the ALICE detector, including a description of the muon arm, can be found in reference [70]. The subsystems used for the measurement presented in this thesis are described in more detail in the following sections.

3.2.1. T0 detector

The T0 detector [70] is used to discriminate against beam-gas interactions, which are collisions of the beam with residual molecules from the almost perfect vacuum in the beam pipe Additionally, it provides the earliest trigger signal which is used as the start time of the TOF system. The detector is split into two parts, called T0A and T0C, situated at a distance of 375 cm and 72.7 cm up- and downstream of the nominal collisions point. Both consist of 12 Cherenkov counters using photomultiplier tubes for signal generation. T0A and T0C cover an acceptance of 2π in azmiuth and $4.61 \leq \eta \leq 4.92$ and $-3.28 \leq \eta \leq -2.97$ in pseudorapidity, respectively.

3.2.2. V0 detector

The V0 detector [70, 77] is, similar to the T0 detector, a forward detector that is used for triggering and the rejection of beam related background. It consists of two scintillator arrays, separated into an up- and downstream component called

V0A and V0C. The segments are located at 340 cm and 90 cm on either side of the nominal collision point and cover an acceptance of 2π in azimuth as well as $2.8 \leq \eta \leq 5.1$ and $-3.7 \leq \eta \leq -1.7$ in pseudorapidity. The detector provides the Minimum Bias (MB) trigger signal where different configurations in terms of the combination of signals in the two scintillator arrays are possible. During Run-2, the MB trigger was operated using a coincidence between hits in the V0A and V0C counters. The V0 system furthermore acts as a fast multiplicity counter that can provide a High Multiplicity (HM) trigger or an estimate for the collision centrality in lead-lead or proton-lead collisions. In addition to providing these trigger signals, the V0 detector is also the main device used to reject background events related to beam interactions. Such background events like beam-gas interactions or overlapping events from multiple collisions can be rejected using timing cuts. The detector particularly provides protection against overlapping events that happen during the readout time of the Silicon Pixel Detector (SPD).

3.2.3. Inner tracking system

The ITS [70] is the detector closest to the interaction point, located at radii between 3.9 and 43 cm. It is a cylindrical, silicon-based detector utilizing three different designs that is separated into layers with couples of layers sharing one architecture and a total of six layers. This is shown in the zoomed in version of the sketch of the detector in figure 3.2. The cylindrical design provides an acceptance of 2π in azimuthal direction and, due to the separation into layers, a coverage of at least $|\eta| < 0.9$ in pseudorapidity with some layers extending beyond. The two innermost layers are silicon pixel detectors, aptly named the SPD, and have the highest granularity and thus spatial resolution in direction of the beam-pipe of the whole system. This is required to enable a good primary vertex resolution and secondary vertex separation in the high track density environment close to the interaction point. The SPD is followed by two layers of silicon drift detectors, the Silicon Drift Detector (SDD), and two layers of silicon strip detectors, the Silicon Strip Detector (SSD). In comparison to the SPD, these detector types have a reduced spatial resolution due to their reduced granularity. The spatial resolution for primary vertices reconstructed with the ITS is better than 100 μm and the relative momentum resolution for low transverse momentum pions in the range $p_{\mathrm{T}} \in [0.1, 3]$ GeV/c is better than 2% [70].

As has been mentioned previously, several collisions can occur during one bunch crossing of the beams and will thus lead to overlapping events in the detector. These in-bunch pile-up events result in vertices that are slightly displaced along the beam axis and can therefore be rejected due to the good vertex resolution of the SPD. The beams inside the LHC circulate with more than 11×10^3 revolutions per second, leading to a full orbit for one proton in the beam in less than 90 μs. Comparatively slow readout times of some subsystems of the ALICE detector, like the TPC, can therefore lead to overlapping events from different bunch crossings. This effect is called out-of-bunch pile-up in order to distinguish it from in-bunch pile-up which does not depend on the readout time of any detector. Tracks from out-of-bunch pile-up events can largely be removed by requiring SPD information due to its fast readout time.

In addition to the tracking information, the analog readout of the ITS also allows for the measurement of the energy of each cluster attributed to a track segment in the ITS. Thus, the specific energy loss per unit length, i.e. $\mathrm{d}E/\mathrm{d}x$, can be measured and used for particle identification. However, in the analysis presented in this thesis, the ITS is not used for PID since the TPC provides sufficient performance.

3.2.4. Time projection chamber

The TPC [70, 78, 79] acts as the main tracking and particle identification device in the central barrel. It is a cylindrical drift chamber with a gas volume of almost 90 m^3 that surrounds the ITS and has an acceptance of 2π and $|\eta| < 0.9$ in azimuth and pseudorapidity, respectively. The TPC is, just like the ITS, designed to handle large multiplicities with up to 2×10^4 [79] charged particles, including secondaries, within its own acceptance.

The drift volume is divided into two sections by a central electrode at $z = 0$, where a high voltage of 100 kV is applied. This generates a voltage gradient of 400 V/cm towards the readout chambers at the endcaps on either side of the cylinder. The gradient translates to a maximum drift time of 92 μs for electrons created in the ionization of the gas from interaction with charged particles traversing it. The readout chambers of the TPC are multi-wire proportional chambers and segmented into 18 sectors in azimuthal direction with pads closer to the beam pipe having higher granularity to cope with the high track density. Tracks inside the

TPC are reconstructed in three dimensions from the hit positions of the ionization charges in the readout chambers and the drift times, where the start time is given by the T0 detector. Amplification of the readout signal close to the multi-wire proportional chambers produces positively charged ions that can drift back into the main volume of the TPC following the voltage gradient in opposite direction. This would lead to distortions in the drift field and these are prevented by a gating grid placed in front of the readout pads where a voltage can be applied to counteract the gradient of the drift field. The whole TPC is enveloped in a field cage that prevents the distortion of the drift field close to the edges of the detector.

The maximum drift time of charges in the electric field ultimately defines the readout time of the TPC since parts of the event would be lost otherwise. The readout time lags behind the revolution frequency of the beams in the LHC and therefore limits the maximum luminosity that can be processed by the central tracking system of ALICE. However, even after adjusting the collision rate, the long drift time can still lead to overlapping out-of-bunch pileup events inside the TPC. Tracks from such events can only be rejected by requiring information from a faster detector like the SPD as described above.

The drift gas is a mixture of argon (90%) and CO_2 (10%), where the latter is used as a quencher to reduce the number of charges that are freed in the avalanches during the amplification of the ionization signal close at the readout chambers. This mixture was used in the data taking periods in 2016 and 2018 but argon was replaced by neon in 2017, which also required an adjustment of the gain in the readout chambers. Slight differences can thus be observed for certain track quantities reconstructed with the TPC for the data periods of 2017 with respect to 2016 and 2018. However, this has no impact on the results of this analysis.

The transverse momentum of tracks inside the TPC is reconstructed from the curvature of the tracks inside the magnetic field of the L3 solenoid. The minimum p_{T} that can be reconstructed is limited by both the tracking algorithm as well as the curvature of the track due to the magnetic field. Secondary tracks, i.e. tracks that do not originate in the primary vertex, are hereby limited to transverse momenta not lower than 50 MeV/c. Primary tracks can be reconstructed with good p_{T} resolution in a range from about 100 MeV/c to 100 GeV/c due to the curvature of the tracks in the magnetic field.

Particle identification inside the TPC is based on the specific energy loss from

ionization of the tracks inside the drift gas. The hits in the readout chambers of the TPC provide energy information, in addition to the position information, that is used to calculate the energy loss for each reconstructed track. The energy loss is then described by the Bethe-Bloch formula which relates the mean energy loss of a certain particle to its velocity. After the calibration of the energy loss curves, these can be used together with the momentum information of the track to identify the species. Energy loss curves for different species of particles reconstructed in the TPC are shown as a function of the total track momentum in figure 3.3. The figure shows the measured energy loss in proton-proton collisions at $\sqrt{s} = 13$ TeV as well as the parametrizations according to the Bethe-Bloch formula. It can be seen, that the curves of different species cross at certain momenta which complicates the precise identification in these regions. This is apparent, for example, for electrons and pions at very low momenta. At large momenta, the energy loss curves of different particle species naturally approach each other and solely TPC based particle identification becomes difficult.

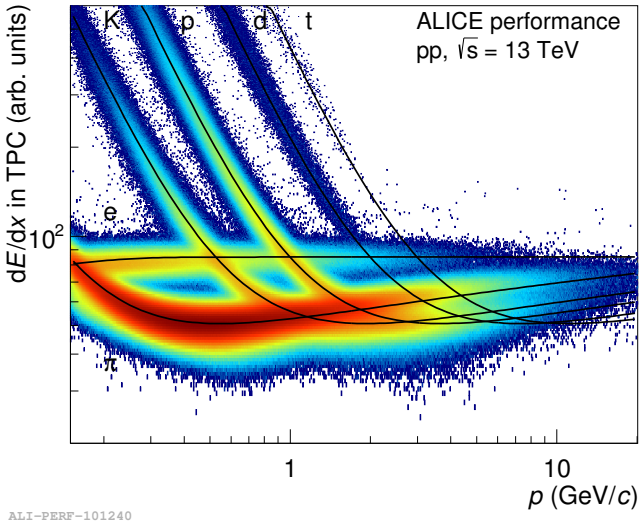

Figure 3.3.: Energy loss distributions for different particle species and corresponding parametrizations as reconstructed in the TPC in proton-proton collisions at $\sqrt{s} = 13$ TeV. [76]

3.2.5. Electromagnetic calorimeter

The electromagnetic calorimeters EMCal [70, 80] and DCal [81] are lead-scintillator calorimeters that utilize a sampling architecture and have identical design. They are located at the outer edge of the central barrel, behind the TRD. EMCal covers an acceptance of $|\eta| < 0.7$ and $\Delta\varphi = 107°$ in pseudorapidity and azimuth, while DCal has a smaller acceptance and flanks PHOS, as can be seen in the schematic in figure 3.2. It has a total acceptance of $\Delta\eta = 1.4$ and $\Delta\varphi = 60°$ with half of the acceptance in pseudorapidity on either side of PHOS.

Each calorimeter is separated into so-called super modules which all span $\Delta\eta = 0.7$ in pseudorapidity but have different acceptance in azimuth. So-called full size super modules cover $\Delta\varphi = 20°$ while one-third size super modules are limited to an acceptance of $\Delta\varphi = 7°$. EMCal is segmented into ten full size and two one-third sized super modules while DCal consists of six full size super modules. The super modules themselves are further segmented into 288 and 96 modules for the full and one-third size super modules, respectively. These modules are self-contained detector units consisting of four sampling calorimeter towers of size $\Delta\eta \times \Delta\varphi = 0.014 \times 0.014$, leading to a total number of 12288 and 6912 towers for EMCal and DCal, respectively.

Electrons (or photons) entering the calorimeter create electromagnetic showers via bremsstrahlung and pair creation effects. Photons released from interaction with such showers in the scintillator layers of the calorimeter towers are guided through optical fibers to the photodiodes where the signal is read out. The EMCal and DCal towers are designed to have a Molière radius that approximately corresponds to the size of the towers. This allows to contain most of the electromagnetic shower and reduce leakage into neighboring towers. The energy resolution of the calorimeter is energy dependent and determined by different factors such as the the energy sampling, shower leakage and others. Test beam measurements and simulations showed a resolution better than $12\%/\sqrt{E} + 1.7\%$ [82].

While the granularity of the calorimeters is less than that of PHOS, clusters from hits of charged particles typically still cover several towers. This allows the determination of the shape of clusters which provides a rudimentary particle identification method with, for example, clusters from photons or electrons being mostly circular. In addition, the matching of calorimeter clusters to particle tracks can improve the track-only PID by providing an additional measurement of the

energy. This can be used to reject non-electron background by requiring an energy to momentum ratio (E/p) close to one as the electron mass becomes negligible at higher momenta.

PHOS, on the other hand, delivers a better position and energy resolution due to its higher granularity and non-sampling architecture. However, it has a very limited acceptance and is therefore not used in the analysis presented in this thesis.

3.2.6. Trigger System

During proton-proton collisions, ALICE typically operates at target instantaneous luminosities in the range of 10^{29} cm^{-2}s^{-1} to 10^{31} cm^{-2}s^{-1} [71], limited by the long readout time of the TPC. Thus, a downscaling of 'uninteresting' events is necessary for the study of rare probes in order to be able to reach sufficient integrated luminosities. This is achieved by applying triggers that select quickly on event signatures and determine if an event should be read out or not. The main requirement of such triggers, aside from a reasonable selection criteria for events, is a short latency after the collision. Triggers in ALICE [70, 71] are grouped into different levels according to their latency. Level 0 (L0) trigger decisions are made about 0.9 μs after the interaction, followed by the Level 1 (L1) triggers after roughly 6.5 μs in addition. The last triggers that are applied are Level 2 (L2) triggers whose decisions are taken about 100 μs after L0, corresponding approximately to the readout time of the TPC. The L0 and L1 triggers send a trigger signal directly to the different detectors to initiate the buffering of data in the frontend electronics. The L2 triggers, on the other hand, differ slightly in their application but are not described in more detail here since they are not used in the analysis presented in this thesis. More details to the different levels and the trigger system can be found in references [70, 71]. The trigger decisions are generated by the Central Trigger Processor (CTP), which evaluates the inputs of the trigger detectors approximately every 25 ns and distributes the trigger signal. Additional latencies are hereby caused by computation and signal distribution and must be accounted for by using data buffering in the frontend electronics of the different detectors.

The analysis presented in this thesis exploits several triggers in order to improve the statistics in different kinematical regimes. In a technical sense, MB events are

accepted by a dedicated L0 trigger that requires a coincidence signal in the two sections of the V0 detector. However, MB trigger accepted events are typically not referred to as triggered events since the latter expression is used to indicate rare events selected according to more stringent requirements directly related to the specific physics case under study. In this analysis in addition to the MB trigger, a high multiplicity trigger and a trigger dedicated to events containing high p_{T} electrons are exploited in order to enhance the available statistics. These triggers, called V0 high multiplicity trigger (V0HM) and EMCal electron/gamma trigger (EMCEGA), are L0 and L1 triggers, respectively. The V0HM trigger replaces the MB trigger in selected events and triggers on a minimum multiplicity observed in the V0 counters that corresponds to the 0.1% highest multiplicity events. The trigger threshold has been continuously adapted over the period of data taking to account for the aging of the scintillators in the V0 detector. The EMCEGA triggers on a cluster in the EMCal or DCal above a certain energy threshold following the L0 MB trigger. This means, that EMCEGA accepted events also fulfill the MB requirements but the rate is scaled down in comparison by the required cluster energy. Clusters used for the trigger algorithm are combinations of 4×4 towers, summed in a sliding window over the full calorimeter acceptance. There are two EMCEGA triggers available which use different cluster energy thresholds: 9 GeV and 4 GeV, which are referred to as EMCEGA1 and EMCEGA2, respectively. The rate of the lower threshold trigger is scaled down further in comparison to the higher threshold trigger since every event accepted by EMCEGA1 would otherwise also fulfill the EMCEGA2 trigger condition. A more detailed description of the EMCal trigger can also be found in reference [82].

3.3. Track reconstruction

The event reconstruction and track finding procedure employed by ALICE is summarized in figure 3.4, and a detailed description can be found in reference [71]. Before the track and event reconstruction can begin, the separate detector signals are read out and combined into clusters. This so-called clusterization process is necessary to, for example, combine hits in different towers of the calorimeters into clusters that are associated to a single particle interaction. Then, a preliminary version of the primary vertex is determined using the two innermost layers of the

ITS, i.e. the SPD. The identification of the primary vertex uses a linear extrapolation of all pairs of hits in the two SPD layers and is based on the maximum number of such tracklets that converge in a single point. If such a point is not found, the algorithm defaults to a one dimensional search along the z axis. Due to the magnetic field, the resolution of the primary vertex in z is better than in the transverse plane. The primary vertex will later be re-evaluated using the full tracking information as is noted in the third to last step of the flow diagram in figure 3.4.

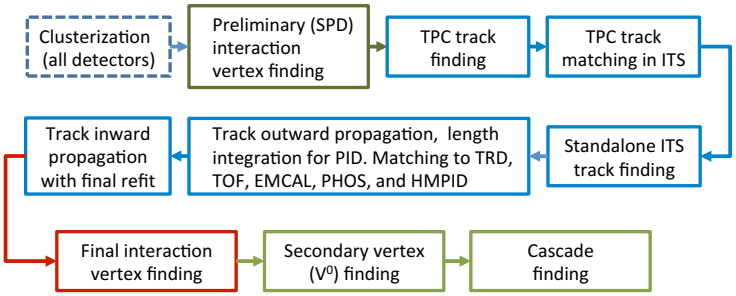

Figure 3.4.: Flow diagram of the event and track reconstruction procedure as employed by ALICE. [71]

After the identification of a preliminary primary vertex, track finding starts with the reconstruction of the track segments in the TPC. These segments are built in three dimensions from the measured clusters and the corresponding timing information using a Kalman filter algorithm. The reconstruction starts at the outer edge of the TPC and follows the nearest cluster inwards, towards the ITS. This is done once with and once without the constraint that the track must point to the (preliminary) primary vertex and the results are stored for both cases. Clusters in the TPC are hereby added to the track segment following a χ^2 minimization. The track segments in the TPC are then propagated to the ITS, where a similar track finding algorithm is performed, using the TPC track segments as seeds. If clusters in the ITS can not be matched unambiguously to the TPC track segments, all possibilities are calculated and the most probable candidate is kept.

Then, the scheme of the track reconstruction is reversed and the combination of ITS and TPC track segments is used as a seed for another Kalman filter track

reconstruction going outwards and starting at the SPD. This step concludes with a matching of possible additional detector information to the track. Such information can include clusters in any of the calorimeters or TRD track segments as noted in the corresponding step in figure 3.4. The last step of the track reconstruction is a final propagation from the outermost space point of the track inwards. Again, the tracks are determined and stored under both assumptions, that they do and do not point to the (preliminary) primary vertex.

The event reconstruction culminates in the reevaluation of the primary vertex using the full track information. This is done via a minimization of the distances of closest approach for track pairs using a χ^2 fit. Due to pile-up, several primary vertices can be found which complicates the procedure and might lead to a later rejection of the event.

The last two steps of the event reconstruction mentioned in the flow diagram in figure 3.4 are the calculation of higher level objects, namely the reconstruction of secondary vertices, and the detection of cascade decays. Such objects are not relevant for the analysis presented and these reconstruction steps are thus not explained in the scope of this thesis. However, details on these steps can be found in reference [71].

3.4. Analysis framework

The large amounts of data produced by big experiments like ALICE pose particular challenges on the computing in terms of data reconstruction and analysis. Typically, centralized computing is not possible due to the sheer size of data, the large number of users and limited resources. Thus, distributed computing is used for data storage and processing with many cites spread all over the globe. This network is the Worldwide LHC Computing Grid (WLCG), or grid for short, of which ALICE is one user amongst the main four LHC experiments [83]. A brief introduction to the computing for ALICE can be found in reference [70] and an in-depth review is given in reference [84].

Computing is a vital part of the effort in experimental physics and typical tasks are, amongst others, the reconstruction, compression and processing of experimental data as well as the generation of MC events and the simulation of the corresponding detector response. These tasks can be split into several steps for

illustration. First, raw data of the experiment is reconstructed as was described in section 3.3, and possibly compressed or filtered in order to reduce the amount of storage space that is needed. Second, physics analyses, i.e. the calculation of physics observables, can then be performed on the high level objects that were generated during the reconstruction step. The first steps are typically performed on the grid due to the high demand for resources while the latter, depending on the compression rate, can be performed either locally or also in a distributed manner. A last step of a typical analysis chain is post-processing which rarely requires the use of distributed computing facilities due to the comparatively low demand of resources. Typical post-processing tasks are the application of corrections or the evaluation of (systematic) uncertainties. In parallel to the processing of real data, simulated events and detector responses are often required in order to correct, for example, for detection efficiencies. The processing chain for simulated events is very similar to that of real data but must obviously start with the generation of MC events and the simulation of the detector response. Since these steps are also very demanding in terms of computing resources, the grid is also utilized for MC productions.

The framework used for data reconstruction, processing and analysis is to the largest part written in C++, an object oriented programming language. The two main parts of the reconstruction and analysis framework are AliRoot [85] and AliPhysics [86], which are based on the ROOT [87] package that was developed at CERN. The ROOT framework is a statistics and physics analysis toolset, also written in C++, that offers a wide variety of tools for a multitude of purposes like histograms and fitting algorithms. External tools are interfaced with the AliRoot and AliPhysics frameworks for tasks that are not implemented in the framework. Examples of such tasks are the simulation of particle decays or possible machine learning applications that are based on modules available for Python. The AliRoot framework acts as a fundamental part of the analysis and reconstruction code and, amongst other things, holds classes utilized during the reconstruction of the data. It also contains calibration objects which are used by the AliPhysics framework that is (mainly) responsible for physics analyses. This means, that the AliPhysics framework comprises a plethora of analysis tools for different use cases and is generally the framework most frequently interacted with by end users, read physicists doing data analysis.

The generation of simulated data, including the detector response, is done with a variety of external tools that are interfaced with the software framework described above. ALICE uses event generators such as PYTHIA [88, 89], while the simulation of the interaction of the generated particles with the detector is based on tools like GEANT [90, 91, 92]. Interactions with the detector material can produce secondary particles that were not part of the initial event but become available after simulation of the detector response. Simulated events are also reconstructed by the same algorithms as the data, based on the simulated response of the detector. The ALICE detector is fully implemented in these simulations, including support structures and dead material. The reconstructed information as well as the original MC information is stored for each particle which enables the calculation of reconstruction efficiencies from MC.

The analysis code that has been used in the analysis presented in this thesis is largely part of the AliPhysics framework. This includes tools for the filtering of the data, the calculation of observables as well as tools for the signal extraction. Some of the classes used for filtering were expanded to accommodate features required in this analysis. The calculation of the observables was based on a pre-existing framework, but new functionalities were added to allow for the correlation study. A comprehensive toolset was designed for the determination of the correlation signal and implemented from scratch. In addition, some parts of the analysis chain are not contained in the official framework and had to be developed separately. These are either used to provide input quantities like cut functions or during post-processing of the results. Any code that was developed for this analysis has been preserved and made available to the collaboration.

4. Data sample and Monte Carlo simulations

In this chapter, the data sample as well as the corresponding MC productions are introduced. The data presented consists of proton-proton collision events at center-of-mass energies of 13 TeV provided by the LHC and recorded by ALICE in the years 2016 to 2018. During this period, events with different collision systems, namely proton-lead and lead-lead, and energies were also recorded but are not used in this analysis. An overview of the available statistics in the data and MC samples is presented in table 4.1. The numbers represent the total amount of recorded collision events for the different trigger selections included in the analysis. Since trigger responses were not simulated, a similar differentiation is irrelevant in the MC sample. The minimum bias sample provides the largest number of events but statistics in terms of J/ψ candidates is significantly enhanced in the HM triggered events. There is about an order of magnitude fewer events available in the EMCal triggered samples since these triggers were not active during the full data taking period.

	2016	2017	2018	total
data				
MB	4.87×10^8	6.90×10^8	7.97×10^8	1.97×10^9
HM	2.73×10^8	4.48×10^8	3.68×10^8	1.09×10^9
EMCEGA1	1.89×10^7	4.63×10^7	3.32×10^7	9.83×10^7
EMCEGA2	3.19×10^7	5.90×10^7	4.10×10^7	1.32×10^8
MC productions				
J/ψ injected	1.63×10^7	6.22×10^7	3.73×10^7	1.16×10^8
general purpose	1.95×10^8	4.88×10^8	1.75×10^7	8.58×10^8

Table 4.1.: Overview of the number of available events in data and MC for the different years of data taking as well as the total samples.

4.1. Data sample

Several triggers are included in the analysis in order to enhance the available statistics and gain access to a larger region of phase space. These triggers, which have previously been mentioned in section 3.2.6, are the MB and HM triggers as well as the high and low threshold EMCal and DCal triggers, called EMCEGA1 and EMCEGA2 respectively. For simplicity, the calorimeter triggers are referred to as EMCal triggers since both the EMCal and DCal are not only identical in design but so is the corresponding trigger definition. No distinction is made between events triggered by EMCal or DCal which maximizes the effective acceptance of the calorimeter trigger.

The data consists of a total of three years worth of data taking that is split into separate so-called runs corresponding to periods of continuous data taking with steady detector conditions. In between runs, detector conditions can change, for example, due to issues with certain sub-systems of the ALICE detector. Reconstruction efficiencies may thus vary from run to run and MC productions are therefore anchored to said runs in order to properly represent the corresponding detector performance.

Some of these runs have to be discarded from the analysis due to limited performance of relevant sub-systems. Lists of runs with good data quality are prepared centrally by the ALICE Data Preparation Group (DPG), which is an internal working group responsible for steering and coordinating data reconstruction and the generation of MC productions. Such lists are compiled according to the status of the different detector systems and various lists are available for different requirements. All available lists prepared by the DPG can be found online [93]. The data samples for the different triggers are first and foremost restricted to the availability of the corresponding trigger in a specific run. Especially the EMCal triggers were only available with satisfactory performance from the second half of data taking during 2016 onwards. The number of events and integrated luminosities quoted in table 4.1 reflect the availability of the corresponding triggers in the data sample.

All runs used in the analysis are required to have good V0 performance since it provides the trigger signal for the MB and HM events as well as the overall earliest L0 trigger signal. Selected runs must also have good performance of the central barrel tracking detectors, namely the ITS and TPC due to the reconstruction

of J/ψ mesons from the di-electron decay at mid rapidity. Runs with limited acceptance in the central barrel are rejected because full acceptance, especially in azimuthal direction, is favorable for an analysis of two particle correlations. While the MB and HM triggered samples only require good performance of the V0 and tracking detectors, the EMCal triggered samples are furthermore restricted to runs with good EMCal and DCal performance.

In addition to the general requirements on detector conditions, the data is checked for satisfactory and consistent quality as well as reasonable reproduction of the present features in the MC sample. This step is typically referred to as quality assurance (QA) and performed on a run-by-run basis before the data is analyzed. One important step during the QA process is the check for availability and meaningful application of all relevant calibrations. The most important calibrations in this analysis are the specific energy loss curves of charged particles traversing the TPC as well as the cluster energy of the calorimeters. General event quantities like the vertex position and kinematic quantities of reconstructed tracks, for example the mean azimuthal angle, are also checked in order to identify possible issues with the data. No issues that could significantly affect this analysis are found in the runs selected for the data and MC samples.

The MB triggered data sample, while providing the largest number of events as quoted in table 4.1, provides only few J/ψ candidates due to the rarity of the probe. The number of available candidates is significantly increased in the HM trigger sample since higher multiplicity events have a larger probability to contain J/ψ mesons as was shown in [94]. The HM trigger therefore also provides a larger p_{T} coverage for J/ψ than the MB sample due to the increased statistics. Furthermore, the trigger allows to study a potential modification of the correlation signal in high multiplicity environments. Figure 4.1 shows the integrated multiplicities in both V0 counters for minimum bias and high multiplicity triggered data, as well as the ratio of these distributions. The ratio of the multiplicity distributions in the right panel of the figure exhibits an ostensible onset behavior for the HM trigger which is due to the different trigger thresholds used during the period of data taking [94]. Nevertheless, a plateau region at high multiplicities can be observed from which the rejection factor of the HM trigger can be determined. This rejection factor denotes the rate of downscaling of events not passing the trigger selection and is obtained from a constant fit to the plateau region. The fit yields a rejection factor

of 367.3 ± 4.5, where the uncertainty is given by the uncertainty of the fit. Since the multiplicity distribution in HM triggered events does not resemble the natural one, potential biases could arise if the analysis would be performed differentially in the event multiplicity. But such an analysis goes beyond the scope of this thesis and similar biases are therefore negligible since the results are only presented in an event multiplicity integrated form.

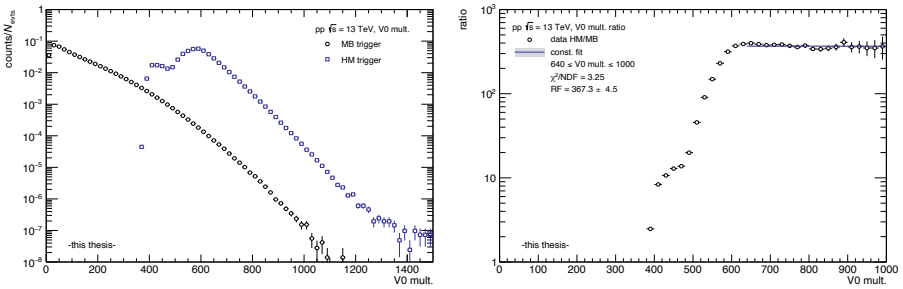

Figure 4.1.: V0 multiplicity distributions (*left*) for MB and HM triggered events as well as the ratio of the two distributions (*right*). The right panel also shows the rejection factor of the HM trigger as a constant fit to the plateau region.

The employment of the EMCal trigger allows to significantly extend the observable phase space to larger J/ψ transverse momenta. The trigger thresholds of the EMCEGA1 and EMCEGA2 triggers can clearly be seen in the cluster energy distributions shown in the left panel of figure 4.2. The right panel of figure 4.2 shows the ratios of cluster energy distributions in EMCEGA2 triggered events to MB events as well as the ratio of the high to low threshold EMCal triggers. This figure shows, that the EMCal triggers exhibit some onset behavior and become fully efficient at around 5 and 10 GeV, where the ratios reach a plateau. The trigger rejection factors are again determined from constant fits to these plateau regions, where the rejection factor for EMCEGA1 is given by the product of the two factors quoted in the figure. Thus, the rejection factors are found to be 401.68 ± 4.03 and 4932.63 ± 55.05 for the low and high threshold EMCal triggers, respectively. The uncertainties are given by the uncertainties of the fits and additional error propagation in the case of the high threshold EMCal trigger.

Finally, the integrated luminosities for the different trigger samples can be calculated from a reference luminosity, $\mathcal{L}_{\text{ref.}} = 21.6 \pm 1.1$ nb^{-1}, that was determined

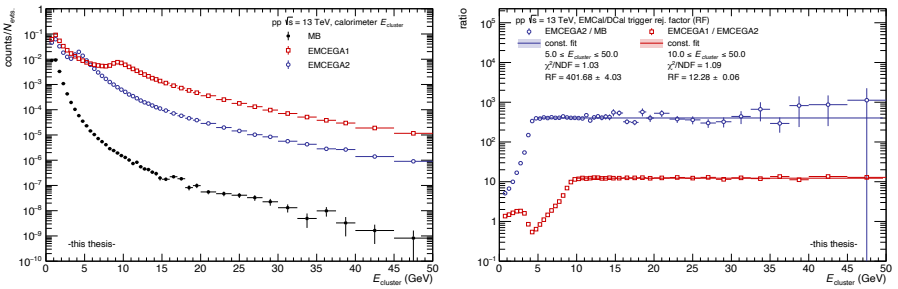

Figure 4.2.: EMCal cluster energy distributions for MB, EMCEGA1 and EMCEGA2 triggered events (*left*) as well as the ratios of the distributions (*right*). The right panel also show the EMCal trigger rejection factors as constant fits to the plateau regions.

in ref. [94] for a slightly different selection of runs in the same MB triggered data sample. The integrated luminosities for the different trigger samples are given by:

$$\mathcal{L}_i = \frac{N_{\text{evts.},\,i}}{N_{\text{evts.,\,ref.}}} \times \mathcal{L}_{\text{ref.}} \times \text{RF}_i\,, \tag{4.1}$$

where index i indicates the trigger. The reference luminosity is scaled by the ratio of the number of events in the corresponding trigger sample, $N_{\text{evts.},\,i}$, to the number of reference events, $N_{\text{evts.,\,ref.}}$. The numbers of events are hereby taken from table 4.1, while the reference is given by $N_{\text{evts.,\,ref.}} = 1.25 \times 10^9$ [94]. The scaled reference luminosity, however, represents MB triggered events and must further be modified using the trigger rejection factors, RF_i, in order to properly account for the different triggers. Said rejection factors are quoted above for the HM as well as EMCal triggers and no additional scaling is applied in the case of the MB trigger where $\text{RF}_{\text{MB}} = 1$ by definition. The integrated luminosities for the different trigger samples are quoted in table 4.2.

	MB	HM	EMCEGA1	EMCEGA2
$\mathcal{L}_{\text{int.}}$	34.04 ± 1.73 nb^{-1}	6.92 ± 0.36 pb^{-1}	8.38 ± 0.44 pb^{-1}	0.92 ± 0.05 pb^{-1}

Table 4.2.: Integrated luminosities for the different trigger samples.

4.2. Monte Carlo simulations

While the results presented in this thesis are based on real collision data taken by the ALICE experiment, simulations of such events are required for a number of different reasons. The J/ψ signal shape from MC, including energy loss via bremsstrahlung of the produced electrons and positrons, is used during the signal extraction in section 5.5. The reconstructed J/ψ mesons and associated hadrons are corrected for their reconstruction inefficiencies, where the efficiencies are obtained from MC as described in section 5.6. Furthermore, the determination of the pseudo-proper decay length cut, which is used for the separation of prompt and non-prompt J/ψ as described in section 5.7.3, is partly based on MC. Different MC productions are needed for these purposes, which either reproduce the full MB event or are enhanced in terms of the available statistics for J/ψ. These productions are referred to as 'general purpose' or 'J/ψ injected', respectively. The total number of events available for the different MC productions are listed in table 4.1. Due to the enhanced statistics in the J/ψ injected MC sample, considerably less events than in the data are required to reach a satisfying statistical precision.

The general purpose MC productions are based on the simulation of proton-proton collision events using the PYTHIA event generator tuned to LHC data. The subsequent transport of generated particles through a realistic model of the ALICE detector is based on GEANT, which simulates the interactions of the generated particles with the detector material. Secondary particles[1] produced in such interactions are also further propagated through the detector and can in turn interact with it. The detector response is fully modeled and all particles, primaries as well as secondaries from interactions with the detector material, are reconstructed with the same framework as is used for real data. Thus, reconstructed quantities are available in addition to the 'true', read generated, MC data. The MC productions are anchored to the runs in data and all data taking conditions are hereby respected and reproduced. This ensures that, for example, the re-

[1] Following ALICE convention, primary particles are distinguished from secondaries according to their displacement from the event vertex. The production point of primary particles can not be distinguished from the event vertex within the available resolution. Secondary particles, on the other hand, originate in weak decays or interactions with the detector material and are therefore produced at an observable distance. A more in-depth description of the definition of primary particles can be found in reference [95].

construction efficiencies obtained from the simulations reflect the real efficiencies present in the data.

J/ψ injected productions are based on general purpose MC productions where every MB event is enhanced with an additionally generated J/ψ on top of the underlying event. The injected J/ψ mesons are further forced to decay into an electron-positron pairs where the decay is handled by the PHOTOS [96] package for QED. This package particularly accounts for NLO radiative corrections from bremsstrahlung processes. During this procedure, injected J/ψ mesons contribute according to a mixture of 70% prompt and 30% non-prompt J/ψ. The non-prompt component originates in the decays of b-hadrons, which is incorporated in PYTHIA. Prompt J/ψ mesons, on the other hand, are added directly following a natural p_{T} spectrum. This spectrum follows a power law parametrization tuned to proton-proton collisions at 5 TeV. The natural shape of the generated spectrum ensures a meaningful distribution of produced J/ψ mesons in the enhanced MC sample. However, in order to improve the statistics at larger transverse momenta, a flat p_{T} spectrum is used in addition for $p_{\mathrm{T}} > 6$ GeV/c. The total p_{T} spectrum of all produced J/ψ mesons in the sample is thus not physical as can be seen in figure 4.3. The distribution clearly exhibits a constant at large transverse momenta as well as a step at $p_{\mathrm{T}} = 6$ GeV/c, where the two components meet. Therefore, an additional weighting procedure has to be applied during the analysis of the J/ψ injected MC sample to reproduce a meaningful p_{T} spectrum before the sample is used, for example, to determine the reconstruction efficiency. The weights hereby account for the difference between the natural shape of the J/ψ p_{T} spectrum and the combined distribution including the flat component at high transverse momenta. The p_{T} spectrum of generated J/ψ after the application of the weighting procedure is compared to the original, unweighted spectrum in figure 4.3. It can be seen that a physical spectrum is reinstated while still retaining good statistical significance at high transverse momenta.

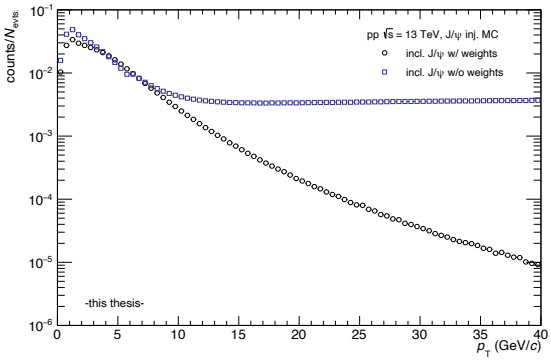

Figure 4.3.: Transverse momentum spectra of generated J/ψ mesons in the J/ψ enhanced MC sample before and after application of the p_{T} weighting procedure.

5. Analysis

In this chapter, the data selection criteria and analysis method are described. The goal of the analysis is the determination of the correlation of inclusive, non-prompt and prompt J/ψ with unidentified, charged hadrons in different kinematical regimes. The different triggers included in the analysis cover different regions of phase space and the inclusion of the HM trigger enables the study of potential modifications to the correlation in a high multiplicity environment. Comparison to model calculations can help to improve the understanding of the production mechanism of the J/ψ.

The analysis consists of several components which build upon each other and will be described separately in the sections below. In order to provide the reader with a better understanding of the different parts of the analysis, it is sensible to start with a brief overview of the procedure. The approach can be sketched as follows and applies to all trigger samples in the same way:

First, events as well as electron or positron and hadron tracks within these events are selected. Then, J/ψ candidate pairs are built from electron and positron tracks and the angular correlation with hadron tracks in the same event is calculated. The inclusive J/ψ-hadron correlations are determined from these preliminary correlations by applying an acceptance correction and signal extraction procedure. The resulting correlation functions are normalized to the number of J/ψ and expressed in terms of the associated yield per trigger, differential in the azimuthal difference $\Delta\varphi$. Hereby, an efficiency correction is applied on the J/ψ candidate pair and hadron track level, which is naturally also considered in the normalization. Additionally, the correlation functions are also determined for non-prompt J/ψ, which are selected by a cut exploiting the separation from the event vertex due to their origin in a weak decay, following the same procedure. Finally, the prompt J/ψ-hadron correlations can be calculated using the superposition principle based on the fraction of non-prompt J/ψ in the data.

5.1. Event selection

Events must fulfill a number of criteria in order to be selected for the analysis. Any event must naturally correspond to a proton-proton collision and background events, like beam-gas interactions, are rejected. Furthermore, events are selected according to either one of the four triggers, i.e. MB, HM, EMCEGA1 and EMCEGA2, that are included in the analysis. These two criteria yield the numbers of events quoted in table 4.1.

In addition to the trivial requirements, events must also have a reconstructed vertex with at least one contributing track. Said vertex must be within ± 10 cm of the nominal interaction point along the beam direction to maximize the available acceptance of the detector. In-bunch pile-up is rejected based on multiple reconstructed vertices where two different algorithms are applied. The first one is based solely on SPD information and rejects events that have several vertices reconstructed from at least three SPD tracklets each. This selection is modified in HM triggered events where vertices must be reconstructed from at least five tracklets to reduce the number of false positives. The second method for in-bunch pile-up rejection is also based on the reconstruction of more than one collision vertex but uses the full track information for vertex finding. In contrast to the SPD based pile-up removal, the second method has wider coverage since SPD information is not required for the tracks that are considered. Even after the removal of in-bunch pile-up, however, a contamination from out-of-bunch pile-up can still be present due to the long readout time of the TPC. These contaminations have to be taken care of in the track selection and will thus be described in the corresponding sections below.

Pile-up is not simulated in the MC productions and a rejection of non-collision events is therefore unnecessary. All MC events correspond to a minimum bias selection since no trigger response has been simulated. Similar to the real data, the MC events are selected according to their vertex position as events are simulated according to a physical distribution around the nominal interaction point.

Depending on the trigger, the selected events exhibit different multiplicity distributions as can be seen in figure 5.1. The figure shows the event multiplicities at mid-rapidity in terms of the number of SPD tracklets in $|\eta| < 1.0$. The MB trigger shows a continuously falling distribution while the HM and EMCal trigger samples display certain multiplicity biases. The HM trigger, while selecting based

on multiplicities observed in forward direction, largely rejects events with small multiplicities at mid-rapidity. Similarly, the EMCal triggered data also shows some bias towards larger event multiplicities, possibly due to an overlap with events containing jets or the presence of hard probes. The mean numbers of SPD tracklets are also quoted in the figure.

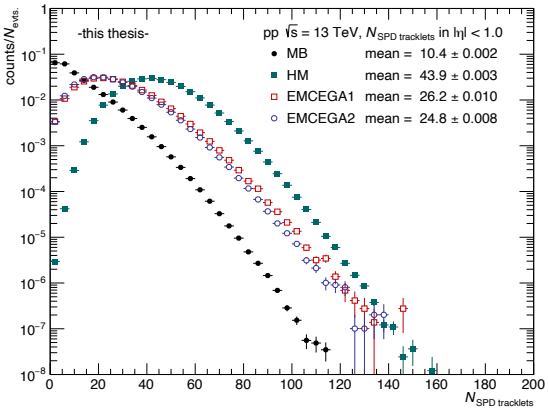

Figure 5.1.: Distribution of number of SPD tracklets in $|\eta| < 1.0$ for the different triggers. The mean mean numbers of SPD tracklets are also quoted.

The average event multiplicity for the different triggers can be estimated from the mean number of SPD tracklets. These values are necessary to provide common grounds for theory or model comparisons since the different triggers might probe different types of events. In MB events, the average multiplicity is given by $\langle \mathrm{d}N_{\mathrm{ch}}/\mathrm{d}\eta \rangle_{\mathrm{INEL>0}} = 6.46 \pm 0.19$ [97], where the 'INEL>0' label refers to events with at least one charged particle in $|\eta| < 1.0$. The multiplicity of HM and EMCal triggered events can then be calculated according to:

$$\langle \mathrm{d}N_{\mathrm{ch}}/\mathrm{d}\eta \rangle^{i}_{\mathrm{INEL>0}} = \langle \mathrm{d}N_{\mathrm{ch}}/\mathrm{d}\eta \rangle_{\mathrm{INEL>0}} \times \frac{\langle N^{i}_{\mathrm{SPD\ tracklets}} \rangle}{\langle N^{\mathrm{MB}}_{\mathrm{SPD\ tracklets}} \rangle}, \tag{5.1}$$

where index i labels the trigger and the $\langle N_{\mathrm{SPD\ tracklets}} \rangle$ are the mean numbers of SPD tracklets as quoted in figure 5.1. The uncertainty on the average multiplicity is calculated using error propagation from the individual uncertainties on the values in equation 5.1. The trigger dependent multiplicities are summarized in table 5.1. It can be seen that HM and EMCal triggered events have about 4 and 2.5 times the average multiplicity as minimum bias events, respectively.

	$\langle N_{\text{SPD tracklets}} \rangle$	$\langle \mathrm{d}N_{\text{ch}}/\mathrm{d}\eta \rangle_{\text{INEL}>0}$
MB	10.39 ± 0.002	6.46 ± 0.19
HM	43.89 ± 0.003	27.30 ± 0.80
EMCEGA1	26.20 ± 0.010	16.30 ± 0.48
EMCEGA2	24.84 ± 0.008	15.45 ± 0.45

Table 5.1.: Mean number of SPD tracklets in $|\eta| < 1.0$ and corresponding average event multiplicities per trigger.

5.2. Electron track selection

Electron and positron tracks are reconstructed in the central barrel of the ALICE detector using ITS and TPC. In the EMCal triggered sample, clusters measured in the EMCal and DCal calorimeters are used in addition to improve the particle identification at high transverse momenta. The tracks are selected according to a list of cuts that specify requirements on kinematical quantities as well as the reconstruction quality of the track. Furthermore, electrons and positrons tracks are subject to a set of particle identification cuts. These selection criteria are summarized in table 5.2 and will be described in detail in the following.

Kinematical cuts

Some kinematical cuts are applied in order to ensure full available acceptance and to reject some of the background tracks. A pseudorapidity cut of $|\eta| < 0.9$ is applied in order to guarantee that all tracks are within the full acceptance of the TPC. The minimum p_{T} requirement of 1 GeV/c removes background from soft particles which would yield large combinatorial background contributions in the J/ψ signal extraction. This cut does not pose a limitation on the J/ψ reconstruction due to the comparatively large rest mass of the J/ψ that requires a momentum transfer of about 1.5 GeV/c per electron in the rest frame. Thus, J/ψ mesons can still be reconstructed down to zero transverse momentum even though a minimum p_{T} cut is applied on the electron legs.

Track quality cuts

Several cuts are applied in order to guarantee a satisfying track quality. A cut on the Distance of Closest Approach (DCA) to the primary vertex is applied both

variable	cut	condition
kinematical cuts		
$\|\eta\|$	< 0.9	
p_{T}	> 1 GeV/c	
track quality cuts		
$\|\mathrm{DCA}_{xy}\|$	< 1 cm	
$\|\mathrm{DCA}_{z}\|$	< 3 cm	
ITS refit	yes	
TPC refit	yes	
TPC $N_{\mathrm{cls.}}$	≥ 70	
TPC $N_{\mathrm{track\ seg.}}$	≥ 6	
TPC χ^2	< 4	
ITS χ^2	< 30	
SPD hits	any layer	
kink tracks	reject	
particle identification		
TPC $n\sigma$ electron	$\in [-1.5, 3]$	
TPC $n\sigma$ pion	> 3.5	MB and HM trigger, EMCal trigger and no matched cluster
TPC $n\sigma$ proton	> 3.5	
cluster-track ΔR	≤ 0.005	EMCal trigger and matched cluster
cluster E/p	$\in [0.8, 1.3]$	EMCal trigger and matched cluster
cluster M_{02}	$\in [0.01, 0.7]$	EMCal trigger and matched cluster

Table 5.2.: Electron and positron track selection cuts, separated into kinematical, track quality and PID requirements. Calorimeter cluster cuts (cluster E/p and M_{02}) are only applied if the track is matched to an EMCal or DCal cluster.

in the transverse plane (DCA_{xy}) and along the beam pipe (DCA_{z}). This removes secondary particles from material interactions or weak decays, which will show a larger displacement from the primary vertex than electrons originating in the strong or electromagnetic decay of the J/ψ. Additionally, the cut along the beam pipe will suppress some tracks from out-of-bunch pile-up events due to the their longer drift time in the TPC as compared to tracks in the current event. Figure 5.2 shows the DCA_{xy} and DCA_{z} distributions for selected electron tracks in the left and right panel, respectively. The DCA_{xy} distributions show sharp peaks around zero and broader shoulders while the DCA_{z} exhibit a less steeply falling slope. This difference in slope is due to the drift of electric charges in the TPC along the direction of the beam pipe. The shoulders of the distribution in the

transverse plane is most likely due to a contamination from secondary particles which can not fully be removed by the selection criteria. This, however, does not affect the analysis due to the reconstruction of the J/ψ from the invariant mass of the electron-positron pairs. Some small differences between the trigger samples are expected and observed but have no negative effect on the analysis.

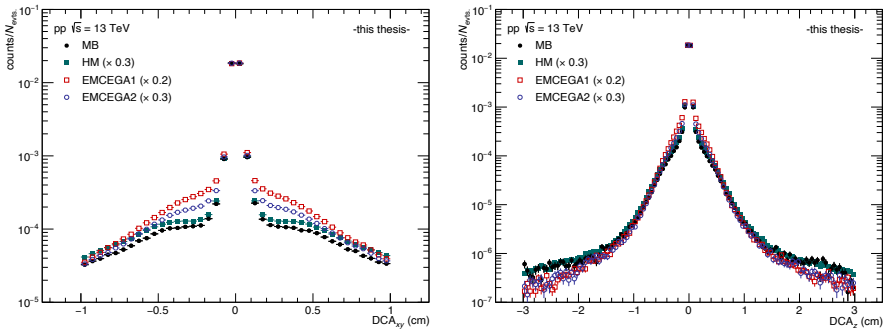

Figure 5.2.: DCA$_{xy}$ (*left*) and DCA$_z$ (*right*) distributions for selected electrons in all trigger samples. All distributions are scaled to the MB sample.

All electron tracks are furthermore required to have undergone the final step of the fit procedure in the ITS and TPC, referred to as 'refit' in table 5.2, during track reconstruction. This requirement ensures that the tracks have hits in the ITS and that ITS track segments are matched to those in the TPC. On top of that, electron tracks must have at least one hit in any of the SPD layers. Such a selection removes electrons from photon conversions in the detector material following the SPD layers. Due to the lower material budget of the ITS, mainly electrons from photon conversions in the beam pipe remain as background and will be removed through the electron-positron pair selection criteria. The SPD requirement also removes out-of-bunch pile-up tracks due to the fast read-out time of the silicon detector.

Good quality of the tracks reconstructed in the TPC is ensured by requiring at least 70 clusters out of a possible total of 159 and six track segments for any electron track. A track segment in the TPC is hereby given by 20 consecutive rows of readout pads where at least five clusters must be found per segment. In total, a track can consist of up to eight segments and the minimum requirement ensures a uniform distribution of clusters along the track as well as a reasonable

length of the track in the TPC for reconstruction. The track reconstruction in the ITS and TPC is furthermore required to have a maximum χ^2 of 30 and 4, respectively, where the requirement for the ITS is kept very loose to account for the smaller number of tracking points.

Background tracks are additionally rejected via topological decay signatures. Weak leptonic decays, for example of charged pions or kaons into muons and neutrinos, result in tracks that show kink topologies due to momentum transfer to the decay products where the neutrino is invisible to the detector. Such background tracks are removed by requiring the absence of kinks in reconstructed electron tracks. Bremsstrahlung processes of electrons can also produce tracks with kink topologies if a relatively large energy loss occurs in a single interaction. In such cases, the electron track will also be removed by the kink rejection.

Particle identification

The main device for particle identification in this analysis is the TPC. However, two different strategies are used for the MB or HM and EMCal triggered samples due to the different reach in p_{T} and the availability of detectors. At high transverse momenta, electron and pion separation in the TPC becomes worse since the energy loss curves approach each other as can be seen in figure 3.3. Calorimeters, on the other hand, can be used for electron identification particularly at high p_{T} by comparing the energy deposited in the calorimeter to the absolute momentum of the track. Furthermore, the MB and HM triggered samples are not restricted to runs that have good EMCal and DCal performance, which prevents the use of the calorimeters in these data. Therefore, the particle identification is solely based on the TPC in the MB and HM trigger data while EMCal and DCal are used in addition in the EMCal triggered sample.

Particle identification in the TPC is based on the energy loss of charged particles traversing in the gas. Tracks can be selected or rejected according to their deviation from a parametrization of the Bethe-Bloch energy loss curves in the drift gas. The parametrizations for different species are calibrated on data and deviations for a given particle hypothesis are expressed in terms of the resolution of the distributions:

$$n\sigma_i = \frac{(\mathrm{d}E/\mathrm{d}x)_{\mathrm{meas.}} - (\mathrm{d}E/\mathrm{d}x)^i_{\mathrm{exp.}}}{\sigma^i_{\mathrm{exp.}}}, \tag{5.2}$$

where $(\mathrm{d}E/\mathrm{d}x)^{i}_{\mathrm{exp.}}$ and $\sigma^{i}_{\mathrm{exp.}}$ are the expected energy loss and resolution for a particle of species i at a given momentum. The measured energy loss associated with a track is denoted by $(\mathrm{d}E/\mathrm{d}x)_{\mathrm{meas.}}$. Electron candidates are accepted for $n\sigma_{\mathrm{e}} \in [-1.5, 3]$ while pions and protons are rejected by requiring $n\sigma_{\pi} > 3.5$ and $n\sigma_{\mathrm{p}} > 3.5$, respectively. The momentum dependent $n\sigma_{\mathrm{e}}$ distributions for selected electron tracks are shown in figure 5.3. Towards higher momenta, the distributions become more asymmetric due to the rejection of pions. However, due to the different particle identification strategy that is used in the EMCal triggered sample, the bottom panels in figure 5.3 show a significantly different behavior at high momenta.

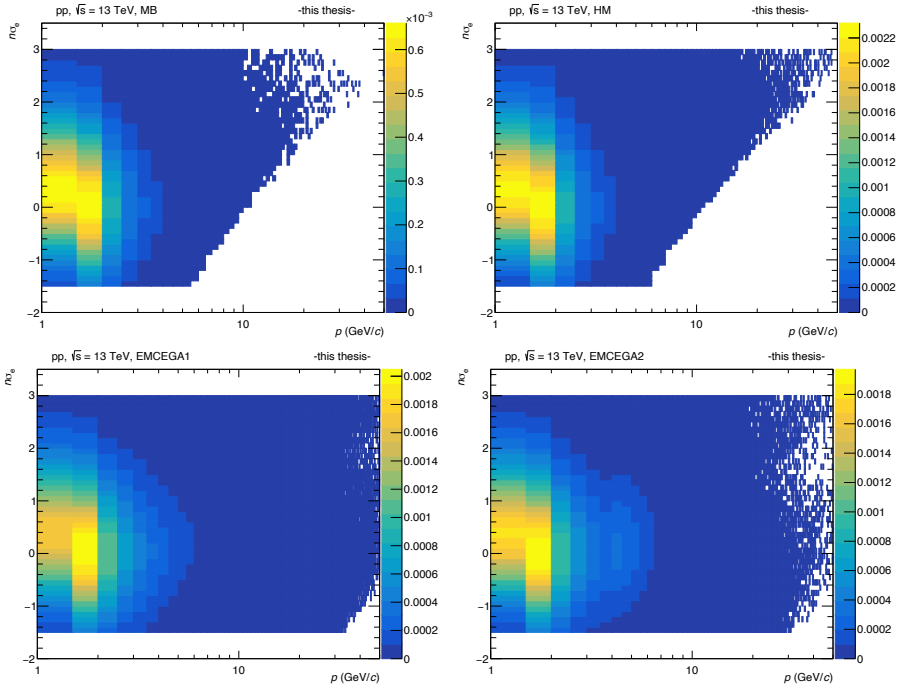

Figure 5.3.: Distributions of $n\sigma_{\mathrm{e}}$ as a function of momentum for selected electrons in MB (*top left*), HM (*top right*), EMCEGA1 (*bottom left*) and EMCEGA2 (*bottom right*) triggered events.

In the EMCal triggered samples, calorimeter clusters are used for particle identification in addition to the TPC information. This improves the separation between electrons and pions at high transverse momenta where the triggers are

active. However, in order to do so, calorimeter clusters need to be selected and matched to tracks reconstructed in the tracking detectors. Calorimeter clusters are built by combining cells via a so-called clustering algorithm. They must consists of at least two cells and the clustering starts with a seed cell that must have an energy above 0.5 GeV. Adjacent cells are added to the cluster as long as they have an energy above 0.1 GeV. Clusters are then selected according to very few, non-restricting selection criteria based on the shape of the cluster. The cluster shape can be defined by the long and short axes of an ellipse, called M_{02} and M_{20}, respectively. Electron clusters are expected to be rather circular in shape and can be selected with satisfactory performance by a fairly loose cut on the long axis, which is required to be within $M_{02} \in [0.01, 0.7]$. The minimum requirement of $M_{02} \geq 0.01$ is necessary to remove so-called exotic clusters consisting of very few cells that passed the clustering algorithm but do not correspond to electrons. Selected clusters are further required to be matched to tracks reconstructed in the central barrel to remove clusters from photons. Tracks are hereby propagated to calorimeter surface and matched to a cluster if the distance between the track and cluster centroid is below a maximum distance. The distance is given by $\Delta R = \sqrt{\Delta\eta^2 + \Delta\varphi^2}$, as quoted in table 5.2. The cut on the distance is tuned in such a way that the number of matches of multiple tracks to the same cluster is minimized.

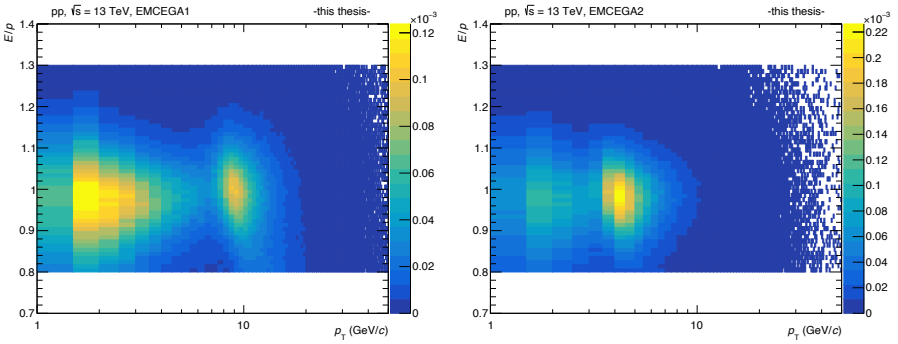

Figure 5.4.: Ratio of calorimeter cluster energy to absolute track momentum, E/p, for selected electrons with matched clusters in EMCEGA1 (*left*) and EMCEGA2 (*right*) triggered events.

The identification of electrons in the EMCal triggered sample is very similar to the selection in the MB and HM trigger data. Electrons are selected while

pions and protons are rejected with the same $n\sigma$ cuts, as listed in table 5.2, in the case where the track has no matched cluster in any of the calorimeters. The selection criteria are adapted, however, if a matched cluster is found. In this case, the pion rejection is replaced by a cut on the ratio of the cluster energy to the absolute momentum of the track, E/p. This is useful for electron identification due to the low rest mass of the electron and the high probability to deposit the full energy in the calorimeter. The ratio is therefore expected to be close to one for an electron and a selection criterium of $E/p \in [0.8, 1.3]$ is applied. The window is chosen to be asymmetric since very little non-electron contamination is expected at high E/p values. Figure 5.4 shows the E/p distributions for selected tracks with matched clusters for the EMCal trigger data. The distributions peak around $E/p \sim 1$ and the areas of increasing track density correspond to the EMCal trigger thresholds at $p_{\mathrm{T}} \sim 10$ GeV/c and ~ 5 GeV/c for EMCEGA1 and 2, respectively. The use of calorimeter information allows to reject less misidentified electrons at high transverse momenta while still retaining good performance of the particle identification as can be seen figure 5.3. This dramatically improves the statistics at high p_{T} in comparison to what would be achieved with a particle identification that is solely on the TPC.

The p_{T} distributions for selected electron tracks in all trigger samples are shown in the left panel of figure 5.5. The EMCal trigger thresholds as well as the significant increase in statistics at high p_{T} that is provided by the calorimeter trigger can clearly be seen. In comparison to minimum bias events, the increase in statistics from the high multiplicity trigger is also obvious.

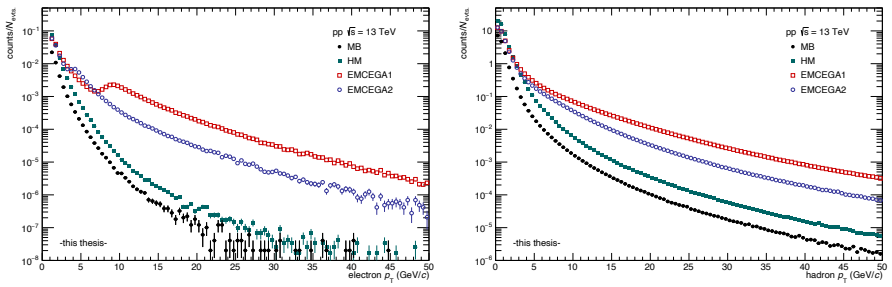

Figure 5.5.: Transverse momentum distributions for selected electron (*left*) and associated hadron (*right*) tracks in all trigger samples.

5.3. Associated track selection

The associated tracks are selected according to criteria that are similar to the electrons but generally more open. No particle identification is applied since the analysis presented in this thesis is based on unidentified charged hadrons. The selection cuts are summarized in table 5.3, where kinematical and track quality requirements are distinguished.

variable	cut
kinematical cuts	
$\|\eta\|$	< 0.9
p_{T}	> 150 MeV/c
track quality cuts	
$\|\mathrm{DCA}_{xy}\|$	< 1 cm
$\|\mathrm{DCA}_{z}\|$	< 3 cm
ITS refit	yes
TPC refit	yes
TPC $N_{\mathrm{cls.}}$	≥ 70
kink tracks	reject

Table 5.3.: Track selection cuts for charged, unidentified hadrons, separated into kinematical and track quality requirements.

Similar to the electron tracks, hadron tracks are reconstructed in the ITS and TPC with the same requirements on pseudorapidity and DCA. Hadron tracks are reconstructed down to very low p_{T}, but a limitation of $p_{\mathrm{T}} > 150$ MeV/c is imposed by the tracking resolution of the TPC. As is the case for electrons, tracks with kink topologies are rejected to remove tracks associated with weak particle decays. The tracks are furthermore required to have undergone the final reconstruction steps in the ITS and TPC and have at least 70 of the maximum possible 159 clusters in the TPC to guarantee a sufficiently good track quality. It should be noted, that no hit in any of the SPD layers is requested to maximize the available statistics. This, however, does not significantly increase the contamination from out-of-bunch pile-up tracks or affect the analysis negatively as is shown in section 6.2 where the selections quoted in table 5.3 are compared to an additional SPD requirement. The remaining track quality criteria used for electron tracks are omitted. The requirements listed in table 5.3 are sufficient for the correlation analysis and statistics is favored over ultimate track quality.

The right panel of figure 5.5 shows the p_{T} distributions for selected hadrons in the different trigger samples. It can be seen, that the slopes of the distributions are smaller in the EMCal triggered events, resulting in more statistics at higher transverse momenta. Nevertheless, no trigger threshold can be observed in the p_{T} distributions since the EMCal trigger does not select on hadrons. The increase of statistics at high p_{T} is most likely due to associated production in jet events. The HM trigger shows a constant increase in amplitude over the minimum bias sample as expected from the average multiplicities listed in table 5.1. A comparison to the distributions for selected electrons, shown in the left panel of figure 5.5, shows that the unidentified, charged hadrons are much more abundant.

5.4. Electron-positron pair selection

Electron-positron pairs are built from all combinations of oppositely charged tracks that pass the electron selection cuts within an event. These J/ψ candidates are further filtered by applying some additional selection criteria on all pairs that are found. Two different sets of requirements are hereby used to select inclusive and non-prompt J/ψ candidates. It is not possible to select prompt candidates directly in the data with the methods described in this thesis but the corresponding correlation functions can ultimately be calculated using superposition. Therefore, no selection criteria for prompt J/ψ candidates are introduced in this section.

5.4.1. Inclusive J/ψ candidate selection

All inclusive J/ψ candidate pairs are required to be within $|y| < 0.9$. An important source of background pairs originates in photon conversions in the detector material. The ITS and SPD requirements on the electron tracks already suppress a large portion of such background, particularly those created after the ITS. However, it is still possible that some of the conversion legs pass the electron selection and an invariant mass cut is therefore used in addition. The background rejection is further optimized by pairing electrons with tracks where the selection criteria are relaxed. In particular the ITS and SPD requirements are hereby removed, which allows to properly account for photon conversions in the whole detector. The pair candidates are required to have an invariant mass above 50 MeV/c^2, rejecting the vanishing mass pairs expected from conversions. It should be noted,

that the relaxed electron selection criteria are only used for the invariant mass cut. The final J/ψ candidate pairs are built from electrons selected according to the standard criteria described in section 5.2.

In addition to the trivial pair selection criteria that apply in the same way for all triggers, an additional cut is used in the EMCal triggered samples. Here, at least one of the electron legs of the pair is required to pass the trigger selection. Therefore, either one or both of the electron legs must have an associated cluster in the EMCal or DCal above the trigger threshold of $E = 5$ or 10 GeV for the low and high threshold trigger, respectively. This selection ensures, that the J/ψ candidate is not a byproduct of an otherwise triggered event but caused, or at least could have caused, the trigger signal.

The p_{T} distributions of selected inclusive J/ψ candidates are shown in the left panel of figure 5.6. The distributions for the MB and HM trigger samples have a much steeper slope than those of the EMCal trigger samples. It can clearly be seen, that the EMCal trigger significantly enhances the statistics at high transverse momenta. Additionally, the cluster energy requirement in the EMCal trigger sample is visible in the sharp rise up to the trigger threshold.

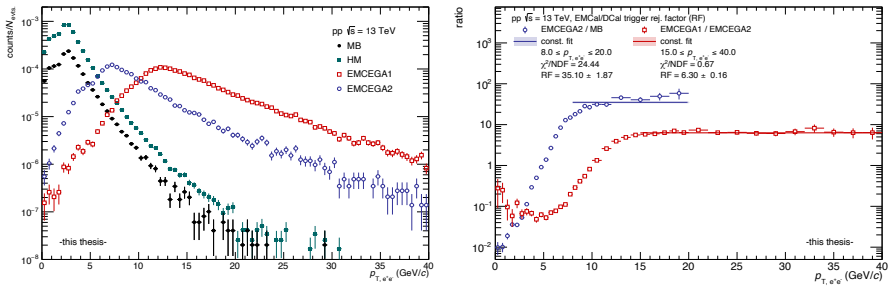

Figure 5.6.: Transverse momentum distributions for selected inclusive J/ψ candidates (*left*) and EMCal trigger onset in terms of the J/ψ p_{T} (*right*). The right panel shows a constant fit to the plateau regions to indicate the range in which the trigger is used.

The right panel of figure 5.6 shows the ratio of the p_{T} distributions of selected inclusive J/ψ candidates in EMCEGA2 to MB as well as high to low threshold EMCal triggered events. In this comparison, the minimum bias sample is limited to runs with good calorimeter performance and the PID approach for EMCal triggered events is used. This is done in order to provide a fair comparison of the

distributions, since the different slopes that are visible in the left panel of the figure arise not only from the trigger type but largely from the electron identification. The ratio displays the EMCal trigger onset which is distributed over the pair and therefore much slower than observed on the cluster energy in figure 4.2. The distributions reach approximate plateaus for transverse momenta above 8 and 15 GeV/c for the low and high threshold EMCal trigger, respectively. These plateaus are highlighted by the constant fits in the figure and signify the regimes where the EMCal trigger is fully efficient on the J/ψ level.

5.4.2. Non-prompt J/ψ candidate selection

The selection criteria for non-prompt J/ψ candidate pairs are based on those applied for the inclusive ones and all cuts described in section 5.4.1 apply. However, an additional cut is required to select non-prompt candidates from the inclusive sample. This selection is based on the so-called pseudo-proper decay length, or decay length for short, which quantifies the separation of the J/ψ decay vertex from the primary vertex of the event. A common decay vertex is determined for each electron-positron pair in the event and the decay length can be written as:

$$x = \frac{c\left(\vec{L} \cdot \vec{p}_{\mathrm{T}}\right) m_{\mathrm{J}/\psi}}{p_{\mathrm{T}}}, \tag{5.3}$$

where the vector $\vec{L}$ points from the primary to the decay vertex and $m_{\mathrm{J}/\psi}$ is the rest mass of the J/ψ [33]. The momentum $\vec{p}_{\mathrm{T}}$ is defined in the transverse plane and p_{T} is the absolute value of the vector.

Prompt J/ψ mesons are produced with no measurable separation from the primary vertex, their decay length distribution is symmetric and defined by the resolution of the reconstruction. Non-prompt J/ψ, on the other hand, can be produced at a considerable distance since they originate in weak decays of heavier particles. This results in a decay length distribution that corresponds to the convolution of the resolution and an exponential distribution attributed to the half life of the decay of the mother particle. The differences in shape can be exploited to distinguish prompt and non-prompt J/ψ. Typically, this is done by fitting the decay length and invariant mass distributions of the candidate pairs simultaneously, see for example references [98, 99], which allows for a high precision measurement. Unfortunately, such a simultaneous fit is not possible in this

analysis due to the limited statistics and further complication that the signal must ultimately be reconstructed on the basis of a correlation distribution. Nevertheless, the different decay length distributions of prompt and non-prompt J/ψ can still be utilized to define a cut that removes prompt J/ψ candidates from the inclusive sample since these are contained at smaller decay lengths. Such a selection yields a sample of non-prompt J/ψ candidates from which the non-prompt J/ψ signal and correlation function can be determined.

The decay length cut is determined from the decay length distributions for prompt and non-prompt J/ψ, which are obtained from the J/ψ injected MC productions. In order to properly reproduce the data, an additional smearing procedure is hereby applied that matches the DCA distributions in MC to data. This smearing is only required for the evaluation of the decay length cut since the relevant resolutions are naturally quite sensitive to the DCA to the primary vertex. The cut is furthermore anchored to data using an interpolation of the measured fraction of non-prompt J/ψ mesons, called f_B, instead of relying on the mixture in MC. The working point of the cut depends on p_{T} and additionally on a quantity that is referred to as the SPD pair type. Electron-positron pairs can have one of three possible SPD pair type values: first-first (FF), first-second (FS) or second-second (SS), which denote the combination of hits in the corresponding SPD layers. The SPD pair type is used as a classification since the decay length resolution improves with the number of hits in the first layer. The decay length distribution for inclusive J/ψ, which is used in the determination of the working point of the cut, is calculated according to:

$$R_{\text{inclusive J/}\psi}(x) = (1 - f_B) \times R_{\text{prompt J/}\psi}(x) + f_B \times R_{\text{J/}\psi\leftarrow h_B}(x), \tag{5.4}$$

where $R_{\text{prompt J/}\psi}(x)$ and $R_{\text{J/}\psi\leftarrow h_B}(x)$ are the decay length distributions of prompt and non-prompt J/ψ, respectively, given as probability density functions and weighted with the non-prompt fraction. The interpolation of the non-prompt fraction, presented in figure 5.11, is hereby evaluated at the average p_{T} for inclusive J/ψ in the given p_{T} bin. The determination of the prompt and non-prompt decay length distributions as well as the interpolation of the non-prompt fraction are described in the sections below. Figure 5.7 shows the decay length distributions for inclusive, prompt and non-prompt J/ψ for an exemplary p_{T} range and more bins can be found in figure A.3 in section A.1 of the appendix. It can be

seen that the distributions for inclusive J/ψ are dominated by the prompt component at low p_{T} but still exhibit an asymmetric shape due to the contribution from non-prompt J/ψ. At larger transverse momenta, the contribution from non-prompt J/ψ becomes more prominent and therewith also the asymmetry of the distribution. The resolution improves with increasing p_{T} and number of hits in the first layer of the SPD.

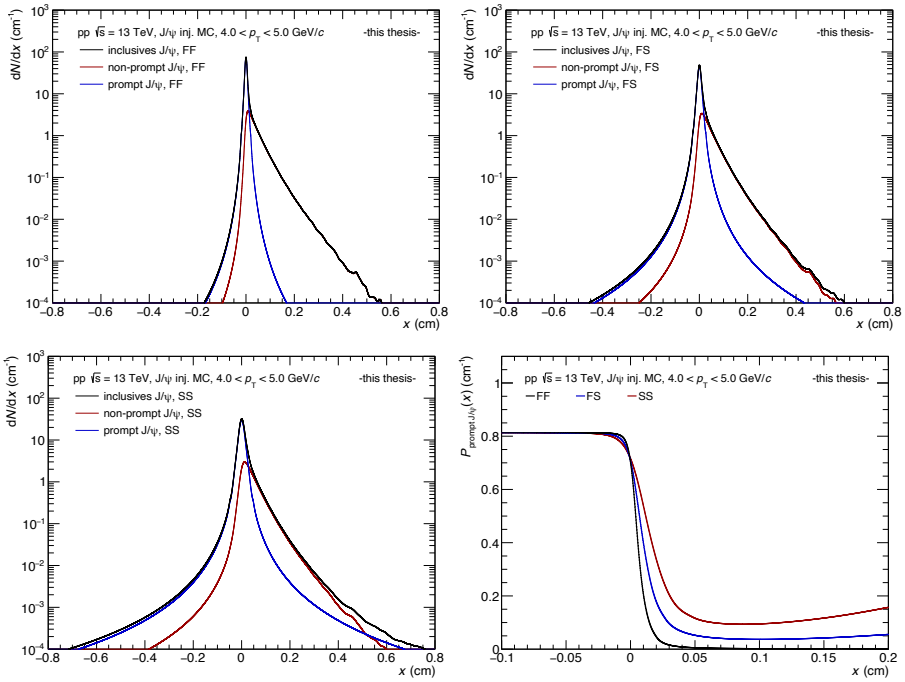

Figure 5.7.: Inclusive, prompt and non-prompt J/ψ decay length distributions for FF (*top left*), FS (*top right*) and SS (*bottom left*) pairs. The prompt and non-prompt distributions are probability-density functions multiplied with f_B and $(1 - f_B)$, respectively. The cumulative fraction of prompt J/ψ according to equation 5.5 is also shown (*bottom right*).

The working point of the decay length cut is determined from the so-called cumulative fraction of prompt J/ψ, which determines the percentage of prompt J/ψ in the inclusive sample above a certain decay length value. This allows the determination of a p_{T} and SPD pair type dependent decay length value above which only a given fraction of prompt J/ψ candidates remain. The fraction is calculated

from the decay length distributions of prompt and inclusive J/ψ according to the following formula:

$$P_{\text{prompt J/}\psi}(x) = \frac{\int_x^\infty \mathrm{d}\tilde{x}\,(1 - f_B) \times R_{\text{prompt J/}\psi}(\tilde{x})}{\int_x^\infty \mathrm{d}\tilde{x}\, R_{\text{inclusive J/}\psi}(\tilde{x})}, \tag{5.5}$$

where the integration is performed over the decay length. The cumulative fraction of prompt J/ψ, shown in the bottom right panel of figure 5.7, must by definition decrease monotonously with increasing x due to the symmetry of the decay length distribution of prompt J/ψ. At large values of x, the cumulative fraction can increase again due to the resolution for prompt J/ψ which has long tails in MC, but this has no impact on the determination of the cut. Significantly faster decreases can be observed at larger transverse momenta shown in the additional p_{T} bins displayed in figure A.4.

The decay length cut can easily be determined from $P_{\text{prompt J/}\psi}(x)$ by finding the value x_{cut} at which the fraction drops below a desired maximum percentage of prompt J/ψ surviving the cut. The complete rejection of all prompt J/ψ candidates is not reasonably possible with such a cut but sufficiently low contaminations can be achieved and a potentially remaining fraction of prompt J/ψ is regarded a systematic uncertainty on the measurement. A value of $\leq 10\%$ surviving prompt J/ψ is used as the default choice in this analyses and variations of $\leq 5\%$ and $\leq 20\%$ are evaluated for systematic tests. Figure 5.8 shows the p_{T} distribution of the working point of the decay length cut for the different SPD pair types in the default case. In order to obtain the cut as a continuous function of p_{T}, a power law fit is performed where the different SPD pair types are treated separately. The figure shows, that the decay length cut function decreases rapidly with p_{T} but strongly depends on the SPD pair type, especially at low transverse momenta. The alternative choices of $\leq 5\%$ and $\leq 20\%$ surviving prompt J/ψ, shown in figure A.5, exhibit a similar behavior.

The decay length cuts shown in figure 5.8 are applied for all electron-positron pairs to determine the non-prompt J/ψ candidate sample. The decay length distributions for selected candidates are shown in figure 5.9 together with the corresponding decay length cut functions. The same distributions are also shown for the two alternative choices of working point definitions in figure A.5. The application of the decay length selection translates to a significant loss of statistics due to the required asymmetry of the cut. Furthermore, the experimental resolution

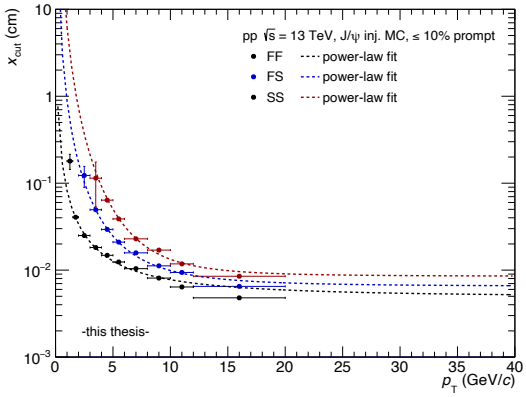

Figure 5.8.: Decay length cut working points as determined for a 10% contamination of surviving prompt J/ψ. Power-law fits to the cut values are also displayed separately for the different SPD pair types.

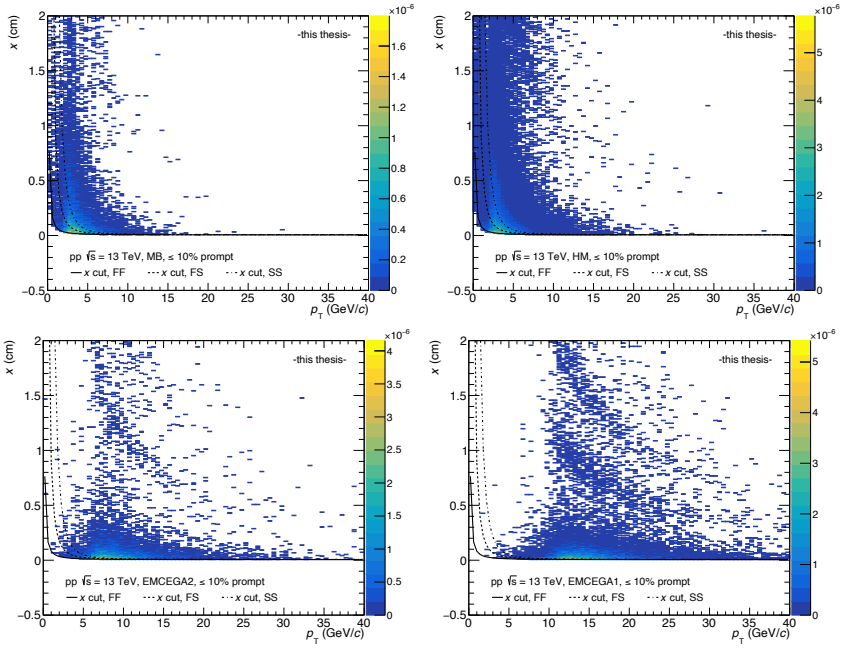

Figure 5.9.: Decay length distributions for selected non-prompt J/ψ candidates in MB (*top left*), HM (*top right*), as well as low (*bottom left*) and high (*bottom right*) threshold EMCal triggered events. The cuts for the different SPD pair types are also displayed and the distributions are shown for a 10% contamination of surviving prompt J/ψ.

on the decay length ultimately prevents the separation of prompt and non-prompt J/ψ below $p_{\mathrm{T}} = 1$ GeV/c in this analysis.

Decay length distributions for prompt and non-prompt J/ψ

The decay length distributions for prompt and non-prompt J/ψ are determined from the J/ψ injected MC production. In the prompt case, the distributions are obtained for reconstructed J/ψ and reflect the experimental resolution from the simulation of the detector response. The distributions are obtained in bins of p_{T} and SPD pair type and normalized to their integrals such that they represent probability density functions. Since the distributions are obtained in decay length bins, they are further described by a fit of the following functional form:

$$R_{\text{prompt J}/\psi}(x) = \omega_1 \times G(x;\mu_1,\sigma_1) + \omega_2 \times G(x;\mu_2,\sigma_2) + \omega_3 \times p(x;\alpha,\lambda), \tag{5.6}$$

where the ω_i are normalization constants and $G(x;\mu_i,\sigma_i)$ are gaussian functions with mean μ_i and standard deviation σ_i. The function $p(x;\alpha,\lambda)$ is a symmetric power law distribution which has the step-wise form:

$$p(x;\alpha,\lambda) = \begin{cases} \frac{\lambda-1}{2\alpha\lambda} & |x| \leq \alpha \\ \frac{\lambda-1}{2\alpha\lambda}\alpha|x|^{-\lambda} & |x| > \alpha \end{cases} . \tag{5.7}$$

The left panel of figure 5.10 shows an example of the fits of equation 5.6 to the decay length distributions for reconstructed prompt J/ψ from MC. The distributions and fits for additional p_{T} bins can be found in figure A.1. It can be seen, that the distributions are symmetric and well described by the fit. The resolution improves with increasing p_{T} and number of hits in the first layer of the SPD.

Non-prompt J/ψ have a significantly different decay length distribution than prompt J/ψ due to their origin in weak decays. As previously mentioned, the distributions are not only determined by the resolution but are asymmetric with a strong exponential tail. The distributions are given by the convolution of the prompt J/ψ resolution fits, presented in the left panel of figure 5.10, with a template of the decay length distribution for non-prompt J/ψ where no detector response is included. An example of the calculated decay length distributions for non-prompt J/ψ is shown in the right panel of figure 5.10, where the decay length template is shown as well. The distributions are normalized in such a way, that the maximum value is one in order to provide equal grounds for comparison in

the figure. The significant difference in shape between prompt and non-prompt J/ψ becomes obvious when comparing to the two panels of the figure. The decay length distributions for more p_{T} bins can be found in figure A.2.

Interpolation of non-prompt J/ψ fraction

Preliminary measurements of the non-prompt J/ψ fraction by ALICE [100] and ATLAS [101] in proton-proton collisions at $\sqrt{s} = 13$ TeV are available and shown in figure 5.11. These data, however, can not be used directly in this analysis since they are presented in a finite p_{T} binning that might not agree with the bins chosen in this analysis. An interpolation procedure is therefore employed in order to obtain a continuous description of the p_{T} dependence of f_B.

The interpolation procedure was already used by ALICE previously [102] and is based on a fit to the data. The functional form of the fit can be written as the following ratio of p_{T} differential cross sections:

$$f_B(p_{\mathrm{T}}) = \frac{\mathrm{d}\sigma^{\mathrm{FONLL}}_{\mathrm{J}/\psi\leftarrow h_B}/\mathrm{d}p_{\mathrm{T}}}{C \times \frac{p_{\mathrm{T}}}{\langle p_{\mathrm{T}}\rangle} \times \left(1 + \left(\Gamma\left(\frac{3}{2}\right) \times \Gamma\left(n - \frac{3}{2}\right)/\Gamma\left(n-1\right)\right)^2 \times \left(\frac{p_{\mathrm{T}}}{\langle p_{\mathrm{T}}\rangle}\right)^2\right)^{-n}}, \tag{5.8}$$

where the numerator is given by the non-prompt J/ψ cross section obtained from a FONLL pQCD calculation [103, 104] in proton-proton collisions at $\sqrt{s} = 13$ TeV. The denominator is a phenomenological parametrization of the inclusive J/ψ cross section [105] with free parameters C, $\langle p_{\mathrm{T}}\rangle$ and n. The fit is performed three times, once with the central values of the FONLL prediction and again after a shift in either direction by the model uncertainties. This is done in order to properly account for the uncertainties of the prediction for the non-prompt J/ψ cross section. Figure 5.11 shows the fit using the central values as well as the total 1σ envelope, including the FONLL and fit uncertainties. The fit describes the data reasonably well but shows a fairly low reduced χ^2 value due to an overlap of the data points at intermediate transverse momenta. The data provides good constraints for the fit in the p_{T} range covered in this analysis and the f_B values can be obtained from the fit at arbitrary transverse momenta.

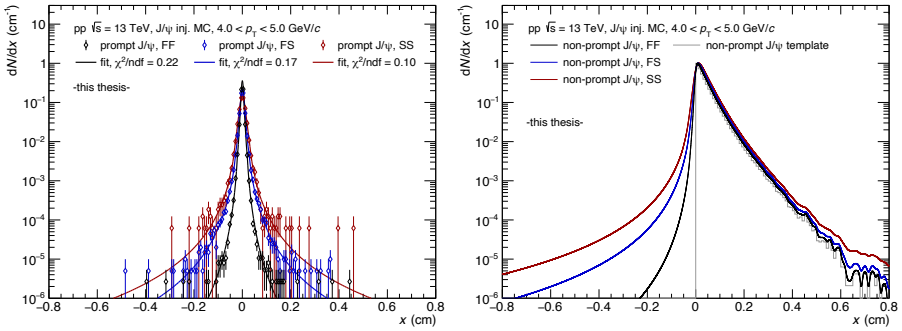

Figure 5.10.: Decay length distributions for prompt (*left*) and non-prompt (*right*) J/ψ from MC for FF, FS and SS pairs in an exemplary p_{T} bin. The fits to the decay length distributions for prompt J/ψ according to equation 5.6 are shown as well.

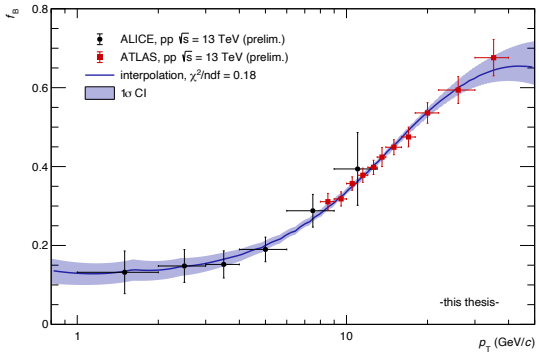

Figure 5.11.: Fraction of non-prompt J/ψ as measured by ALICE [100] and ATLAS [101] in proton-proton collisions at $\sqrt{s}$ = 13 TeV. A fit to the data is shown with the 1σ confidence interval depicted by the shaded area around the fit.

5.5. J/ψ reconstruction

Since the J/ψ decays quickly, it can not be measured directly but is reconstructed statistically from the invariant mass of electron-positron pairs. In this section, the J/ψ reconstruction as well as the determination of the mean transverse momentum is described.

The J/ψ mesons, and ultimately the correlation functions, are reconstructed in the different kinematical regimes listed in table 5.4. The different trigger samples give access to different ranges in p_{T} and the HM trigger provides the widest coverage since it amounts the largest sample of J/ψ mesons. The EMCal triggered sample is limited to a p_{T} range where the trigger is fully efficient on the J/ψ level, as shown in the right panel of figure 5.6. All bins are chosen in such a way that the J/ψ can be reconstructed with reasonable statistical significance. Additionally, overlaps of the different trigger samples in some of the p_{T} bins are provided to allow for a comparison of the results.

p_{T} (GeV/c)	MB	HM	EMCEGA2	EMCEGA1
inclusive J/ψ only				
$[0, 3]$	X	X		
$[3, 5]$	X	X		
$[5, 8]$	X	X		
$[8, 15]$		X	X	
$[15, 20]$				X
$[20, 40]$				X
inclusive, non-prompt and prompt J/ψ				
$[1, 7]$	X	X		
$[5, 12]$		X		
$[8, 15]$		X	X	
$[15, 20]$				X
$[20, 40]$				X

Table 5.4.: Transverse momentum bins for J/ψ reconstruction in different trigger samples where 'X' indicates the available bins. Two sets of p_{T} bins are listed, where one is only used for the reconstruction of inclusive J/ψ while the other is also used for the non-prompt and prompt J/ψ measurement.

Two different sets of kinematical bins are selected and listed in table 5.4, where one is used only for the inclusive J/ψ. Hereby, the number of bins is maximized

with respect to the available statistics to provide the most differential measurement possible. The other set consists of fewer bins, limited to $p_{\mathrm{T}} \geq 1$ GeV/c, to account for the more limited statistics in the measurement of non-prompt J/ψ. The inclusive J/ψ, however, has to be reconstructed in all bins listed in the table since the eventual calculation of the prompt J/ψ-hadron correlation is based on the superposition of inclusive and non-prompt J/ψ.

5.5.1. Signal extraction

The J/ψ signal extraction is based on the invariant mass distribution of selected electron-positron pairs. Said distributions contain both signal and background contributions and the background must therefore be described and subtracted to determine the signal counts. First, the signal extraction for inclusive J/ψ is described before a similar procedure for non-prompt J/ψ is introduced. The reconstruction is performed in the p_{T} bins listed in table 5.4.

Signal extraction for inclusive J/ψ

The inclusive J/ψ signal is determined from the candidate pairs selected in section 5.4.1. The background is determined from either a hybrid approach, where the combinatorial contribution is first obtained from an event mixing technique, or directly from a fit procedure. In the case of the hybrid approach, the residual background remaining after subtraction of the combinatorial contributions is described by a fit in a second step. The two different approaches are employed depending on the p_{T}, where the hybrid approach provides a good description of the background at low transverse momenta. The fit procedure, on the other hand, is favorable for $p_{\mathrm{T}} \geq 5$ GeV/c.

In the event mixing procedure, electrons from one event are paired with positrons from a different event. This removes any possible correlation and leaves purely combinatorial pairs with the invariant mass shape being dictated by kinematics. The mixing is performed in certain classes in order to ensure that events are compatible. These event classes are given by the position of the primary vertex along the beam-pipe as summarized in table 5.5.

The invariant mass distributions obtained from the event mixing procedure are further scaled to the same event distributions. The scaling factor is obtained by dividing the like-sign distributions, i.e. the average of the invariant mass

variable	N_{bins}	range				
$z_{\text{vtx.}}$ (cm)	20	$[-10,-9)$	$[-9,-8)$	$[-8,-7)$	$[-7,-6)$	$[-6,-5)$
		$[-5,-4)$	$[-4,-3)$	$[-3,-2)$	$[-2,-1)$	$[-1,0)$
		$[0,1)$	$[1,2)$	$[2,3)$	$[3,4)$	$[4,5)$
		$[5,6)$	$[6,7)$	$[7,8)$	$[8,9)$	$[9,10]$

Table 5.5.: Event classes in terms of $z_{\text{vtx.}}$ bins for event mixing procedure.

distributions of e^+e^+ and e^-e^- pairs, of the same event by those from event mixing. It is beneficial to calculate the scaling factor from the like-sign distributions since the full invariant mass range can such be used.

Figure 5.12 shows the invariant mass distributions of selected electron-positron pairs as well as the combinatorial background from event mixing for the first p_{T} bins of the MB and HM triggered samples. The remaining p_{T} bins can be found in figures A.7 and A.8 for the MB and HM triggered data, respectively, in section A.2 of the appendix. A clear signal peak situated at the J/ψ rest mass can be observed with a low mass tail originating in energy loss of the electrons from bremsstrahlung. The signal sits on top of a background continuum that strongly depends on the transverse momentum of the pair. Background pairs can have different sources and the largest contribution, at least at low to intermediate p_{T}, is typically combinatorial, where the electron and positron in a pair do not share a common physical source. While the combinatorial background is well determined from event mixing, it is apparent that the background is not fully described by this approach. Additional background contributions can be pairs from common sources like $c\bar{c}$ or $b\bar{b}$ decays as well as jet fragmentations, which is referred to as residual background and can not be described by event mixing. The fraction of residual to combinatorial background increases with p_{T} as can be seen in the comparison of figure 5.12 to figures A.7 and A.8.

After the subtraction of the combinatorial background, the residual background is estimated by an empirical fit. In the case of J/ψ candidates with $p_{\text{T}} \geq 5$ GeV/c, said fit is directly applied to the full invariant mass distribution of the pairs without first subtracting the combinatorial background from mixed events. The fit function consists of two parts: the J/ψ signal shape, which is obtained from MC, and an empirical function that describes the background. Hereby, the signal shape is used to describe the low mass tail of the signal peak which improves the

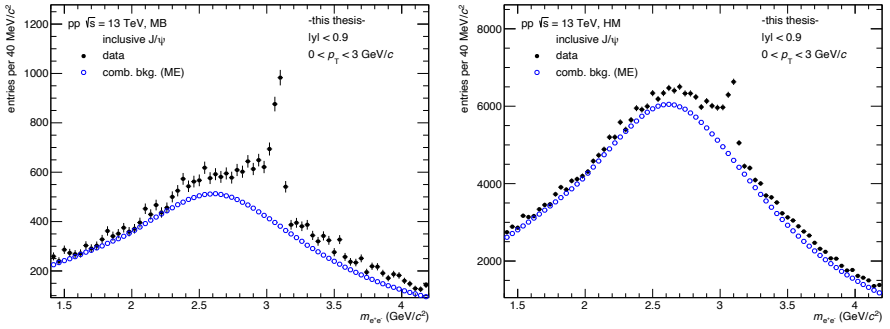

Figure 5.12.: Invariant mass distributions for selected electron-positron pairs and combinatorial background from event mixing in the MB (*left*) and HM (*right*) triggered sample.

fit quality significantly. The signal shape distribution is obtained with the same cuts as in data for reconstructed J/ψ. The fit function can be written as:

$$f\left(m_{\mathrm{e^+e^-}}\right) = p_0 \times S_{\mathrm{MC}}\left(m_{\mathrm{e^+e^-}}\right) + f_{\mathrm{bkg.}}\left(m_{\mathrm{e^+e^-}}\right), \tag{5.9}$$

where S_{MC} is the signal shape from MC, p_0 is a scaling parameter and $f_{\mathrm{bkg.}}$ is the empirical function describing the residual (or full) background. Due to the strong p_{T} dependence of the background shape, different functional forms are used for the background fit:

$$f_{\mathrm{bkg.}}\left(m_{\mathrm{e^+e^-}}\right) = \begin{cases} p_1 + p_2\, m_{\mathrm{e^+e^-}} + p_3\, m^2_{\mathrm{e^+e^-}} & \text{if} \quad p_{\mathrm{T}} \leq 3 \text{ GeV}/c \\ \exp\left(p_1 + p_2\, m_{\mathrm{e^+e^-}}\right) & \text{else} \end{cases}, \tag{5.10}$$

where it was found that a second order polynomial describes the background well at low transverse momenta while it follows an exponential at higher p_{T}.

The (residual) background fits are shown in the first p_{T} bin of each trigger in figure 5.13. The remaining p_{T} bins can be found in figures A.9 to A.11. The distributions are reasonably well described by the fits with reduced χ^2 values close to one and deviations are in agreement with statistical fluctuations. The figures also show the inclusive J/ψ signal distributions after background subtraction, which agrees very well with the expected signal shape from MC. The J/ψ signal counts are determined from bin counting in the J/ψ signal window: $2.92 \leq m_{\mathrm{e^+e^-}} \leq 3.16$ GeV/c^2. It can be seen, that the J/ψ is reconstructed with reasonable statistical significance in all p_{T} bins for all triggers. The signal-to-background (S/B) ratio increases

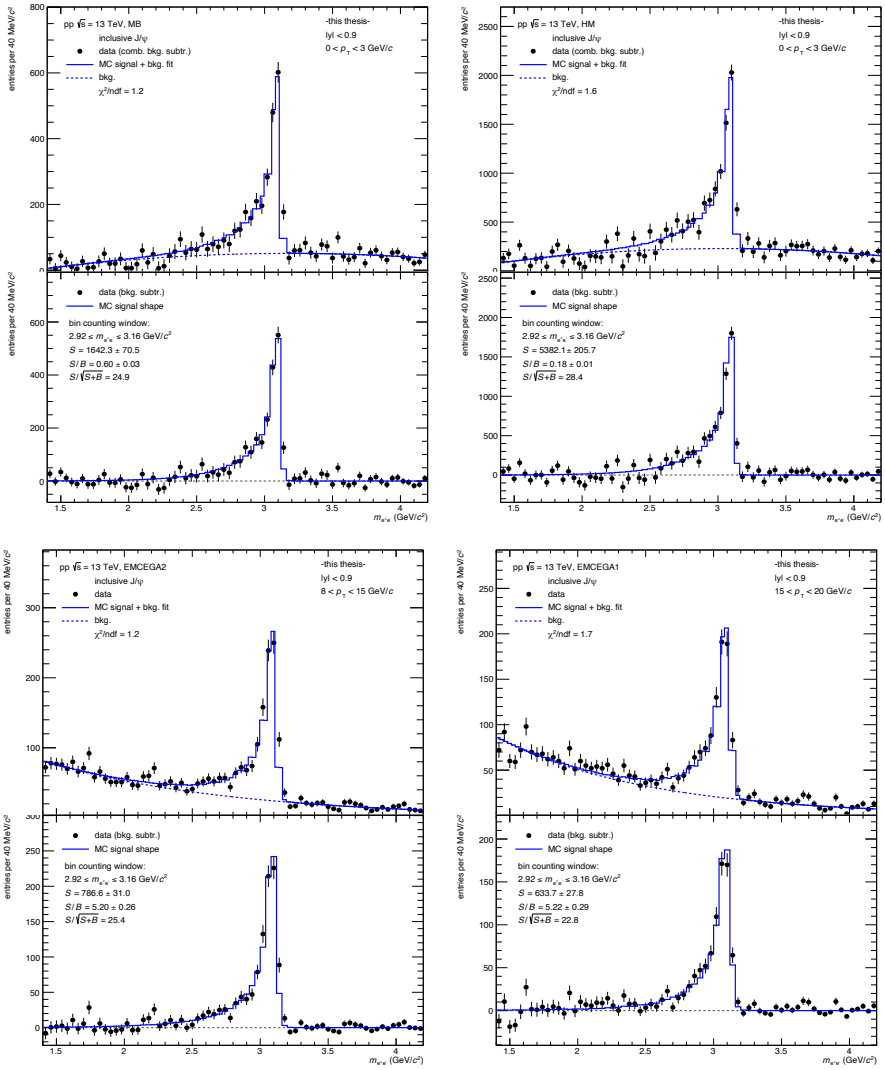

Figure 5.13.: Fit to (residual) background and inclusive J/ψ signal after background subtraction for MB (*top left*), HM (*top right*), low (*bottom left*) and high (*bottom right*) threshold EMCal triggered events.

continuously with p_{T} while the significance ($S/\sqrt{S+B}$) is affected negatively by increasing statistical uncertainties.

Signal extraction for non-prompt J/ψ

The signal extraction for non-prompt J/ψ is very similar to the inclusive J/ψ, however starting with non-prompt candidates selected in section 5.4.2. Since the non-prompt candidates are selected via a decay length cut, the mixed event approach for the estimation of combinatorial background can not be used. This is due to the fact, that the decay length is not well defined for pairs where either leg originates in a different event. Therefore, the full background is determined from a fit like independent of the transverse momentum.

The invariant mass distributions of the candidate pairs are again described by equation 5.9. However, a different functional form must be chosen for the background and a fourth order polynomial is found to provide a good description independent of p_{T}. The background fits as well as the signal distributions are shown in the first p_{T} bin of each trigger in figure 5.14. The remaining p_{T} bins for the different triggers can be found in figure A.12 and A.13. The distributions are well described by the fits in all p_{T} bins with reduced χ^2 values close to one. It is apparent, that the statistics are significantly reduced with respect to the inclusive J/ψ. The S/B values are generally comparable to those observed for inclusive J/ψ while the significance suffers from the reduction in statistics.

5.5.2. Mean p_{T} determination

In order to provide common grounds for the comparison between the data and models, the mean p_{T} of reconstructed J/ψ mesons is determined in the kinematical windows in which they are measured. This is required since the J/ψ p_{T} bins are rather broad and the correlation functions determined in this analysis are thus not particularly sensitive to the spectral shape of the J/ψ. The mean p_{T} allows a more precise comparison to theory that would otherwise not be possible with the limited statistics that is available. Additionally, the mean p_{T} is used for the evaluation of the non-prompt fraction from section 5.7.4 in the calculation of the prompt J/ψ correlation. The average transverse momenta are therefore determined for all trigger samples and J/ψ p_{T} bins listed in table 5.4.

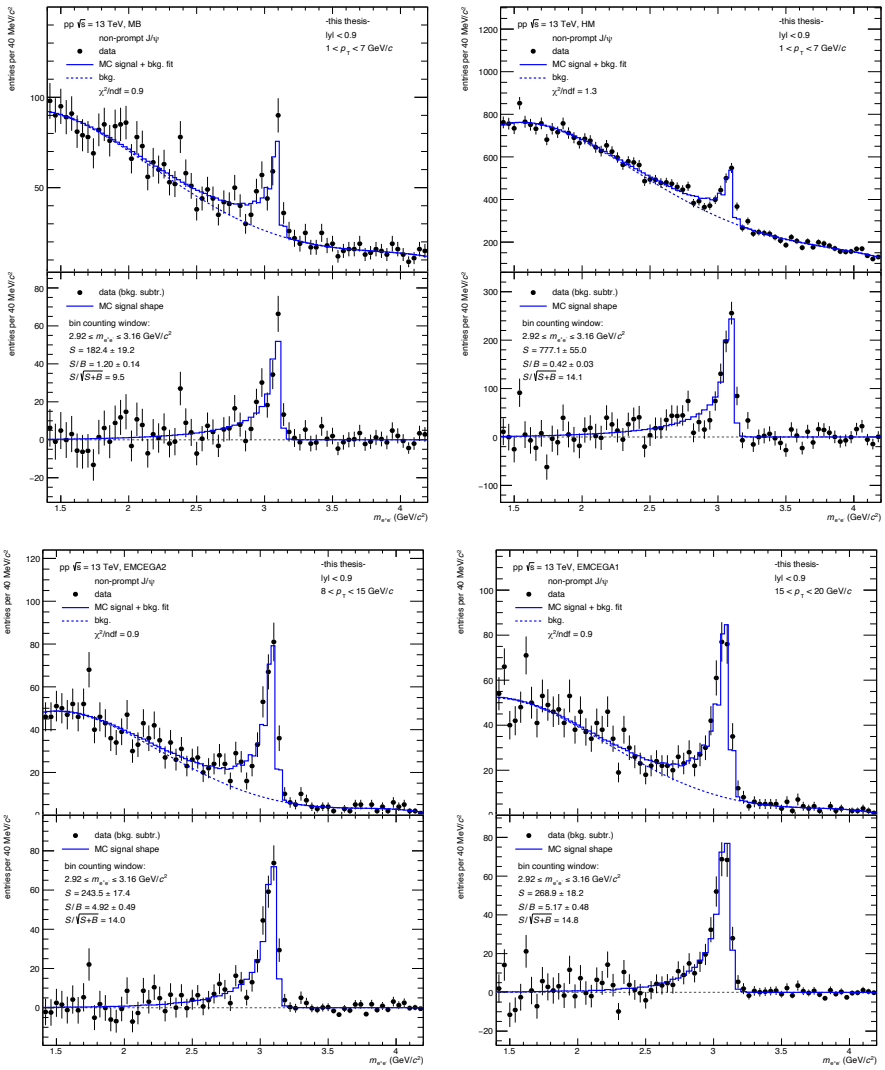

Figure 5.14.: Fit to background and non-prompt J/ψ signal after background subtraction for MB (*top left*), HM (*top right*), low (*bottom left*) and high (*bottom right*) threshold EMCal triggered events.

It should be noted, that the J/ψ candidate electron-positron pairs that are used for the determination of the average p_{T} are already corrected for the J/ψ reconstruction efficiency and acceptance. This is necessary since the efficiencies are not constant and will therefore affect the mean p_{T}. The J/ψ reconstruction efficiency and acceptance is described in section 5.6.

Mean p_{T} for inclusive J/ψ

While the mean p_{T} for the full transverse momentum spectrum of the (inclusive) J/ψ could easily be evaluated from a fit to the spectrum, a different approach must be chosen for selected p_{T} windows. The approach is based on the mean p_{T} distribution for all selected electron-positron pairs, determined as a function of invariant mass, and the superposition of signal and background pairs. In a two-step fitting procedure, the background mean p_{T} distribution is first initialized before the full distribution is described using superposition and the signal-to-background ratio from the J/ψ signal extraction. The background can be described empirically by the following polynomial function, which depends on the p_{T} of the pair:

$$f_{\mathrm{bkg.}}\left(m_{\mathrm{e^+e^-}}\right) = \begin{cases} p_0 + p_1\, m_{\mathrm{e^+e^-}} & \text{if} \quad p_{\mathrm{T}} \geq 5 \text{ GeV}/c \\ p_0 + p_1\, m_{\mathrm{e^+e^-}} + p_2\, m^2_{\mathrm{e^+e^-}} + p_3\, m^3_{\mathrm{e^+e^-}} & \text{else} \end{cases} . \quad (5.11)$$

The background fit is performed in a range of $2 < m_{\mathrm{e^+e^-}} < 4$ GeV/c^2, excluding the J/ψ signal range as well as the low mass tail in $2.6 < m_{\mathrm{e^+e^-}} < 3.2$ GeV/c^2. After this initial fit, the mean p_{T} of the J/ψ is found by a fit to the full invariant mass range using superposition and the signal-to-background ratio from the J/ψ signal extraction. The S/B depends on the invariant mass and is given by the ratio of the scaled signal shape from MC to the full background in order to reduce statistical fluctuations. The full fit function can be written as:

$$f\left(m_{\mathrm{e^+e^-}}\right) = \frac{S/B\left(m_{\mathrm{e^+e^-}}\right) \times \langle p_{\mathrm{T}} \rangle_{\mathrm{J}/\psi} + f_{\mathrm{bkg.}}\left(m_{\mathrm{e^+e^-}}\right)}{1 + S/B\left(m_{\mathrm{e^+e^-}}\right)}, \quad (5.12)$$

where the background distribution, $f_{\mathrm{bkg.}}\left(m_{\mathrm{e^+e^-}}\right)$, is given by equation 5.11 and the parameters determined in the previous step are used as start parameters. The mean p_{T} of the J/ψ, $\langle p_{\mathrm{T}} \rangle_{\mathrm{J}/\psi}$, is a free parameter and determined by the fit. Figure 5.15 shows the fits to the full invariant mass range, according to equation 5.12, as well as the initial background fits for the first p_{T} bin of each trigger. The remaining p_{T} bins can be found in figures A.14 to A.16 in section A.2 in the appendix. The

shaded area shows the 1σ confidence interval of the fit. The fits describe the data well and show a reasonable reduced χ^2 with values close to one in most cases. Additionally, the S/B distributions used in equation 5.12 are also shown.

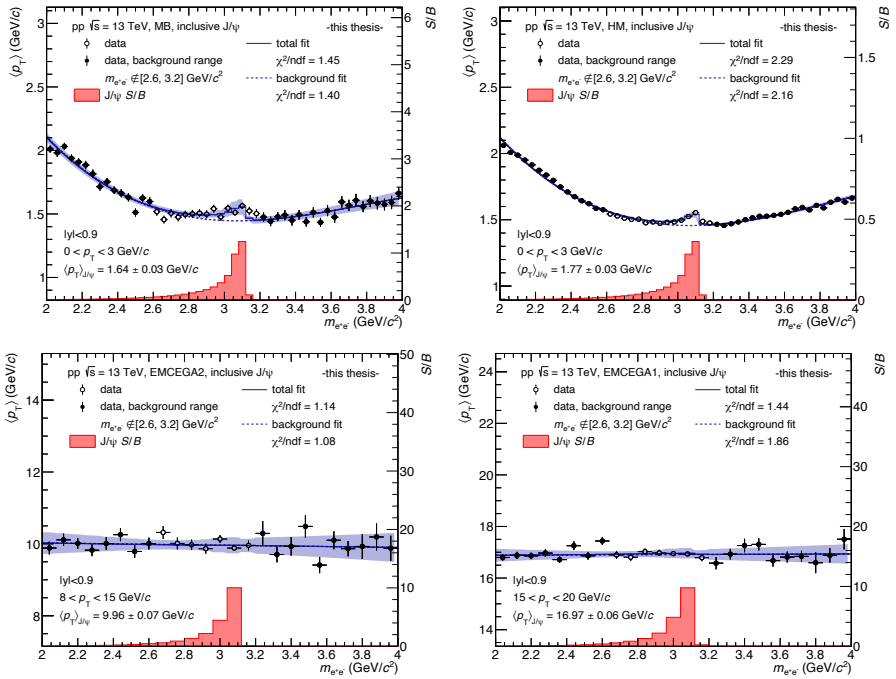

Figure 5.15.: Mean p_{T} determination from fitting procedure for inclusive J/ψ in MB (*top left*), HM (*top right*), low (*bottom left*) and high (*bottom right*) threshold EMCal triggered events. The S/B ratio is also shown with the corresponding axis displayed on the right.

The mean p_{T} values are summarized in table 5.6, where the uncertainty is given by the uncertainty from the fit. It can be seen, that the values for the different triggers mostly agree, at least within 3σ of the quoted uncertainties, for the overlapping p_{T} windows.

Mean p_{T} for non-prompt J/ψ

The determination of mean p_{T} for non-prompt J/ψ is identical to the procedure described in the previous section. However, just like for the non-prompt J/ψ signal extraction, the approach is based on electron-positron pairs selected according to

	$\langle p_{\mathrm{T}} \rangle_{\mathrm{J}/\psi}$ (GeV/c)			
p_{T} (GeV/c)	MB	HM	EMCEGA2	EMCEGA1
$[0, 3]$	1.64 ± 0.03	1.77 ± 0.03		
$[3, 5]$	3.81 ± 0.03	3.86 ± 0.02		
$[5, 8]$	6.05 ± 0.04	6.11 ± 0.02		
$[8, 15]$		10.19 ± 0.08	9.96 ± 0.07	
$[15, 20]$				16.97 ± 0.06
$[20, 40]$				25.08 ± 0.26
$[1, 7]$	2.96 ± 0.04	3.14 ± 0.03		
$[5, 12]$		6.83 ± 0.04		

Table 5.6.: Inclusive J/ψ mean p_{T} values in different p_{T} bins for all triggers.

the criteria introduced in section 5.4.2. The S/B ratio used in equation 5.12 is naturally obtained from the non-prompt J/ψ signal extraction procedure.

The fit results are shown in figure 5.16 for the first p_{T} bin of each trigger. The remaining p_{T} bins can be found in figures A.17 and A.18. As was the case for the inclusive J/ψ, the fits describe the data well with reasonable reduced χ^2 values. However, the significantly reduced statistics is visible in larger fluctuations as well as the increased fit uncertainty displayed by the 1σ confidence interval.

The mean p_{T} values obtained for the different triggers are summarized in table 5.7, where the uncertainties are determined from the fit. The different triggers yield comparable values in the overlapping p_{T} bins. The mean transverse momenta are larger than those quoted in table 5.6 for inclusive J/ψ. This is due to the non-prompt J/ψ p_{T} spectrum being harder than the inclusive one, which is caused by the missing contribution from the comparatively soft prompt J/ψ. Significantly larger uncertainties than for inclusive J/ψ are observed because of the dramatic reduction in statistics from the decay length cut.

	$\langle p_{\mathrm{T}} \rangle_{\mathrm{J}/\psi}$ (GeV/c)			
p_{T} (GeV/c)	MB	HM	EMCEGA2	EMCEGA1
$[1, 7]$	3.70 ± 0.18	3.80 ± 0.10		
$[5, 12]$		7.40 ± 0.10		
$[8, 15]$		10.71 ± 0.16	10.23 ± 0.13	
$[15, 20]$				17.03 ± 0.09
$[20, 40]$				25.80 ± 0.37

Table 5.7.: Non-prompt J/ψ mean p_{T} values in different p_{T} bins for all triggers.

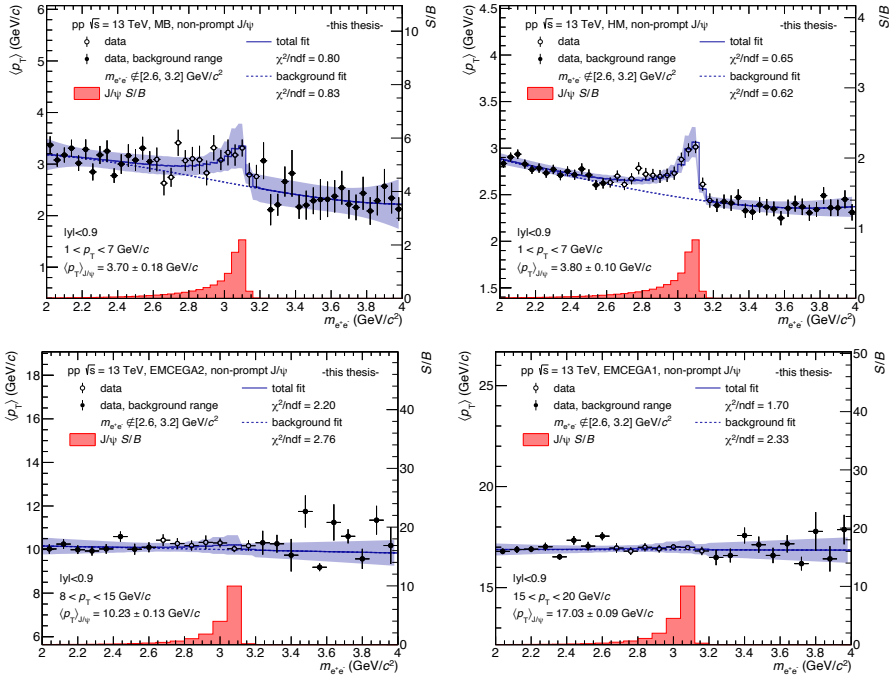

Figure 5.16.: Mean p_{T} determination from fitting procedure for non-prompt J/ψ in MB (*top left*), HM (*top right*), low (*bottom left*) and high (*bottom right*) threshold EMCal triggered events. The S/B ratio is also shown with the corresponding axis displayed on the right.

Mean p_{T} for prompt J/ψ

The mean p_{T} values for prompt J/ψ can be calculated from those determined for inclusive and non-prompt J/ψ. Hereby, superposition is used with the interpolated non-prompt fraction as determined in section 5.4.2:

$$\langle p_{\mathrm{T}} \rangle_{\text{prompt J}/\psi} = \frac{1}{1 - f_B} \times \left(\langle p_{\mathrm{T}} \rangle_{\text{inclusive J}/\psi} - f_B \times \langle p_{\mathrm{T}} \rangle_{\mathrm{J}/\psi \leftarrow h_{\mathrm{B}}} \right) , \tag{5.13}$$

where f_B is evaluated at $\langle p_{\mathrm{T}} \rangle_{\text{inclusive J}/\psi}$. The uncertainty is calculated from the uncertainties on the mean p_{T} values for inclusive and non-prompt J/ψ via error propagation. The interpolation uncertainty of f_B is ultimately treated as a systematic uncertainty and therefore not included here. The prompt J/ψ mean p_{T} values are quoted in table 5.8 for all triggers. The different triggers provide comparable values in the overlapping p_{T} bins. As expected, the values are smaller than those for inclusive or non-prompt J/ψ listed in tables 5.6 and 5.16, respectively.

	$\langle p_{\mathrm{T}} \rangle_{\mathrm{J}/\psi}$ (GeV/c)			
p_{T} (GeV/c)	MB	HM	EMCEGA2	EMCEGA1
$[1, 7]$	2.82 ± 0.06	3.02 ± 0.04		
$[5, 12]$		6.65 ± 0.06		
$[8, 15]$		9.92 ± 0.15	9.82 ± 0.12	
$[15, 20]$				16.91 ± 0.15
$[20, 40]$				24.04 ± 0.82

Table 5.8.: Prompt J/ψ mean p_{T} values in different p_{T} bins for all triggers.

5.6. Acceptance and efficiency corrections

Both J/ψ mesons and associated particles are reconstructed with imperfect acceptance and efficiency, leading to a certain loss of signal. While the correlation functions are ultimately normalized to the number of J/ψ trigger particles, the efficiency of the hadron reconstruction has a direct impact on the amplitude of the correlation. Additionally, even the J/ψ efficiency can have a non-negligible impact on the shape and amplitude of the correlation due to its strong dependence on p_{T} and the large p_{T} bins that are used in the analysis. The correlation distributions must therefore be corrected for the J/ψ and associated hadron reconstruction efficiencies. This correction is applied 'on-the-fly' when the correlation is calculated.

Each J/ψ candidate and associated particle combination is hereby attributed a weight that corresponds to the inverse of the product of the two acceptance and efficiency factors. The J/ψ efficiency must then obviously also be considered during the normalization of the correlation. The efficiency correction is applied in this way to maximize the p_{T} resolution and not be limited to the analysis binning. Considering the J/ψ efficiency in particular, the application both at pair and normalization level acts as a re-weighting that accounts for the strong p_{T} shape of the J/ψ efficiency. The effect can be visualized by a possible migration of signal counts between bins, which the analysis might not be particularly sensitive to due to the large p_{T} windows that are required.

The determination of the J/ψ and hadron acceptance and efficiency factors are described in the two sections below. In either case, the efficiencies are obtained from MC simulations but different productions are used. Hereby, the knowledge of reconstructed as well as initially generated particles in the MC events is exploited.

5.6.1. J/ψ acceptance and efficiency

The J/ψ acceptance and efficiency correction is determined from the J/ψ injected MC sample introduced in section 4.2. The different selections of runs are hereby considered when calculating the efficiency for the corresponding trigger sample. While the triggers themselves are not simulated, no trigger dependence is expected in the p_{T} regimes selected for the analysis. This can be understood from the similarities of the pair p_{T} spectra shown in figure 5.6. The J/ψ candidate p_{T} shapes in the relevant ranges in EMCal triggered events are mainly modified by the PID approach, as explained in section 5.4.1. The increased statistics over minimum bias events in the HM and EMCal trigger samples does not affect the reconstruction efficiency.

The reconstruction efficiency and acceptance is calculated according to:

$$(A \times \epsilon)_{\mathrm{J}/\psi}(p_{\mathrm{T}}) = \frac{\sum_i \left(N_{\mathrm{evts.}}^{\mathrm{data}}/N_{\mathrm{evts.}}^{\mathrm{MC}}\right)_i \times \left(\mathrm{d}N_{\mathrm{J}\psi}^{\mathrm{MC,\ rec.}}/\mathrm{d}p_{\mathrm{T}}\right)_i}{\sum_i \left(N_{\mathrm{evts.}}^{\mathrm{data}}/N_{\mathrm{evts.}}^{\mathrm{MC}}\right)_i \times \left(\mathrm{d}N_{\mathrm{J}\psi}^{\mathrm{MC,\ gen.}}/\mathrm{d}p_{\mathrm{T}}\right)_i}, \tag{5.14}$$

where the summation is performed over the runs considered in the corresponding trigger sample. The reconstructed and generated J/ψ in the MC event are denoted by $N_{\mathrm{J}\psi}^{\mathrm{MC,\ rec.}}$ and $N_{\mathrm{J}\psi}^{\mathrm{MC,\ gen.}}$, respectively. Each run is attributed a weight that is

given by the ratio of the number of accepted events in data and MC in that run. This is done to account for possible differences in the relative weight of a given run in data and MC. However, the difference between the summation with and without use of these weights is negligible.

The reconstruction efficiency and acceptance is calculated for inclusive, non-prompt and prompt J/ψ according to equation 5.14. Hereby, all electron and J/ψ candidate selection criteria are considered except for the decay length requirement on non-prompt J/ψ candidates. The decay length cut only amounts to a kinematical selection of a subset of J/ψ candidates, which does not affect the individual efficiency of a given J/ψ. The efficiencies are compared for the MB sample in the left panel of figure 5.17 and found to be very similar. Differences between the efficiencies are negligible, particularly since the efficiency correction only amounts to a re-weighting on the basis of the correlation functions. Therefore, the inclusive J/ψ efficiency is used in all cases.

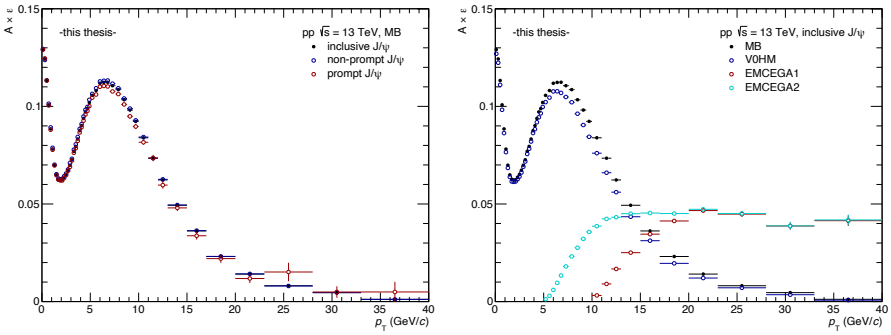

Figure 5.17.: Reconstruction efficiency times acceptance for inclusive, non-prompt and prompt J/ψ (*left*) in the MB sample and for inclusive J/ψ (*right*) in the different trigger samples.

The right panel of figure 5.17 shows the inclusive J/ψ acceptance and efficiency for all trigger samples. The efficiencies for MB and HM triggered events are comparable, with minor differences only arising from the corresponding selection of runs. The different PID approach in the EMCal trigger samples, however, modifies the efficiency dramatically and significantly larger values are reached at high p_{T}. It can also be seen, that the efficiencies vanish below transverse momenta corresponding to the minimum cluster energy cuts that are used on the electron legs of the J/ψ candidate pairs.

5.6.2. Associated hadron acceptance and efficiency

The associated hadron acceptance and efficiency is obtained from the general purpose MC sample described in section 4.2. The efficiencies are determined separately for the different trigger samples whereby only relevant runs are considered. No trigger simulation is performed since the single hadron track reconstruction efficiency is not expected to depend on the trigger.

The associated hadrons are unidentified charged particles and the reconstruction efficiency is calculated from a proxy for primary charged particles. This proxy considers primary charged pions, kaons, protons as well as electrons and muons. The efficiency for primary particles is then calculated according to:

$$(A \times \epsilon)_{\text{had.}}(p_{\text{T}}) = \frac{\sum_i \left(N_{\text{evts.}}^{\text{data}}/N_{\text{evts.}}^{\text{MC}}\right)_i \times \left(\mathrm{d}N_{\text{proxy}}^{\text{MC, rec.}}/\mathrm{d}p_{\text{T}}\right)_i}{\sum_i \left(N_{\text{evts.}}^{\text{data}}/N_{\text{evts.}}^{\text{MC}}\right)_i \times \left(\mathrm{d}N_{\text{proxy}}^{\text{MC, gen.}}/\mathrm{d}p_{\text{T}}\right)_i}, \tag{5.15}$$

where the summation is performed over the runs considered in the corresponding trigger sample. The reconstructed and generated primary particles, $N_{\text{proxy}}^{\text{MC, rec.}}$ and $N_{\text{proxy}}^{\text{MC, gen.}}$, are given by the proxy. Similar to the calculation of the J/ψ efficiency, each run is attributed a weight that is given by the ration of the number of accepted events in data and MC.

The hadron selection cuts introduced in section 5.3, however, do not guarantee that only primary particles pass the requirements. Therefore, an additional correction using the fraction of primary particles in the data set must be employed. This correction modifies the efficiency given by equation 5.15 in the following way:

$$(A \times \epsilon)_{\text{had.}}(p_{\text{T}}) \rightarrow (A \times \epsilon)_{\text{had.}}(p_{\text{T}}) \times \left(1 + \frac{f_{\text{sec.}}(p_{\text{T}})}{f_{\text{prim.}}(p_{\text{T}})}\right) = \frac{(A \times \epsilon)_{\text{had.}}(p_{\text{T}})}{f_{\text{prim.}}(p_{\text{T}})}, \tag{5.16}$$

where $f_{\text{prim.}}$ and $f_{\text{sec.}} = 1 - f_{\text{prim.}}$ are the fractions of primary and secondary particles. The primary fraction depends on p_{T} and is determined for the different data samples from a fit procedure based on the DCA distributions in the transverse plane (DCA_{xy}) or along the beam pipe (DCA_z). Hereby, template distributions for primary and secondary particles from MC are used and a superposition of both is fitted to the data. This is necessary, since the primary fraction in MC does not necessarily correspond to the data. The fits are performed in transverse momentum bins and an exemplary bin for minimum bias data is shown in figure 5.18. The template fits describe the DCA_{xy} and DCA_z distributions in data well

and it can be seen, that the distributions for secondaries are significantly broader than for primaries.

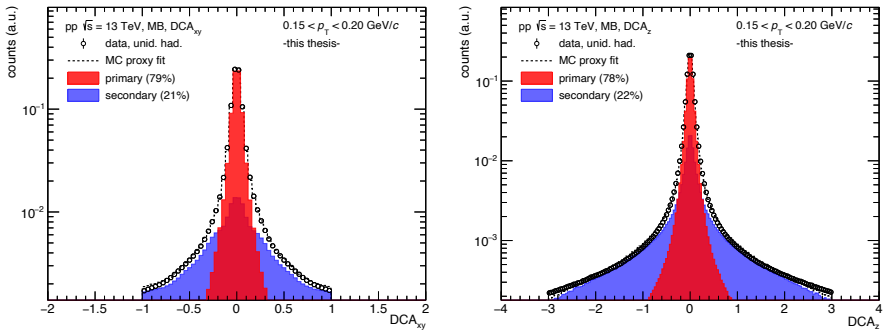

Figure 5.18.: DCA template fits for associated hadrons transverse plane (*left*) and longitudinal direction (*right*) in MB events. The MC templates are displayed in color and the primary and secondary fractions are quoted.

The primary fraction determined by the DCA fits is shown in the left panel of figure 5.19 for the MB sample. Figure A.19 in section A.3 in the appendix shows the same distributions for the remaining triggers. The primary fraction increases rapidly with transverse momentum at low p_{T} and exceeds 90% at intermediate p_{T}. It can be seen, that the fractions determined from DCA_{xy} and DCA_z generally agree with only minor variations. The primary fraction determined in the transverse plane is used for the correction described in equation 5.16, but the comparison to DCA_z is considered in the systematic uncertainties. The different trigger samples show slight variations in the primary fraction which can be attributed to the different runs that are considered in the calculation.

The acceptance and efficiency distributions for associated hadrons after the correction for the primary fraction are shown in the right panel of figure 5.19. The efficiencies increase rapidly at low p_{T} and are mostly larger than 90% with a maximum between $p_{\mathrm{T}} = 1$ and 2 GeV/c. Only minor differences between the trigger samples are observed which are mainly due to differences in the primary fraction determined for the corresponding selection of runs.

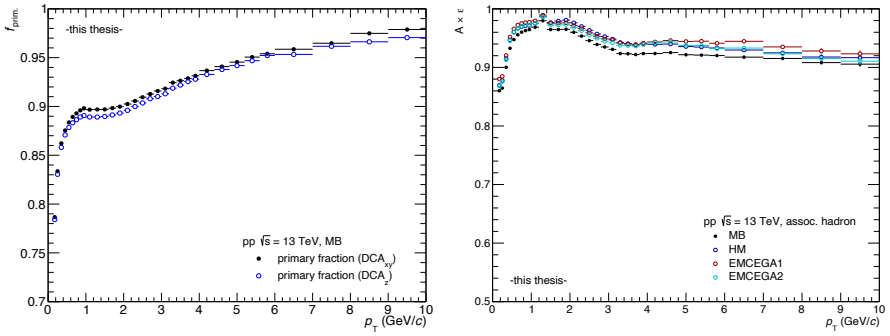

Figure 5.19.: Primary fraction (*left*) in MB events and acceptance times efficiency (*right*) in all trigger samples for associated hadrons.

5.7. Determination of correlation function

Finally, the correlation functions can be constructed where the J/ψ serve as the trigger particles and the hadrons as the associated ones. First, the determination of the signal-plus-background correlation using all J/ψ candidates is introduced. This includes an acceptance correction which must be applied due to the limited pseudorapity coverage of the detector. Then, the correlation signal extraction procedures for inclusive as well as non-prompt J/ψ are presented. Finally, the prompt J/ψ-hadron correlation is calculated via superposition from the inclusive and non-prompt components.

The correlation functions are determined in transverse momentum bins of the J/ψ and associated tracks. The J/ψ p_{T} windows are listed in table 5.4 and hadrons are used in the ranges $p_{\mathrm{T}}^{\mathrm{assoc.}} \in [0.15, 1]$, $[1, 3]$ and $[3, 10]$ GeV/c, where the lower bound $p_{\mathrm{T}}^{\mathrm{assoc.}} \geq 150$ MeV/c is governed by the momentum resolution of the TPC. The correlation is furthermore evaluated in ranges of pseudorapidity difference, denoted by $\Delta\eta$. Different ranges are hereby used to allow for some sensitivity in pseudorapidity. It is known from two-particle correlations, see for example ref. [106], that the correlation is typically more narrow in $\Delta\eta$ in the near- than the away-side. Ideally, the correlation would be determined two-dimensionally in $\Delta\eta$-$\Delta\varphi$ but this is prohibited by the limited statistics available for the analysis. Therefore, the following ranges are used as a best estimate to probe the $\Delta\eta$ dependence: $|\Delta\eta| < 0.5$, < 1 and < 2. The range $|\Delta\eta| < 1$ is considered the default range to which the remaining ones are ultimately compared.

The correlation functions are normalized to the p_{T} and η ranges of the associated hadrons, such that their integrals correspond the respective average multiplicities. All J/ψ-hadron correlations presented in this section are corrected for the J/ψ and hadron reconstruction efficiencies, which are described in the previous section. The signal-plus-background correlation, on the other hand, is shown without efficiency correction applied since it still contains background.

5.7.1. Signal-plus-background correlation

The signal-plus-background correlation is given by the associated yield per J/ψ candidate in terms of the angular distance $\Delta\varphi$ and $\Delta\eta$ before signal extraction. The candidate pairs are hereby selected according to sections 5.4.1 or 5.4.2, but only inclusive J/ψ candidates are shown for simplicity. The associated yield is determined as a function of $\Delta\varphi$ and $\Delta\eta$, where the symmetric azimuthal range $\Delta\varphi \in [0, \pi]$ is used to reduce fluctuations and allow for a higher resolution binning. This yields the so-called 'raw' signal-plus-background correlation function:

$$C^{\mathrm{raw}}_{\mathrm{e^+e^-}}(\Delta\varphi, \Delta\eta) = \frac{1}{N_{\mathrm{e^+e^-}}} \frac{\mathrm{d}^2 N_{\mathrm{assoc.,\,SE}}(\Delta\varphi, \Delta\eta)}{\mathrm{d}(\Delta\varphi)\mathrm{d}(\Delta\eta)}, \tag{5.17}$$

where the label 'SE' denotes that the associated tracks are taken from the same event as the electron-positron pairs. The distributions is normalized to the number or trigger pairs $N_{\mathrm{e^+e^-}}$ and different ranges of the invariant mass of the pair can be used, which is exploited in the signal extraction procedure.

The raw correlation function further has to be corrected for the geometrical acceptance of the detector. There is a non-negligible likelihood to miss associated tracks due to the finite acceptance if the J/ψ candidate was produced close to the detector edges in pseudorapidity. This effect translates to $\Delta\eta$, where no modification is present for $\Delta\eta \sim 0$ but an increasing suppression is observed for larger values of $|\Delta\eta|$. The acceptance correction is obtained from an event mixing procedure where correlation structures can only arise from trivial kinematical dependences. In this procedure, electron-positron pairs from one event are combined with hadrons from a different event, respecting the event classes introduced in table 5.5. A special case is presented by the EMCal trigger sample where the mixing must be performed between triggered and minimum bias events in order to account for the acceptance of the calorimeters. The J/ψ candidates are hereby

taken from the EMCal triggered event while hadrons from minimum bias events are used. The acceptance correction from event mixing is given by:

$$C^{\mathrm{ME}}_{\mathrm{e^+e^-}}(\Delta\varphi,\Delta\eta) = \frac{1}{N_{\text{assoc., ME}}(\Delta\varphi=0,\Delta\eta=0)}\frac{\mathrm{d}^2 N_{\text{assoc., ME}}(\Delta\varphi,\Delta\eta)}{\mathrm{d}(\Delta\varphi)\mathrm{d}(\Delta\eta)}, \tag{5.18}$$

which is normalized to the associated yield at $\Delta\varphi = 0$ and $\Delta\eta = 0$. The distribution is shown for an exemplary kinematical selection in minimum bias events in the left panel of figure 5.20. It exhibits a roughly triangular shape, symmetric in $\Delta\eta$, due to the finite geometrical acceptance of the detector.

The signal-plus-background correlation is calculated by applying the acceptance correction to the raw correlation function and can therefore be written as the ratio of equations 5.17 and 5.18:

$$C_{\mathrm{e^+e^-}}(\Delta\varphi,\Delta\eta) = \frac{1}{\Delta p_{\mathrm{T}}^{\text{assoc.}}\Delta\eta^{\text{assoc.}}}\frac{C^{\mathrm{raw}}_{\mathrm{e^+e^-}}(\Delta\varphi,\Delta\eta)}{C^{\mathrm{ME}}_{\mathrm{e^+e^-}}(\Delta\varphi,\Delta\eta)}. \tag{5.19}$$

The signal-plus-background correlation is defined in the $\Delta\varphi$-$\Delta\eta$-plane, since the acceptance correction only affects $\Delta\eta$. After the application of the correction, however, the correlation is integrated over a given $\Delta\eta$ range and and normalized to said range in order to reduce fluctuations. This process essentially yields the average over pseudorapidity for a given range and variations of that range provide some sensitivity to $\Delta\eta$. As was noted before, the correlation is additionally normalized to the p_{T} and η ranges of the associated hadrons. The signal-plus-background correlation can be evaluated in any invariant mass range of the J/ψ candidate pair and an example is shown in the right panel of figure 5.20. The figure shows the correlation before signal extraction in the J/ψ signal range $2.92 \leq m_{\mathrm{e^+e^-}} \leq 3.16$ GeV/c for an exemplary kinematical bin in minimum bias events. It should be noted, that no efficiency correction is applied at this stage. Figure 5.20 shows the projections in the different $\Delta\eta$ ranges, which are fairly similar but a near-side suppression can be observed for broader windows.

Based on the signal-plus-background correlation introduced here on the example of inclusive J/ψ candidates, the inclusive and non-prompt J/ψ-hadron correlation functions can be extracted. Signal extraction procedures are applied for this purpose and described in the following sections.

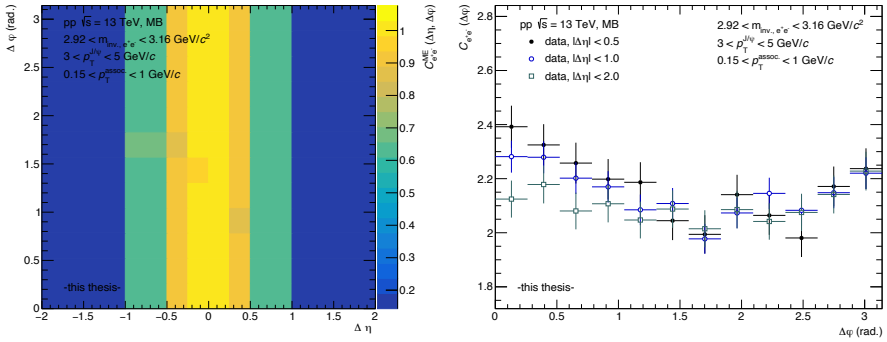

Figure 5.20.: Mixed-event (*left*) and same-event signal-plus-background (*right*) correlation in exemplary kinematical bin for inclusive J/ψ candidate electron-positron pairs in minimum bias events.

5.7.2. Inclusive J/ψ-hadron correlation

The inclusive J/ψ-hadron correlation is obtained from the distributions determined in the previous section by employing a signal extraction procedure based on the invariant mass of the J/ψ candidate pairs. This is required since an a priori unknown background correlation must be isolated and removed from the signal-plus-background distributions. Such a background might be combinatorial and correspond to the underlying event or relate to a common physical source, similar to the background considerations during the J/ψ signal extraction. The correlation signal extraction must be performed with care since there is no reason to believe that the background is constant in $\Delta\varphi$.

Different signal extraction procedures have been developed and implemented in the course of this analysis. The most sophisticated and least restrictive of such methods is a fit approach, that is ideologically similar to the determination of the average p_{T} in section 5.5.2. Other methods include a like-sign and an interpolation method, which are based on different assumptions to estimate the background correlation. The different approaches are introduced below and a qualitative comparison between the methods is presented. Potential deviations between the methods should not be considered alarming since they can largely be explained by shortcomings in the like-sign or interpolation approaches. These methods are only presented to provide a more comprehensive picture that lends additional credibility to the signal extraction.

The inclusive J/ψ-hadron correlations presented in this section are corrected for the J/ψ and associated hadron reconstruction efficiencies. The J/ψ reconstruction efficiency cancels hereby partially since it is naturally also considered in the normalization. The correlation functions are also normalized to the associated hadron p_{T} and η ranges, as was the case for the signal-plus-background correlation.

Fit method

The fit method is the default signal extraction procedure and it allows to extract the J/ψ correlation signal directly. While other methods are limited to certain invariant mass ranges, no such restrictions apply for this approach. The method is based on the signal-plus-background correlation expressed as a function of the electron-positron pair mass in bins of $\Delta\varphi$. Due to the limited statistics, the pseudorapidity dimension is integrated over in the different ranges that are considered. The signal extraction is performed separately in the $\Delta\varphi$ bins.

The procedure is separated into two steps. First, the background correlation is described by a fit in the range $1.4 \leq m_{\mathrm{e^+e^-}} \leq 4.2$ GeV/c^2, where a window around the signal, $2.6 \leq m_{\mathrm{e^+e^-}} \leq 3.2$ GeV/c^2, is excluded. The exclusion range contains both the J/ψ signal as well as the low mass tail from radiative energy loss of the electrons. The background correlation, $C^{\mathrm{bkg.}}_{\mathrm{e^+e^-}}\left(m_{\mathrm{e^+e^-}}\right)$, is parametrized reasonably well by a polynomial function of order five for $p_{\mathrm{T}}^{\mathrm{J}/\psi} \leq 3$ GeV/c and order three at higher transverse momenta. After the initialization of the parameters by the pure background fit, the full invariant mass range $1.4 \leq m_{\mathrm{e^+e^-}} \leq 4.2$ GeV/c^2 can be described by a fit using superposition:

$$C_{\mathrm{e^+e^-}}\left(m_{\mathrm{e^+e^-}}\right) = \frac{S/B\left(m_{\mathrm{e^+e^-}}\right) \times C_{\mathrm{J}/\psi} + C^{\mathrm{bkg.}}_{\mathrm{e^+e^-}}\left(m_{\mathrm{e^+e^-}}\right)}{1 + S/B\left(m_{\mathrm{e^+e^-}}\right)}, \tag{5.20}$$

where $S/B\left(m_{\mathrm{e^+e^-}}\right)$ is the signal-to-background ratio obtained from the J/ψ signal extraction procedure. The inclusive J/ψ-hadron correlation, $C_{\mathrm{J}/\psi}$, is determined as a fit parameter in each $\Delta\varphi$ bin. Error propagation is performed such that the uncertainty on the J/ψ correlation properly accounts for the statistical uncertainty on the J/ψ counts:

$$\Delta C_{\mathrm{J}/\psi} = \sqrt{\left(\Delta C^{\mathrm{fit}}_{\mathrm{J}/\psi}\right)^2 + \left(\frac{\Delta S}{S} \times C_{\mathrm{J}/\psi}\right)^2}, \tag{5.21}$$

where $\Delta C_{\mathrm{J}/\psi}^{\mathrm{fit}}$ is the uncertainty on the fit parameter $C_{\mathrm{J}/\psi}$ and ΔS is the statistical uncertainty on the J/ψ signal counts S.

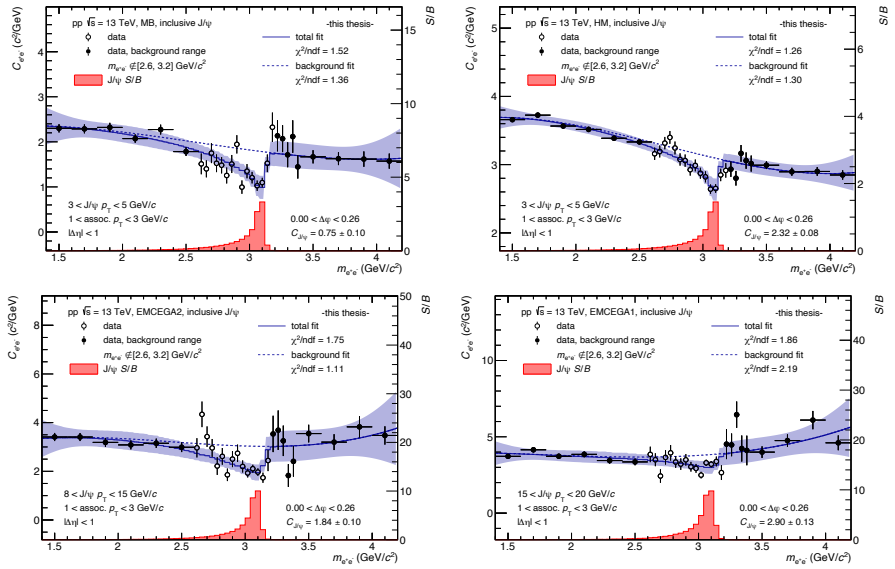

Figure 5.21.: Inclusive J/ψ correlation signal extraction via fitting method for exemplary $\Delta\varphi$ and kinematical bin in MB (*top left*), HM (*top right*) and EMCal (*bottom*) triggered events.

The J/ψ correlation signal extraction is shown for an exemplary kinematical selection with typical statistical significance in figure 5.21. The figure only shows the first $\Delta\varphi$ bin for each trigger and the remaining bins can be found in figures A.20 to A.23 in section A.4 of the appendix. Different kinematical selections yielding comparatively low and high statistics samples are displayed in figure A.24, where only the first $\Delta\varphi$ bin is shown again. The background and full fits according to equation 5.20 are displayed as dashed and solid lines, respectively, with the shaded area representing the 1σ confidence interval around the full fit. The figures also show the S/B ratio, with the corresponding axis depicted on the right. It can be seen, that the data is reasonably well described by the fit even in the lowest statistics cases at large transverse momenta. The S/B ratio improves with increasing transverse momentum which naturally benefits the procedure. The signal extraction is ultimately limited by statistical fluctuations at very high transverse momenta which limits the measurement to the ranges quoted above.

Other methods

In contrast to the fitting method, where the J/ψ correlation is determined directly on the basis of the signal-plus-background correlation, the background can also be estimated and subtracted. The background correlation can be determined from different approaches and the J/ψ correlation is then calculated according to:

$$C_{\mathrm{J}/\psi}(\Delta\varphi) = \frac{1}{S/B} \times \left[(1 + S/B) \times C_{\mathrm{e^+e^-}}(\Delta\varphi) - C_{\mathrm{bkg}}(\Delta\varphi)\right], \tag{5.22}$$

where S/B is the J/ψ signal-to-background ratio in the J/ψ signal region and $C_{\mathrm{bkg}}(\Delta\varphi)$ is the estimate of the background correlation. The statistical uncertainty is calculated according to error propagation from the uncertainties on the signal-plus-background and background correlations as well as the uncertainties on the J/ψ signal and background counts.

Two different approaches are used to determine the background correlation: the like-sign and the interpolation method. The methods are introduced below and the J/ψ correlation calculated according to equation 5.22 is compared to the standard approach. This comparison should mainly be understood in qualitative terms as both alternative methods have certain disadvantages with respect to the fitting method.

Like-sign method An estimate of the background correlation can be obtained from like-sign pairs, i.e. electron-electron and positron-positron pairs, where no J/ψ signal can be present. This approach allows the direct determination of the background correlation in the J/ψ signal region without relying on any interpolation procedures with respect to the invariant mass. However, it will mainly describe a combinatorial background since common physical sources of electron-positron pairs are completely disregarded. The like-sign method is therefore not considered fully adequate but it provides a first-order approximation of the background correlation. In regimes with a high S/B ratio, namely for high p_{T} J/ψ, the approach is expected and observed to perform better due to the diminishing impact of the background.

The background correlation is given by the average of the $\mathrm{e^+e^+}$- and $\mathrm{e^-e^-}$-hadron correlations in the range $2.92 \leq m_{\mathrm{ee}} \leq 3.16$ GeV/c^2. The like-sign pair correlations are hereby calculated exactly like those for electron-positron pairs as described in section 5.7.1, with electron-positron pairs replaced by electron-electron

or positron-positron pairs. After determination of the background correlation, the inclusive J/ψ correlation function is calculated according to the superposition in equation 5.22.

The inclusive J/ψ-hadron correlation from the like-sign method is compared to the standard approach in figure 5.22 for HM triggered events and the remaining trigger samples can be found in figure A.25. The comparison is only shown for associated hadrons in the lowest p_{T} bin since the hadron p_{T} range has little impact on the signal extraction aside from increased statistical fluctuations at higher transverse momenta. At low transverse momenta of the J/ψ, some differences are observed between the like-sign and fitting methods, which are largest in the HM trigger sample. The methods start to agree for $p_{\mathrm{T}} > 3$ GeV/c and differences are consistent with statistical fluctuations for $p_{\mathrm{T}} > 5$ GeV/c in all samples. This behavior can be explained by the p_{T} dependence of S/B. The like-sign method therefore corroborates the results of the fit method at intermediate to high transverse momenta.

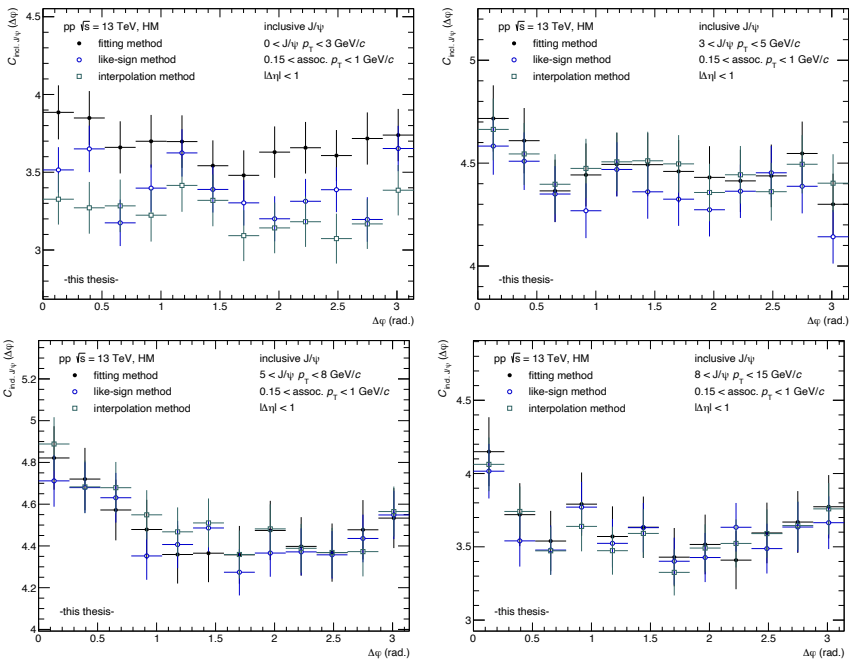

Figure 5.22.: Inclusive J/ψ-hadron correlations from the different correlation signal extraction methods in HM triggered events.

Interpolation method Alternatively, the background correlation can be interpolated from the invariant mass sideband regions outside the J/ψ signal range. The most simple approach hereby is a linear combination of two regions on either side of the J/ψ signal peak. Since the background correlation will in general not be flat or even linear as a function of invariant mass, the sideband regions are chosen to be as close to the J/ψ signal range as possible. This is, however, difficult on the left side of the signal region due to the low mass tail of the J/ψ that results in some signal contribution at relatively low masses. The two sideband regions are therefore chosen to be $m_{\mathrm{e^+e^-}} \in [2.6, 2.68]$ and $[3.2, 3.28]$ GeV/c^2, with the right sideband almost directly adjacent to the J/ψ signal range.

The background correlation is calculated from a linear interpolation of the $\mathrm{e^+e^-}$-hadron correlations evaluated in the two sideband regions:

$$C_{\mathrm{bkg}}(\Delta\varphi) = \frac{1}{\frac{\Delta m_L}{|m_S - m_L|} + \frac{\Delta m_R}{|m_S - m_R|}} \times \left[\frac{\Delta m_L}{|m_S - m_L|} \times C^L_{\mathrm{e^+e^-}}(\Delta\varphi) + \frac{\Delta m_R}{|m_S - m_R|} \times C^R_{\mathrm{e^+e^-}}(\Delta\varphi) \right], \tag{5.23}$$

where S, L and R index the J/ψ signal range as well as the left and right sideband regions, respectively. The center of mass range i is given by m_i, while Δm_i denotes the width of the window. The correlations in the sideband regions are the $C^L_{\mathrm{e^+e^-}}(\Delta\varphi)$ and $C^R_{\mathrm{e^+e^-}}(\Delta\varphi)$. The statistical uncertainty is calculated from the sideband correlations using error propagation. With the background determined, the inclusive J/ψ correlation is evaluated according to equation 5.22.

The comparison between the interpolation method and the fit approach is shown in figure 5.22 for high multiplicity events and the remaining trigger samples can be found in figure A.25. Similar to the like-sign method, there is a good agreement between the interpolation and fitting methods for $p_{\mathrm{T}} > 3$ GeV/c. The interpolation method tends to deviate stronger from the fit approach than the like-sign method at very low p_{T}, at least in the HM sample. This can be attributed to the low mass tail of the J/ψ signal peak which biases the background estimate towards higher values. The interpolation method can be interpreted as a (very) simplified version of the fitting method that only considers linear dependencies of the background correlation on the invariant mass. There is, however, an additional disadvantage with respect to the fit that lies in the specific choice of the invariant mass re-

gions that are considered for the sidebands. Naturally, the interpolation method can therefore only be worse than a fit that is based on the full invariant mass range. It nevertheless confirms the correlation distributions determined from the fit approach, at least at intermediate to high p_{T}.

5.7.3. Non-prompt J/ψ-hadron correlation

The same approaches employed for the inclusive J/ψ are also used to determine the non-prompt J/ψ correlation functions. As for the inclusive J/ψ, the fitting method is considered the standard approach providing the best performance while the two alternative procedures are only serve the purpose of a qualitative comparison. The non-prompt J/ψ-hadron correlations determined in this section are also already corrected for the J/ψ and associated hadron reconstruction efficiencies and normalized the associated hadron p_{T} and η ranges.

Fit method

The fit approach is identical to the inclusive J/ψ as described above, but a different functional form is used to describe the background correlation. Independent of the transverse momentum, the background is well described by fourth order polynomial. The correlation signal extraction is shown in figure 5.23 for an exemplary kinematical selection with typical statistical significance. The figure only shows the first $\Delta\varphi$ bin and the remaining bins can be found in figures A.26 to A.29 in the appendix. Figure A.30 shows the first $\Delta\varphi$ bin for different kinematical selections yielding comparatively low and high statistics samples. The fits provide a reasonable description of the data over the whole kinematical regime, even in the lowest statistics cases. However, larger fluctuations are observed than in the inclusive sample due to the statistical limitations which result in increased uncertainties on the fits. Naturally, the non-prompt J/ψ-hadron correlation is attributed a greater statistical uncertainty than the inclusive J/ψ as can be seen by the values quoted in the figure.

Other methods

The non-prompt J/ψ-hadron correlation functions are also determined from the like-sign and interpolation approaches. Both methods are hereby identical to

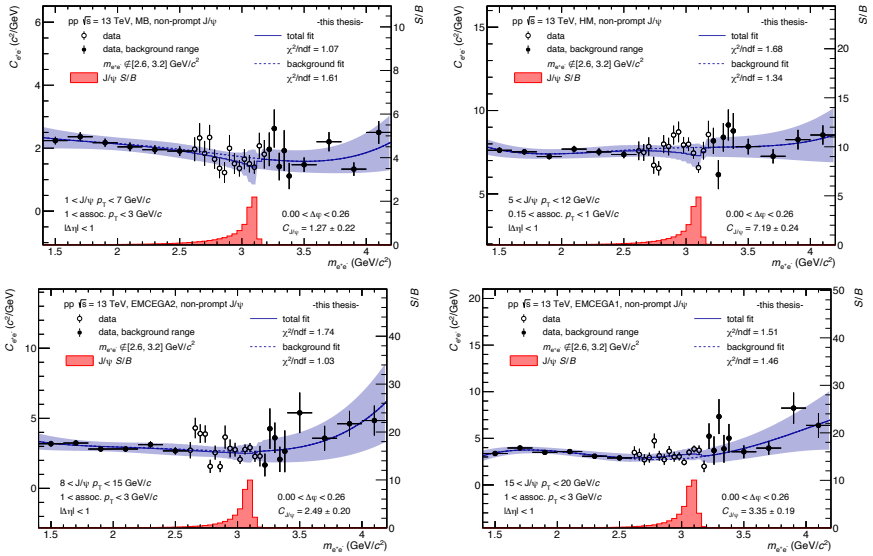

Figure 5.23.: Non-prompt J/ψ correlation signal extraction via fitting method for exemplary $\Delta\varphi$ and kinematical bin in MB (*top left*), HM (*top right*) and EMCal (*bottom*) triggered events.

those employed for the inclusive J/ψ, with the same invariant mass ranges for the sideband regions in the interpolation method. The like sign pairs have to pass the same non-prompt J/ψ candidate selection criteria as the electron-positron pairs, namely the decay length cut. After determination of the background, the signal correlation for either method is calculated according to equation 5.23 where S/B from the non-prompt J/ψ signal extraction is used.

The non-prompt J/ψ-hadron correlations from the like-sign and interpolation methods are compared to the standard approach in figure 5.24. The figure shows the correlations for different J/ψ p_{T} in high multiplicity events but is limited to a singular choice for the p_{T} of associated hadrons. Figure A.31 in the appendix shows the same comparison for the remaining trigger samples. The deviations between the different signal extraction methods are compatible with those observed for inclusive J/ψ, except for the like-sign method at very low transverse momenta. This can, however, be explained by the impact of the decay length cut that affects like-sign pairs differently than actual non-prompt J/ψ candidates. The agreement between the methods improves with S/B at larger transverse momenta and differ-

ences agree with statistical fluctuations for $p_{\mathrm{T}} > 5$ GeV/c. It should be noted, that the p_{T} bins shown for the non-prompt J/ψ are not identical to those presented for the inclusive ones.

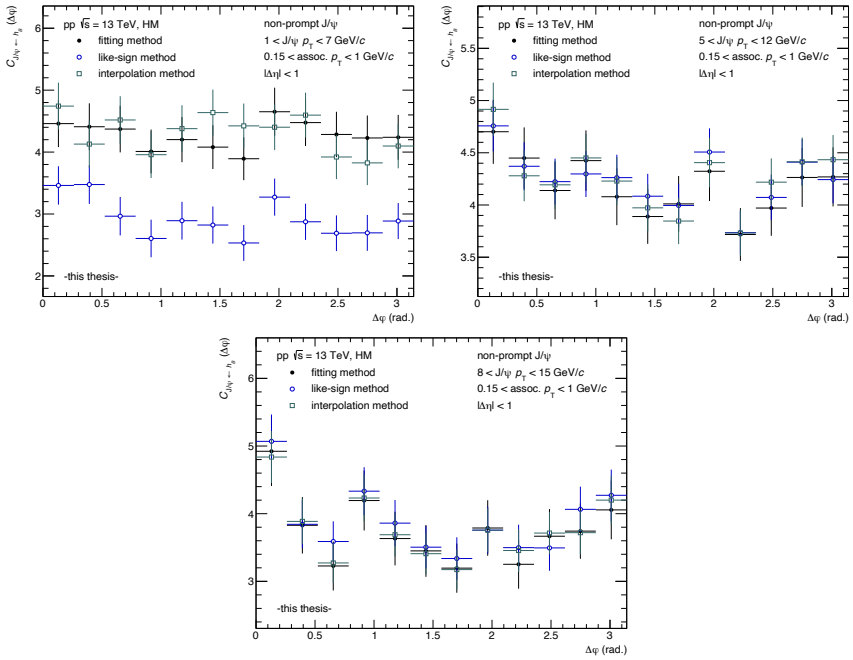

Figure 5.24.: Non-prompt J/ψ-hadron correlations from the different correlation signal extraction methods in HM triggered events.

5.7.4. Prompt J/ψ-hadron correlation

The prompt J/ψ-hadron correlation can not be directly determined from the signal-plus-background correlation since prompt J/ψ candidates can not be selected by a cut on the decay length of the pair. However, it can be calculated from the results of the previous sections via superposition:

$$C_{\text{prompt J}/\psi}(\Delta\varphi) = \frac{C_{\text{inclusive J}/\psi}(\Delta\varphi) - f_B \times C_{\text{J}/\psi\leftarrow h_B}(\Delta\varphi)}{1 - f_B}, \tag{5.24}$$

where f_B is the fraction of non-prompt J/ψ provided by the interpolation introduced in section 5.4.2. The $C_{\text{inclusive J}/\psi}(\Delta\varphi)$ and $C_{\text{J}/\psi\leftarrow h_B}(\Delta\varphi)$ are the inclusive

and non-prompt J/ψ correlation functions, respectively. The statistical uncertainty on the prompt J/ψ correlation is calculated via error propagation from the inclusive and non-prompt contributions. The non-prompt fraction is taken at face value without consideration of statistical uncertainty and associated uncertainties are included into the systematic uncertainty of the measurement.

The calculation is performed separately for the different kinematical selections where the J/ψ p_{T} is limited to the choices for non-prompt J/ψ as listed in table 5.4. The interpolation of f_B is given as a continuous function in transverse momentum and must be evaluated at a certain p_{T} to yield the value used in equation 5.24. This evaluation is done at the average p_{T} of the inclusive J/ψ in the given transverse momentum bin. Results on the prompt J/ψ-hadron correlation are presented in chapter 7 as this section only describes the procedure.

6. Systematic uncertainties

In this section, the systematic uncertainties associated with the measurement of the inclusive, non-prompt and prompt J/ψ-hadron correlations are evaluated and discussed. Such uncertainties can arise, for example, from an imperfect description of the data by the MC simulations, sensitivities of the signal extraction procedure or interpolations that must be used where no data is available. The main approach in dealing with systematic uncertainties is to eliminate or at least minimize possible sources but this is, unfortunately, not always possible.

The following sources of systematic uncertainties are considered in this analysis: sensitivity to S/B, tested via the electron identification criteria, possible contamination from pile-up, assessed through the hadron selection criteria, track matching between ITS and TPC, primary hadron fraction, J/ψ signal extraction, correlation signal extraction, non-prompt candidate selection and the interpolation of the non-prompt fraction. While electrons are required to have a hit in either of the SPD layers, no such selection is employed for the associated hadrons in order to maximize the available statistics. This could lead to some residual contamination from pile-up tracks which must be considered during the determination of the systematic uncertainties. There is an uncertainty associated with the matching of track segments between ITS and TPC that must be considered on the basis of the associated hadrons. Such an uncertainty cancels out on the level of the electron pair due to the normalization to the number of J/ψ in the correlation. Some of the uncertainties are considered for the inclusive, non-prompt and prompt J/ψ while others apply only for some types. The uncertainty on the interpolation of the non-prompt fraction applies only to the prompt J/ψ correlations while the non-prompt candidate selection has to be considered for both the non-prompt and prompt J/ψ. The remaining sources affect all J/ψ types.

The different sources can be classified according to correlated and uncorrelated uncertainties. The correlated uncertainties concern only the overall scale of the correlation while uncorrelated uncertainties can depend on $\Delta\varphi$. Merely the cor-

relation signal extraction and the non-prompt candidate selection are hereby regarded as uncorrelated uncertainties. There might, however, still be some level of residual correlation in the uncorrelated class, which is considered in the evaluation of the total uncertainty.

The different sources of uncertainties are introduced and evaluated separately below. Finally, the total systematic uncertainties are determined where the different sources are combined according to their classification.

6.1. Electron track selection

The electron track selection, or more specifically the electron identification, has a direct impact on the S/B of the J/ψ. More stringent electron selection criteria reduce the contamination from misidentified particles, and therefore improve S/B, at the expense of reduced statistics. This trade-off is considered in the definition of the electron selection cuts but variations of these criteria must be tested since the correlation signal extraction is quite sensitive to the S/B ratio. Therefore, the standard electron identification cuts are compared to a more open as well as a tighter set of requirements. These criteria are summarized in table 6.1, where the standard case is compared to the two variations. As described in section 5.2, the electron selection criteria differ between the MB or HM and EMCal trigger samples due to the availability of the calorimeter cluster information. This is naturally also considered in the variations listed in the table, where the condition refers to the availability of a calorimeter cluster that is matched to the track. The J/ψ reconstruction efficiency depends on the electron selection criteria and is therefore recalculated and applied correspondingly.

variable	open	standard	strict	condition
TPC n_σ electron	$\in [-2, 3.5]$	$\in [-1.5, 3]$	$\in [-1, 2.5]$	
TPC n_σ pion	> 3	> 3.5	> 4	no cluster match
TPC n_σ proton	> 3	> 3.5	> 4	
cluster E/p	$\in [0.7, 1.4]$	$\in [0.8, 1.3]$	$\in [0.9, 1.2]$	cluster match

Table 6.1.: Systematic variations of electron identification criteria given by a 'strict' and 'open' set of cuts as compared to the standard case. The condition quoted in the last column refers to the availability of a calorimeter cluster matched to the electron track in the EMCal triggered data sample.

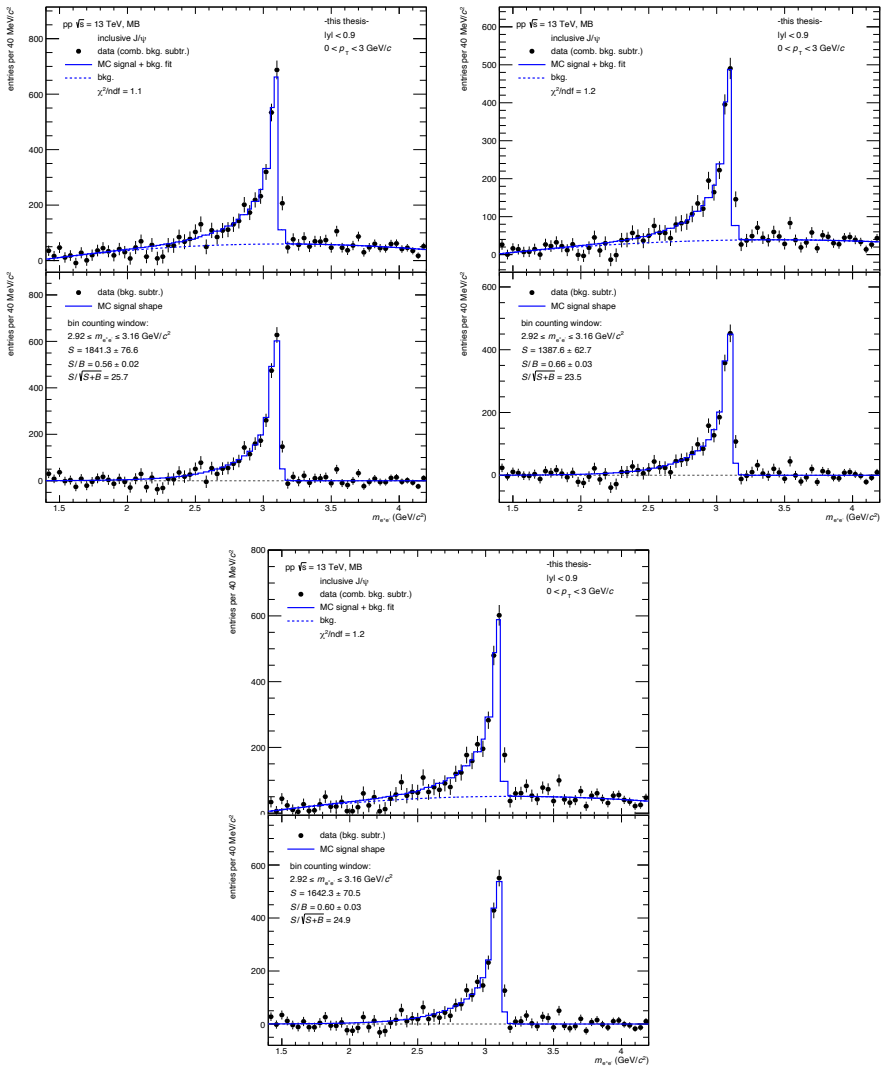

Figure 6.1.: Inclusive J/ψ signal extraction at low p_{T} in minimum bias events with electrons selected according to the open (*top left*), strict (*top right*) and standard (*bottom*) identification criteria as listed in table 6.1.

The impact of the different electron identification cuts listed in table 6.1 is exemplified in figure 6.1. The figure shows the inclusive J/ψ signal extraction for low transverse momenta in minimum bias trigger events for the standard electron selection as well as the variations. S/B increases while the number of reconstructed J/ψ decreases with a sharpening of the selection criteria.

The systematic uncertainty associated with the electron identification is considered a correlated uncertainty and therefore evaluated as a scale uncertainty on the correlation function. The sensitivity to S/B is a general aspect of the correlation signal extraction and can not fully be removed from the analysis. It is furthermore evaluated on the basis of the inclusive J/ψ since the non-prompt candidate selection is a mere additional kinematical. Consequently, the scale uncertainty determined on the inclusive J/ψ is also attributed to the non-prompt and prompt J/ψ-hadron correlation functions.

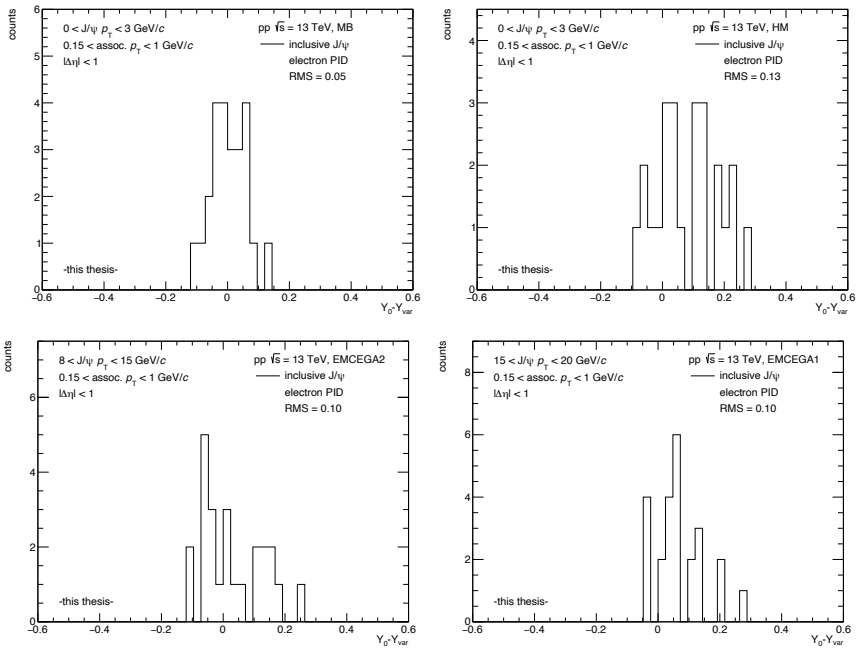

Figure 6.2.: Distribution of differences between standard electron selection and cut variations on the inclusive J/ψ-hadron correlation in an exemplary kinematical bin for the MB (*top left*), HM (*top right*) and EMCal (*bottom*) trigger samples.

The systematic uncertainty is evaluated from the difference between the inclusive J/ψ-hadron correlation for the standard electron selection and the variations. The distributions of differences are shown in figure 6.2 for an exemplary kinematical selection in all trigger samples. Herby, each variation and $\Delta\varphi$ bin of the correlation contributes one entry and the distributions are, up to some minor variations, reasonably symmetric around zero. The uncertainties are given by the root mean square (RMS) of the variations and quoted in the figure. The scale uncertainty attributed to the electron identification does not strongly depend on the kinematical regime and is reasonably stable with p_{T} and $\Delta\eta$. Some kinematical regimes with lower statistics show larger scale uncertainties due to influences from statistical fluctuations which unfortunately can not be fully removed.

6.2. Hadron track selection

Systematic uncertainties can enter the analysis with respect to the hadron tracks in three areas. As mentioned above, the missing requirement on SPD information as well as the matching of ITS and TPC track segments must be considered. Additionally, the primary fraction used in the efficiency correction is attributed a systematic uncertainty. All of these are treated as correlated uncertainties since they only affect the overall scale of the correlation function. The different sources are introduced separately in the paragraphs below. The uncertainty associated with the SPD requirement is, just like the uncertainty on the electron selection, evaluated on the level of the inclusive J/ψ. The remaining uncertainties are provided in relative terms and can be directly applied to the correlation functions.

SPD requirement The standard hadron selection is compared to a stricter cut that requires a hit in any of the two SPD layers, as is used for the electron selection. Naturally, the hadron reconstruction efficiency is evaluated again for the stricter hadron selection and applied correspondingly. The systematic uncertainty associated with the (missing) SPD requirement on the hadron tracks is determined similar to the uncertainty associated with the electron track selection. The variation is compared to the standard selection criteria on the basis of the inclusive J/ψ-hadron correlation and the distribution of differences is shown in figure 6.3 for an exemplary kinematical selection. The distributions are more

sharply peaked than those observed for the electron selection in figure 6.2. The systematic uncertainty attributed to the hadron selection is again evaluated from the RMS of the differences and quoted in the figure. The kinematical dependence of the uncertainty is comparable to that of the electron selection and reasonably stable. Kinematical regimes with comparatively lower statistics can show larger fluctuation between the different hadron selections which translate into a slightly increases systematic uncertainty. The narrow and symmetric distributions in figure 6.3 show that there is no notable contamination from pile-up tracks due to the missing SPD requirement in the standard selection.

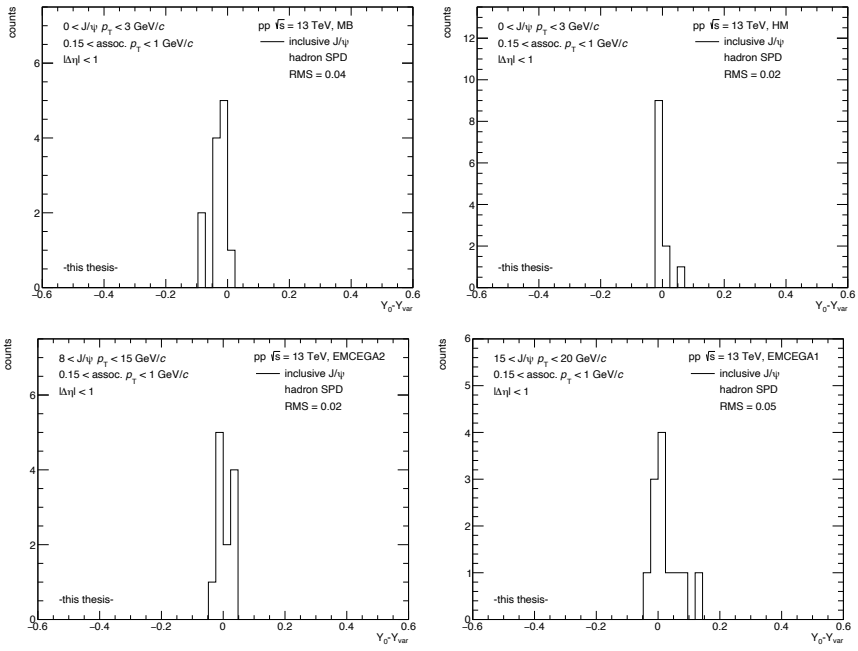

Figure 6.3.: Distribution of differences between standard hadron selection and cut variation on the inclusive J/ψ-hadron correlation in an exemplary kinematical bin for the MB (*top left*), HM (*top right*) and EMCal (*bottom*) trigger samples.

ITS-TPC matching The ITS-TPC matching uncertainties [107] for single tracks are provided by the DPG separately for different collections runs. The uncertainties are determined for the different trigger samples, considering the correspond-

ing selection of runs as well as the relative weight in terms of number of selected events per run. They must furthermore be evaluated in the p_{T} bins of the associated hadrons, which is done by calculating the weighted average using the efficiency corrected number of reconstructed hadrons in the respective p_{T} ranges. Figure 6.4 shows the uncertainties before and after the reweighting for the different trigger samples as well as the associated hadron p_{T} distributions. Minor differences between the trigger samples arise from the corresponding selection of runs and the respective p_{T} distributions of associated hadrons. It can be seen, that the reweighted uncertainties are fairly similar for the different trigger samples and range from about 1.5% at low to 2.5% at high transverse momenta. The uncertainties shown in figure 6.4 directly apply to the inclusive, non-prompt and prompt J/ψ-hadron correlation functions.

Primary fraction The fraction of primary particles is determined from a MC template fit using the DCA$_{xy}$ distributions in section 5.6.2. It can alternatively also be determined using the distributions in the longitudinal direction which yields similar values as compared in the left panel of figure 5.19. Nevertheless, the particular choice is somewhat arbitrary and therefore considered in the systematic uncertainties. The hadron efficiency is corrected for the primary fraction according to equation 5.16, which shows that an uncertainty on the primary fraction has an immediate effect on the scale of the correlation function. This scale uncertainty is estimated from the difference in primary fractions:

$$\left(\frac{\Delta C_{\mathrm{J}/\psi}}{C_{\mathrm{J}/\psi}}\right)_{f_{\mathrm{prim.}}} = \frac{\left| f_{\mathrm{prim.}}^{\mathrm{DCA}_{xy}} - f_{\mathrm{prim.}}^{\mathrm{DCA}_{z}} \right|}{f_{\mathrm{prim.}}^{\mathrm{DCA}_{xy}}}, \tag{6.1}$$

where $f_{\mathrm{prim.}}^{\mathrm{DCA}_{xy}}$ and $f_{\mathrm{prim.}}^{\mathrm{DCA}_{z}}$ are the primary fractions determined in the transverse plane and longitudinal direction, respectively. The relative scale uncertainty calculated according to equation 6.1 is shown in figure 6.5. Similar to the ITS-TPC matching uncertainty, a reweighting procedure is employed to determine the uncertainty in the analysis binning using the efficiency corrected hadron p_{T} spectrum. Both the initial and reweighted uncertainties are shown in the figure as well as the hadron p_{T} distribution. It can be seen, that the uncertainty has no strong p_{T} dependence and is on the sub-percent level for all triggers and kinematical regimes. The uncertainty, while negligible in size, is nevertheless included.

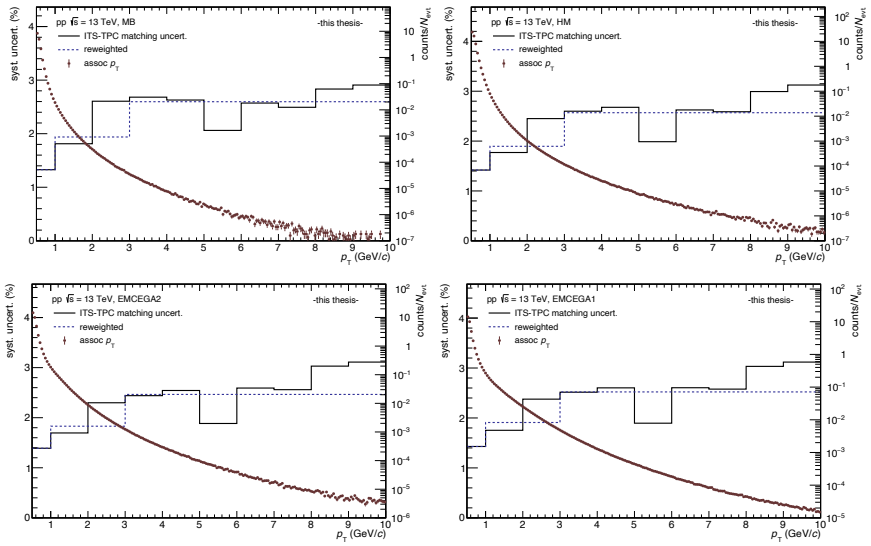

Figure 6.4.: Systematic uncertainties associated with the ITS-TPC matching in the MB (*top left*), HM (*top right*) and EMCal (*bottom*) trigger samples.

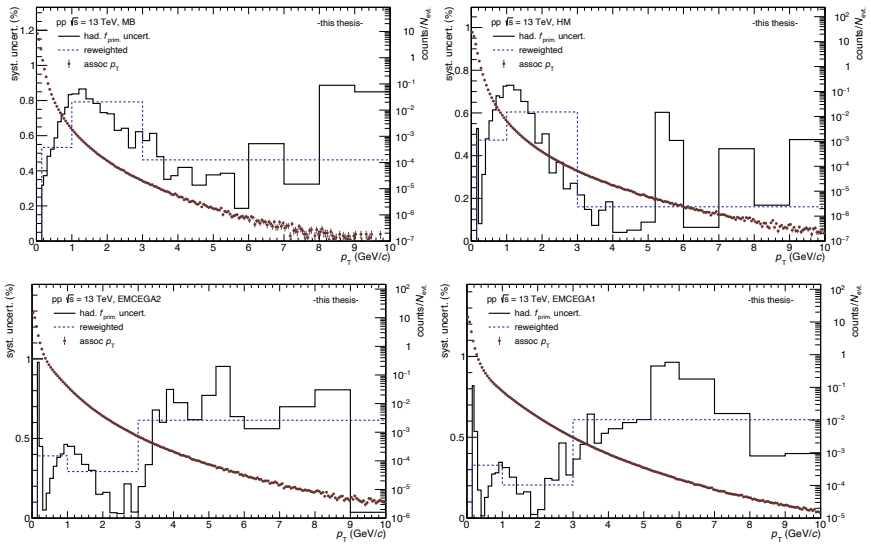

Figure 6.5.: Systematic uncertainties associated with the primary fraction correction of the hadron efficiency in the MB (*top left*), HM (*top right*) and EMCal (*bottom*) trigger samples.

6.3. J/ψ signal extraction

The J/ψ signal extraction is regarded as a possible source of correlated systematic uncertainty due to the normalization of the correlation function. Hereby, the determination of the background is tested by variation of the fit range in both the hybrid and full background fit approaches. There is no reason to test modifications of the functional form since the parametrizations introduced in section 5.5.1 provide the best possible description of the background for both inclusive and non-prompt J/ψ. The standard fit range is given by $m_{\mathrm{e^+e^-}} \in [1.4, 4.2]$ GeV/c^2 and the following variations are considered: $[1.4, 3.8]$, $[1.8, 4.2]$ and $[1.8, 3.8]$ GeV/c^2. The fit range variations provide reasonable coverage to test the background shape and amplitude while minimizing the impact from unjust fluctuations.

The J/ψ signal range could furthermore be regarded as a parameter that requires systematic testing due to the low invariant mass tail. This is, however, not necessary since the correlation functions are determined from a fitting procedure which makes use of the full invariant mass range and has thus no sensitivity to the J/ψ signal range.

The scale uncertainty associated with the J/ψ signal extraction is evaluated in a similar way to the sources described above. The inclusive J/ψ-hadron correlation is determined for each J/ψ background fit range, and differences between the variations and the standard range are displayed in figure 6.6 for all trigger samples. It can be seen, that the distributions are symmetric around zero and very narrow with RMS values well below those observed for the electron cut variations. The scale uncertainties associated with the J/ψ signal extraction are found to be negligible but nevertheless included. There is no strong kinematical dependence, neither on the J/ψ nor the associated hadron p_{T}. In contrast to the previous sources of systematic uncertainty, the J/ψ signal extraction must be evaluated separately for non-prompt J/ψ due to the differences in the signal extraction procedure. The scale is determined following the same procedure with identical background fit range variations and similar uncertainties are obtained.

The uncertainty on the prompt J/ψ-hadron correlation is determined in a slightly different way. Since the correlation functions for prompt J/ψ are calculated following superposition, no fit range variation can be applied directly. However, the correlation functions are calculated for the different fit range variations where the same variations are used in the inclusive and non-prompt components in

the superposition. Then, the different fit ranges are compared on the basis of the prompt J/ψ-hadron correlation and the corresponding systematic uncertainty is evaluated in the same manner as discussed above. Naturally, the scale uncertainties are found to be comparable to those observed for inclusive and non-prompt J/ψ as they must lie between the two by definition. The systematic uncertainty associated with the J/ψ signal extraction is therefore found to be negligible also for the prompt J/ψ correlation.

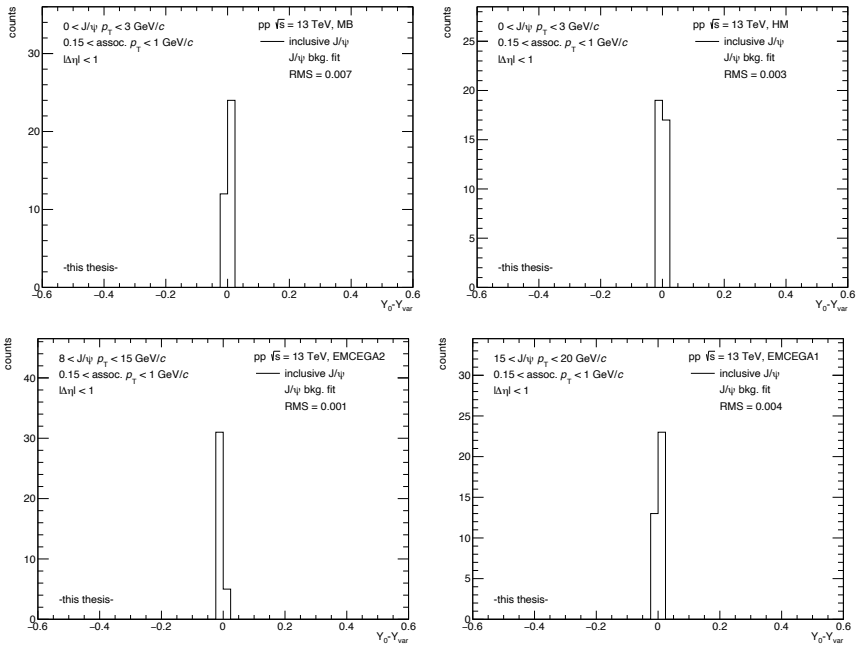

Figure 6.6.: Distribution of differences between different J/ψ background fit ranges and the standard range on the inclusive J/ψ-hadron correlation in an exemplary kinematical regime for the MB (*top left*), HM (*top right*) and EMCal (*bottom*) trigger samples.

6.4. Correlation signal extraction

The correlation signal extraction corresponds to an important, albeit small, source of systematic uncertainty. It is treated as an uncorrelated systematic uncertainty, meaning it can vary from bin to bin in $\Delta\varphi$ and is therefore not evaluated in

terms of a scale uncertainty. In the case of the inclusive J/ψ, it is the only uncorrelated source of uncertainty while the correlation of non-prompt and prompt J/ψ have an additional one. The $\Delta\varphi$ dependence of the correlation inherently requires the uncertainty associated with the determination of said correlation to be treated in an uncorrelated manner. Nevertheless, the term 'uncorrelated' is in this context mainly used to differentiate to the systematic uncertainties that solely affect the scale of the correlation function. Some level of correlation between the uncertainties on the different $\Delta\varphi$ bins might remain and is considered during the calculation of the total systematic uncertainty.

While different correlation signal extraction methods are introduced in section 5.7, only the fitting method is considered here. The remaining methods are regarded as inferior and only discussed to provide a qualitative comparison. Similar to the evaluation of the J/ψ signal extraction, the fit ranges are varied to determine the uncertainty. The standard fit range is hereby identical to the range used for the J/ψ signal extraction, $m_{\mathrm{e^+e^-}} \in [1.4, 4.2]$ GeV/c^2, and the variations are given by: $[1.4, 4.0]$, $[1.6, 4.2]$ and $[1.6, 4.0]$ GeV/c^2. It should be noted, that the fit range variations do not correspond to those used for the J/ψ signal extraction. This is due to the limited statistics available for the analysis which requires broader invariant mass bins in the correlation. In order to have a reasonable number of data points available for the fit, the variations to the fit range are bound to be less distinct.

The uncertainty associated with the correlation signal extraction is evaluated on the basis of the inclusive J/ψ-hadron correlation by comparison of the fit range variations to the standard range. In contrast to the correlated uncertainties, this comparison must be performed in bins of $\Delta\varphi$ and the distribution of differences is shown as a function of the azimuthal angle in figure 6.7. The uncertainty is evaluated separately for each $\Delta\varphi$ bin where, due to the small number of contributions, the RMS is not a reasonable estimate of the uncertainty anymore. However, a uniform distribution of the differences can be assumed and the uncertainty is thus given by the standard deviation of the uniform distribution. Therefore, each slice in $\Delta\varphi$ is associated with a systematic uncertainty given by the maximum difference divided by $\sqrt{12}$. The maximum uncertainty observed in the given kinematical selection is quoted in the figure. Typically, the uncertainties are quite small and in the sub-percent level but the absolute values depend on the kinematical regime.

A strong dependence on $\Delta\varphi$ can often be associated with fluctuations, which is considered during the calculation of the total uncertainty. The systematic uncertainty on the non-prompt J/ψ correlation is evaluated in the exact same manner with identical fit range variations. The uncertainties are slightly larger for non-prompt J/ψ due to the reduced statistics and thus larger sensitivity to statistical fluctuations which, unfortunately, can not fully be removed.

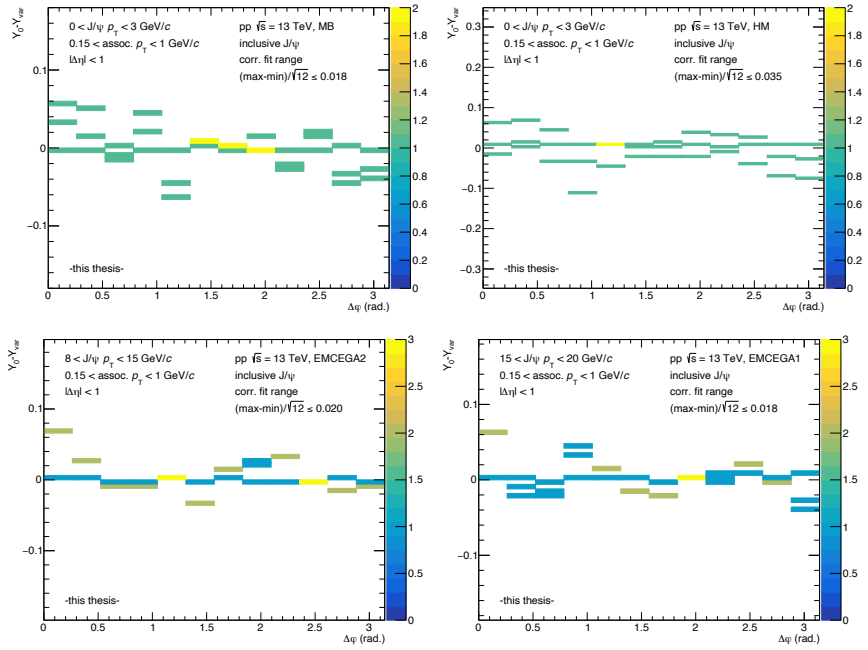

Figure 6.7.: Distribution of differences between different correlation fit ranges and the standard range on the inclusive J/ψ-hadron correlation in an exemplary kinematical regime for the MB (*top left*), HM (*top right*) and EMCal (*bottom*) trigger samples.

The uncertainty on the prompt J/ψ-hadron correlation is evaluated similarly to the uncertainty associated with the J/ψ signal extraction, but determined in dependence of the azimuthal angle. Hereby, the correlation for prompt J/ψ as determined with the standard fit range is compared to the correlation calculated from the fit range variations on the inclusive and non-prompt J/ψ. As was the case for the J/ψ signal extraction, the systematic uncertainties are comparable to those obtained for the inclusive and non-prompt J/ψ.

6.5. Non-prompt J/ψ candidate selection

The non-prompt J/ψ candidates are selected via a decay length cut as introduced in section 5.4.2. The definition of this cut retains a small but finite contamination from prompt J/ψ in the non-prompt sample. In the standard case, this contamination is kept at 10% remaining prompt J/ψ, which translates into a systematic uncertainty by design. This uncertainty affects both the non-prompt and prompt J/ψ-hadron correlations, but not the correlation of inclusive J/ψ and is evaluated by means of varying the contamination in the definition of the cut. It is regarded as an uncorrelated systematic uncertainty since the shape of the correlation can depend on the non-prompt fraction in the selected sample. In a simplified physical picture, this can be understood from the additional decay products in the vicinity of the J/ψ that are produced in the decay of heavy hadrons containing b-quarks from which the non-prompt J/ψ originate. This can modify the correlation function, particularly in the near-side, but naturally depends on the kinematical regime due to the boost that the decay products experience. Nevertheless, an increased or reduced contamination from prompt J/ψ might affect the near-side of the correlation function more than the away-side or baseline, which is why the uncertainty must be evaluated as a function of $\Delta\varphi$. As was the case for the correlation signal extraction, a potential residual correlation of the systematic uncertainty is considered during the calculation of the total uncertainty.

The surviving prompt fraction is varied from the standard value of 10% to 5 and 20%, resulting in two additional samples of non-prompt J/ψ candidates with less and more contamination, respectively. The non-prompt J/ψ hadron correlation is then calculated for the two variations and compared to the standard case. Figure 6.8 shows the differences between the standard selection and the two variations as a function of $\Delta\varphi$ in an exemplary kinematical bin for all trigger samples. The uncertainties are evaluated for each $\Delta\varphi$ bin separately by dividing the maximum difference by $\sqrt{12}$, assuming a uniform distribution similar to the correlation signal extraction. These systematic uncertainties are considerably larger than those observed for the correlation signal extraction, often by a factor four to five, but nevertheless still significantly smaller than the statistical uncertainties.

The uncertainty on the prompt J/ψ-hadron correlation is determined by using the decay length cut variations for the non-prompt J/ψ component in the superposition calculation. The inclusive J/ψ component remains unchanged and

the uncertainty is evaluated from the differences on the basis of the prompt J/ψ correlation. Due to the relatively small fraction of non-prompt J/ψ in the inclusive sample, which is below 20% for all kinematical regimes, the uncertainties are smaller by some margin than those observed for non-prompt J/ψ. Nevertheless, the uncertainties attributed to the decay length cut are still larger than those associated with the correlation signal extraction.

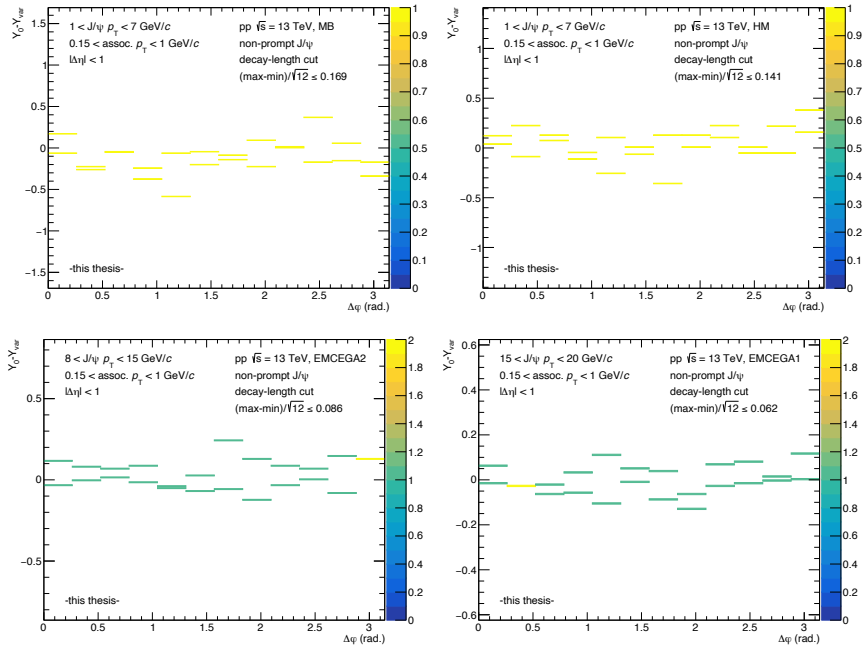

Figure 6.8.: Distribution of differences for the non-prompt J/ψ-hadron correlation between the decay length cut variations and the standard case in an exemplary kinematical regime for the MB (*top left*), HM (*top right*) and EMCal (*bottom*) trigger samples.

6.6. Interpolation of non-prompt fraction

The prompt J/ψ-hadron correlation is attributed an additional systematic uncertainty that is given by the uncertainty on the non-prompt fraction f_B. The non-prompt fraction is determined from an interpolation procedure and evaluated at the average p_{T} of the J/ψ in the kinematical bin. Both, the interpolation as

well as the mean p_{T} values, have associated uncertainties that must be considered. Since f_B enters as a constant factor in the calculation of the correlation for prompt J/ψ via superposition, the corresponding systematic uncertainty is provided as a scale uncertainty. First, the uncertainty on f_B is calculated and then propagated to the prompt J/ψ-hadron correlation according to:

$$\left(\Delta C_{\text{prompt J}/\psi}(\Delta\varphi)\right)^2_{f_B} = \left(\frac{C_{\text{incl. J}/\psi}(\Delta\varphi) - C_{\text{J}/\psi\leftarrow h_B}(\Delta\varphi)}{\left(1-f_B\right)^2} \times \Delta f_B\right)^2, \tag{6.2}$$

where $C_{\text{incl. J}/\psi}(\Delta\varphi)$ and $C_{\text{J}/\psi\leftarrow h_B}(\Delta\varphi)$ are the inclusive and non-prompt J/ψ-hadron correlation functions, respectively. The uncertainty Δf_B combines the uncertainties from the interpolation and average p_{T}:

$$\Delta f_B = \frac{1}{2} \times \left| f_B^{\text{up}}\left(\langle p_{\mathrm{T}}\rangle + \Delta\langle p_{\mathrm{T}}\rangle\right) - f_B^{\text{down}}\left(\langle p_{\mathrm{T}}\rangle - \Delta\langle p_{\mathrm{T}}\rangle\right)\right|, \tag{6.3}$$

where f_B^{up} and f_B^{down} are the upper and lower edges of the 1σ confidence interval of the fit shown in figure 5.11. The f_B confidence interval is evaluated at $\langle p_{\mathrm{T}}\rangle \pm \Delta\langle p_{\mathrm{T}}\rangle$, where $\Delta\langle p_{\mathrm{T}}\rangle$ is the uncertainty of the average p_{T}.

The propagation of the uncertainty according to 6.2 naturally yields a $\Delta\varphi$ dependence due to the evaluation of the inclusive and non-prompt J/ψ correlation functions. Therefore, an approach similar to the previously described correlated systematic uncertainties is employed to determine the scale uncertainty on the prompt J/ψ-hadron correlation. The prompt J/ψ correlation function is shifted by the $\Delta\varphi$ dependent uncertainties in either direction, resulting in two variations that can be compared to the standard case. The distributions of differences between the variations and the standard case are shown in an exemplary kinematical window in figure 6.9. These distributions are symmetric by construction and the systematic uncertainty is identified with the RMS of the variations. The uncertainties are negligible in comparison with the previously described scale uncertainties but nevertheless included. There is only a marginal dependence on the kinematical regimes, which is mainly driven by the magnitude of f_B and the amplitude of the correlation function.

6.7. Total systematic uncertainty

Finally, the total systematic uncertainties for the inclusive, non-prompt and prompt J/ψ-hadron correlation functions can be calculated from the different sources.

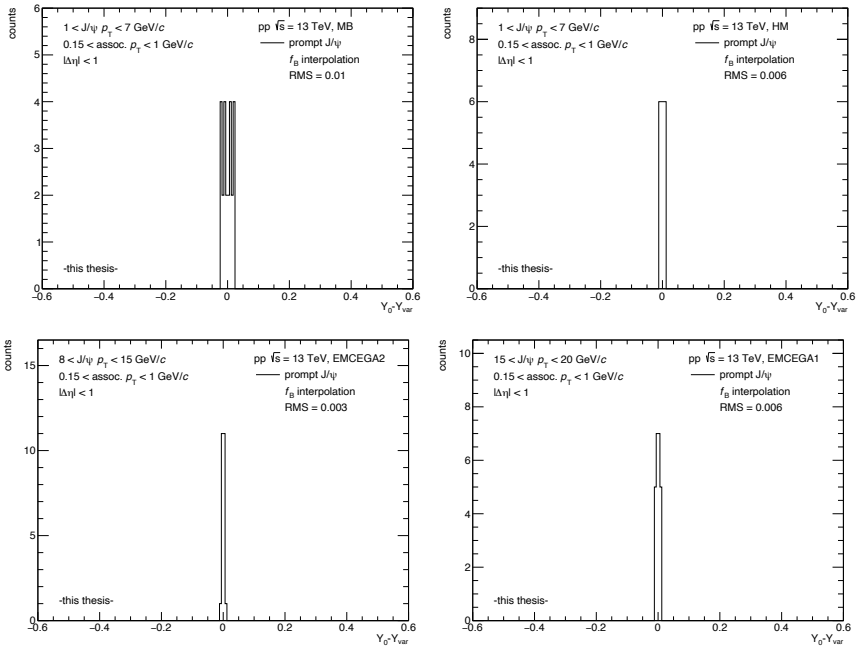

Figure 6.9.: Distribution of differences between the standard and the Δf_B shifted prompt J/ψ-hadron correlation in an exemplary kinematical regime for the MB (*top left*), HM (*top right*) and EMCal (*bottom*) trigger samples.

The different contributions are hereby considered independent and the total uncertainty is thus given by the sum of squares. The uncertainties are summed according to their class, where scale (correlated) and bin-wise (uncorrelated) uncertainties are distinguished. In the case of the inclusive J/ψ, the correlation signal extraction is the sole contribution to the uncorrelated class while non-prompt and prompt J/ψ are additionally attributed the uncertainty associated with the non-prompt J/ψ candidate selection.

The total uncorrelated systematic uncertainties are further smoothed by a third order polynomial fit to reduce statistical fluctuations. This approach furthermore allows some level of correlation in $\Delta\varphi$, which was not considered during the determination of the uncertainty. Figure 6.10 shows the initial and smoothed uncertainties for inclusive J/ψ in an exemplary kinematical bin, as well as the polynomial fits. The initial uncertainties can show a noticeable level of fluctuations which

are considerably decreased by the procedure. The polynomial fits to the uncorrelated uncertainties are displayed as a dashed line in the figure and the smoothed uncertainties are given by the average of the fits in the respective $\Delta\varphi$ bins. The same comparison is shown for non-prompt J/ψ in figure 6.11, which shows larger uncertainties due to the additional contribution from the non-prompt candidate selection. Nevertheless, the smoothing performs just as well and fluctuations are reduced by the polynomial fit.

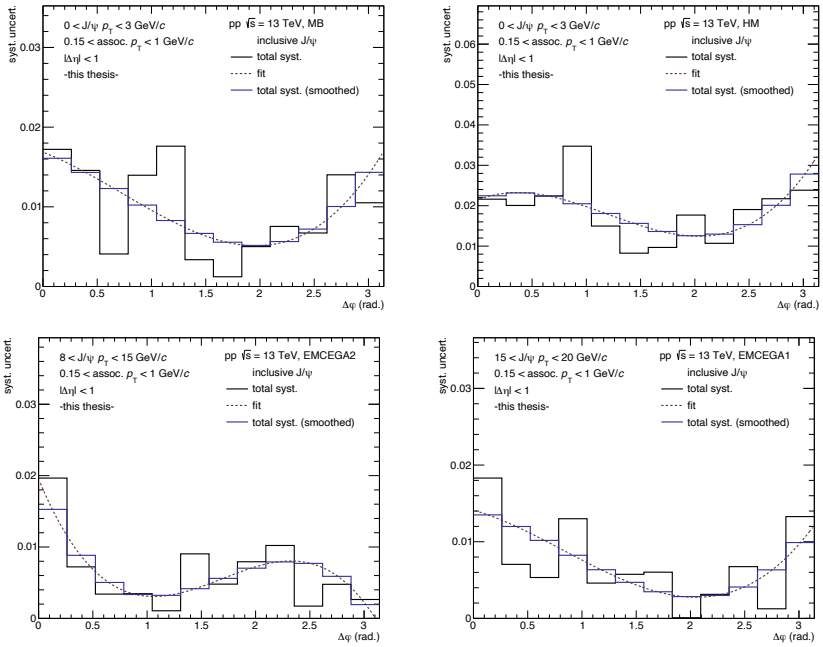

Figure 6.10.: Initial and smoothed uncorrelated uncertainties for inclusive J/ψ in MB (*top left*), HM (*top right*) and EMCal (*bottom*) trigger events.

The central values of the final correlation functions are given by the average of the standard and fit range variations used during the determination of the correlation signal extraction uncertainty. This is a typical approach which is employed to reduce the sensitivity to a somewhat arbitrary prior choice of a 'standard case' and helps to reduce fluctuations. Furthermore, since the uncertainties are presented as a symmetric envelope around a common mean, such an arbitrary choice should be avoided on principle. The different samples provided by the variations

are fully correlated statistically since only the fit range is modified when the correlation signal is extracted. The statistical uncertainties associated with the central values of the correlation functions are therefore given by the arithmetic mean of the statistical uncertainties of the contributions.

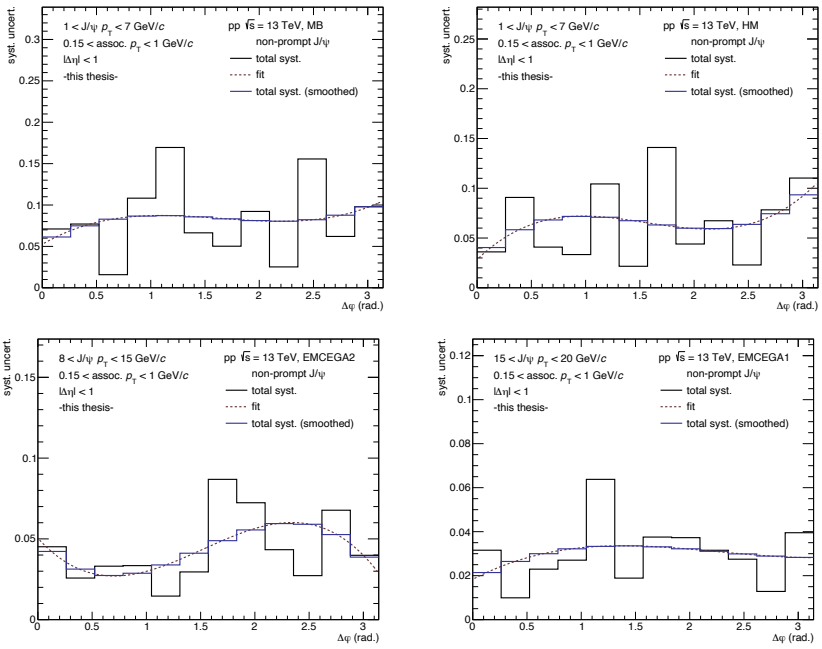

Figure 6.11.: Initial and smoothed uncorrelated uncertainties for non-prompt J/ψ in MB (*top left*), HM (*top right*) and EMCal (*bottom*) trigger events.

The uncertainties associated with this measurement are generally dominated by the statistical component, and not the systematic one. This is due to the limited statistics available for the measurement and cancellation of systematic uncertainties on the level of the correlation function. Cross section measurements, for example, are typically much more sensitive to a proper description of the data in MC since absolute yields are measured. This is not the case in this measurement since the correlation functions are self-normalized. The amplitude of the correlation function is mainly sensitive to the reconstruction of the associated hadrons. However, this reconstruction is performed in such a general way that few uncertainties contribute substantially. The systematic uncertainties are typically

on a level of a few percent but the relative size obviously depends on the amplitude of the correlation function. While the scale uncertainties can reach fairly large values for extreme kinematic cases, the impact on the physics message of the measurement is hardly affected. This is due to the separation of the uncertainties on the scale and the fact, that the interest lies more in the shape of the correlation than the amplitude. Even when fairly large systematic uncertainties are observed the statistical uncertainty still dominates and provides the ultimate limitation on this measurement.

7. Results and discussion

In this section, the results are presented and discussed. The measured correlation functions are shown for inclusive, non-prompt and prompt J/ψ in the different kinematical regimes and for all trigger samples. The different triggers are compared directly in section 7.1. The results are presented for $|\Delta\eta| < 1$ but a comparison to the remaining pseudorapidity ranges is presented in section 7.2. Additionally, the correlated yields in the near- and away-side regions of the correlation functions are determined in section 7.3.

At the time of writing, no model predictions for the correlation functions are available. The effective models introduced in section 2.3 are mainly concerned with the 'in-vacuum' description of the fundamental J/ψ production mechanisms. A more comprehensive description of the collision event is, however, required for the comparison to data on the basis of the correlation functions. This is due to the impact of the underlying event which can not be fully disentangled in the measurement. Furthermore, the associated production of J/ψ, for example, during the fragmentation of jets or heavier quarks can modify the correlation function in non-trivial ways. The results are therefore compared to simulations of full proton-proton collisions using PYTHIA 8 [89] without considering detector effects. The simulations employ the Monash 2013 [108] tune, which is commonly used in LHC experiments and constrains the hadronization parameters and parton distribution functions used in the simulation. These constraints are based on data provided by the SPS and Tevatron colliders. The default J/ψ production and hadronization settings available in PYTHIA are used in the simulations, which in particular include color-singlet and -octet contributions to the J/ψ production mechanism. Additionally, a rudimentary mimicking of the V0HM trigger is performed to provide equal grounds for the comparison to data. Similar to the data, this mimicking selects the 0.1% events with highest multiplicity in the acceptance of the V0 counters, which significantly decreases the available statistics in comparison to the minimum bias sample. It should be noted, though, that the event

multiplicities in PYTHIA are not identical to the data and the comparison should thus be taken with a grain of salt. The HM trigger threshold furthermore changed slightly during the period of data taking to account for the aging of the scintillator counters, which is not considered in the simulation. Nevertheless, the simulations provide reasonable grounds for comparison to the data up to a potential constant offset that can be explained by differences in the selected multiplicity.

The inclusive J/ψ-hadron correlation functions are displayed in figures 7.1 and 7.2. The PYTHIA predictions are depicted as solid lines with shaded areas indicating statistical uncertainties. The dashed lines mark the baselines of the correlation functions, estimated from the average of two bins around $\Delta\varphi = \pi/2$. The systematic uncertainties on the measurement are distinguished by their source, as described in section 6, but statistical uncertainties clearly dominate in all regimes. At low transverse momenta, the correlation functions are mostly flat within uncertainties with the notable exception of HM triggered events with associated hadrons in the lowest p_{T} bin. Near-side signatures at $\Delta\varphi \sim 0$ can be observed for J/ψ with $p_{\mathrm{T}} > 5$ GeV/c and clear away-side peaks at $\Delta\varphi \sim \pi$ become visible at even larger momenta. The near-side peaks become sharper with increasing p_{T} while the away-side does not seem to show the same behavior. This is expected and can be understood in terms of di-jet system kinematics where a low p_{T} trigger is either part of a less collimated jet or just an isolated object. The away-side is even less collimated because of the pseudorapidity swing due to which much of the associated yield can leave the detector acceptance.

The correlation signatures observed can have different sources and the separate correlation functions for prompt and non-prompt J/ψ shown below help to identify these features. The significant near-side correlation at high transverse momenta most likely originates in additional decay products in the vicinity of the non-prompt J/ψ. This contribution becomes important at larger p_{T} due to the increase of the non-prompt fraction as well as the significant boost provided by the mother b-hadrons. The away-side correlation might, correspondingly, originate in back-to-back production of b$\bar{\mathrm{b}}$-pairs and subsequent hadronization. In the lab frame, however, the heavy quark pair must not be produced back-to-back so other di-jet scenarios, for example with a light flavor recoil jet, are also possible. The HM triggered data naturally displays larger amplitudes in all kinematical regimes as is expected from the increase in event multiplicities.

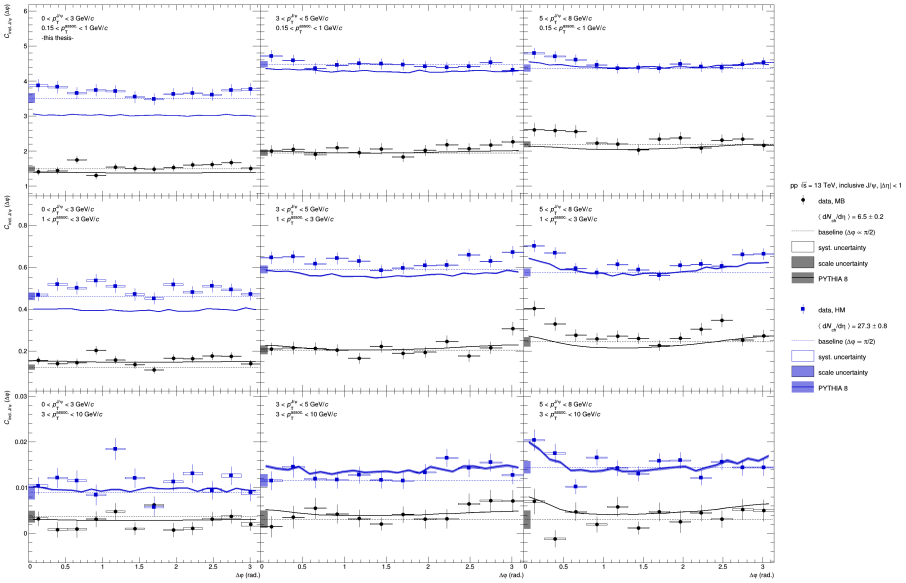

Figure 7.1.: Inclusive J/ψ-hadron correlation in MB and HM triggered events.

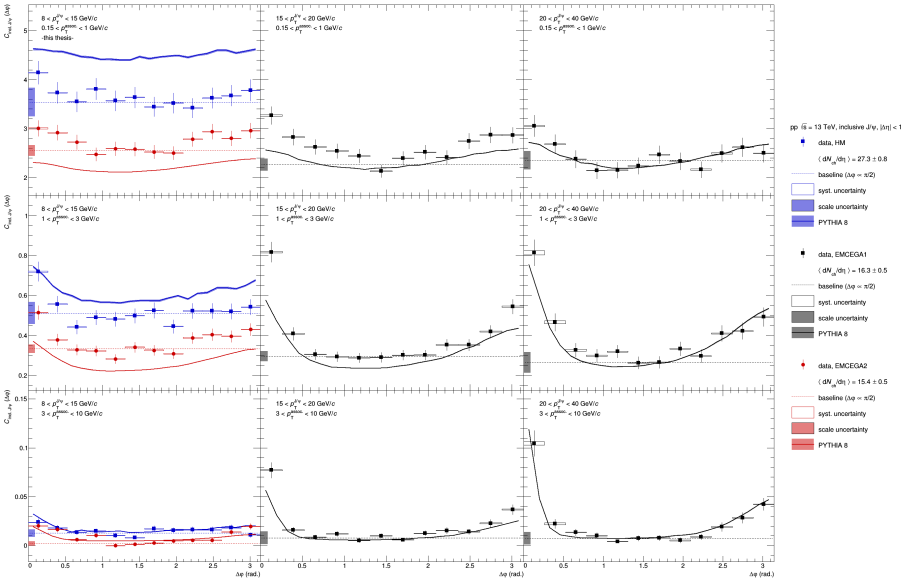

Figure 7.2.: Inclusive J/ψ-hadron correlation in HM and EMCal triggered events.

The data is qualitatively well described by the PYTHIA simulations but some differences in amplitude can be observed. These differences can be attributed to the event multiplicities and larger differences are observed for the HM trigger sample due to the additional complication introduced by the trigger mimicking. Nevertheless, the shapes of the correlation functions produced by the simulation are generally in good agreement with the data. Some minor deviations can be observed, for example for the HM triggered sample in the range $5 < p_{\mathrm{T}}^{\mathrm{J}/\psi} < 8$ GeV/c, but hold little significance due to the large uncertainties associated with the measurement.

Figures 7.3 and 7.4 show the measured non-prompt J/ψ-hadron correlation functions and corresponding PYTHIA curves. Naturally, the data shows larger statistical fluctuations and corresponding uncertainties than in the inclusive sample. The correlation functions show a stronger near-side peak in comparison to the inclusive J/ψ but the away-side is clearly suppressed. Such a behavior is expected from the origin of the non-prompt J/ψ and well described by PYTHIA. At low transverse momenta, however, the correlation functions are constant within uncertainties. Additional decay products associated with the J/ψ experience only negligible boost and can thus be distributed over broader azimuthal angles with respect to the J/ψ direction. The simulations reproduce this behavior but also indicate an increase of the near-side peak with increasing p_{T} of the associated particles. While this is expected according to trivial kinematical considerations, it can not be observed for the lowest p_{T} J/ψ in the data due to large uncertainties. A small away-side correlation signature can be observed at larger transverse momenta and is also present in the simulations. As previously noted, such a signature could potentially be attributed to $\mathrm{b\bar{b}}$ production but other scenarios are obviously also possible.

Finally, the correlation functions for prompt J/ψ are shown in figures 7.5 and 7.6. The correlation functions are constant within uncertainties for most of the kinematical windows and few significant features can be observed. Indications of near- and away-side peaks can be observed at high transverse momenta but are generally smaller in amplitude than those observed for inclusive or non-prompt J/ψ. The away-side signatures appear to be more expressed than in the non-prompt sample. The near- and away-side peaks at large transverse momenta could indicate the production of J/ψ in jet fragmentation processes, which is

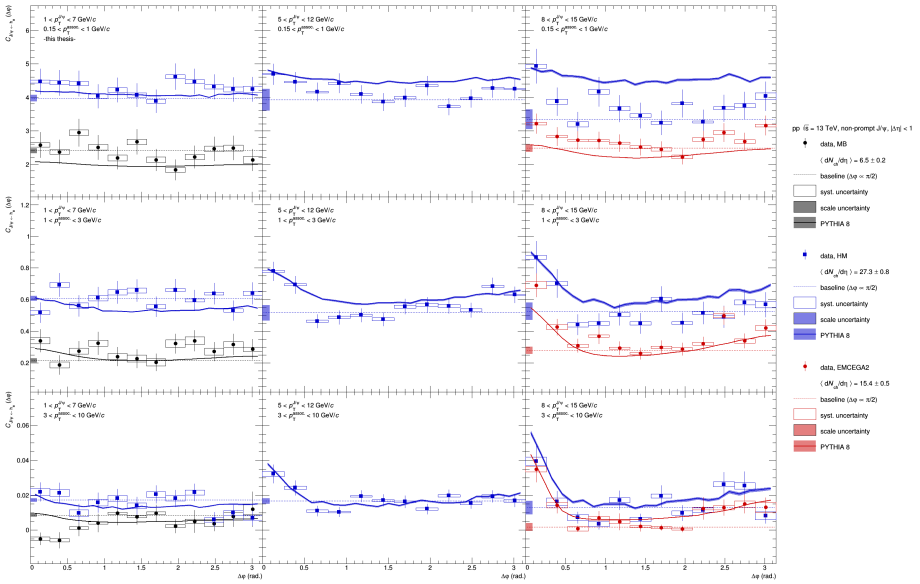

Figure 7.3.: Non-prompt J/ψ-hadron correlation in MB, HM and EMCal triggered events.

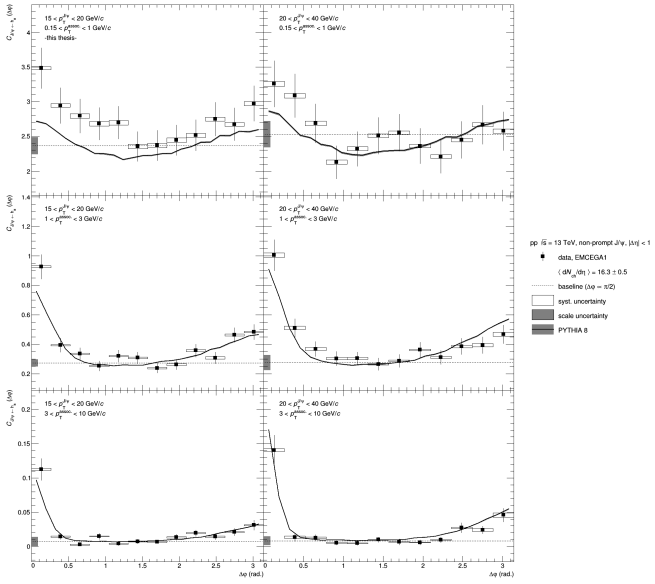

Figure 7.4.: Non-prompt J/ψ-hadron correlation in EMCal triggered events.

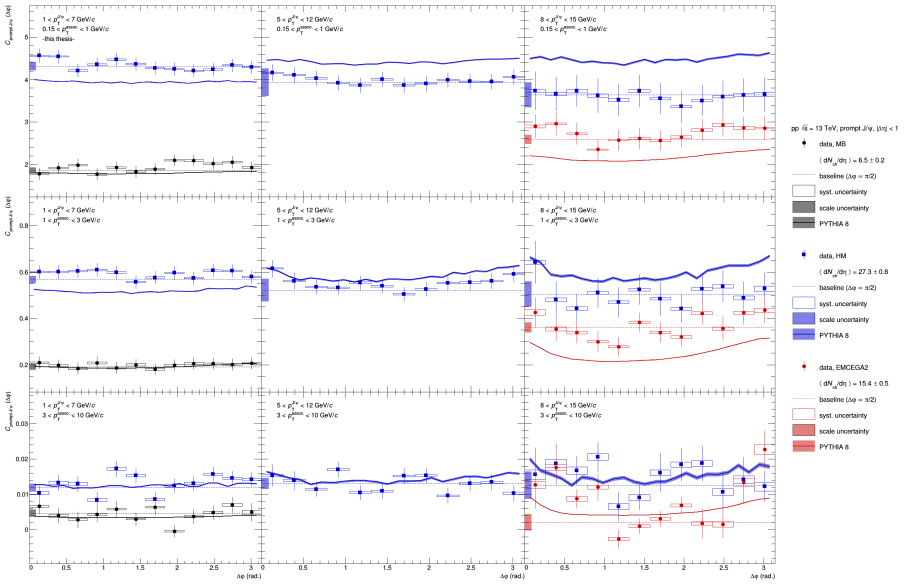

Figure 7.5.: Prompt J/ψ-hadron correlation in MB, HM and EMCal triggered events.

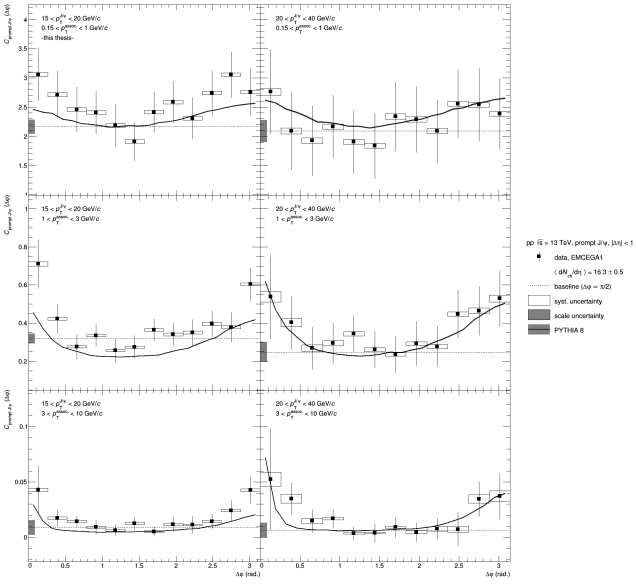

Figure 7.6.: Prompt J/ψ-hadron correlation in EMCal triggered events.

in accordance with previous experimental studies [109, 110]. PYTHIA agrees reasonably well with the data up to constant factors corresponding to differences in the event multiplicities. CMS, on the other hand, observed that the production of J/ψ in jets is underpredicted by PYTHIA [110] but this does not directly relate to the results presented here since no jet reconstruction is performed. Near-side correlation signatures, particularly at low transverse momenta could also indicate the preference of color-octet over -singlet production due to the color neutralization processes required in the formation of the bound state. Color-octet channels largely dominate in the NRQCD implementation in PYTHIA which, due to the good agreement between data and simulations, supports the notion of dominance of the color-octet mechanisms in the production of J/ψ. There are, however, still caveats to this interpretation since the correlation functions contain not only the contributions relevant to the fragmentation of c$\bar{\text{c}}$ into J/ψ but also the underlying event and the whole jet in which the heavy quark system might be embedded. More differential studies based on larger statistics data samples will be needed to gain further insight. Different production processes can ultimately only be disentangled on the basis of a comparison to model predictions and the data presented here should proof useful for such studies.

7.1. Trigger comparison

The correlation functions obtained for the different trigger samples are compared directly in the kinematical windows in which the triggers overlap. The comparison is hereby based on the difference of the correlation functions and quantified using a fit procedure. In this approach, the difference of the correlation functions is described by a superposition of a two gaussian distributions and a constant factor. The gaussian contributions are fixed at mean values of $\Delta\varphi = 0$ and π to quantify the significance of potential differences in the near- and away-side of the correlation function. The constant factor provides the baseline of the difference and is initialized with the average value of four data points around $\Delta\varphi = \pi/2$. Before the fit, the statistical and bin-wise systematic uncertainties are summed in quadrature such that the full significance of the difference can determined from the fit. The systematic scale uncertainty can hereby be neglected as it only contributes a constant offset which is irrelevant for the difference of the correlation functions in

terms of their shape. After the fit, the differences between the triggers are determined from the integral of the fit in the ranges $0 \leq \Delta\varphi \leq \pi/3$ and $2\pi/3 \leq \Delta\varphi \leq \pi$ for the near- and away-side, respectively. The contribution from the baseline is subtracted and the statistical and systematic uncertainties are propagated such that the uncertainty on the difference reflects their combined value.

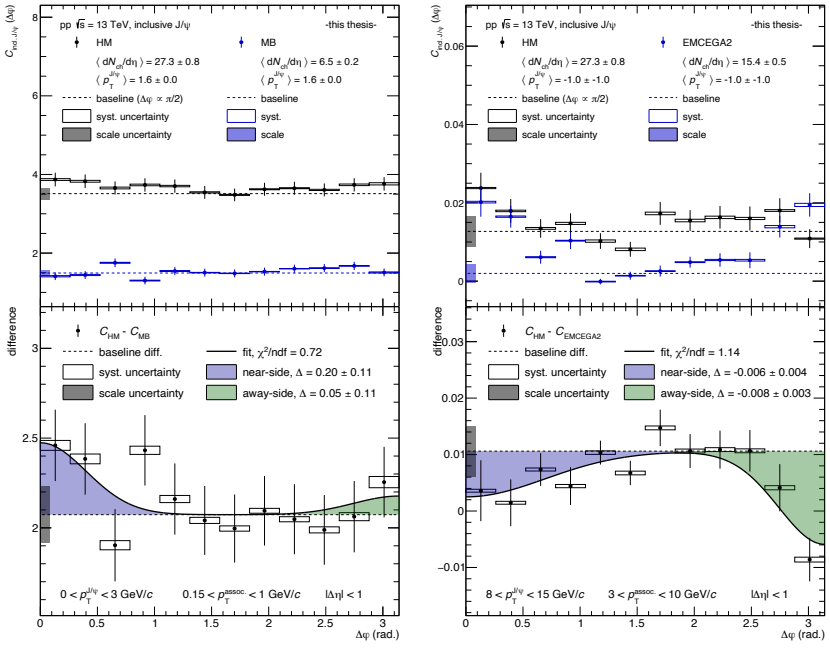

Figure 7.7.: Comparison of inclusive J/ψ-hadron correlations in HM and MB (*left*) as well as HM and EMCal (*right*) triggered events. The near- and away-side differences are quantified by a fit and quoted.

Figure 7.7 shows the trigger comparison for inclusive J/ψ in two selected kinematical regimes where comparatively large differences are observed. The remaining bins can be found in figures A.37 to A.40 in section A.6 of the appendix. The figures show the correlation functions as well as their differences and the corresponding fits. The integrated differences in the near- and away-side are quoted with uncertainties. The left panel of the figure indicates a near-side excess for HM events above minimum bias. This could point towards a modification of the fragmentation function in high multiplicity events, but the significance is only of the order of 2σ. Another possible explanation could be a trigger bias due

to a potential multiplicity dependence of the non-prompt fraction. The correlation function in EMCal triggered events is compared to high multiplicity events in the right panel of the figure. An away-side suppression in HM events with roughly 3σ significance can be observed. This could be explained by a bias towards back-to-back jet events in the EMCal trigger or a potential modification of the away-side correlation in the high multiplicity environment. Such an observation would be similar to jet suppression in QGP studies. Additionally, there could be a non-trivial bias introduced by the HM trigger that depletes the away-side of the correlation function for J/ψ at large transverse momenta. This can be due to the recoil jet from a di-jet event causing the HM trigger signal which will therefore not be reconstructed in the acceptance of the detector. However, none of the observations discussed above are significant but should be regarded as intriguing indications to spark further studies with increased statistics.

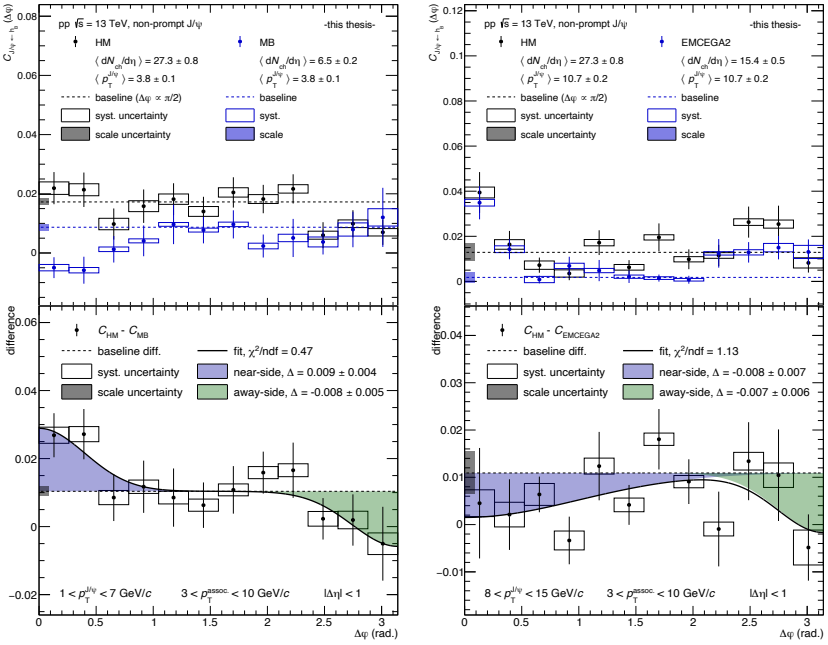

Figure 7.8.: Comparison of non-prompt J/ψ-hadron correlations in HM and MB (*left*) as well as HM and EMCal (*right*) triggered events. The near- and away-side differences are quantified by a fit and quoted.

The non-prompt J/ψ-hadron correlation functions are compared in two selected

kinematical regimes in figure 7.8. The selected windows show the largest observed differences and the remaining bins can be found in figures A.41 and A.42. Similar to the inclusive J/ψ, the HM triggered events show an indication of an excess in the near-side above minimum bias events with an approximately 2σ significance. In the case of non-prompt J/ψ, however, this excess is only observed for high p_{T} associated hadrons and can not be due to an implicit trigger bias on the non-prompt fraction. No suppression of an away-side peak in high multiplicity events can be observed since the correlation functions show no significant away-side signatures in the relevant kinematical regimes. The correlation functions in high multiplicity and EMCal triggered events agree within uncertainties.

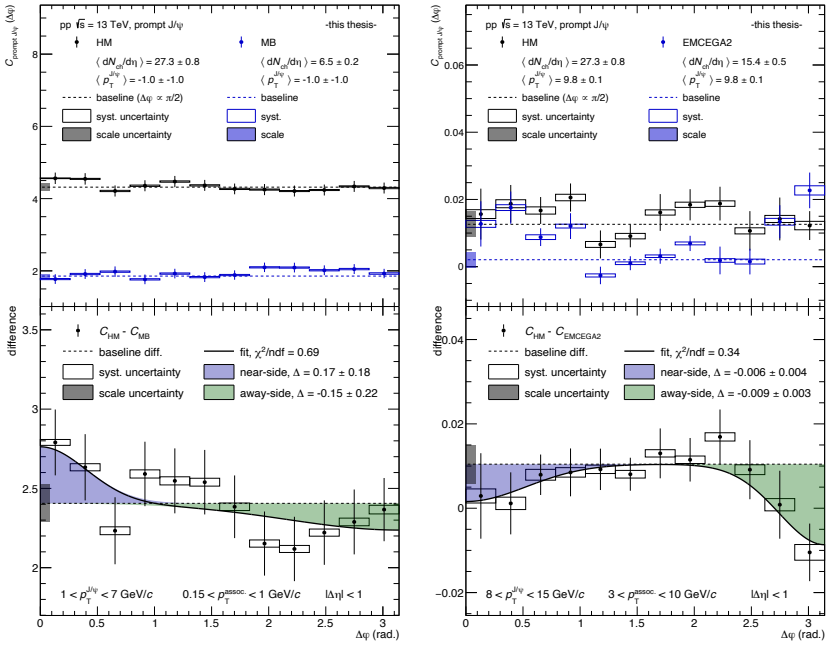

Figure 7.9.: Comparison of prompt J/ψ-hadron correlations in HM and MB (*left*) as well as HM and EMCal (*right*) triggered events. The near- and away-side differences are quantified by a fit and quoted.

Figure 7.9 shows the trigger comparison for prompt J/ψ-hadron correlations in similar kinematical regimes as presented in figure 7.8. The comparison to the MB sample, however, is displayed for low p_{T} associate hadrons. The remaining kinematical windows are shown in figure A.43 and A.44 and exhibit less significant

differences. A hint of an excess in high multiplicity over minimum bias events can again be observed in the near-side in the left panel of the figure. In contrast to the inclusive and non-prompt J/ψ, however, this excess is compatible with the baseline within uncertainties. The HM triggered sample shows a suppression in the away-side in comparison to the EMCal trigger with a significance of roughly 3σ. These features strengthen the conclusions made on the basis of the inclusive J/ψ correlation functions and could indicate a modification in high multiplicity events. In particular the away-side suppression could provide an interesting additional probe for small system studies in high multiplicity environments while the apparent near-side excess is most likely due to fluctuations. Further studies based on higher statistics data samples are needed to verify or disprove these observations.

7.2. Pseudorapidity dependence

In the previous sections, the results are only presented for $|\Delta\eta| < 1$. The correlation functions, however, inherit some dependence on the pseudorapidity range. This sensitivity is tested by variations in the $\Delta\eta$ selection, where three different choices are available: $|\Delta\eta| < 0.5$, < 1 and < 2. Figure 7.10 shows the correlation functions for inclusive J/ψ in HM and high threshold EMCal triggered events in a few exemplary kinematical windows that are favorable for the comparison. The pseudorapidity dependence can be deduced from the different ranges displayed in the figure.

The near-side peak is typically contained in a rather narrow window in pseudorapidity and larger $\Delta\eta$ ranges thus hardly increase the associated yields. This appears as a suppression in the correlation functions due to the normalization to the pseudorapidity window. The stronger collimation of associated particles with increasing p_{T} makes this effect particularly obvious at large transverse momenta. The away-side peak, conversely, is usually much broader distributed in pseudorapidity and therefore benefits from an increase in the integration range. Associated yield that is lost for smaller integration windows can thus be recovered in larger ranges. The figure clearly shows this behavior in the away-side where larger integration windows result in amplitudes that are comparable or even larger than those observed for smaller ranges.

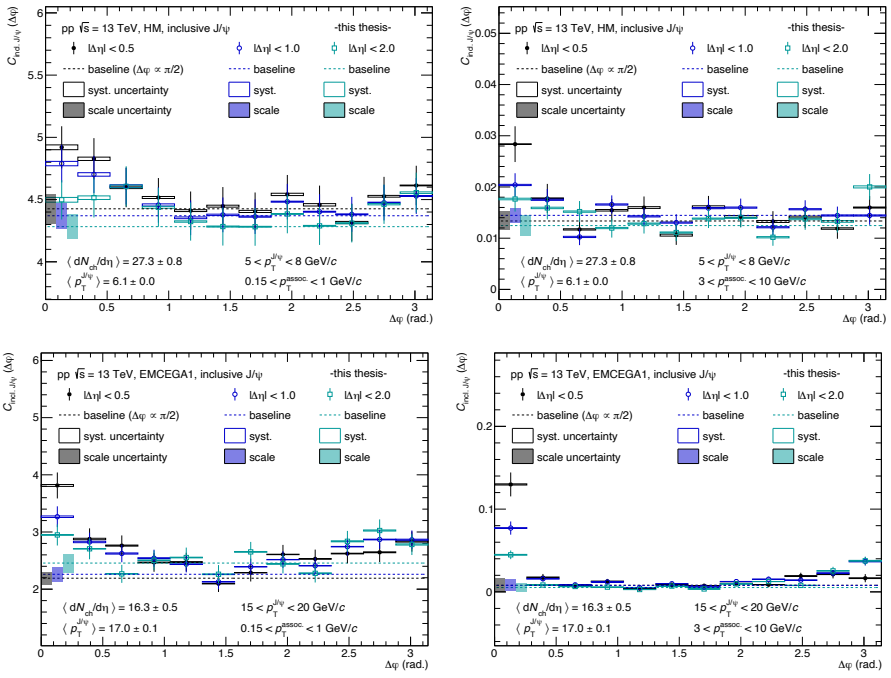

Figure 7.10.: Inclusive J/ψ-hadron correlation functions in exemplary kinematical bins and different $\Delta\eta$ ranges for HM and EMCal triggered events.

7.3. Correlated yields

In addition to the correlation functions presented in the previous sections, the extraction of the correlated yields can provide further insight into the underlying physics. Such an approach has the benefit of disentangling the different contributions to the correlation function. Namely the correlated yields in the near- and away-side can be distinguished from the uncorrelated contribution that is regarded as a baseline. This baseline provides little relevant information on the J/ψ since it is mainly attributed to the multiplicity of the underlying event. It is, of course, possible that correlated yield is distributed over such broad ranges in azimuthal angle that it can not be distinguished from the baseline. But in such cases, the data unfortunately provides no method of disentangling it from the uncorrelated contributions. The scale uncertainty on the correlation function furthermore becomes irrelevant when considering correlated yields and can be disregarded, reducing the systematic uncertainties significantly.

Two different approaches are used to determine the near- and away-side correlated yields from the correlation functions. The correlation functions can be described by the superposition of two gaussian distributions with their respective mean values fixed at $\Delta\varphi = 0$ and π, and a constant contribution attributed to the baseline. This fit approach allows to disentangle potentially broad correlation structures and the baseline of the distribution but it is limited by the fairly low number of available data points due to statistics. Additionally, a simple bin counting procedure is used where the baseline is determined at the approximate minimum of the correlation function from the average of four data points around $\Delta\varphi = \pi/2$. In either case, the correlated yields are determined separately in the near- and away-side by subtracting the baseline estimate from the integral of the fit or the correlation distribution in the bin counting method. Hereby, fixed ranges of $0 \leq \Delta\varphi \leq 1/3$ and $2\pi/3 \leq \Delta\varphi \leq \pi$ are used to allow the comparison of both methods on equal footing. This is necessary since the bin counting method is naturally restricted to the binning of the data. The fit approach, on the other hand, also provides an estimate on the width of the near- and away-side peaks from the gaussian contributions to the fit function. The yields from both methods are thus furthermore scaled to represent a 3σ range using the gaussian fit parameters. The scaling accounts for the kinematical dependencies of the near- and away-side peak widths, which are not considered in the fixed integration range.

The statistical and bin-wise systematic uncertainties are summed in quadrature before the determination of the correlated yields. The uncertainties on the yields therefore reflect the combined statistical and systematic contributions.

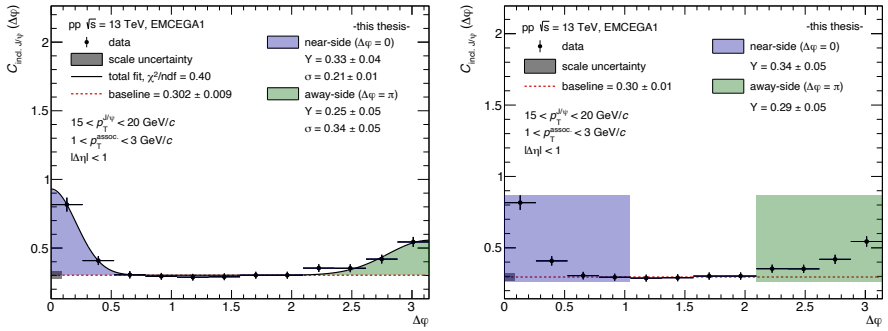

Figure 7.11.: Correlated yield extraction via fit method (*left*) and bin counting approach (*right*) for exemplary kinematical bin in high threshold EMCal triggered events. The gaussian contributions and bin counting ranges are depicted as colored areas.

An example of both approaches is shown in figure 7.11 for high threshold EMCal triggered events. The figure shows the correlation function in an exemplary kinematical bin where near- and away-side peaks are clearly visible. Further selected kinematical ranges can be found in figures A.32, A.33 and A.34 for inclusive, non-prompt and prompt J/ψ, respectively, in section A.5 in the appendix. The data is described reasonably well by the fit and the near- and away-side contributions are indicated in the figures. The right panel of figure 7.11 additionally shows the integration ranges used for the determination of the yields via bin counting as colored areas. The error bars displayed in the figures represent the combined statistical and bin-wise systematic uncertainties while the scale uncertainty is shown separately. The scale uncertainty does not affect the associated yields since it only reflects a constant up- or downward shift of the whole distribution. The figures also quote the correlated yields which agree within uncertainties for both methods. A direct comparison of the yields determined from either method can be found in figures A.35 and A.36. The yields are displayed separately for the near- and away-side at the average p_{T} of the J/ψ in the respective kinematical bin. A good agreement between the two methods can be observed over the whole kinematical range. The bin counting method, however, should only be considered

a confirmation of the results obtained from the fit method as it is less sophisticated and often yields larger uncertainties. Only the associated yields determined with the fit approach are presented and discussed in the following.

Figure 7.12 shows the correlated yields in the near-side for inclusive, non-prompt and prompt J/ψ. The data are displayed at the average p_{T} of the J/ψ and compared to predictions from PYTHIA. The yields from the simulations are hereby determined following the same procedure as used for the data, albeit in finer p_{T} bins. The near-side yields generally show a continuously increasing trend, independent of the J/ψ type or associated p_{T}. This trend exhibits a smaller slope for prompt J/ψ, which additionally show less significant yields due to the large uncertainties, particularly for low p_{T} associated hadrons. No significant difference between HM and MB or EMCal triggered events can be observed. High multiplicity events, however, show indications of larger yields for inclusive and prompt J/ψ at low transverse momenta. Nevertheless, the near-side yields at low p_{T} are negligible and agree with zero within 2 or 3σ for all J/ψ types. Significant near-side yields can be observed for inclusive and non-prompt J/ψ with $p_{\mathrm{T}} > 5$ or 8 GeV/c, depending on the transverse momentum of the associated hadrons. The PYTHIA curves reproduce the trends observed in the data reasonably well and show a similar level of agreement between MB or EMCal and HM triggered events. The predicted near-side yields for non-prompt J/ψ are larger than for prompt J/ψ, which is in agreement with the data. This can be understood in terms of the production of associated particles in the vicinity of the non-prompt J/ψ from the decay of the heavy mother particles. The trend therefore accelerates with the transverse momentum of the associated particles due to to the increasing boost, and therefore collimation, the hadrons experience.

The correlated yields in the away-side of the correlation functions are shown in figure 7.13 and compared to PYTHIA. The data is again displayed at the average p_{T} of the J/ψ in the respective kinematical window. The correlated yields at low p_{T} are in agreement with zero within 2 or 3σ and only become significant at larger transverse momenta. This is similar to the near-side yields with the exception of non-prompt J/ψ where significant yields are only observed for associated hadrons with $p_{\mathrm{T}} > 1$ GeV/c. Particularly for inclusive and prompt J/ψ, the yields in high multiplicity events are often observed to be below those in the MB or EMCal trigger samples. This might point towards a suppression or modification of the

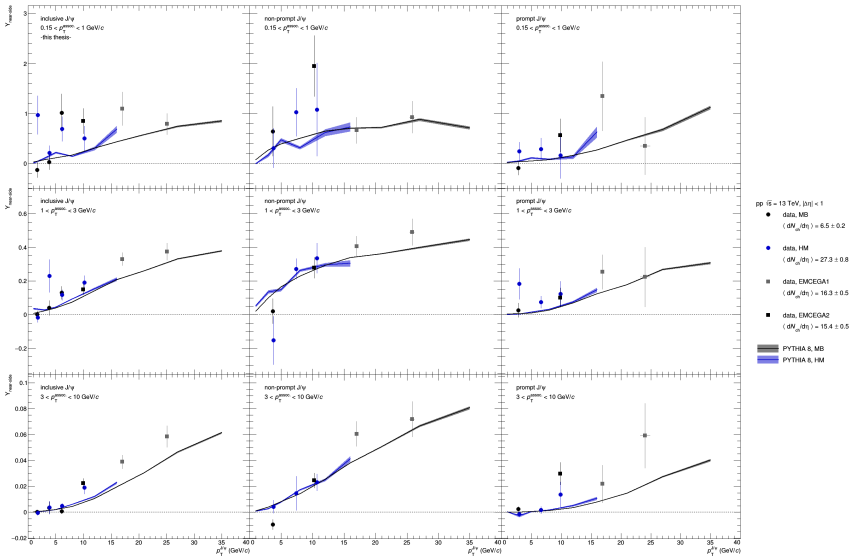

Figure 7.12.: Near-side correlated yields for inclusive (*left*), non-prompt (*center*) and prompt (*right*) J/ψ. The data are compared to PYTHIA.

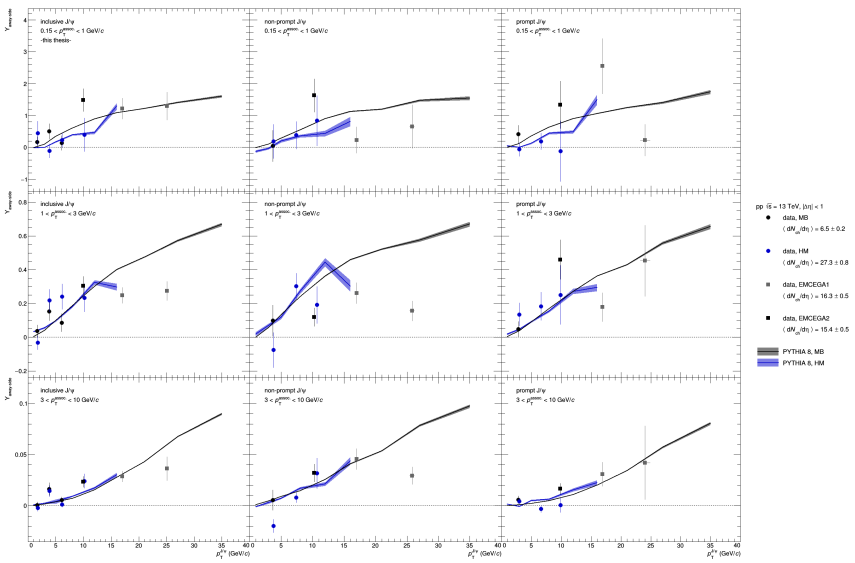

Figure 7.13.: Away-side correlated yields for inclusive (*left*), non-prompt (*center*) and prompt (*right*) J/ψ. The data are compared to PYTHIA.

correlation function in high multiplicity events. While this indication agrees with the previous observations in section 7.1, it has little to no significance due to the large uncertainties associated with the data. The PYTHIA predictions generally agree with the data within a few σ but tend to overestimate the away-side yields at larger p_{T}, particularly for non-prompt J/ψ. The prompt J/ψ do not exhibit such a behavior and it can thus be concluded that the same effect observed on the inclusive J/ψ should originate in the non-prompt component. This might point to differences in the $\mathrm{b\bar{b}}$ production but, as is discussed above, other sources of the away-side yield are also possible and should therefore be considered. The yield extraction in data is furthermore subject to considerable fluctuations and uncertainties which reduces the significance of the comparison. Future measurements based on higher statistics data samples will help to shed light on this intriguing observation.

8. Conclusion and outlook

In the analysis presented in this thesis, the inclusive, non-prompt and prompt J/ψ-hadron correlation functions are measured over a broad kinematical range in different trigger samples. Additionally, associated yields are determined and disentangled from the uncorrelated multiplicity of the underlying event. This provides a starting point for the distinction of soft and hard correlation measurements as well as more detailed studies of J/ψ production and hadronization models. While fairly large uncertainties are observed, the results prove the feasibility of the methods developed in this work and provide indications of interesting features. It is demonstrated, in particular, that the correlation functions of prompt and non-prompt J/ψ can be separated according to the procedures described above. The data was furthermore compared to results from PYTHIA simulations which can help to shed light on the J/ψ production process at generator level.

The correlation functions show no significant structures at low transverse momenta where soft correlations may extend over larger distances in the azimuthal angle. The near- and away-side signatures of the correlation functions become more prominent with increasing transverse momentum, which is corroborated by the trends observed for the correlated yields. The non-prompt J/ψ-hadron correlation functions show clear near-side peaks that qualitatively agree with the expectations from b-hadron decays or b-jet fragmentations and away-side peaks become visible at larger transverse momenta. The correlation functions for prompt J/ψ are, within uncertainties, void of significant structures even at large transverse momenta and the correlated yields are found to be lower than for non-prompt J/ψ. Near- and away-side peaks become visible at high p_{T} and might help to constrain production mechanisms but the significance of these observations is low. PYTHIA describes the data reasonably well and is able to reproduce most of the features but some differences are observed. Differences between MB and HM events can, to first order, be explained by the different event multiplicities but indications of a modification in high multiplicity environments are observed. The data seems

to suggest a modification of the away-side in high multiplicity events which is an intriguing observation that invites further investigation. More differential studies based on larger statistics samples are required to improve on the results and conclusions presented in this work.

At the time of writing, ALICE is finalizing an extensive upgrade project [111] to prepare for the upcoming restart of the LHC. During the future collision programs Run-3 and 4 of the LHC, ALICE will record integrated luminosities of around 200 pb^{-1} [112] for minimum bias proton-proton collisions at $\sqrt{s} = 14$ TeV. Dedicated triggers for rare probes can enhance the collected statistics even further. The total number of selected J/ψ mesons will increase by about a factor 10^4 [113] over the minimum bias sample used in this analysis. This increase in statistics will dramatically reduce statistical uncertainties of similar analyses by up to a factor 100 and allow for much more differential measurements. Lower uncertainties will improve the decisive power of the correlation measurement which can ultimately be useful to restrict models describing the J/ψ production mechanisms. The measurement of J/ψ-hadron correlations might also proof useful to quantify potential modifications in high multiplicity environments. The prospects for future analyses using J/ψ, amongst other probes, are described in great detail in references [112, 113].

This thesis is focussed on the analysis of so-called short-range correlations at small distances in pseudorapidity to study the J/ψ production mechanism. Measurements with a considerable pseudorapidity gap, on the other hand, can reveal long-range, global correlation signatures of the event. Such measurements are used to quantify a potential collective behavior of the system of particles created in the initial collision. Collectivity can arise in dense high multiplicity environments that exhibit a hydrodynamical evolution. An example of such systems is, amongst others, the QGP state of matter created in heavy-ion collisions. It is not clear, if similar systems can be produced in proton-proton collisions but some indications have been observed in high multiplicity events [114] and are the subject of current research. A hydrodynamical evolution of the system can yield flow signatures in the long-range correlations, whose geometric distribution can be decomposed in terms of Fourier coefficients. At low transverse momenta, the central barrel provides sufficient acceptance to reach an adequate pseudorapidity gap for the J/ψ. This is possible because of the fairly high mass that allows to

reconstruct large η values in the geometric acceptance of the detector. While a detailed study of the long-range correlations exceeds the scope of this thesis, a first look is offered in figure 8.1. The long-range correlations for inclusive J/ψ are shown in MB and HM triggered events for $1 < |\Delta\eta| < 3$, and compared to the standard short-range pseudorapidity window. The general trend of the correlation functions appears to differ between the short- and long-range windows in HM triggered events. Such an observation can not be made in the MB sample where the long-range correlations are subject to considerable fluctuations due to the limited statistics.

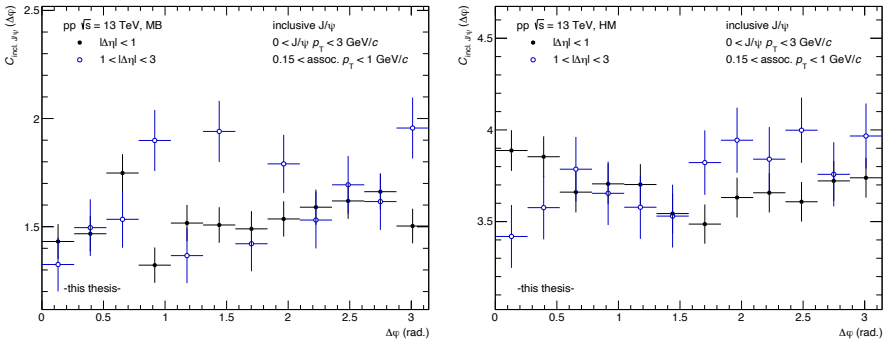

Figure 8.1.: Long-range correlations for inclusive J/ψ in MB (*left*) and HM (*right*) triggered events. The distributions are compared to the usual short-range correlation functions. Only statistical uncertainties are shown.

An analysis of the long-range correlations has been performed previously by ALICE in proton-lead collisions [115], using inclusive J/ψ mesons reconstructed in the muon arm at forward direction. According to this analysis, potential flow signatures in high multiplicity events can be revealed by removing non-collective effects via the subtraction of the long-range correlations in MB events from the HM sample. The resulting distribution only contains possible long-range correlations as well as some additional combinatorial contributions and is shown in figure 8.2. Collective anisotropic flow can, under the assumption of its existence, be quantified through a Fourier series. The long-range correlation correlation function is therefore fitted with a set of trigonometric functions. The different parameters of the full fit, p_0, p_1 and p_2, correspond to a constant baseline as well as so-called directed and elliptic flow. The directed and elliptic flow parameters describe a homogeneous or more elongated geometric evolution of the system,

respectively. Elliptic flow can, for example, originate in an inhomogeneous distribution of pressure gradients that drive the hydrodynamical evolution. The data shown in figure 8.2 is reasonably well described by the fits of the different components as well as the full function which shows a reduced χ^2 value close to one. The flow parameters p_1 and p_2 are in agreement with zero within uncertainties and no significant flow, neither directed nor elliptic, is therefore observed. This is in agreement with the measurements in proton-lead collisions, where no significant flow was observed at low transverse momenta [115]. It should be noted, that the fit parameters quoted in figure 8.2 actually do not directly correspond to the Fourier coefficients but would require an additional normalization. Nonetheless, for the purpose of this brief outlook, the impact from this additional normalization can be ignored since the conclusions are independent of constant factors. The result presented in figure 8.2 provides the first provisional measurement of such kind for J/ψ at mid-rapidity in ALICE. The long-range J/ψ correlations can then prove useful to study high multiplicity proton-proton collisions more thoroughly and complement the measurements at short-range.

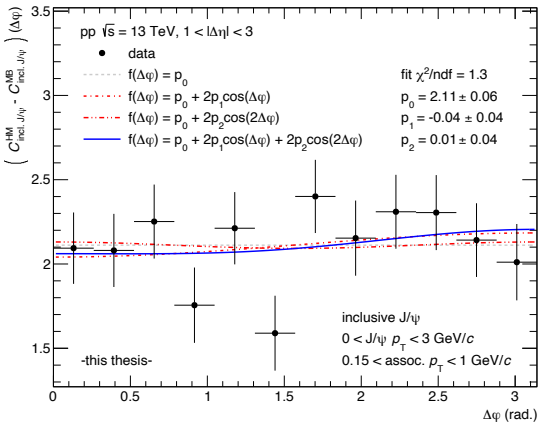

Figure 8.2.: Long-range correlations for inclusive J/ψ after low multiplicity background subtraction. The fits of the different trigonometric components are shown separately as well as the full decomposition. The parameters determined from the full fit (solid line) are quoted.

Bibliography

[1] E. Goldstein, "Ueber eine noch nicht untersuchte Strahlungsform an der Kathode inducirter Entladungen", *Annalen der Physik* **300** (1898), no. 1, 38–48, https://onlinelibrary.wiley.com/doi/pdf/10.1002/andp.18983000105.

[2] J. J. Thomson, "XL. Cathode Rays", *The London, Edinburgh, and Dublin Philosophical Magazine and Journal of Science* **44** (1897), no. 269, 293–316, https://doi.org/10.1080/14786449708621070.

[3] J. J. Thomson, "XXIV. On the structure of the atom: an investigation of the stability and periods of oscillation of a number of corpuscles arranged at equal intervals around the circumference of a circle; with application of the results to the theory of atomic structure", *The London, Edinburgh, and Dublin Philosophical Magazine and Journal of Science* **7** (1904), no. 39, 237–265, https://doi.org/10.1080/14786440409463107.

[4] E. Rutherford, "LXXIX. The scattering of α and β particles by matter and the structure of the atom", *The London, Edinburgh, and Dublin Philosophical Magazine and Journal of Science* **21** (1911), no. 125, 669–688, https://doi.org/10.1080/14786440508637080.

[5] N. Bohr, "I. On the constitution of atoms and molecules", *The London, Edinburgh, and Dublin Philosophical Magazine and Journal of Science* **26** (1913), no. 151, 1–25, https://doi.org/10.1080/14786441308634955.

[6] E. Rutherford, "LIV. Collision of α particles with light atoms. IV. An anomalous effect in nitrogen", *The London, Edinburgh, and Dublin Philosophical Magazine and Journal of Science* **37** (1919), no. 222, 581–587, https://doi.org/10.1080/14786440608635919.

[7] M. Gell-Mann, "The Eightfold Way: A Theory of strong interaction symmetry", Mar 1961, https://doi.org/10.2172/4008239.

[8] G. Zweig, "An SU_3 model for strong interaction symmetry and its breaking; Version 1", Tech. Rep. CERN-TH-401, CERN, Jan 1964.

[9] J. I. Friedman and H. W. Kendall, "Deep Inelastic Electron Scattering", *Annual Review of Nuclear Science* **22** (1972), no. 1, 203–254, https://doi.org/10.1146/annurev.ns.22.120172.001223.

[10] R. P. Feynman, "The behavior of hadron collisions at extreme energies", *Conf. Proc.* **C690905** (1969) 237–258.

[11] J. E. Augustin *et al.*, "Discovery of a Narrow Resonance in e^+e^- Annihilation", *Phys. Rev. Lett.* **33** Dec (1974) 1406–1408.

[12] J. J. Aubert *et al.*, "Experimental Observation of a Heavy Particle J", *Phys. Rev. Lett.* **33** Dec (1974) 1404–1406.

[13] B. Bjorken and S. Glashow, "Elementary particles and SU(4)", *Physics Letters* **11** (1964), no. 3, 255 – 257.

[14] S. L. Glashow, J. Iliopoulos, and L. Maiani, "Weak Interactions with Lepton-Hadron Symmetry", *Phys. Rev. D* **2** Oct (1970) 1285–1292.

[15] S. W. Herb *et al.*, "Observation of a Dimuon Resonance at 9.5 GeV in 400-GeV Proton-Nucleus Collisions", *Phys. Rev. Lett.* **39** Aug (1977) 252–255.

[16] **CDF**, F. Abe *et al.*, "Observation of Top Quark Production in $\overline{p}p$ Collisions with the Collider Detector at Fermilab", *Phys. Rev. Lett.* **74** Apr (1995) 2626–2631.

[17] **D0**, S. Abachi *et al.*, "Search for High Mass Top Quark Production in $p\overline{p}$ collisions at $\sqrt{s} =$ 1.8 TeV", *Phys. Rev. Lett.* **74** Mar (1995) 2422–2426.

[18] **UA1**, G. Arnison *et al.*, "Experimental observation of isolated large transverse energy electrons with associated missing energy at s=540 GeV", *Physics Letters B* **122** (1983), no. 1, 103 – 116.

[19] **UA2**, M. Banner *et al.*, "Observation of single isolated electrons of high transverse momentum in events with missing transverse energy at the CERN $\bar{\text{p}}$p collider", *Physics Letters B* **122** (1983), no. 5, 476 – 485.

[20] **UA1**, G. Arnison *et al.*, "Experimental Observation of Lepton Pairs of Invariant Mass Around 95-GeV/c**2 at the CERN SPS Collider", *Phys. Lett. B* **126** (1983) 398–410.

[21] **UA2**, P. Bagnaia *et al.*, "Evidence for $Z^0 \to e^+e^-$ at the CERN $\bar{p}p$ Collider", *Phys. Lett. B* **129** (1983) 130–140.

[22] **ATLAS**, G. Aad *et al.*, "Observation of a new particle in the search for the Standard Model Higgs boson with the ATLAS detector at the LHC", *Phys. Lett.* **B716** (2012) 1–29, arXiv:1207.7214.

[23] **CMS**, S. Chatrchyan *et al.*, "Observation of a New Boson at a Mass of 125 GeV with the CMS Experiment at the LHC", *Phys. Lett.* **B716** (2012) 30–61, arXiv:1207.7235.

[24] A. Deur, S. J. Brodsky, and G. F. de Teramond, "The QCD Running Coupling", *Prog. Part. Nucl. Phys.* **90** (2016) 1–74, arXiv:1604.08082.

[25] **CMS**, V. Khachatryan *et al.*, "Constraints on parton distribution functions and extraction of the strong coupling constant from the inclusive jet cross section in pp collisions at $\sqrt{s} = 7$ TeV", *Eur. Phys. J.* **C75** (2015), no. 6, 288, arXiv:1410.6765.

[26] K. G. Wilson, "Confinement of quarks", *Phys. Rev. D* **10** Oct (1974) 2445–2459.

[27] G. F. Sterman, "QCD and jets", in "Physics in D >= 4. Proceedings, Theoretical Advanced Study Institute in elementary particle physics, TASI 2004, Boulder, USA, June 6-July 2, 2004", pp. 67–145. 2004. arXiv:hep-ph/0412013.

[28] S. Bethke, "The 2009 World Average of alpha(s)", *Eur. Phys. J. C* **64** (2009) 689–703, arXiv:0908.1135.

[29] D. J. Gross and F. Wilczek, "Ultraviolet Behavior of Nonabelian Gauge Theories", *Phys. Rev. Lett.* **30** (1973)a 1343–1346.

[30] D. J. Gross and F. Wilczek, "Asymptotically Free Gauge Theories. I", *Phys. Rev. D* **8** Nov (1973)b 3633–3652.

[31] H. Politzer, "Reliable Perturbative Results for Strong Interactions?", *Phys. Rev. Lett.* **30** (1973) 1346–1349.

[32] J. L. Kneur and A. Neveu, "$\Lambda^{\rm QCD}_{\overline{\rm MS}}$ from Renormalization Group Optimized Perturbation", *Phys. Rev.* **D85** (2012) 014005, arXiv:1108.3501.

[33] **Particle Data Group**, M. Tanabashi *et al.*, "Review of particle physics", *Phys. Rev. D* **98** Aug (2018) 030001.

[34] M. Thomson, "Modern particle physics", Cambridge University Press, New York, 2013.

[35] N. Brambilla *et al.*, "Heavy Quarkonium: Progress, Puzzles, and Opportunities", *Eur. Phys. J.* **C71** (2011) 1534, arXiv:1010.5827.

[36] H. S. Chung, "Review of quarkonium production: status and prospects", in "13th Conference on Quark Confinement and the Hadron Spectrum (Confinement XIII) Maynooth, Ireland, July 31-August 6, 2018". 2018. arXiv:1811.12098.

[37] S. Okubo, "ϕ-meson and unitary symmetry model", *Physics Letters* **5** (1963), no. 2, 165 – 168.

[38] J. Iizuka, "A Systematics and Phenomenology of Meson Family*", *Progress of Theoretical Physics Supplement* **37-38** 03 (1966) 21–34.

[39] **ALICE**, S. Acharya *et al.*, "Measurement of the inclusive J/ψ polarization at forward rapidity in pp collisions at $\sqrt{s} = 8$ TeV", *The European Physical Journal C* **78** Jul (2018) 562.

[40] F. Halzen, "CVC for gluons and hadroproduction of quark flavours", *Physics Letters B* **69** (1977), no. 1, 105 – 108.

[41] H. Fritzsch, "Producing heavy quark flavors in hadronic collisions-' A test of quantum chromodynamics", *Physics Letters B* **67** (1977), no. 2, 217 – 221.

[42] J. Amundson, O. Éboli, E. Gregores, and F. Halzen, "Quantitative tests of color evaporation: charmonium production", *Physics Letters B* **390** (1997), no. 1, 323 – 328.

[43] G. T. Bodwin, E. Braaten, and J. Lee, "Comparison of the color-evaporation model and the NRQCD factorization approach in charmonium production", *Phys. Rev.* **D72** (2005) 014004, arXiv:hep-ph/0504014.

[44] V. Cheung and R. Vogt, "Production and polarization of prompt J/ψ in the improved color evaporation model using the k_T-factorization approach", *Phys. Rev. D* **98** Dec (2018) 114029.

[45] **ALICE**, S. Acharya *et al.*, "Energy dependence of forward-rapidity J/ψ ψ(2S) production in pp collisions at the LHC", *Eur. Phys. J.* **C77** (2017), no. 6, 392, arXiv:1702.00557.

[46] M. B. Einhorn and S. D. Ellis, "Hadronic production of the new resonances: Probing gluon distributions", *Phys. Rev. D* **12** Oct (1975) 2007–2014.

[47] C. E. Carlson and R. Suaya, "Hadronic production of the $\frac{\psi}{J}$ meson", *Phys. Rev. D* **14** Dec (1976) 3115–3121.

[48] R. Baier and R. Rückl, "Hadronic production of J/ψ and γ: Transverse momentum distributions", *Physics Letters B* **102** (1981), no. 5, 364 – 370.

[49] **ALICE**, B. Abelev *et al.*, "Measurement of quarkonium production at forward rapidity in pp collisions at $\sqrt{s} = 7$ TeV", *The European Physical Journal C* **74** Aug (2014) 2974.

[50] G. T. Bodwin, E. Braaten, and G. P. Lepage, "Rigorous QCD analysis of inclusive annihilation and production of heavy quarkonium", *Phys. Rev.* **D51** (1995) 1125–1171, arXiv:hep-ph/9407339, [Erratum: Phys. Rev. D55, 5853 (1997)].

[51] **ALICE**, S. Acharya *et al.*, "Inclusive J/ψ production at mid-rapidity in pp collisions at $\sqrt{s} = 5.02$ TeV", arXiv:1905.07211.

[52] M. Cacciari, M. Greco, and P. Nason, "The pT spectrum in heavy-flavor hadroproduction", *JHEP* **05** (1998) 007, arXiv:hep-ph/9803400.

[53] M. Cacciari, S. Frixione, and P. Nason, "The pT spectrum in heavy-flavor photoproduction", *JHEP* **03** (2001) 006, arXiv:hep-ph/0102134.

[54] Z.-B. Kang, Y.-Q. Ma, and R. Venugopalan, "Quarkonium production in high energy proton-nucleus collisions: CGC meets NRQCD", *JHEP* **01** (2014) 056, arXiv:1309.7337.

[55] P. Braun-Munzinger and J. Stachel, "The quest for the quark-gluon plasma", *Nature* **448** (2007) 302–309.

[56] B.-J. Schaefer and M. Wagner, "On the QCD phase structure from effective models", *Prog. Part. Nucl. Phys.* **62** (2009) 381, arXiv:0812.2855.

[57] CERN Press release, "New State of Matter created at CERN". https://home.cern/news/press-release/cern/new-state-matter-created-cern, 2000. [Online; accessed 23-August-2020].

[58] R. Fries and B. Müller, "Heavy ions at LHC: Theoretical issues", *The European Physical Journal C - Particles and Fields* **34** Jul (2004) s279–s285.

[59] M. G. Alford, A. Schmitt, K. Rajagopal, and T. Schäfer, "Color superconductivity in dense quark matter", *Rev. Mod. Phys.* **80** (2008) 1455–1515, arXiv:0709.4635.

[60] M. Baldo, M. Buballa, F. Burgio, F. Neumann, M. Oertel, and H. J. Schulze, "Neutron stars and the transition to color superconducting quark matter", *Phys. Lett.* **B562** (2003) 153–160, arXiv:nucl-th/0212096.

[61] T. Matsui and H. Satz, "J/ψ Suppression by Quark-Gluon Plasma Formation", *Phys. Lett.* **B178** (1986) 416–422.

[62] F. Karsch and H. Satz, "The Spectral analysis of strongly interacting matter", *Z. Phys.* **C51** (1991) 209–224.

[63] S. Digal, P. Petreczky, and H. Satz, "Quarkonium feed-down and sequential suppression", *Phys. Rev. D* **64** Oct (2001) 094015.

[64] **PHENIX**, A. Adare *et al.*, "J/ψ suppression at forward rapidity in Au + Au collisions at $\sqrt{s_{NN}} = 200$ GeV", *Phys. Rev. C* **84** Nov (2011) 054912.

[65] **ALICE**, J. Adam *et al.*, "Differential studies of inclusive J/ψ and ψ(2S) production at forward rapidity in Pb-Pb collisions at $\sqrt{s_{\rm NN}} = 2.76$ TeV", *Journal of High Energy Physics* **2016** May (2016) 179.

[66] A. Andronic, P. Braun-Munzinger, K. Redlich, and J. Stachel, "The thermal model on the verge of the ultimate test: particle production in Pb-Pb collisions at the LHC", *J. Phys.* **G38** (2011) 124081, arXiv:1106.6321.

[67] X. Zhao and R. Rapp, "Medium Modifications and Production of Charmonia at LHC", *Nucl. Phys.* **A859** (2011) 114–125, arXiv:1102.2194.

[68] K. Zhou, N. Xu, Z. Xu, and P. Zhuang, "Medium effects on charmonium production at ultrarelativistic energies available at the CERN Large Hadron Collider", *Phys. Rev.* **C89** (2014), no. 5, 054911, arXiv:1401.5845.

[69] E. G. Ferreiro, "Charmonium dissociation and recombination at LHC: Revisiting comovers", *Phys. Lett.* **B731** (2014) 57–63, arXiv:1210.3209.

[70] **ALICE**, K. Aamodt *et al.*, "The ALICE experiment at the CERN LHC", *JINST* **3** (2008) S08002.

[71] **ALICE**, B. B. Abelev *et al.*, "Performance of the ALICE Experiment at the CERN LHC", *Int. J. Mod. Phys.* **A29** (2014) 1430044, arXiv:1402.4476.

[72] L. Evans and P. Bryant, "LHC Machine", *Journal of Instrumentation* **3** Aug (2008) S08001–S08001.

[73] C. Lefèvre, "The CERN accelerator complex. Complexe des accélérateurs du CERN", Dec 2008, unpublished. https://cds.cern.ch/record/1260465

[74] CERN, "The accelerator complex". http://cds.cern.ch/record/1997193, Jan 2012. [Online; accessed 21-August-2020].

[75] M. Benedikt, P. Collier, V. Mertens, J. Poole, and K. Schindl, "LHC Design Report. 3. The LHC injector chain", 2004.

[76] **ALICE**, "Alice figure repository". `https://alice-figure.web.cern.ch`. [Online; accessed 23-August-2020].

[77] **ALICE**, E. Abbas *et al.*, "Performance of the ALICE VZERO system", *JINST* **8** (2013) P10016, `arXiv:1306.3130`.

[78] **ALICE**, G. Dellacasa *et al.*, "ALICE time projection chamber: Technical Design Report", Tech. Rep. CERN-LHCC-2000-001, 2000.

[79] J. Alme *et al.*, "The ALICE TPC, a large 3-dimensional tracking device with fast readout for ultra-high multiplicity events", *Nuclear Instruments and Methods in Physics Research Section A: Accelerators, Spectrometers, Detectors and Associated Equipment* **622** (2010), no. 1, 316 – 367.

[80] **ALICE**, P. Cortese *et al.*, "ALICE Electromagnetic Calorimeter Technical Design Report", Tech. Rep. CERN-LHCC-2008-014, CERN-ALICE-TDR-14, 2008.

[81] **ALICE**, J. Allen *et al.*, "ALICE DCal: An Addendum to the EMCal Technical Design Report Di-Jet and Hadron-Jet correlation measurements in ALICE", Tech. Rep. CERN-LHCC-2010-011. ALICE-TDR-14-add-1, Jun 2010.

[82] **ALICE**, U. Abeysekara *et al.*, "ALICE EMCal Physics Performance Report", `arXiv:1008.0413`.

[83] **ALICE**, P. Saiz, L. Aphecetche, P. Buncic, R. Piskac, J. E. Revsbech, and V. Sego, "AliEn - ALICE environment on the GRID", *Nucl. Instrum. Meth.* **A502** (2003) 437–440.

[84] **ALICE**, P. Cortese, F. Carminati, C. W. Fabjan, L. Riccati, and H. de Groot, "ALICE computing: Technical Design Report", CERN, 2005. Submitted on 15 Jun 2005.

[85] **ALICE**, "AliRoot software repository". `https://github.com/alisw/AliRoot`, [Online; accessed 20-August-2020].

[86] **ALICE**, "AliPhysics software repository". `https://github.com/alisw/AliPhysics`, [Online; accessed 21-August-2020].

[87] R. Brun and F. Rademakers, "ROOT - An object oriented data analysis framework", *Nuclear Instruments and Methods in Physics Research Section A: Accelerators, Spectrometers, Detectors and Associated Equipment* **389** (1997), no. 1, 81 – 86, New Computing Techniques in Physics Research V.

[88] T. Sjostrand, S. Mrenna, and P. Z. Skands, "PYTHIA 6.4 Physics and Manual", *JHEP* **05** (2006) 026, `arXiv:hep-ph/0603175`.

[89] T. Sjostrand, S. Mrenna, and P. Z. Skands, "A Brief Introduction to PYTHIA 8.1", *Comput. Phys. Commun.* **178** (2008) 852–867, `arXiv:0710.3820`.

[90] R. Brun, F. Bruyant, M. Maire, A. C. McPherson, and P. Zanarini, "GEANT3", 1987, CERN-DD-EE-84-1.

[91] **GEANT4**, S. Agostinelli *et al.*, "GEANT4: A Simulation toolkit", *Nucl. Instrum. Meth.* **A506** (2003) 250–303.

[92] J. Allison *et al.*, "Geant4 developments and applications", *IEEE Trans. Nucl. Sci.* **53** (2006) 270.

[93] **ALICE**, Data Preparation Group, "List of good runs for Run2 periods". `https://twiki.cern.ch/twiki/bin/view/ALICE/AliDPGRunLists`. [Online; accessed 18-August-2020].

[94] **ALICE**, S. Acharya *et al.*, "Multiplicity dependence of J/ψ production at midrapidity in pp collisions at $\sqrt{s} = 13$ TeV", *Phys. Lett.* **B** (2020) 135758, `arXiv:2005.11123`.

[95] **ALICE**, "The ALICE definition of primary particles", Jun 2017. `https://cds.cern.ch/record/2270008`

[96] E. Barberio, B. van Eijk, and Z. Was, "PHOTOS: A Universal Monte Carlo for QED radiative corrections in decays", *Comput. Phys. Commun.* **66** (1991) 115–128.

[97] **ALICE**, J. Adam *et al.*, "Pseudorapidity and transverse-momentum distributions of charged particles in proton-proton collisions at $\sqrt{s} = 13$ TeV", *Phys. Lett.* **B753** (2016) 319–329, arXiv:1509.08734.

[98] **ALICE**, J. Adam *et al.*, "Measurement of charm and beauty production at central rapidity versus charged-particle multiplicity in proton-proton collisions at $\sqrt{s} = 7$ TeV", *JHEP* **09** (2015) 148, arXiv:1505.00664.

[99] **ALICE**, S. Acharya *et al.*, "Prompt and non-prompt J/ψ production and nuclear modification at mid-rapidity in p-Pb collisions at $\sqrt{s_{\rm NN}} = 5.02$ TeV", *Eur. Phys. J. C* **78** (2018), no. 6, 466, arXiv:1802.00765.

[100] **ALICE**, "Fraction of J/ψ from beauty hadron decays in pp at 13 TeV compared to lower energy results". http://alice-figure.web.cern.ch/node/16186. [Online; accessed 6-August-2020].

[101] **ATLAS**, "Measurement of the differential non-prompt J/ψ production fraction in $\sqrt{s} = 13$ TeV pp collisions at the ATLAS experiment", Tech. Rep. ATLAS-CONF-2015-030, CERN, Jul 2015.

[102] **ALICE**, J. Adam *et al.*, "Inclusive, prompt and non-prompt J/ψ production at mid-rapidity in Pb-Pb collisions at $\sqrt{s_{\rm NN}} = 2.76$ TeV", *JHEP* **07** (2015) 051, arXiv:1504.07151.

[103] M. Cacciari, S. Frixione, N. Houdeau, M. L. Mangano, P. Nason, and G. Ridolfi, "Theoretical predictions for charm and bottom production at the LHC", *JHEP* **10** (2012) 137, arXiv:1205.6344.

[104] M. Cacciari, M. L. Mangano, and P. Nason, "Gluon PDF constraints from the ratio of forward heavy-quark production at the LHC at $\sqrt{S} = 7$ and 13 TeV", *Eur. Phys. J.* **C75** (2015), no. 12, 610, arXiv:1507.06197.

[105] F. Bossu, Z. C. del Valle, A. de Falco, M. Gagliardi, S. Grigoryan, and G. Martinez Garcia, "Phenomenological interpolation of the inclusive J/ψ cross section to proton-proton collisions at 2.76 TeV and 5.5 TeV", arXiv:1103.2394.

[106] **CMS**, V. Khachatryan *et al.*, "Measurement of Long-Range Near-Side Two-Particle Angular Correlations in *pp* Collisions at $\sqrt{s} = 13$ TeV", *Phys. Rev. Lett.* **116** Apr (2016) 172302.

[107] **ALICE**, Data Preparation Group, "Systematic uncertainties on TPC-ITS matching in various Run-2 data samples". `https://twiki.cern.ch/twiki/bin/viewauth/ALICE/AliDPGtoolsTrackSystematicUncertaintyBookkeping`. [Online; accessed 12-August-2020].

[108] P. Skands, S. Carrazza, and J. Rojo, "Tuning PYTHIA 8.1: the Monash 2013 Tune", *Eur. Phys. J. C* **74** (2014), no. 8, 3024, `arXiv:1404.5630`.

[109] **CMS**, A. M. Sirunyan *et al.*, "Study of J/ψ meson production inside jets in pp collisions at $\sqrt{s} = 8$ TeV", *Phys. Lett. B* **804** (2020) 135409, `arXiv:1910.01686`.

[110] **CMS**, B. Diab, "Fragmentation of J/ψ in jets in pp collisions at $\sqrt{s} = 5.02$ TeV", *Nucl. Phys. A* **982** (2019) 186–188.

[111] **ALICE**, B. Abelev *et al.*, "Upgrade of the ALICE Experiment: Letter Of Intent", *J. Phys. G* **41** (2014) 087001.

[112] **ALICE**, "ALICE upgrade physics performance studies for 2018 Report on HL/HE-LHC physics", Feb 2019. `https://cds.cern.ch/record/2661798`

[113] **ALICE**, "Future high-energy pp programme with ALICE", Jul 2020. `https://cds.cern.ch/record/2724925`

[114] **CMS**, V. Khachatryan *et al.*, "Measurement of long-range near-side two-particle angular correlations in pp collisions at $\sqrt{s}$ =13 TeV", *Phys. Rev. Lett.* **116** (2016), no. 17, 172302, `arXiv:1510.03068`.

[115] **ALICE**, S. Acharya *et al.*, "Search for collectivity with azimuthal J/ψ-hadron correlations in high multiplicity p-Pb collisions at $\sqrt{s_{\rm NN}}$ = 5.02 and 8.16 TeV", *Phys. Lett. B* **780** (2018) 7–20, `arXiv:1709.06807`.

A. Additional figures

A.1. Electron-positron pair selection

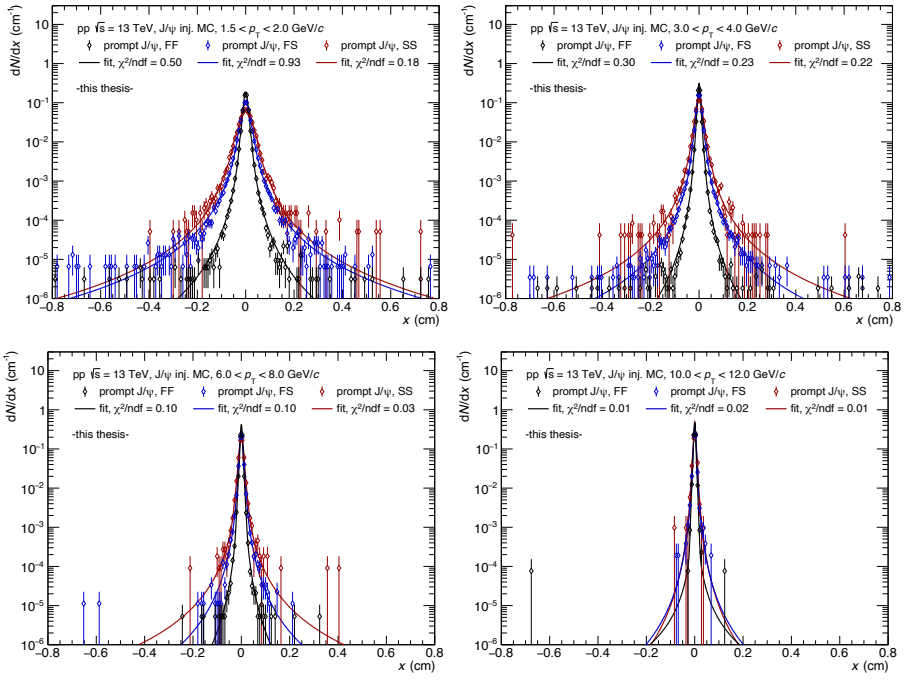

Figure A.1.: Decay length distributions for prompt J/ψ and fits to the distributions.

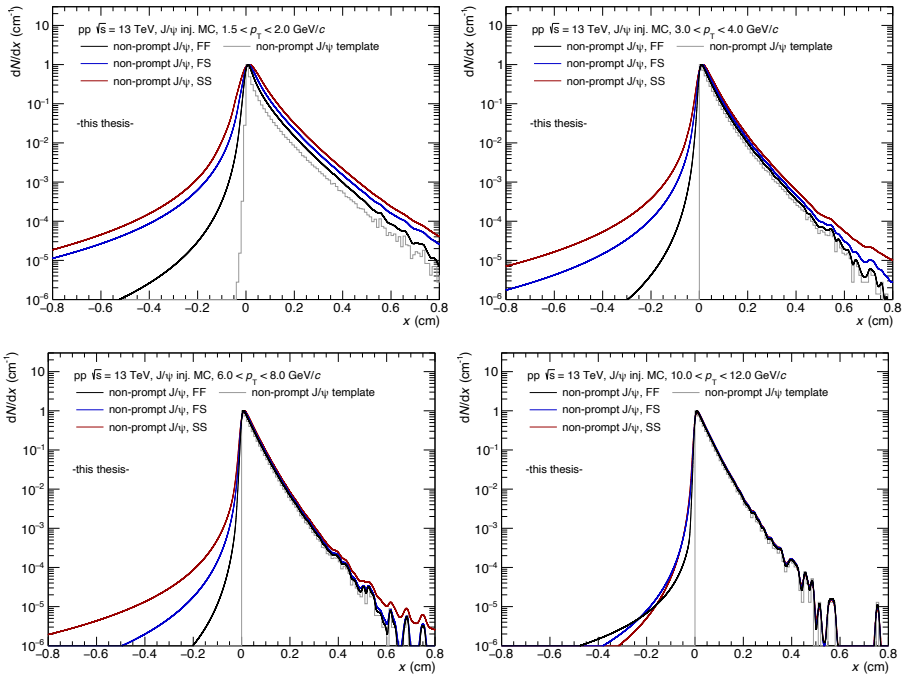

Figure A.2.: Decay length distributions for non-prompt J/ψ, normalized to a maximum of one for better comparison.

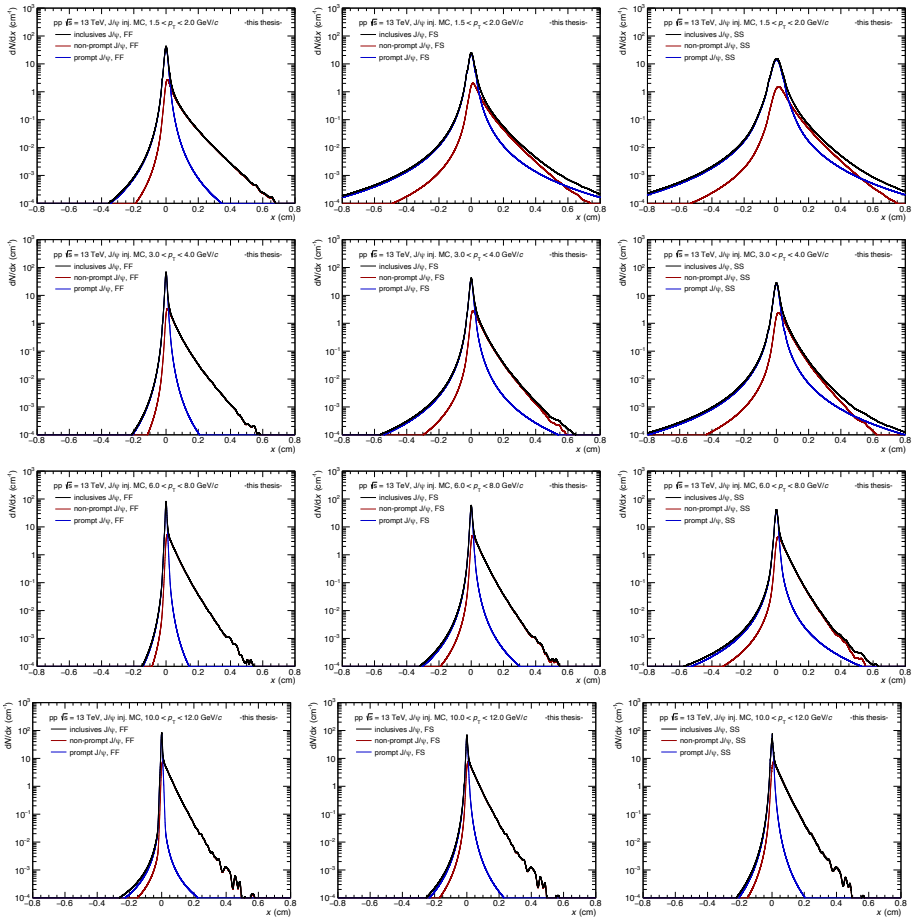

Figure A.3.: Inclusive, prompt and non-prompt J/ψ decay length distributions for FF (*left*), FS (*center*) and SS (*right*) pairs. The prompt and non-prompt distributions are probability-density functions multiplied with f_B and $(1 - f_B)$, respectively. The inclusive distribution is the sum of the prompt and non-prompt components.

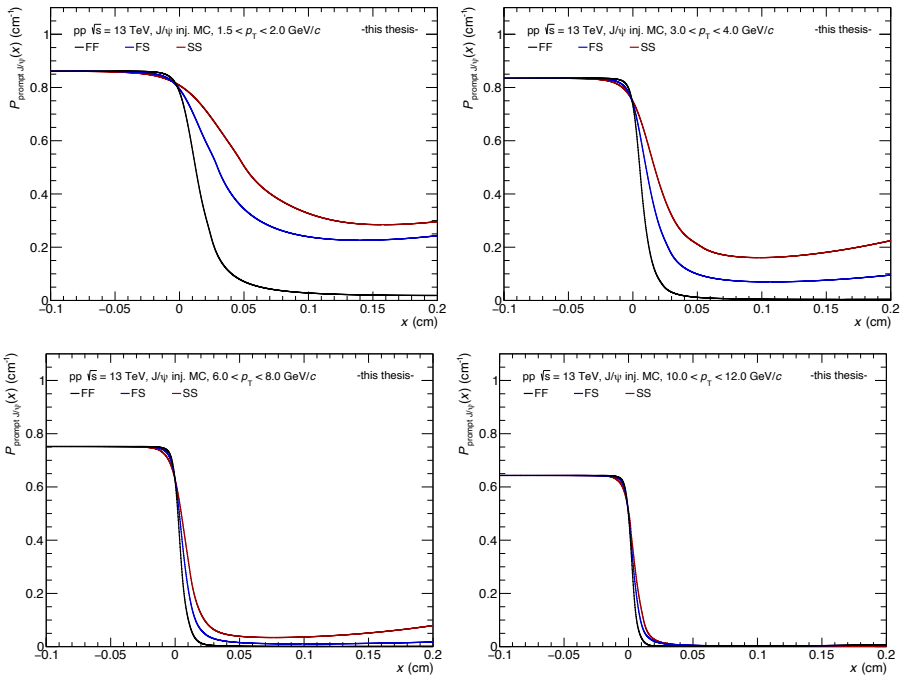

Figure A.4.: Cumulative fraction of prompt J/ψ according to equation 5.5 for FF, FS and SS pairs.

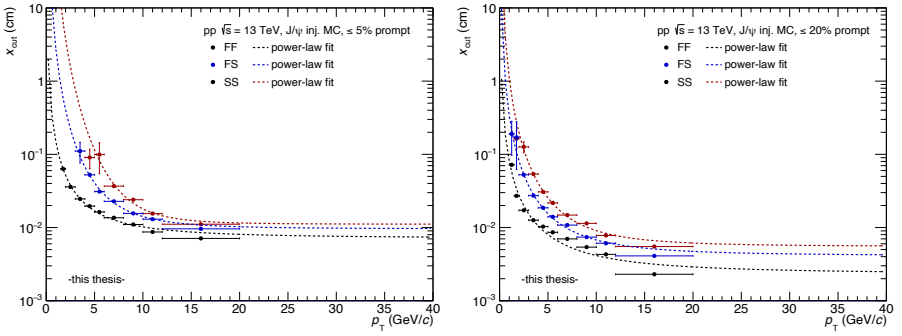

Figure A.5.: Decay length cuts as determined for 5% (*left*) and 20% (*right*) contamination of surviving prompt J/ψ. A power-law fit to the cut values is also displayed separately for the different SPD pair types.

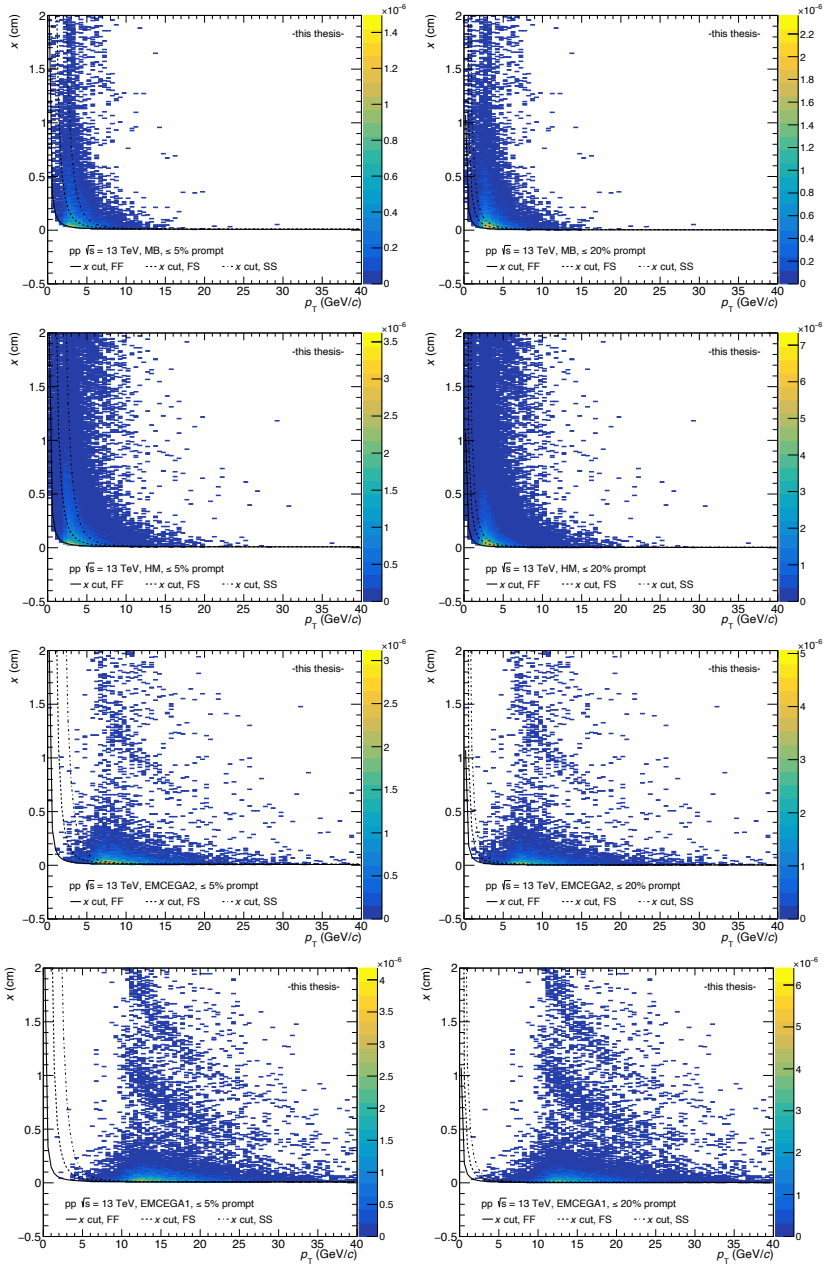

Figure A.6.: Decay length distributions for selected non-prompt J/ψ candidates in MB (*top row*), HM (*second row from the top*), and EMCal (*bottom two rows*) triggered events. The cuts for the different SPD pair types are also displayed and the distributions are shown for 5% (*left*) and 20% (*right*) contamination of surviving prompt J/ψ.

A.2. J/ψ reconstruction

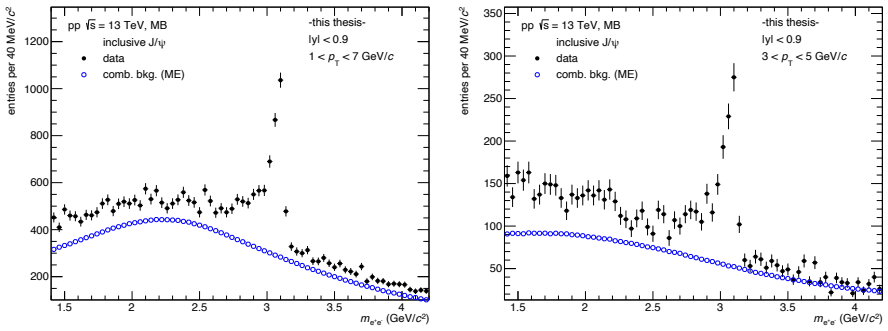

Figure A.7.: Invariant mass distributions for selected electron-positron pairs and combinatorial background from event mixing in the MB triggered sample.

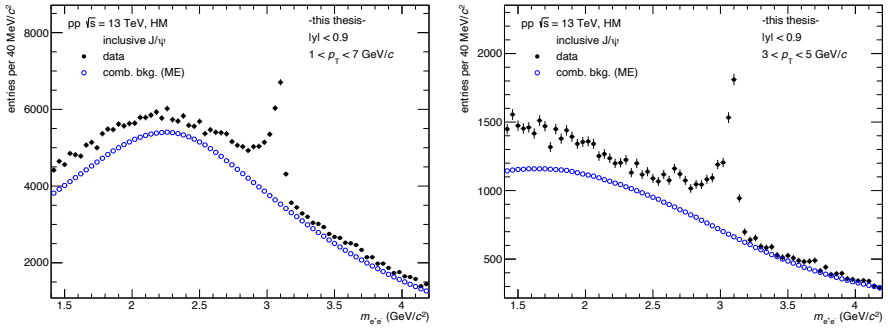

Figure A.8.: Invariant mass distributions for selected electron-positron pairs and combinatorial background from event mixing in the HM triggered sample.

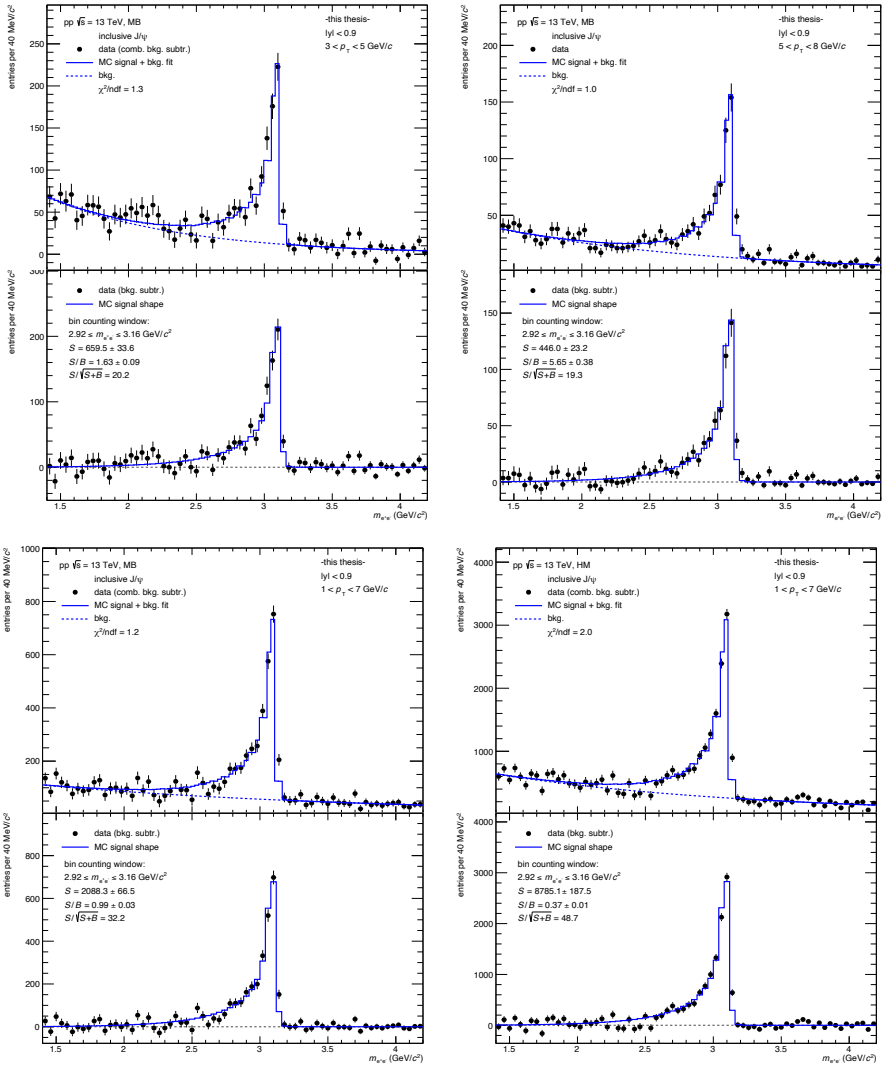

Figure A.9.: Fit to (residual) background and inclusive J/ψ signal after background subtraction for MB (*top, bottom left*) and HM (*bottom right*) triggered events.

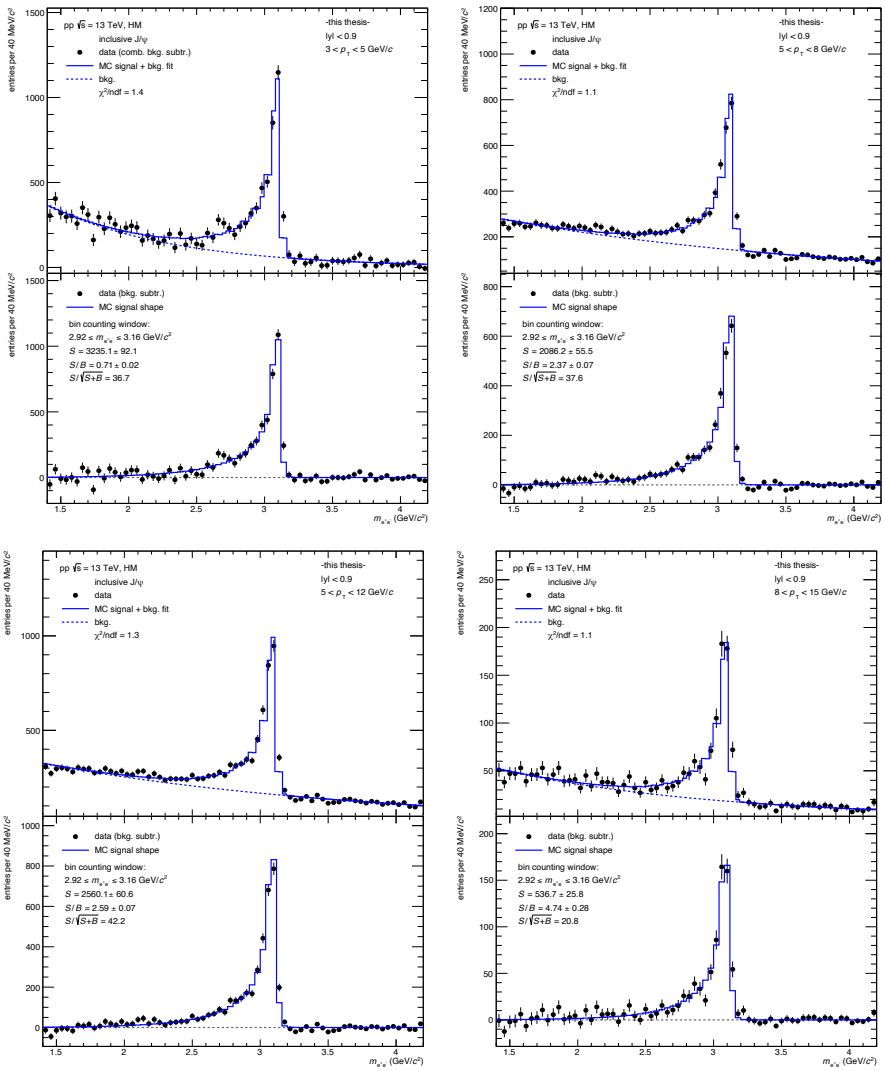

Figure A.10.: Fit to (residual) background and inclusive J/ψ signal after background subtraction for HM triggered events.

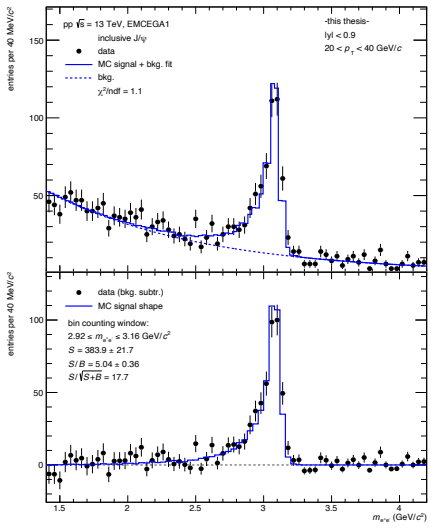

Figure A.11.: Fit to (residual) background and inclusive J/ψ signal after background subtraction for high threshold EMCal triggered events.

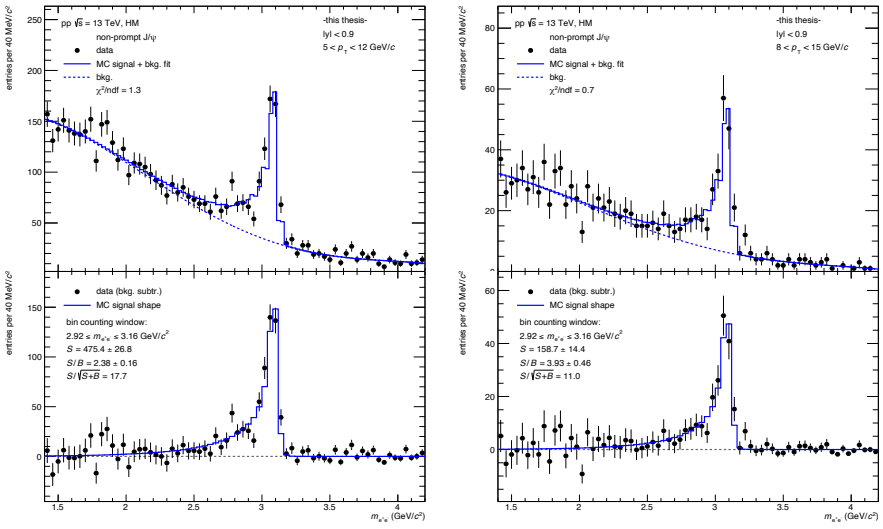

Figure A.12.: Fit to background and non-prompt J/ψ signal after background subtraction for HM triggered events.

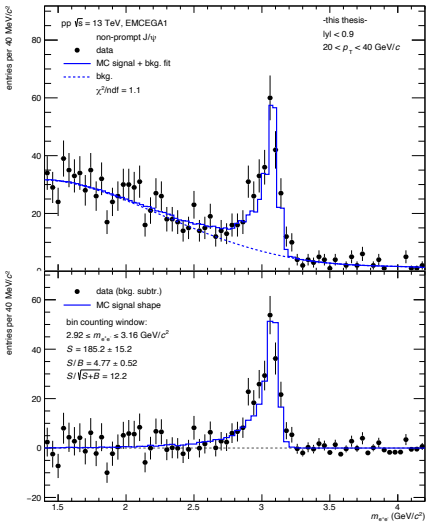

Figure A.13.: Fit to background and non-prompt J/ψ signal after background subtraction for high threshold EMCal triggered events.

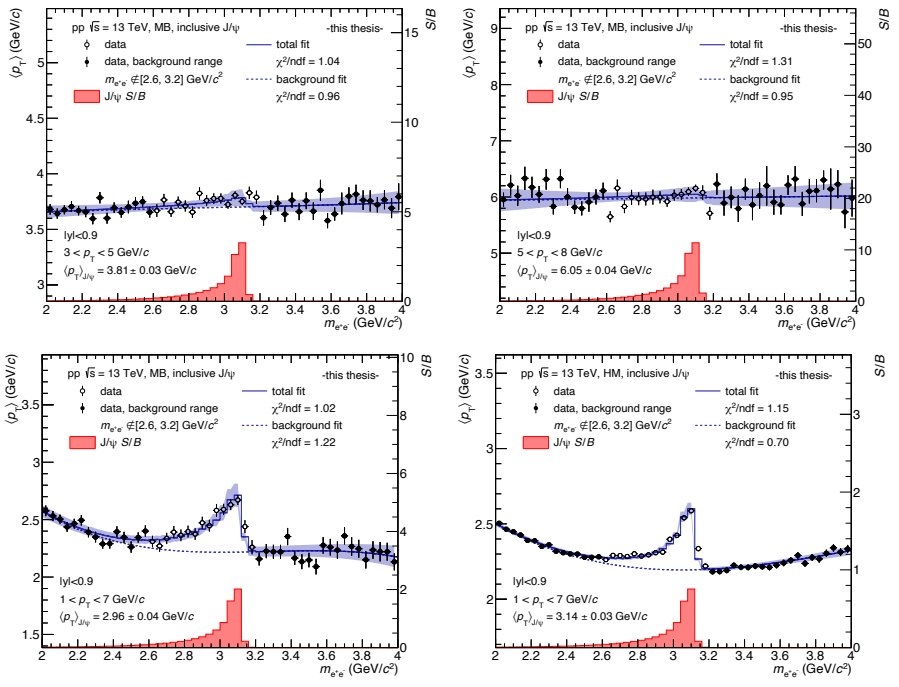

Figure A.14.: Mean p_{T} determination for inclusive J/ψ in MB (*top*, *bottom left*) and HM (*bottom right*) triggered events.

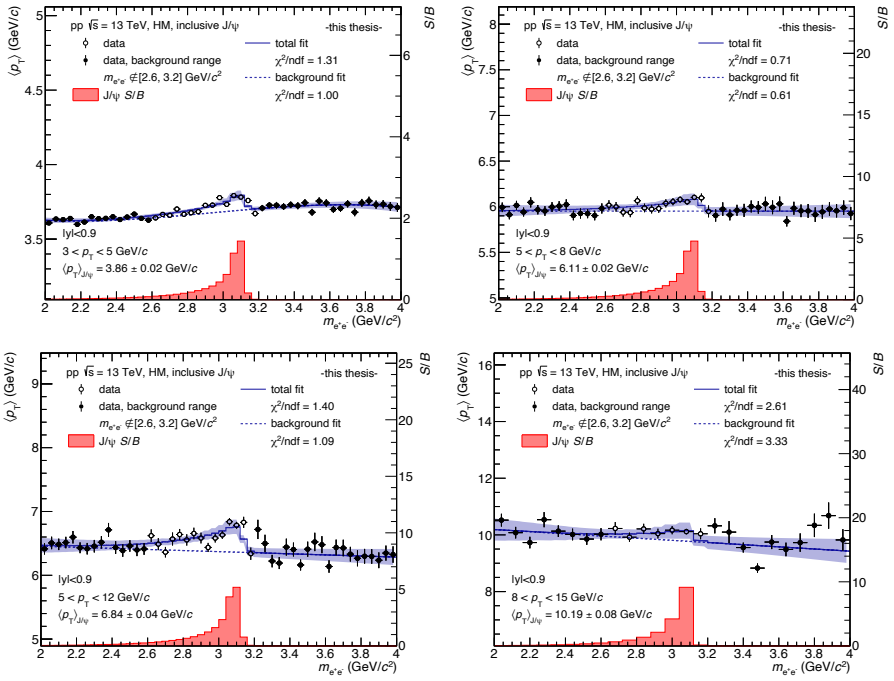

Figure A.15.: Mean p_{T} determination for inclusive J/ψ in HM triggered events.

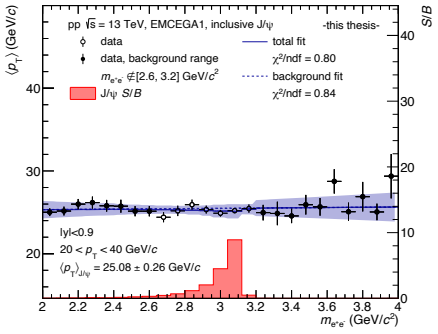

Figure A.16.: Mean p_{T} determination for inclusive J/ψ in high threshold EMCal triggered events.

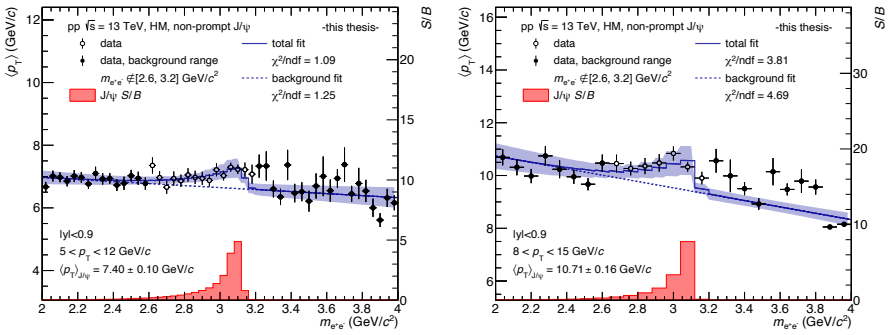

Figure A.17.: Mean p_T determination for non-prompt J/ψ in HM triggered events.

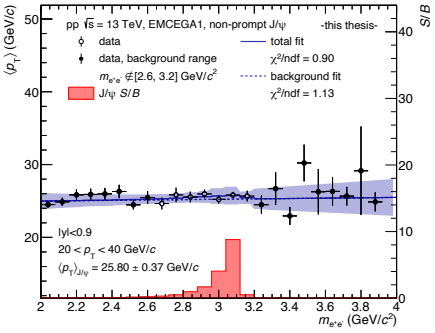

Figure A.18.: Mean p_T determination for non-prompt J/ψ in high threshold EMCal triggered events.

A.3. Acceptance and efficiency correction

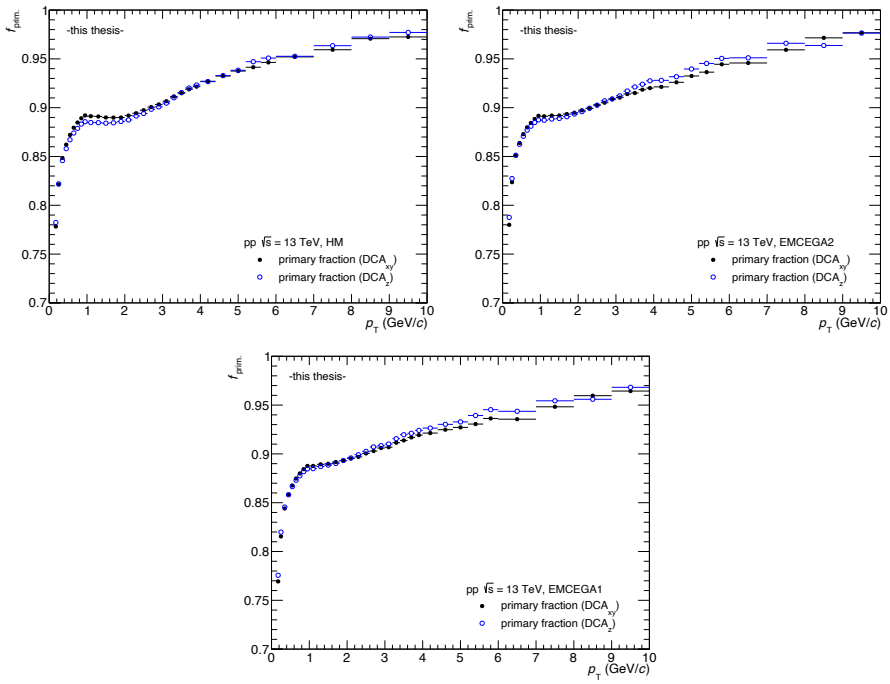

Figure A.19.: Fraction of primary hadrons in HM (*top left*), low (*top right*) and high (*bottom*) threshold EMCal triggered events.

A.4. Correlation signal extraction

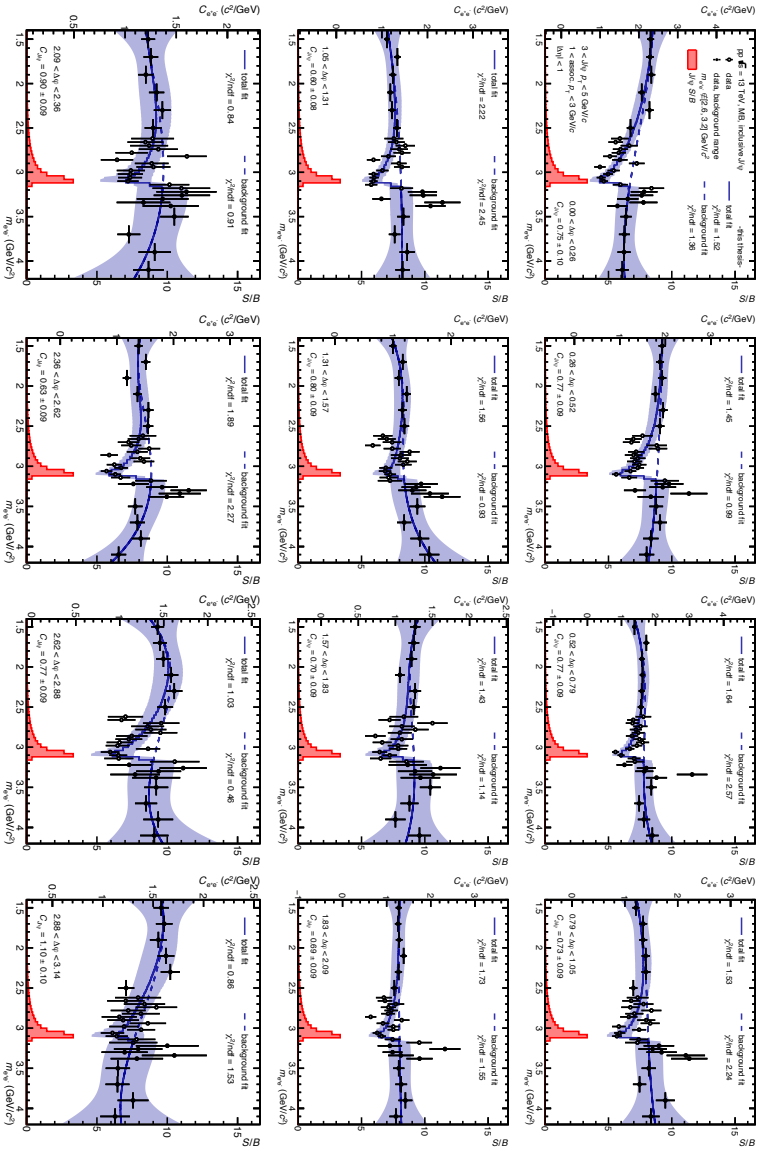

Figure A.20.: Inclusive J/ψ correlation signal extraction via fitting method for exemplary kinematical bin in MB triggered events.

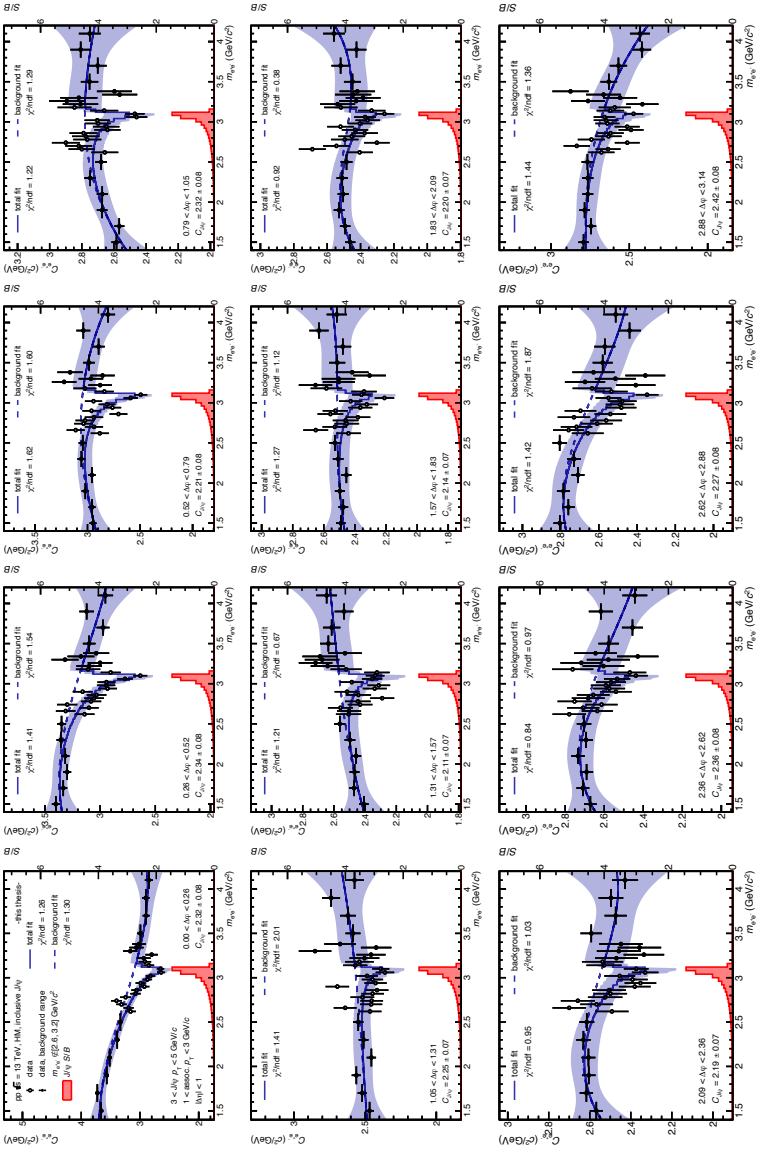

Figure A.21.: Inclusive J/ψ correlation signal extraction via fitting method for exemplary kinematical bin in HM triggered events.

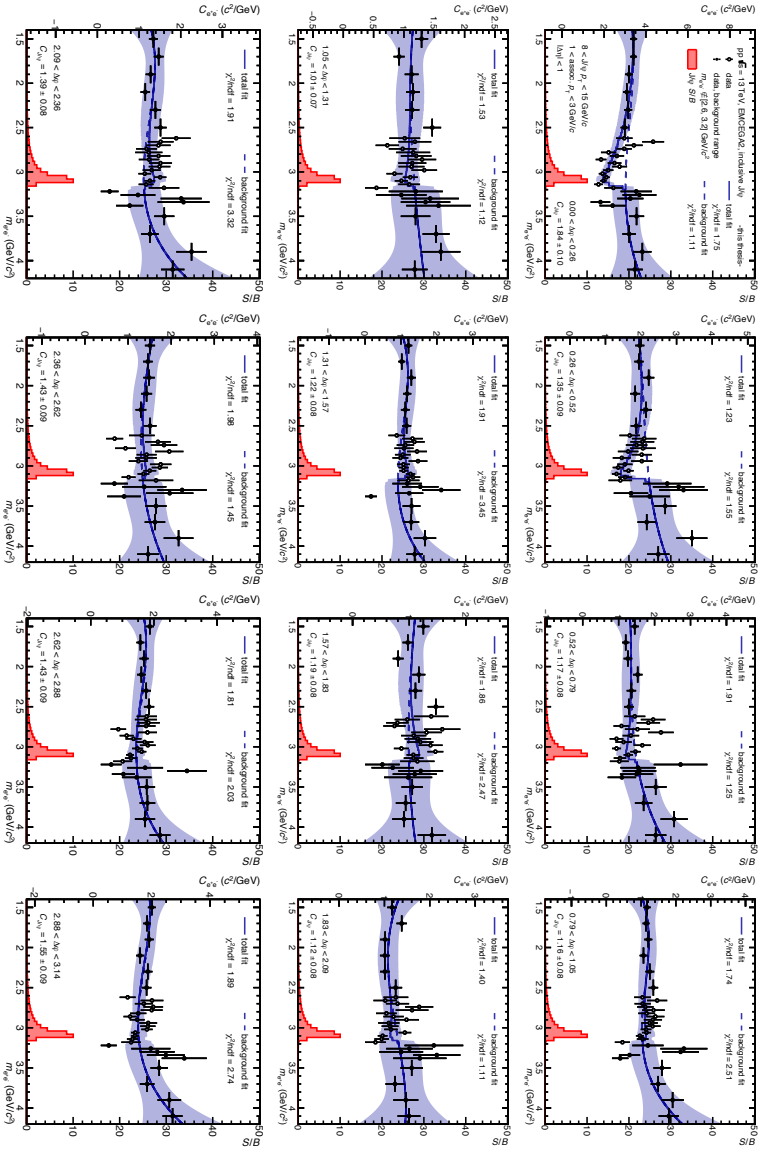

Figure A.22.: Inclusive J/ψ correlation signal extraction via fitting method for exemplary kinematical bin in low threshold EMCal triggered events.

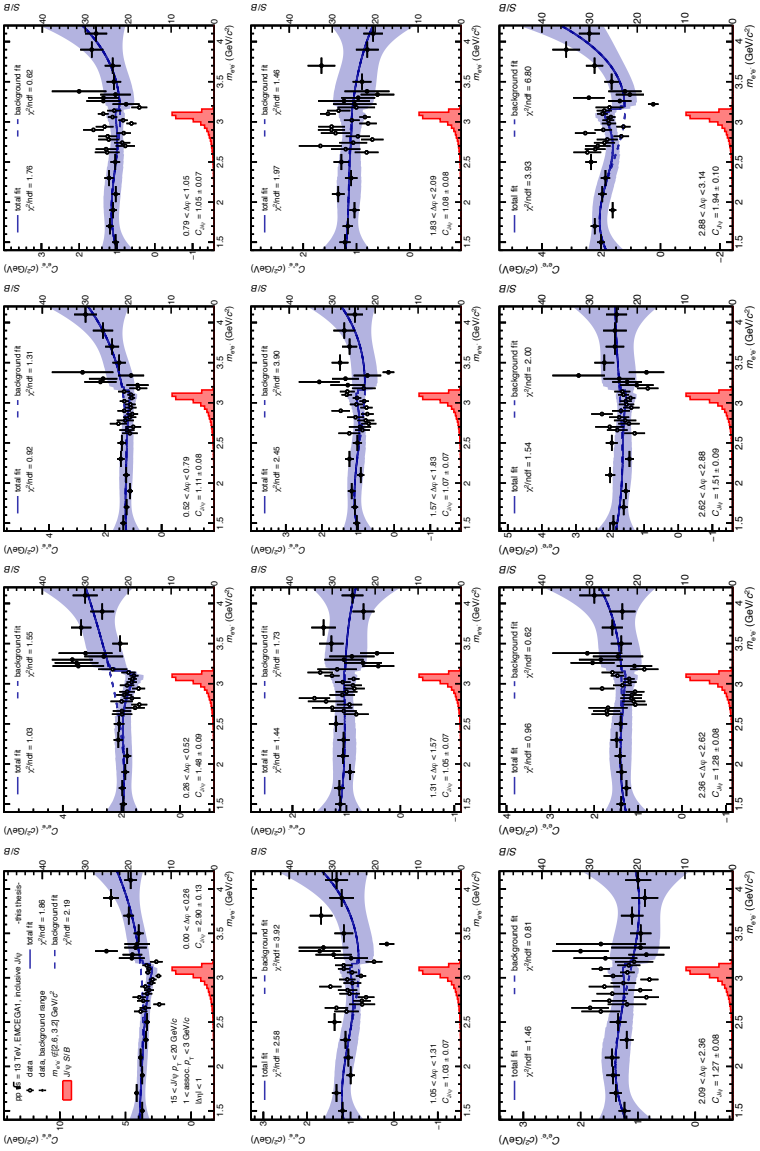

Figure A.23.: Inclusive J/ψ correlation signal extraction via fitting method for exemplary kinematical bin in high threshold EMCal triggered events.

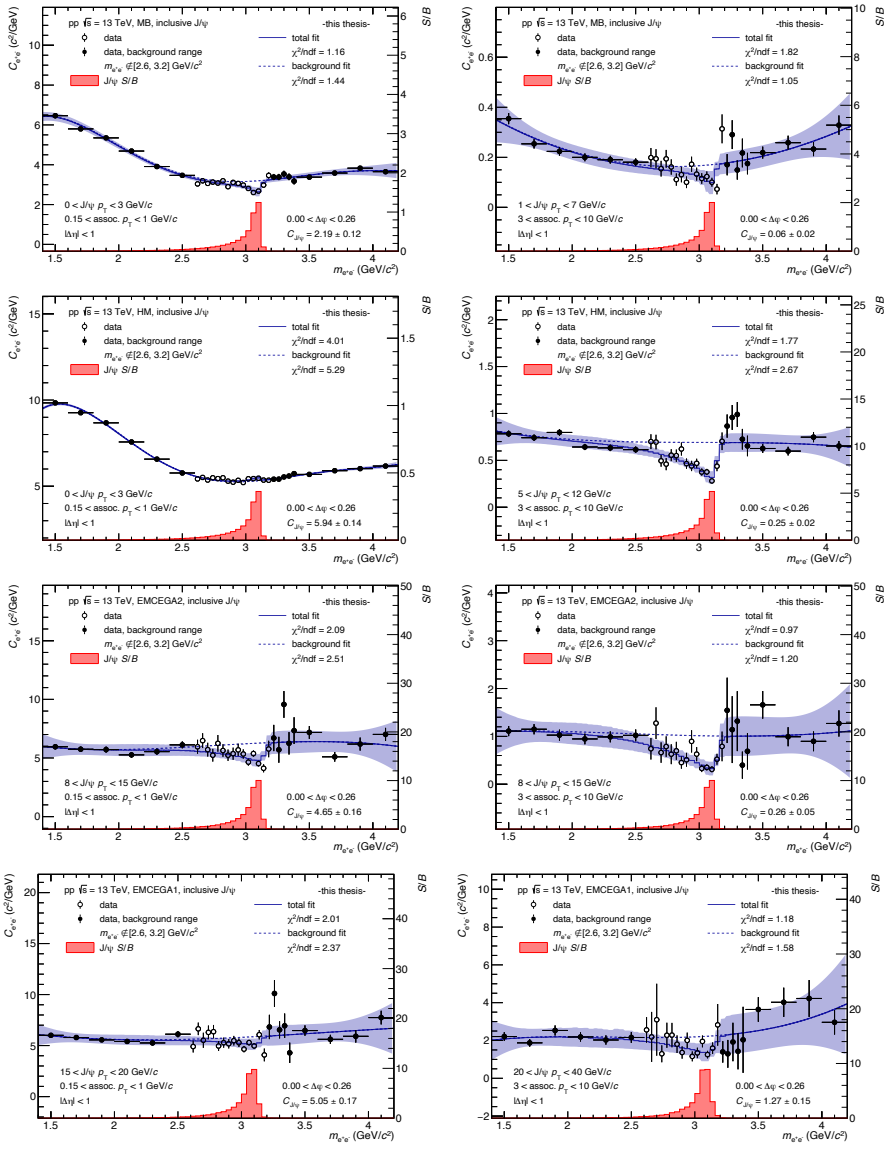

Figure A.24.: Inclusive J/ψ correlation signal extraction via fitting method in exemplary kinematical regimes with high (*left*) and low (*right*) statistics in MB (*top*), HM (*center*) and EMCal (*bottom*) triggered events.

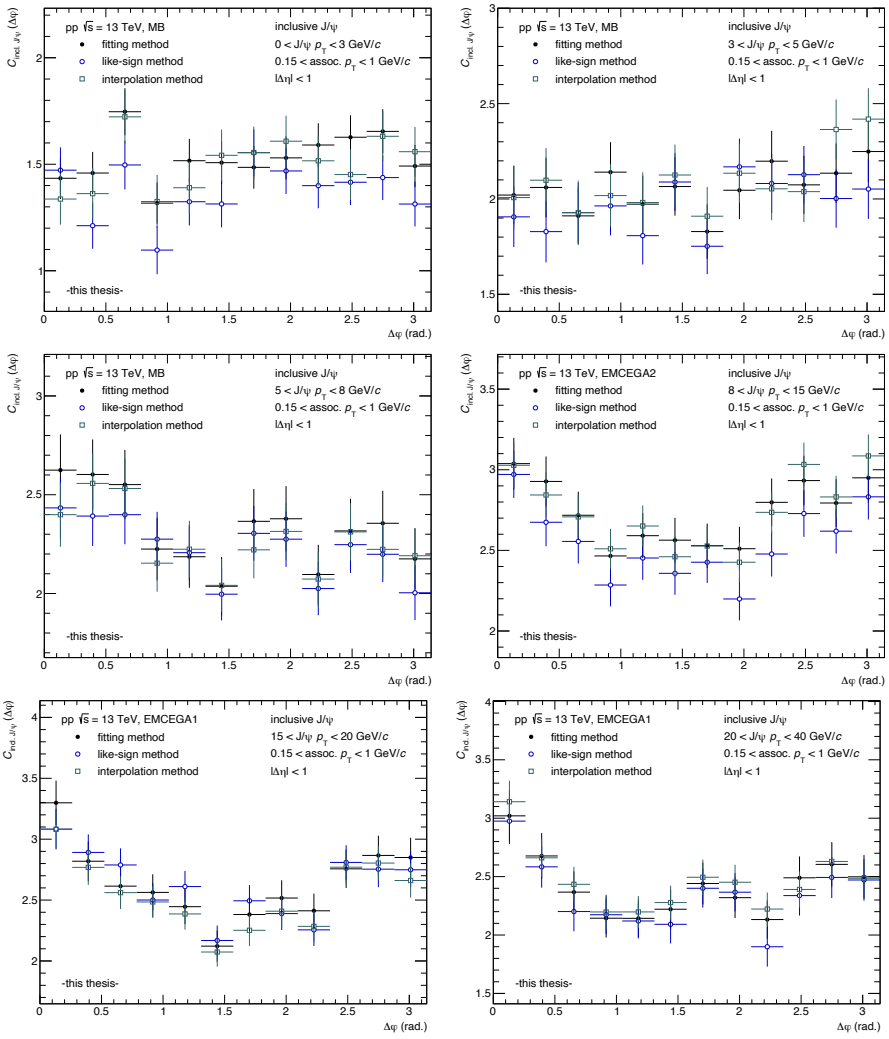

Figure A.25.: Inclusive J/ψ-hadron correlations from the different correlation signal extraction methods in MB (*top*) and EMCal (*bottom*) triggered events.

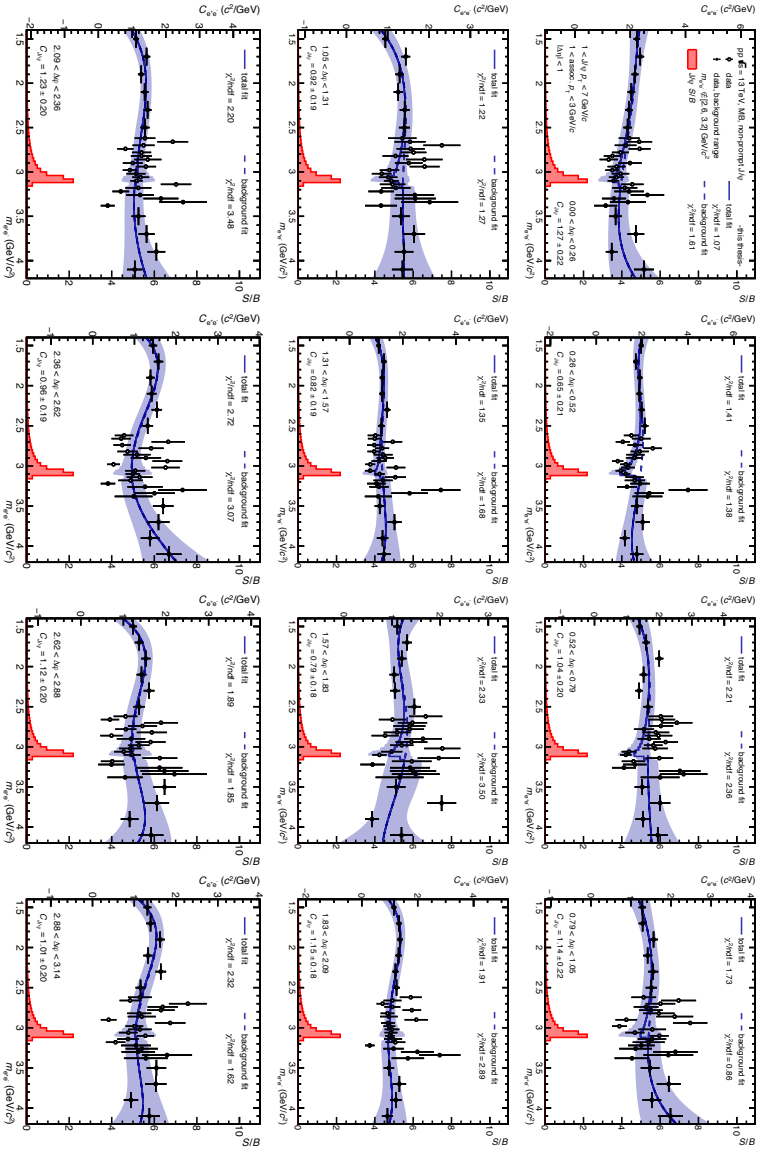

Figure A.26.: Non-prompt J/ψ correlation signal extraction via fitting method for exemplary kinematical bin in MB triggered events.

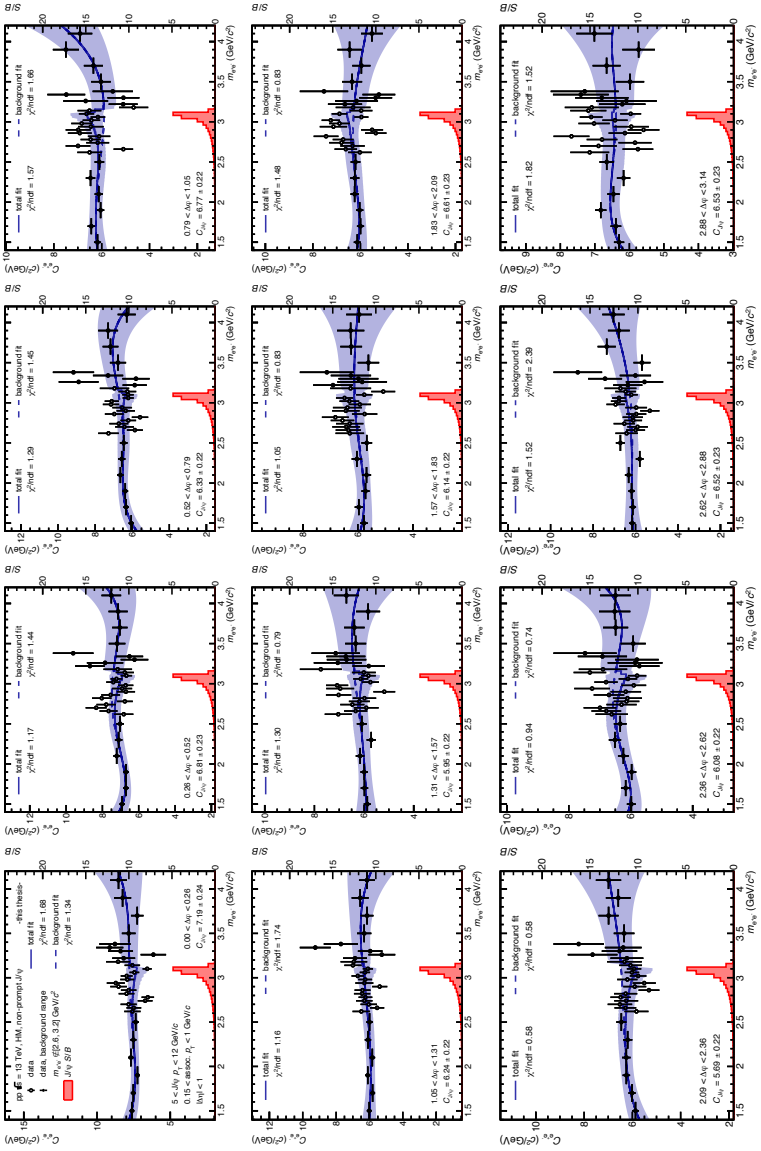

Figure A.27.: Non-prompt J/ψ correlation signal extraction via fitting method for exemplary kinematical bin in HM triggered events.

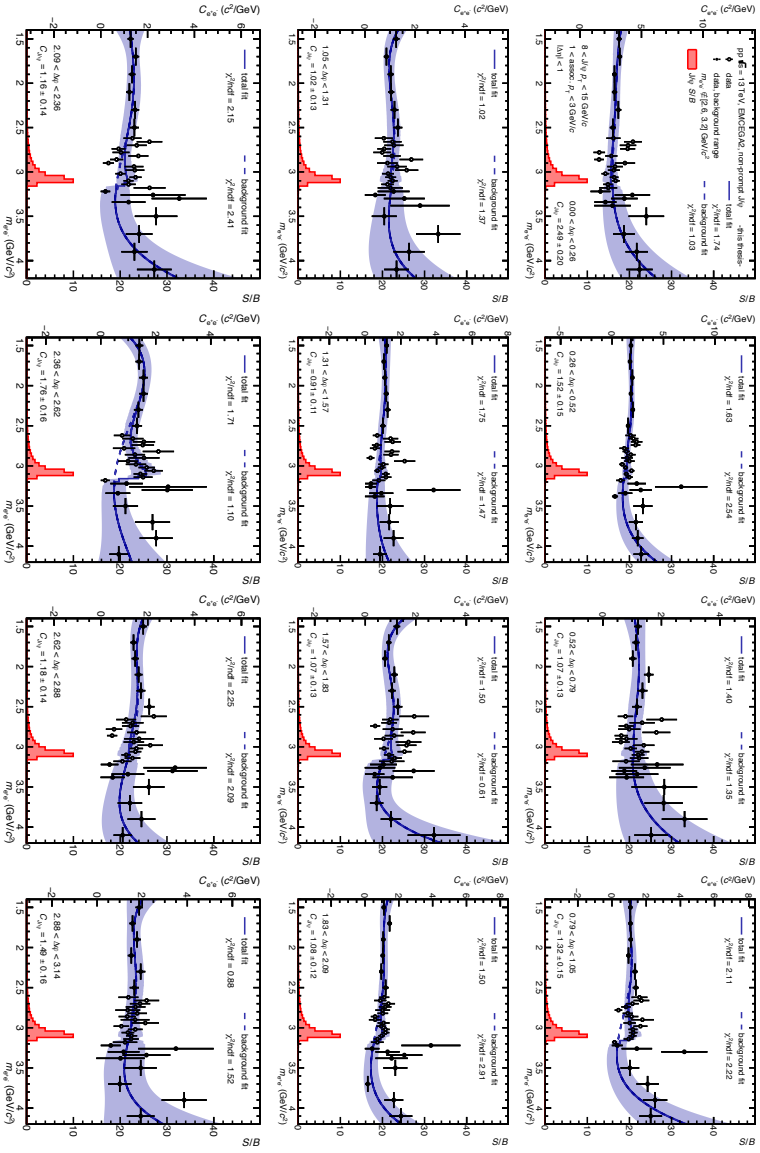

Figure A.28.: Non-prompt J/ψ correlation signal extraction via fitting method for exemplary kinematical bin in low threshold EMCal triggered events.

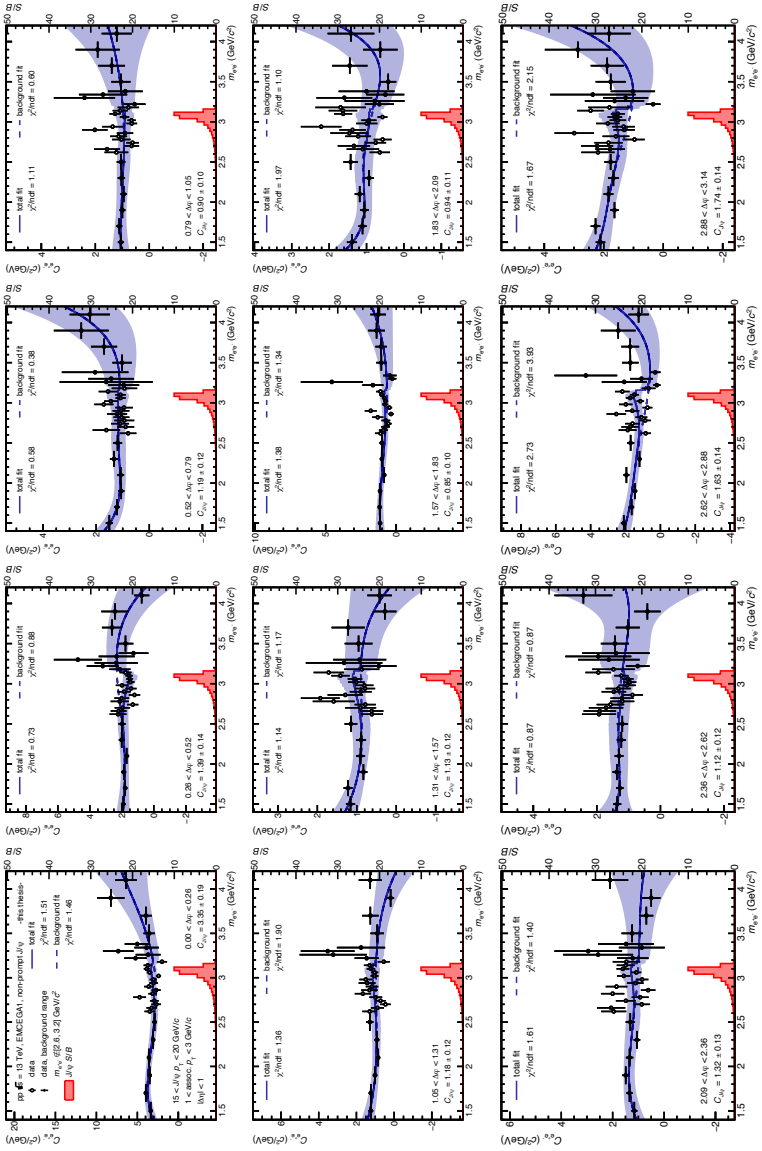

Figure A.29.: Non-prompt J/ψ correlation signal extraction via fitting method for exemplary kinematical bin in high threshold EMCal triggered events.

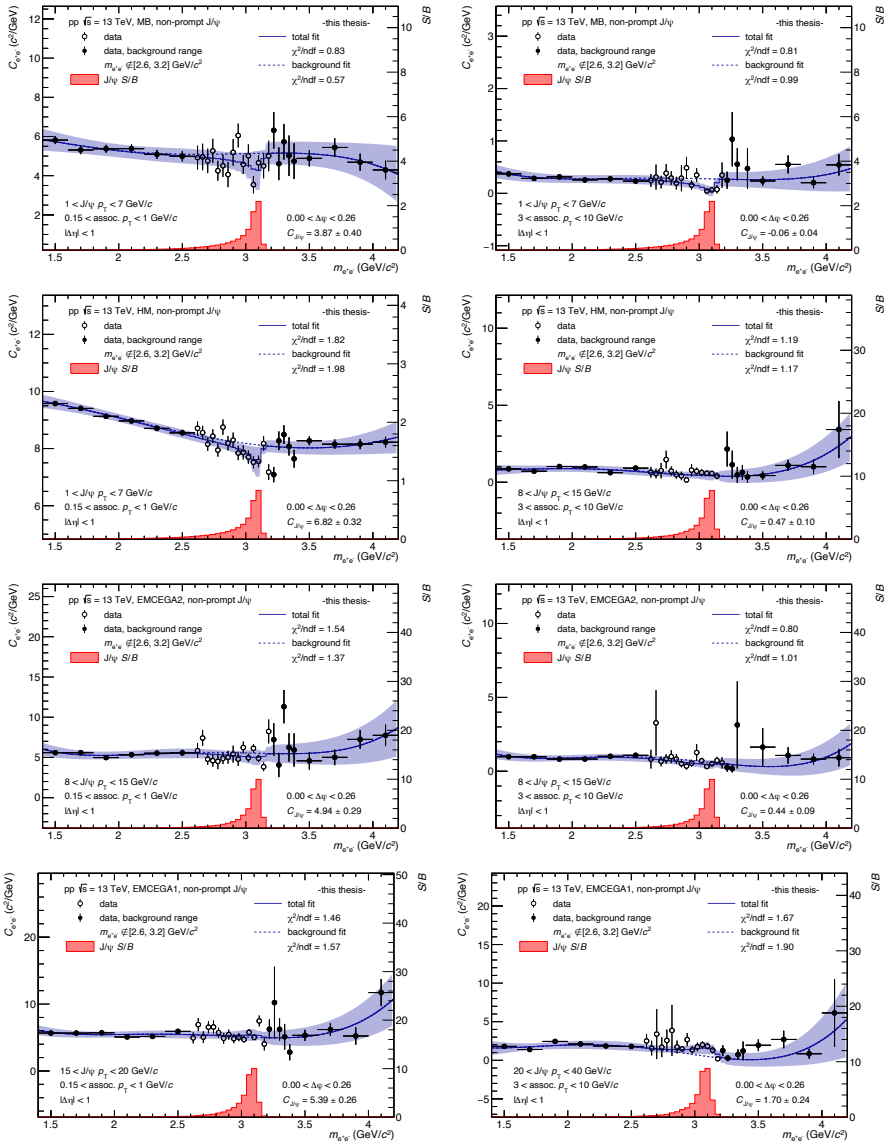

Figure A.30.: Non-prompt J/ψ correlation signal extraction via fitting method in exemplary kinematical regimes with high (*left*) and low (*right*) statistics in MB (*top*), HM (*center*) and EMCal (*bottom*) triggered events.

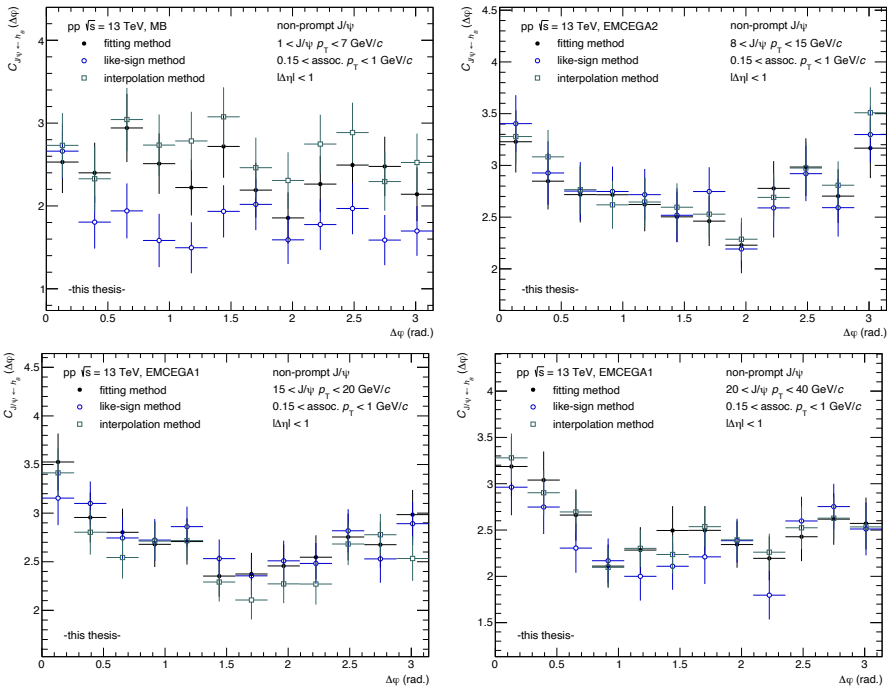

Figure A.31.: Non-prompt J/ψ-hadron correlations from the different correlation signal extraction methods in MB (*top*) and EMCal (*bottom*) triggered events.

A.5. Correlated yield extraction

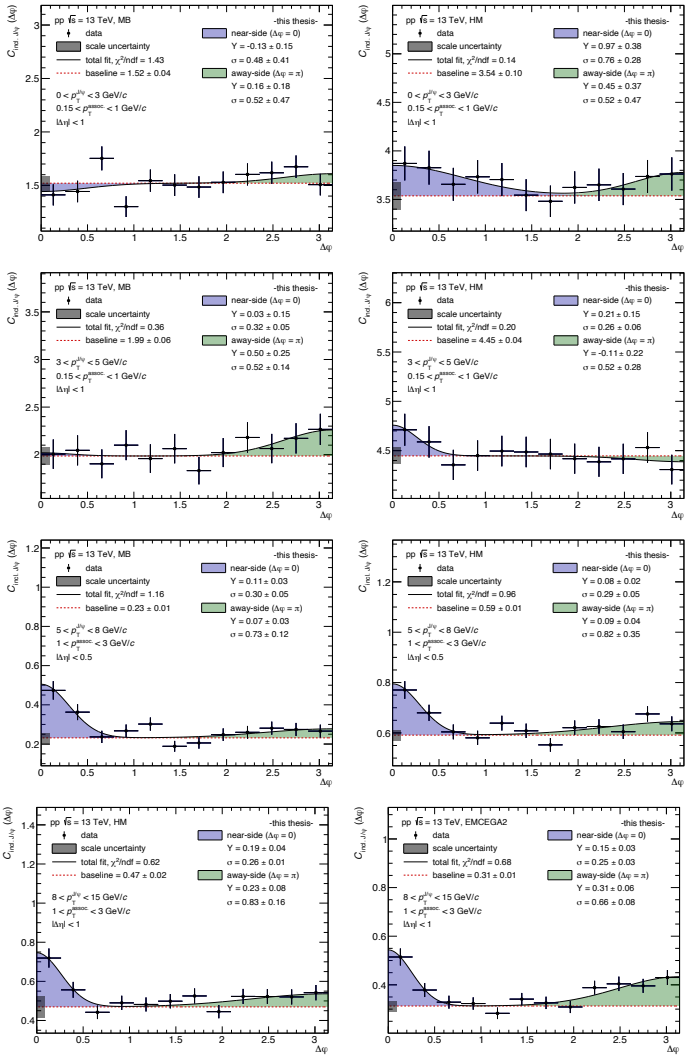

Figure A.32.: Correlated yield extraction for inclusive J/ψ via fit method for selected kinematical bins in MB (*top left*), HM (*top right, bottom left*) and EMCal (*bottom right*) triggered events. The gaussian contributions are depicted as colored areas.

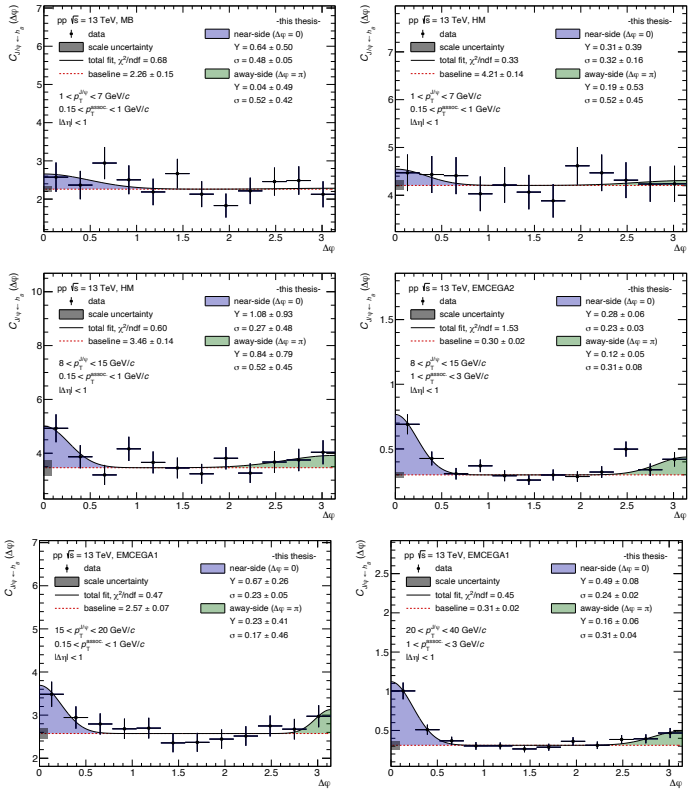

Figure A.33.: Correlated yield extraction for non-prompt J/ψ via fit method for selected kinematical bins in MB (*top left*), HM (*top right, center left*) and EMCal (*center right, bottom*) triggered events. The gaussian contributions are depicted as colored areas.

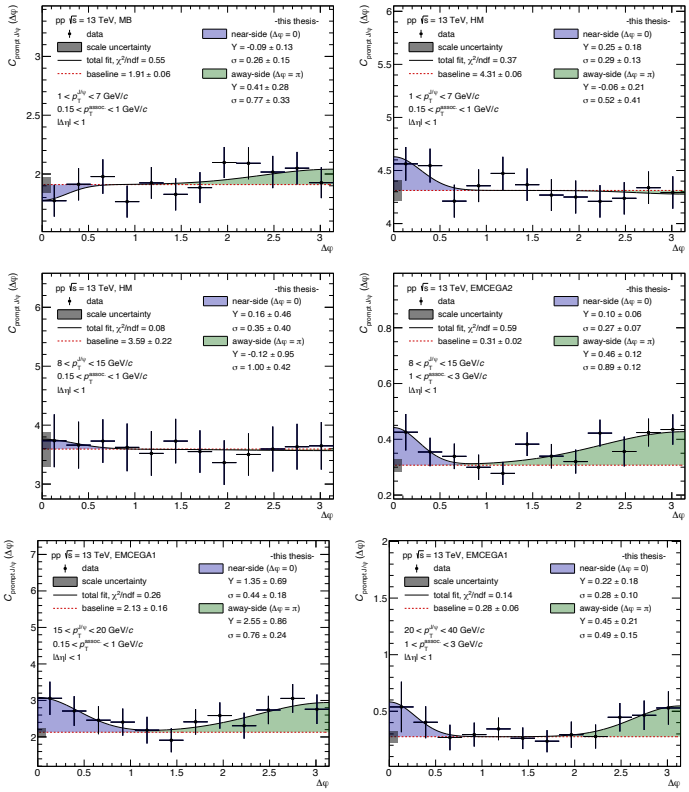

Figure A.34.: Correlated yield extraction for prompt J/ψ via fit method for selected kinematical bins in MB (*top left*), HM (*top right, center left*) and EMCal (*center right, bottom*) triggered events. The gaussian contributions are depicted as colored areas.

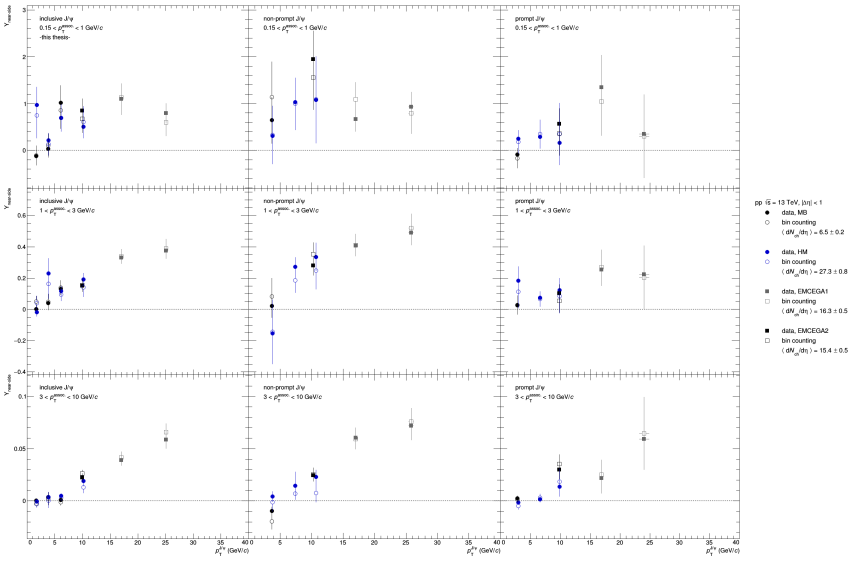

Figure A.35.: Near-side correlated yields from fitting and bin-counting methods for inclusive (*left*), non-prompt (*center*) and prompt (*right*) J/ψ.

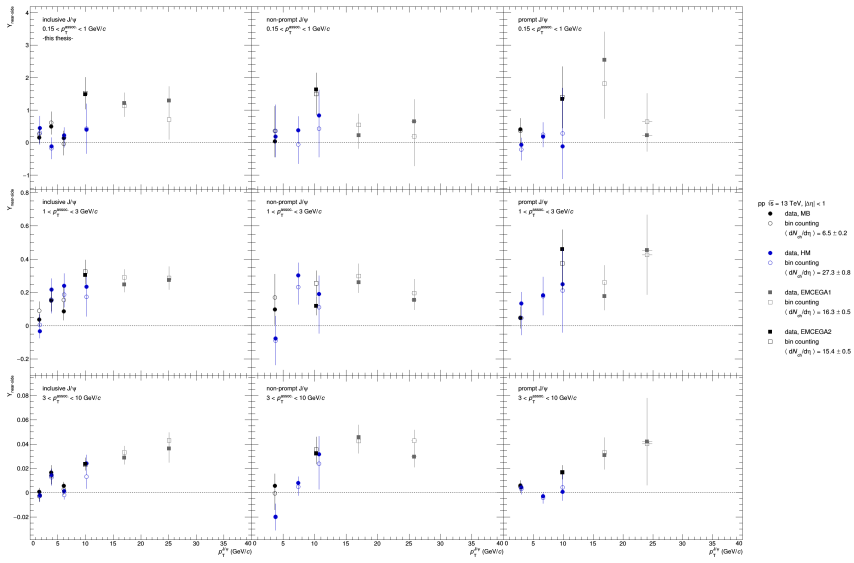

00

Figure A.36.: Away-side correlated yields from fitting and bin-counting methods for inclusive (*left*), non-prompt (*center*) and prompt (*right*) J/ψ.

A.6. Results

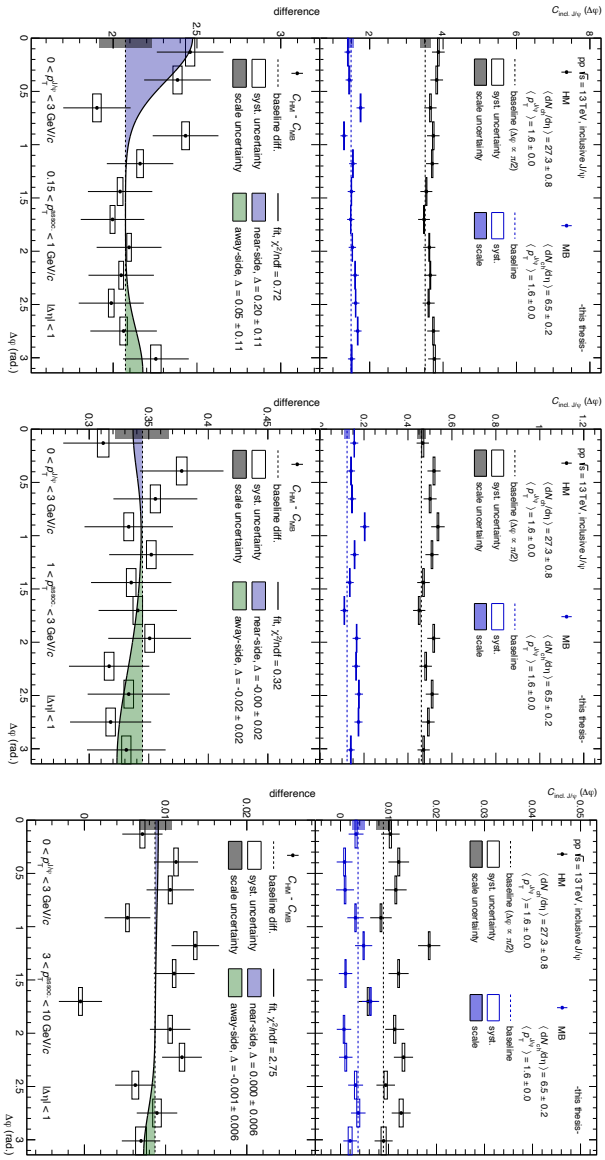

Figure A.37.: Trigger comparison for inclusive J/ψ-hadron correlation function in MB and HM triggered events for J/ψ with $0 \leq p_{\mathrm{T}} \leq 3$ GeV/c.

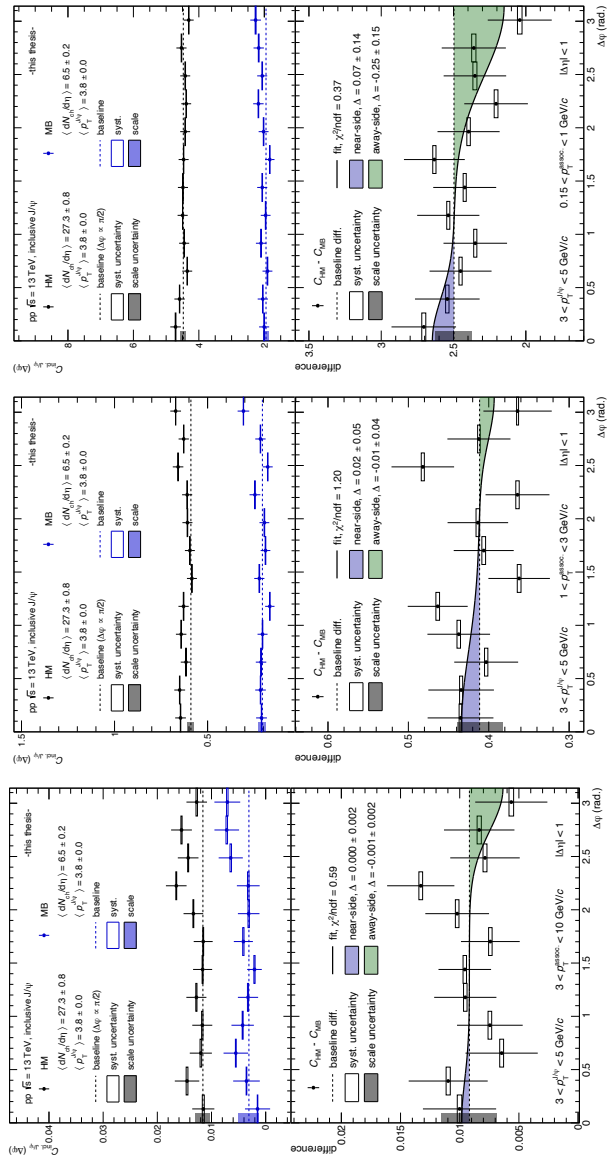

Figure A.38.: Trigger comparison for inclusive J/ψ-hadron correlation function in MB and HM triggered events for J/ψ with $3 \leq p_{\mathrm{T}} \leq 5$ GeV/c.

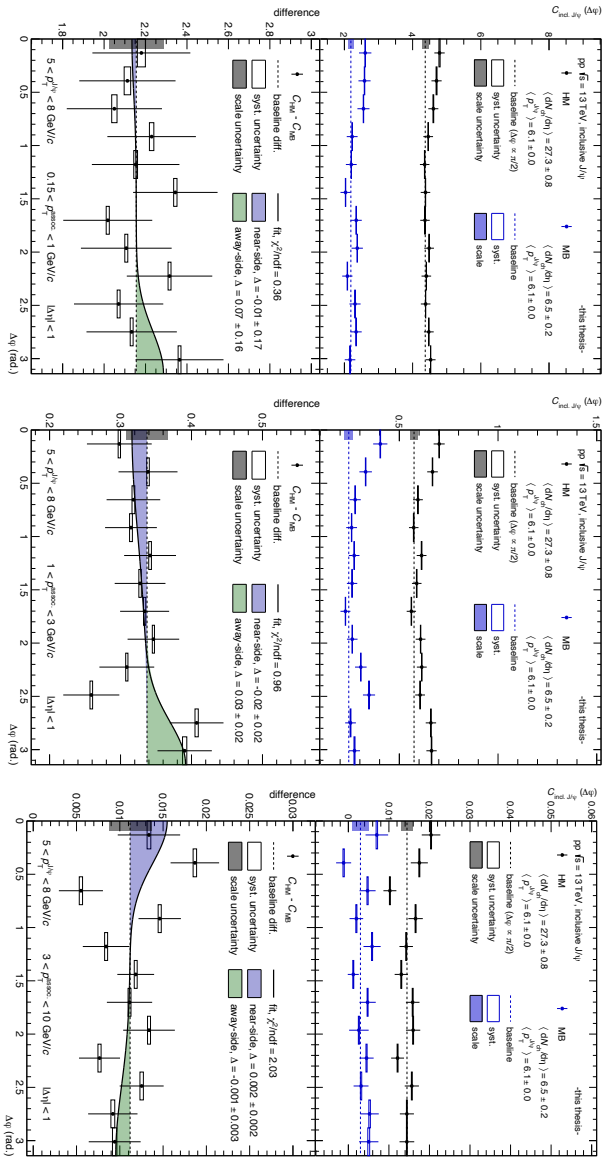

Figure A.39.: Trigger comparison for inclusive J/ψ-hadron correlation function in MB and HM triggered events for J/ψ with $5 \leq p_{\mathrm{T}} \leq 8$ GeV/c.

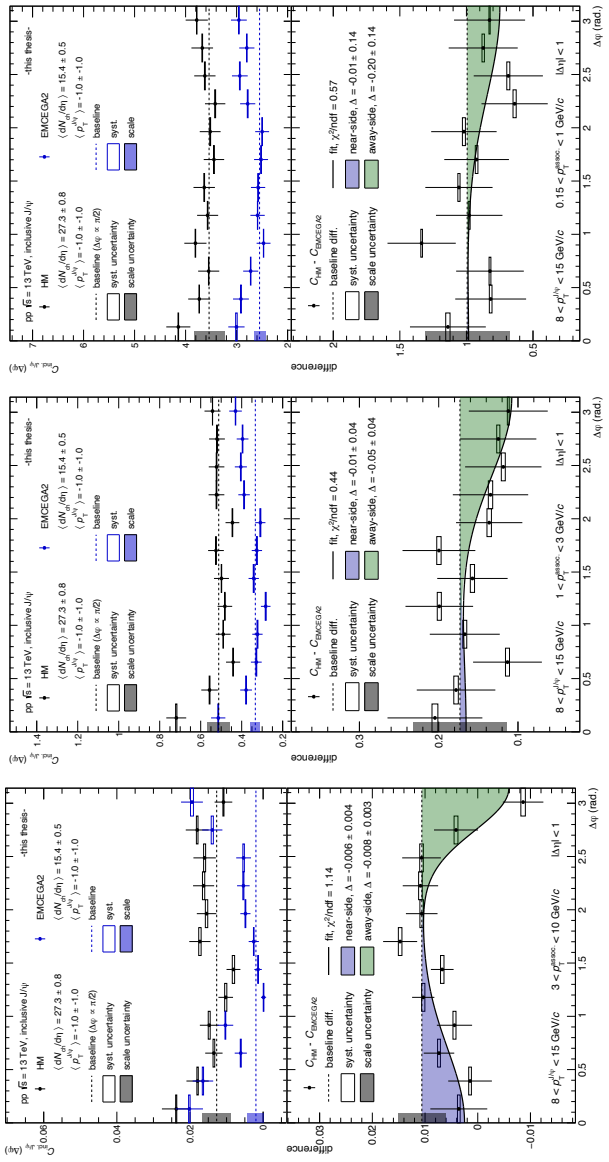

Figure A.40.: Trigger comparison for inclusive J/ψ-hadron correlation function in low threshold EMCal and HM triggered events.

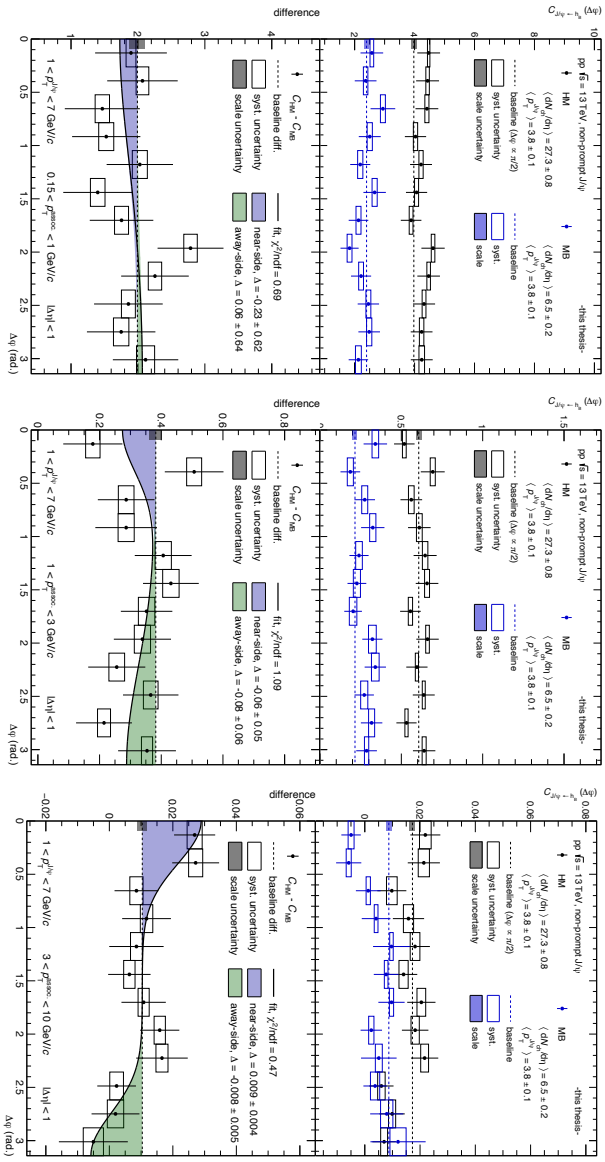

Figure A.41.: Trigger comparison for non-prompt J/ψ-hadron correlation function in MB and HM triggered events for J/ψ.

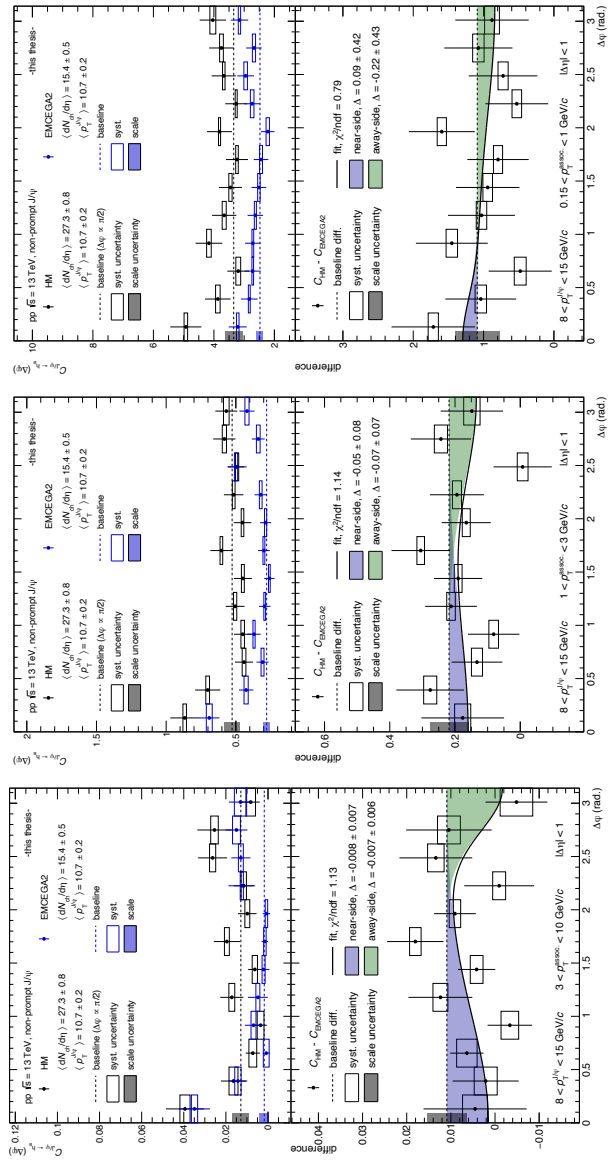

Figure A.42.: Trigger comparison for non-prompt J/ψ-hadron correlation function in low threshold EMCal and HM triggered events.

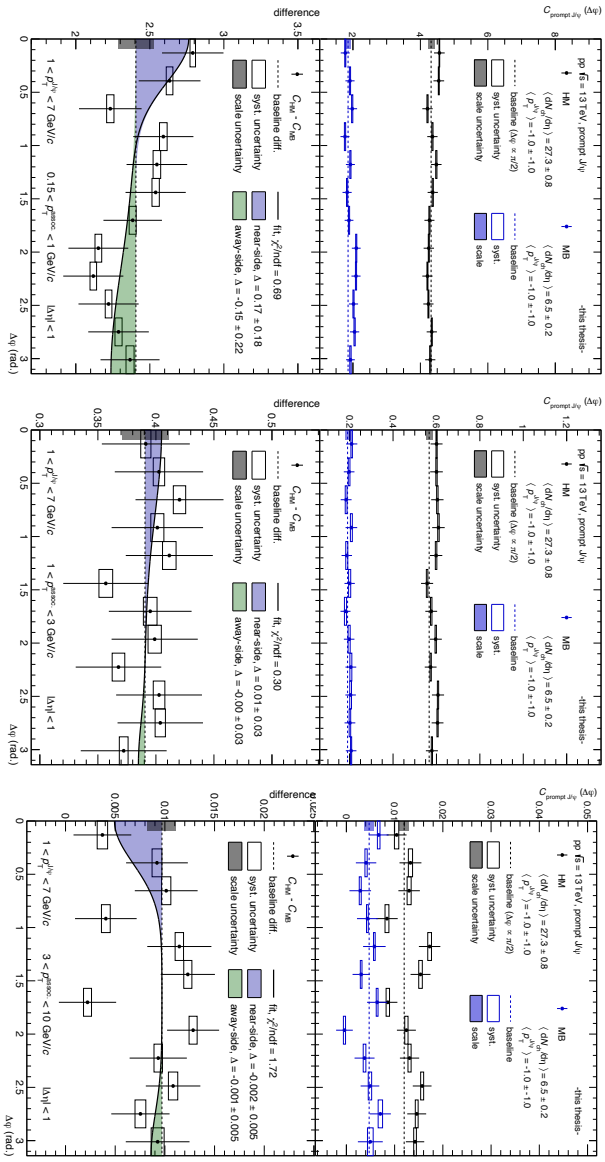

Figure A.43.: Trigger comparison for prompt J/ψ-hadron correlation function in MB and HM triggered events for J/ψ.

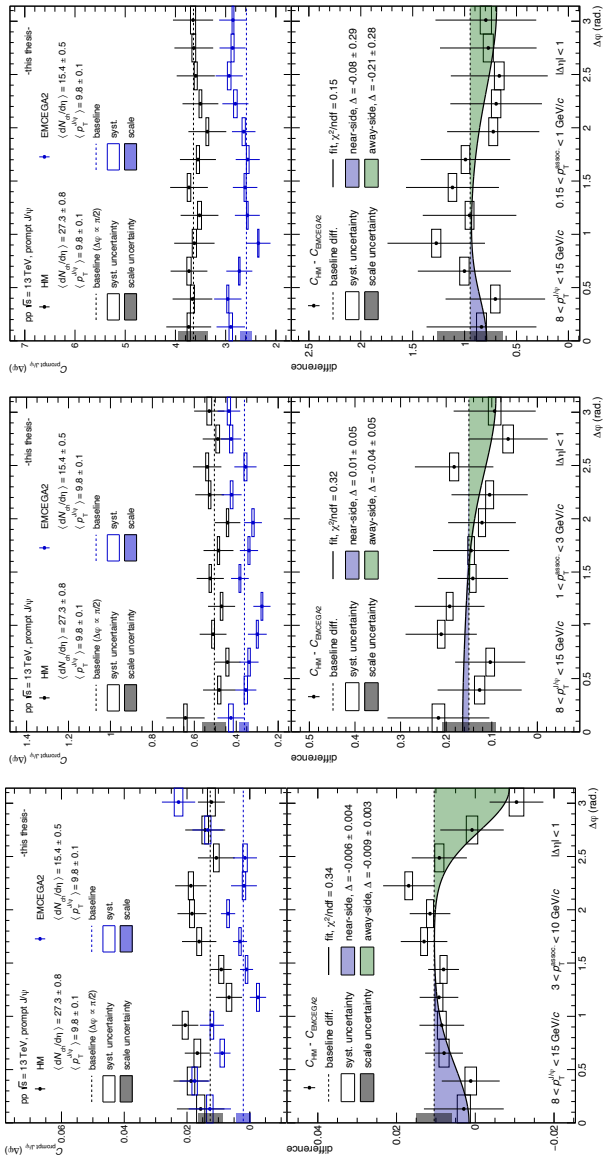

Figure A.44.: Trigger comparison for prompt J/ψ-hadron correlation function in low threshold EMCal and HM triggered events.

B. List of acronyms

AGS Alternating Gradient Synchrotron . . . 23
ALICE A Large Ion Collider Experiment . . . 3
ATLAS A Toroidal LHC Apparatus . . . 3
BNL Brookhaven National Laboratory . . . 3
CEM Color Evaporation Model . . . 16
CERN Conseil Européen pour la Recherche Nucléaire . . . 3
CGC Color Glass Condensate . . . 21
CMS Compact Muon Solenoid . . . 3
CSM Color Singlet Model . . . 16
CTP Central Trigger Processor . . . 38
DCA Distance of Closest Approach . . . 56
DCal Di-Jet Calorimeter . . . 32
DPG Data Preparation Group . . . 46
EMCal Electromagnetic Calorimeter . . . 32
EMCEGA EMCal electron/gamma trigger . . . 39
EWT Electro-Weak Theory . . . 6
FF first-first . . . 67
FONLL Fixed-Order-Next-to-Leading Logarithm . . . 21
FS first-second . . . 67
HEP high-energy physics . . . 14
HM High Multiplicity . . . 33
ICEM Improved Color Evaporation Model . . . 17
ITS Inner Tracking System . . . 31
L0 Level 0 . . . 38
L1 Level 1 . . . 38
L2 Level 2 . . . 38
LEP Large Electron Positron Collider . . . 27
LHC Large Hadron Collider . . . 3

LHCb LHC-beauty . . . 3
LO leading order . . . 18
MB Minimum Bias . . . 33
MC Monte Carlo . . . 4
NLO next-to-leading order . . . 18
NNLO next-to-next-to leading order . . . 18
NRQCD non-relativistic QCD . . . 16
PDF parton distribution function . . . 14
PHENIX Pioneering High Energy Nuclear Interaction eXperiment . . . 25
PHOS Photon Spectrometer . . . 32
PID particle identification . . . 30
PS Proton Synchrotron . . . 29
pQCD perturbative QCD . . . 10
QA quality assurance . . . 47
QCD Quantum Chromodynamics . . . 6
QED Quantum Electrodynamics . . . 6
QGP Quark-Gluon Plasma . . . 4
QFT Quantum Field Theory . . . 6
RHIC Relativistic Heavy Ion Collider . . . 24
RMS root mean square . . . 107
SDD Silicon Drift Detector . . . 33
SLAC Stanford Linear Accelerator Center . . . 2
SPD Silicon Pixel Detector . . . 33
SPS Super Proton Synchrotron . . . 24
SS second-second . . . 67
SSD Silicon Strip Detector . . . 33
TOF Time-Of-Flight . . . 32
TPC Time Projection Chamber . . . 32
TRD Transition Radiation Detector . . . 32
V0HM V0 high multiplicity trigger . . . 39
WLCG Worldwide LHC Computing Grid . . . 41

C. List of publications and conference contributions

111 publications with the ALICE collaboration since 2017 (status 26.09.2020)

Publications with a significant contribution by LA

- L. Altenkämper, F. Bock, C. Loizides and N. Schmidt, *Applicability of transverse mass scaling in hadronic collisions at energies available at the CERN Large Hadron Collider*, published in Phys. Rev. C 96 (2017) 6, 064907
- L. Altenkämper (for the ALICE Collaboration), *Charmonium production in pp collisions with ALICE at the LHC*, published in PoS ICHEP2018 (2019) 040
- ALICE collaboration, J/ψ*-hadron correlations at mid-rapidity in pp collisions at* $\sqrt{s}$ = 13 *TeV*, approved by the collaboration and in preparation [analyzer, paper committee chair]
- ALICE collaboration, *Inclusive* J/ψ *production at mid-rapidity in pp collisions at* $\sqrt{s}$ = 13 *TeV*, approved by the collaboration and in preparation [analyzer, paper committee member]

Conference contributions

- L. Altenkämper (for the ALICE Collaboration), *Angular correlations between* J/ψ *mesons and charged hadrons in proton-proton collisions at* $\sqrt{s} = 13$ *TeV with ALICE*, poster at QM conference 2018 in Venice, Italy
- L. Altenkämper (for the ALICE Collaboration), *Charmonium production in pp collisions with ALICE at the LHC*, presentation at ICHEP conference 2018 in Seoul, South Korea

Graphic design: Communication Division, UiB / Print: Skipnes Kommunikasjon AS

uib.no

ISBN: 9788230855737 (print)
9788230853863 (PDF)